Naval Research Laboratory

Stennis Space Center, MS 39529-5004

NRL/MR/7320--10-9283

Validaton Test Report for the Coupled Ocean/Atmosphere Mesoscale Prediction System (COAMPS) Version 5.0

RICHARD A. ALLARD
TIMOTHY J. CAMPBELL
TRAVIS A. SMITH
TOMMY G. JENSEN
JAMES A. CUMMINGS

Ocean Dynamics and Prediction Branch
Oceanography Division

SUE CHEN
JAMES DOYLE
XIAODONG HONG

Atmospheric Dynamics and Prediction Branch
Marine Meteorology Division

R. JUSTIN SMALL

Jacobs Technology
Stennis Space Center, Mississippi

SUZANNE N. CARROLL

QinetiQ North America
Stennis Space Center, Mississippi

September 27, 2010

REPORT DOCUMENTATION PAGE

Form Approved
OMB No. 0704-0188

1. REPORT DATE *(DD-MM-YYYY)*	**2. REPORT TYPE**	**3. DATES COVERED** *(From - To)*
27-09-2010	Memorandum Report	

4. TITLE AND SUBTITLE

Validation Test Report for the Coupled Ocean/Atmosphere Mesoscale Prediction System (COAMPS) Version 5.0

5a. CONTRACT NUMBER

5b. GRANT NUMBER

5c. PROGRAM ELEMENT NUMBER
0602435N

6. AUTHOR(S)

Richard A. Allard, Timothy J. Campbell, Travis A. Smith, Tommy G. Jensen, James A. Cummings, Sue Chen, James Doyle, Xiaodong Hong, R. Justin Small,* and Suzanne N. Carroll†

5d. PROJECT NUMBER

5e. TASK NUMBER

5f. WORK UNIT NUMBER
73-6057-00-5

7. PERFORMING ORGANIZATION NAME(S) AND ADDRESS(ES)

Naval Research Laboratory
Oceanography Division
Stennis Space Center, MS 39529-5004

8. PERFORMING ORGANIZATION REPORT NUMBER

NRL/MR/7320--10-9283

9. SPONSORING / MONITORING AGENCY NAME(S) AND ADDRESS(ES)

Office of Naval Research
One Liberty Center
875 North Randolph Street
Arlington, VA 22203

10. SPONSOR / MONITOR'S ACRONYM(S)

ONR

11. SPONSOR / MONITOR'S REPORT NUMBER(S)

12. DISTRIBUTION / AVAILABILITY STATEMENT

Approved for public release; distribution is unlimited.

13. SUPPLEMENTARY NOTES

*Jacobs Technology, Stennis Space Center, Mississippi 39529
†QinetiQ North America, Stennis Space Center, Mississippi 39529

14. ABSTRACT

The Coupled Ocean/Atmosphere Mesoscale Prediction System (COAMPS) is coupled utilizing the Earth System Modeling Framework and validated for five test cases: 1) Adriatic Sea, 2) Ligurian Sea, 3) Monterey Bay, CA, 4) Kuroshio Extension System Study and 5) Coastal Peru. The COAMPS system makes use of meteorological observations including radiosondes, satellite data, ship reports, and ocean observations with time-dependent global atmospheric lateral boundary conditions from the Navy Operational Global Atmospheric Prediction System (NOGAPS). Time-dependent ocean boundary conditions are derived from global the Navy Coastal Ocean Model. Atmospheric and oceanographic forecast model output includes surface and upper-air meteorological fields, sea surface temperature (SST), three-dimensional (3D) ocean temperature (T), and salinity (S), velocity, two-dimensional (2D) mixed layer depth (MLD) and ocean acoustic products. The validation efforts contained in this report focus on the upper ocean (mixed layer), heat fluxes, near surface winds, temperature, moisture, the air-sea interaction, and marine boundary layer characteristics.

15. SUBJECT TERMS

ESMF	NCOM	Air-sea interaction
COAMPS	Coupling	Surface fluxes

16. SECURITY CLASSIFICATION OF:			**17. LIMITATION OF ABSTRACT**	**18. NUMBER OF PAGES**	**19a. NAME OF RESPONSIBLE PERSON**
a. REPORT	**b. ABSTRACT**	**c. THIS PAGE**			Richard A. Allard
Unclassified	Unclassified	Unclassified	UL	172	**19b. TELEPHONE NUMBER** *(include area code)* (228) 688-4894

Standard Form 298 (Rev. 8-98)
Prescribed by ANSI Std. Z39.18

TABLE OF CONTENTS

FIGURES AND TABLES

1.0 INTRODUCTION

The increasing awareness of the importance of the ocean and atmosphere (El Niño, hurricane events, etc.) to weather forecasting necessitates the coupling of the Navy Coupled Ocean Model (NCOM) Version 4.0 to the atmospheric COAMPS®[1] model. In a fully coupled mode, COAMPS and NCOM models can be integrated concurrently so that precipitation and surface fluxes of heat, moisture and momentum are exchanged across the air-sea interface. This coupling is facilitated through the Earth System Modeling Framework (ESMF).

The purpose of this document is to validate the performance of COAMPS using available observational data. The system can run in a one-way (atmosphere "forces" ocean) or two-way (atmosphere "forces" ocean and ocean "forces" atmosphere) coupling. The COAMPS system makes use of meteorological observations including radiosondes, satellite data, ship reports, and ocean observations with time-dependent global oceanographic lateral boundary conditions from the Navy Operational Global Atmospheric Prediction System (NOGAPS). Ocean observations and bathymetry for COAMPS are derived from global NCOM. Atmospheric and oceanographic forecast model output includes surface and upper air fields, sea surface temperature (SST), three-dimensional (3D) ocean temperature (T), and salinity (S), velocity, two-dimensional (2D) mixed layer depth (MLD) and ocean acoustic products. The validation efforts contained in this report focus on the upper ocean (mixed layer) heat fluxes, near surface winds, temperature, moisture, the air-sea interaction, and the marine boundary layer characteristics. Coupling is both one-way and two-way (with and without data assimilation) for all test cases except one. Atmospheric data assimilation can be performed using either three-dimensional multi-variate optimum interpolation (MVOI) or three-dimensional variational assimilation (3D-VAR) using the NRL Atmospheric Variational Data Assimilation System (NAVDAS, Daley and Barker, 2000, 2001)). For the purpose of this report, only MVOI was used for the atmospheric data assimilation. Ocean data assimilation is facilitated through the Navy Coastal Ocean Data Assimilation (NCODA) 3D system (only for Test Cases 3 and 5). The NCODA is a fully three-dimensional MVOI routine that produces simultaneous analyses of temperature, salinity, geopotential, and vector velocity (Cummings, 2006). NCODA ingests about 13 GB of observation and global model data for a 48-hour forecast with a 6-hour update cycle. Fig. 1 illustrates how COAMPS operates for a two-way coupled simulation.

[1] COAMPS is a registered trademark of the Naval Research Laboratory.

Manuscript approved September 2, 2010.

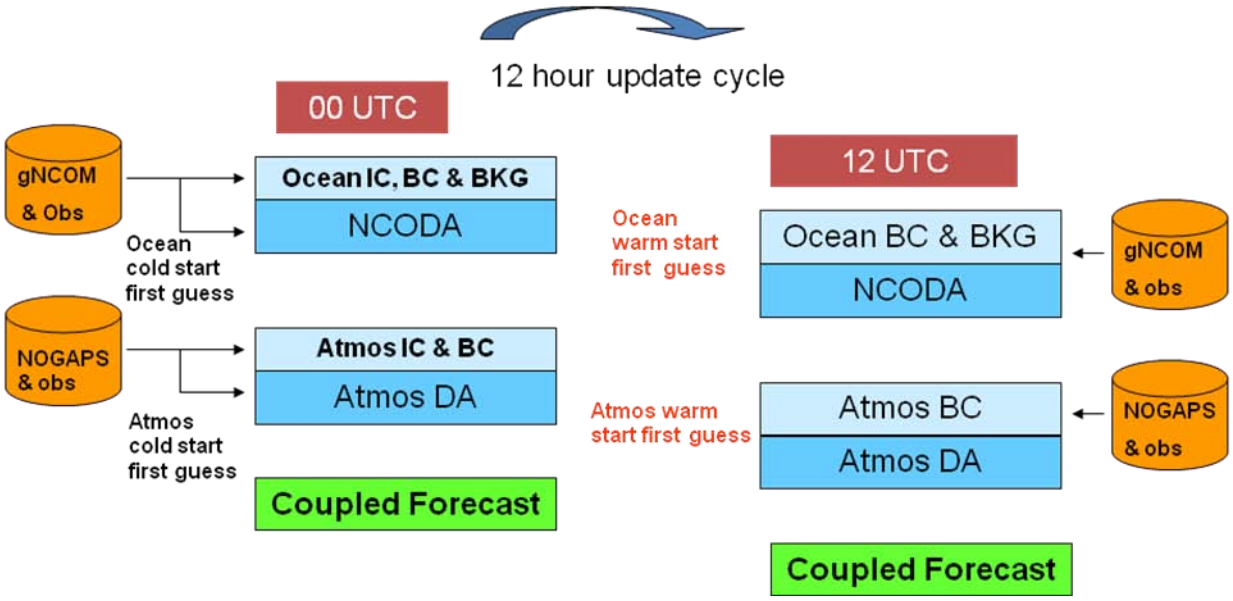

Figure 1: Two-Way Coupled Data Assimilation (DA) System. IC and BC stand for initial and boundary conditions, respectively. BKG stands for background.

2.0 MODEL DESCRIPTIONS

2.1 Coupled Ocean/Atmosphere Mesoscale Prediction System (COAMPS)

The Naval Research Laboratory (NRL) Marine Meteorology Division's COAMPS model makes both mesoscale and microscale predictions of the atmosphere and ocean. The atmospheric elements of COAMPS are used operationally by the U.S. Navy for numerical weather prediction in various regions around the world.

The COAMPS atmospheric model is a finite-difference approximation to the fully compressible, nonhydrostatic equations. The surface fluxes are computed following the Louis et al. (1979) and Fairall et al. (1996) formulations, which make use of Monin-Obukhov similarity theory. A force-restore method is used to parameterize the surface energy budget. The subgrid-scale moist convective processes are parameterized using an approach following Kain and Fritsch (1990). The grid-scale evolution of the moist processes is explicitly predicted from budget equations for cloud water, cloud ice, rain, snow, and water vapor (Rutledge and Hobbs 1983). The parameterization of short- and long-wave radiation processes is accomplished following Harshvardhan et al. (1987), with an option for a four stream method following Fu and Liou (1993). In this study, the Harshvardhan radiation is used exclusively. The planetary boundary-layer and free-atmospheric turbulent mixing and diffusion are modeled using a prognostic equation for the turbulent kinetic energy budget based on a method derived from the level 2.5 formulation of Mellor and Yamada (1982). COAMPS can use an arbitrary number of terrain following vertical levels. In these tests, COAMPS employs 30-40 vertically-stretched levels.

COAMPS consists of two data assimilation options: the 3D MVOI system and the three-dimensional variational analysis, NAVDAS. Both options include data quality control, analysis, initialization, and forecast model components (Hodur, 1997; Chen et al., 2003; Daley and Barker, 2000, 2001). In this validation study, only the MVOI system was tested with the coupled system, however NAVDAS has been fully evaluated as a viable data assimilation system (Goerss et al., 2003). Data assimilation is initiated by the prior 12-hr forecast and incorporates quality-controlled observations from aircraft, radiosondes, satellite, ship, and surface stations. The MVOI analysis employs both *in situ* and satellite SST measurements (Cummings, 2005). COAMPS includes a globally relocatable grid, user-defined grid resolutions and dimensions, nested grids, an option for idealized or real-time simulations, and code that allows for portability between mainframes and workstations (Smith et al., 2010).

2.2 Navy Coastal Ocean Model (NCOM)

The Navy Coastal Ocean Model (NCOM) Version 4.0 (NCOM 4.0) is based primarily on two existing ocean circulation models, the Princeton Ocean Model (POM) (Blumberg and Mellor 1983; Blumberg and Mellor 1987) and the Sigma/*Z*-level Model (SZM) (Martin et al., 1998). It has a free-surface and is founded on the primitive equations and the hydrostatic, Boussinesq,

and incompressible approximations. The Mellor Yamada Level 2 (MYL2) and MYL2.5 turbulence models parameterize the vertical mixing. For parameterization of unresolved mixing processes occurring at near-critical Richardson numbers, the vertical mixing enhancement scheme of Large et al. (1994) is included. A source term included in the model equations allows for the input of river and runoff inflows.

NCOM 4.0 employs a staggered Arakawa C grid (as in POM). Spatial finite differences are mostly second-order centered, but higher-order spatial differences are optional. NCOM has a leapfrog temporal scheme with an Asselin filter to suppress timesplitting. Most terms are handled explicitly in time, but the propagation of surface waves and vertical diffusion are implicit.

NCOM 4.0 has an orthogonal-curvilinear horizontal grid and a hybrid sigma and *z*-level grid with sigma coordinates applied from the surface down to a specified depth. Level coordinates are used below the specified depth. The second, newer, choice of vertical grid is a general vertical coordinate (GVC) grid consisting of a three-tiered vertical grid structure. The GVC grid is comprised of: (1) a "free" sigma grid near the surface that expands and contracts with the movement of the free surface, (2) a "fixed" sigma grid that is immobile within the free surface, and (3) a *z*-level grid that allows for "partial" bottom cells (Martin et al., 2008a,b). The relocatable version of NCOM, called RELO NCOM, is used to generate grids and namelists of parameters for NCOM.

2.3 Earth System Modeling Framework (ESMF)

COAMPS and NCOM 4.0 are integrated together through the ESMF. Funded by the Department of Defense and the National Aeronautics and Space Administration (NASA) and developed by the National Center for Atmospheric Research (NCAR), the ESMF was designed to create a high-performance, flexible software infrastructure to increase ease of use, performance portability, interoperability, and reuse in climate, numerical weather prediction, data assimilation, and other Earth science applications. The software infrastructure allows different weather, climate, and data-assimilation components to work together on an array of platforms, from laptops to supercomputers. ESMF software is component-based, representing models as collections of smaller elements that are coupled together. A component may be a physical domain or a function, such as a coupler or I/O (input/output) system. The framework provides tools for regridding, data decomposition, and communication on parallel computers and for common modeling functions. ESMF enables the passing of variables between atmosphere and ocean in memory, and organizes horizontal interpolation between the fields in the different components.

2.4 Description of Model Coupling

The coupling of model fields is performed as follows. At the beginning of a coupling timestep, the atmospheric model computes the bulk fluxes (stress, sensible heat, and latent heat) using the current ocean model SST and near-surface atmospheric variables. The atmospheric model then integrates forward in time to the next coupling timestep, continuing to compute the bulk fluxes using the same SST and the evolving near-surface atmospheric fields. After the atmospheric

model reaches the next coupling timestep, the ocean model integrates forward in time using the computed atmospheric surface fluxes. By default, the atmospheric surface fluxes are time-averaged over a 12 minute coupling timestep. The resulting SST field (at the end of the coupling interval) is fed back to the atmosphere to begin the next coupling timestep.

In the uncoupled simulations, the surface fluxes are computed using sea surface temperature values from an NCODA 2D analysis (these SST values are updated only once every 12 hours and have no direct relationship with the overlying atmospheric variables). In contrast, the important aspect of the coupled model is the use of the ocean model SST in the bulk fluxes. As SST evolves in the ocean model it is allowed to interact frequently with the atmospheric marine boundary layer (MBL) via the fluxes. The resulting changes in the MBL then feedback onto the ocean via the bulk fluxes. More detail on the bulk fluxes and how they are affected by SST is contained in Annex A.

2.5 Memory and Processor Allocation

As a general example, the operational resource requirements for running a coupled COAMPS simulation are as follows:

An Adriatic Sea 12-hr test case with three COAMPS nests (36/12/4 km), two NCOM 4.0 nests (6/2 km), 41/40 vertical atmospheric levels, and 50 vertical NCOM levels has a run time of 1.23 hours on *BABBAGE* using 64 processors in sequential mode (# of atmospheric processors = # of ocean processors = # of total processors). Figure 1-5 illustrates the grid domains for both the atmosphere and ocean for the Adriatic Sea test case. It is important to note that the vast majority of the computational requirements are utilized by the atmospheric portion of COAMPS.

A test of a $10^o \times 10^o$ Gulf of Mexico simulation with three COAMPS nests (45/15/5 km), one NCOM 4.0 nest (5 km), 41/40 vertical atmospheric levels, and 50 vertical NCOM levels has a 12-hour forecast run time for the following number of processors in sequential mode on *BABBAGE* (# of grid points for the inner atmospheric resolution: 205 × 226; # of grid points for the ocean nest: 199 × 223):

- 8 processors: 196 minutes (3.27 hours)
- 16 processors: 104 minutes (1.73 hours)
- 32 processors: 49 minutes (0.82 hours)
- 64 processors: 33 minutes (0.55 hours).

The efficiency* with respect to eight processors is the following:

- 8 processors: 100%
- 16 processors: 94 %
- 32 processors: 100%
- 64 processors: 74%.

Utilizing 32 processors appears to be a “sweet spot” on *BABBAGE* for COAMPS.

* Efficiency is defined as Efficiency(2N) = (T(N)*100%) / (2*T(2N)), where N is the number of processors and T is time. For example: Efficiency(16) = (T(8)*100%) / (2*T(16)) = (196*100%) / (2*104) = 94%.

2.6 Document Overview

This report details the procedures and results of validating the coupled COAMPS system. A description of the purpose of each test, the test area characteristics, model run specifics, and results from each simulation will be presented here, along with graphical output, statistics, and concluding remarks. The user can refer to the COAMPS Version 5.0 User's Guide (Smith et al., 2010), NCOM 4.0 User's Manual and Software Design Description (Martin et al., 2008 a, b) and the COAMPS Version 3 Model Description (Chen et al., 2003; http://www.nrlmry.navy.mil/coamps-web/web/docs) for further information on the individual models. An online version of the ESMF User's Guide is available at http://www.earthsystemmodeling.org/esmf_releases/public/last/ESMF_usrdoc/ESMF_usrdoc.html

3.0 VALIDATION TEST DESCRIPTIONS AND RESULTS

The COAMPS has been validated and verified successfully for a number of field cases. Field cases evaluate the model's ability to predict hydrodynamic and atmospheric solutions in real situations. The test areas represent regions where significant variability and sufficient data exist to accurately describe variability. Table 1 below provides a summary of test specifications.

In most test cases, there is an uncoupled run and a fully coupled COAMPS run. In the uncoupled run, referred to as [u], the ocean is forced by the atmospheric component, but there is no feedback from ocean to atmosphere and the SST from the ocean is not passed to the atmosphere. Instead, the atmospheric model uses SST from NCODA to compute the bulk fluxes (Annex A). These fluxes are then used within the atmosphere and ocean models. The uncoupled run was referred to as the "Control" in Pullen et al., (2007) and differs from the 'one-way coupled' case of Pullen et al. (2007), which modified the fluxes for the ocean component to include the NCOM SST (but the fluxes felt by the atmosphere were not modified). Full feedback between the atmospheric and ocean model components is activated in the coupled run, [c].

Table 1: Test Case Characteristics.

Test Case	Area/ Program	Lat/Lon	Key Processes	Grid Res.	Time Frame	Obs. Data
1	Adriatic Circulation Experiment (ACE)	43.5°N to 46.0°N, 12.0°E to 15.0°E	Bora winds, ocean eddy response.	Atm: 36, 12, 4 km; Ocean: 6 and 2 km.	1/31-2/21 2003	Ship ADCP, current meters, coastal and oil platform met stations.
2	Ligurian Air-Sea Interaction Experiment (LASIE07)	43.5°N to 44.5°N, 9.5°E to 10°E	Air-sea interaction and boundary layer coupled processes.	Atm: 36, 12, and 4 km; Ocean: 6 and 2 km.	6/15-7/10 2007	300 ocean profiles, 100 radiosondes, two surface met moorings, wave buoys, drifters, gliders, ADCP, thermistor moorings.
3	Autonomous Ocean Sampling Network (AOSN)	36.0°N to 37.4°N; 121.5°W to 123.0°W	Upwelling and relaxation events.	Atm: 81, 27, 9, and 3 km; Ocean: 3 km.	8/3-9/8, 2003	M1 and M2 buoys, glider data, AUVs.
4	Kuroshio Extension System Study (KESS)	30.0°N to 42.0°N, 142.0°E to 152.0°E	Air-sea interaction at a strong SST front: boundary	Atm: 27, 9 and 3 km, 40 levels.	1/30-2/07, 2005; 6/15-7/17	NOAA surface buoy, surface met, T and S, QuikSCAT winds

Test Case	Area/ Program	Lat/Lon	Key Processes	Grid Res.	Time Frame	Obs. Data
			layer processes, air-sea interaction in synoptic storms.	Ocean: Nest 1: 1/16° Nest 2: 1/48°, 50 levels.	2005.	(satellite SST & SSH, and SSMI wind speed are assimilated).
5	VAMOS Ocean-Cloud-Atmosphere-Land Study (VOCALS)	45°S to 10°N; 120°W to 50°W	Feedback among coastal jet, oceanic upwelling, mesoscale eddies and clouds.	Atm: 45, 15, and 5 km; Ocean: 15 km.	10/20-11/30 2008.	Satellite data, QuikSCAT winds, NOAA ship soundings, WHOI buoy data.

3.1 Test Case 1: Adriatic Circulation Experiment (ACE)

3.1.1 Purpose

The Adriatic Sea has recently been the subject of numerous atmospheric and oceanic modeling and observational studies (e.g., Pullen et al. (2006), Pullen et al. (2007), Martin et. al. (2006), Kuzmic et al. (2007), and Book et al. (2007)). Many of these studies focus on the downslope windstorms, or "bora", that occur in the topographic mountain gaps of the Dinaric Alps of Croatia during the late fall and winter months. The circulation patterns of the northern Adriatic Sea are heavily influenced by bora jet flows. Due to the nature of the bora events and the fact that these winds traverse the Adriatic Sea in the form of mesoscale jet flows, this region is of particular interest to air/sea interaction studies at the mesoscale level. This test case will compare the effects of one-way and two-way coupling on atmospheric and ocean forecasting during bora events, as well as study ocean eddy responses and the impact of two-way coupled high-resolution coastal ocean temperatures on the overlying air properties. The primary objective in this test case is to reproduce and possibly extend the results of Pullen et al. (2007) and Dorman et al., (2007) by using COAMPS, incorporating ESMF-based (rather than file-based) two-way coupled simulations.

3.1.2 Test Case Characteristics

3.1.2.1 Test Area and Observations

The specific characteristics of bora events are dependent upon the synoptic meteorological background flow (Jurcec, 1988). For instance, a bora event forced by northeasterly winds from a surface anticyclone or high to the north of the Dinaric Alps is termed "anticyclonic", and a bora event forced by northeasterly winds from a surface cyclone or low southeast of the Diurnic Alps

is termed "cyclonic" (Pullen et al., 2007). In general, the cyclonic bora produces stronger winds while the boundary layer depth tends to be shallower (Defant, 1951). There were two bora events during the study period. Bora 1 was a cyclonic bora occurring for 41 hours from 31 January through 2 February of 2003. The second bora was a 70-hour anticyclonic event from 11-14 February 2003 (See Fig. 1-1). A complete description of the test area is found in Pullen et al., (2007).

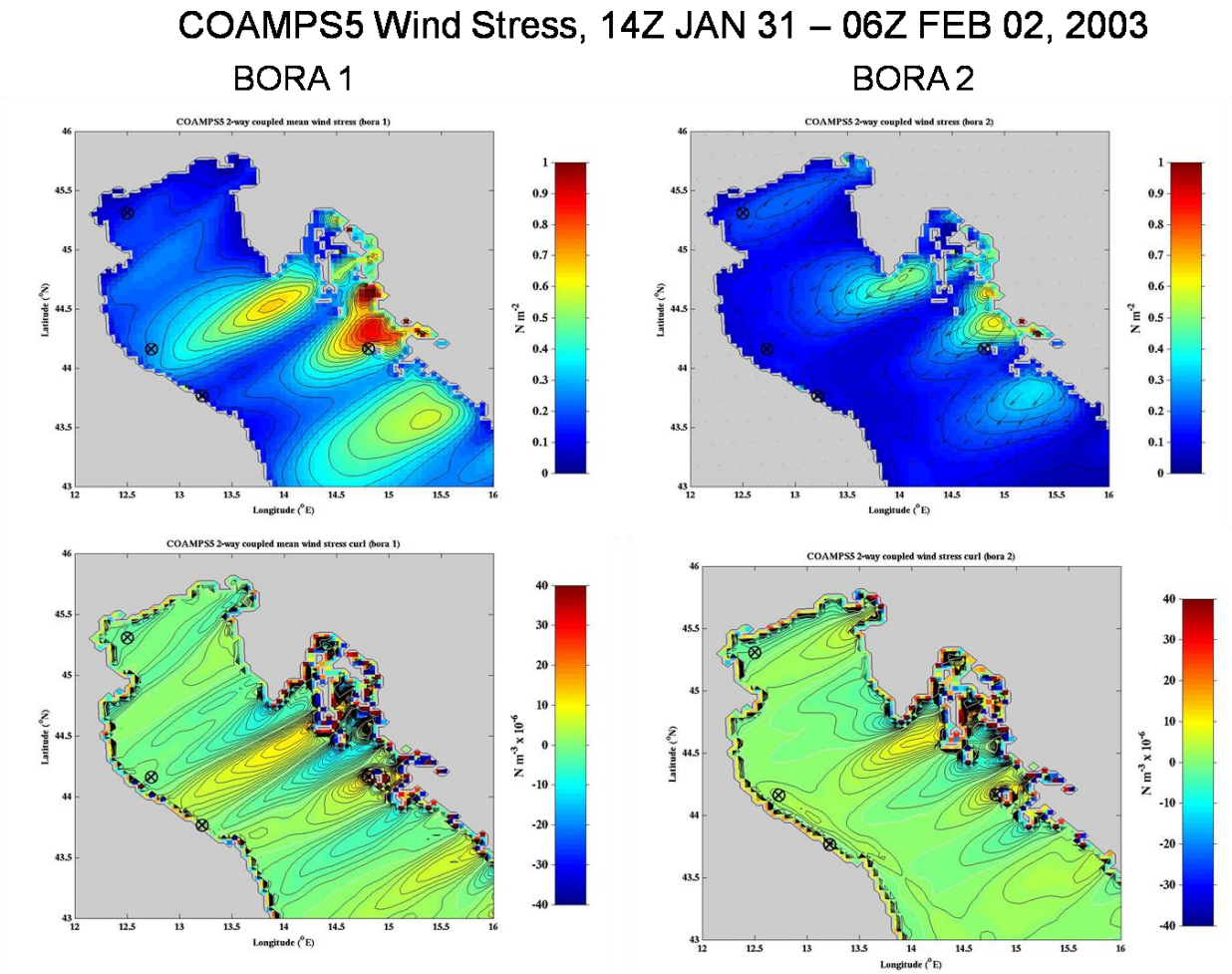

Figure 1-1: The two types of bora events studied in Test Case 1. Bora 1 (left) is cyclonic and bora 2 (right) is anticyclonic. The two-way coupled mean wind stress (top) and wind stress curl (bottom) for each bora event are shown.

Ocean current data obtained from acoustic Doppler current profilers (ADCPs) in February 2003 were utilized for the NCOM portion of the validation. As described by Book et al. (2007), bottom-mounted ADCPs were deployed by the Naval Research Laboratory (NRL) during the Adriatic Circulation Experiment (ACE) together with the NATO Undersea Research Centre (NURC) as a Joint Research Project (JRP) from September 2002 to May 2003. ACE/JRP moorings consisted of 14 trawl-resistant bottom-mounted ADCPs (Perkins et al., 2000) distributed throughout portions of four mooring sections. The particular moorings used in this validation were the VR1, VR2, VR4, VR5, VR6, KB1, CP2, and CP3 (Fig. 1-2). Each ADCP

measured the ocean currents throughout the water column. Data from ACE included latent, sensible, and total heat fluxes, wind stress, and SSTs gathered from meteorological gauges on gas platforms at Acqua Alta (Venice), Azalea, Ancona, and Veli Rat. Ship data from the R/V *KNORR* provided by J. Pullen (Fig. 1-4) was used for comparison of COAMPS wind stresses and heat fluxes. The *KNORR* made 10 minute averaged meteorological measurements over the northern Adriatic from 31 January to 24 February 2003. Bathymetry values came from the NRL-operated Digital Bathymetric Data Base, two minute resolution (DBDB2), available in-house.

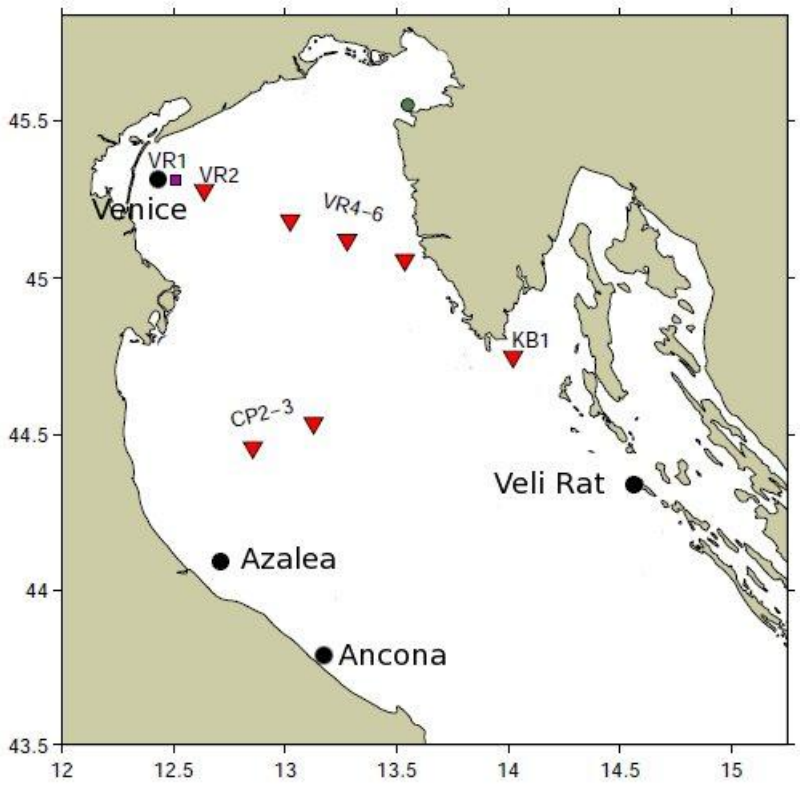

Figure 1-2: Locations of ADCP moorings in the northern Adriatic Sea during the winter of 2002/2003 (Book et al., 2007). Red triangles are ADCP/wave/tide moorings deployed by NRL and NURC. The purple square indicates the location of a JRP ADCP at the Acqua Alta Tower (Venice) of the Institute for the Study of the Dynamics of Great Masses (Italy). The green circle is a mooring deployed by the National Institute of Biology.

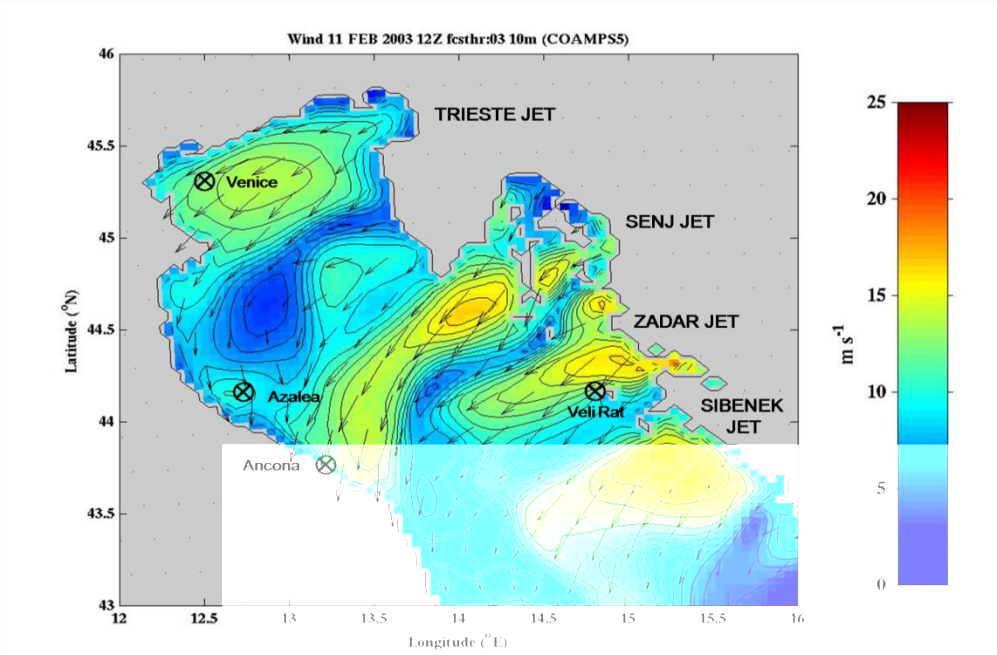

Figure 1-3: COAMPS wind speed (m/s) for 11 February 2003. The location of gas platform meteorological stations (Acqua Alta (Venice), Azalea, Ancona, and Veli Rat) are shown in proximity to four bora jets.

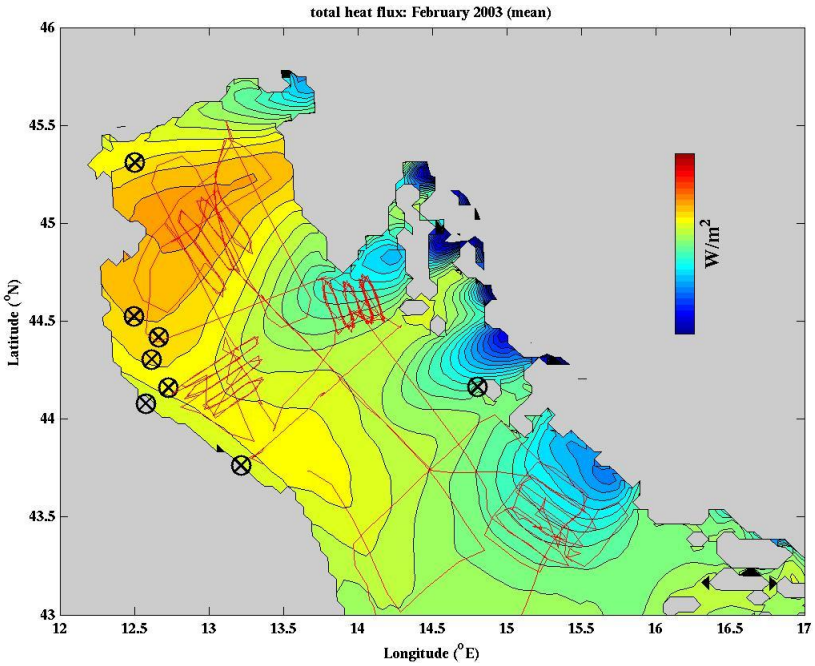

Figure 1-4: Track of the ship R/V *KNORR*, 1-21 February 2003 from Pullen et al. (2006). Color gradients represent mean total heat flux (W/m^2).

3.1.2.2 Model Setup

The COAMPS model setup closely resembled the setup in Pullen et al. (2007). The COAMPS Adriatic Sea configuration was a triply nested (36, 12, 4 km horizontal resolution) domain where nest 3 extended from 39.6°N to 47.3°N and 10.4°E to 20.6°E with horizontal dimensions of 187 × 205 (Fig. 1-5). There were 40 vertical terrain-following levels. At 00 UTC and 12 UTC of each day, a data assimilation cycle was initiated using the prior 12 hr forecast as background, incorporating quality-controlled observations from aircraft, radiosondes, satellite, ship, and surface stations. An MVOI analysis was used for both *in situ* and satellite measurements. The length of the model run extended from 25 January to 21 February 2003, a period of 28 days.

The ocean model NCOM (Martin, 2006) configuration consisted of two nests (6 and 2 km horizontal resolution) where nest 2 covered approximately the same area as nest 3 in the atmospheric model (Fig. 1-5). There were a total of 50 vertical levels, of which 36 were sigma coordinates in the upper 190 m of the water column. NCOM was initialized using global NCOM hindcast data, while the atmospheric and ocean models were coupled every 12 minutes through exchange grid processes.

In all of the coupled runs, the winds, wind stresses, and heat fluxes were interchanged between the atmosphere and ocean (i.e., the ocean feeds back to the atmosphere and the atmosphere feeds back to the ocean). In the uncoupled runs, the ocean *did not* feedback to the atmosphere, i.e., the heat fluxes calculated by the atmospheric model were computed using NCODA SSTs rather than the NCOM SSTs used in the coupled runs. Though wind forcing from the atmospheric model was still passed to NCOM in the uncoupled run, there was no feedback from the ocean to the atmosphere.

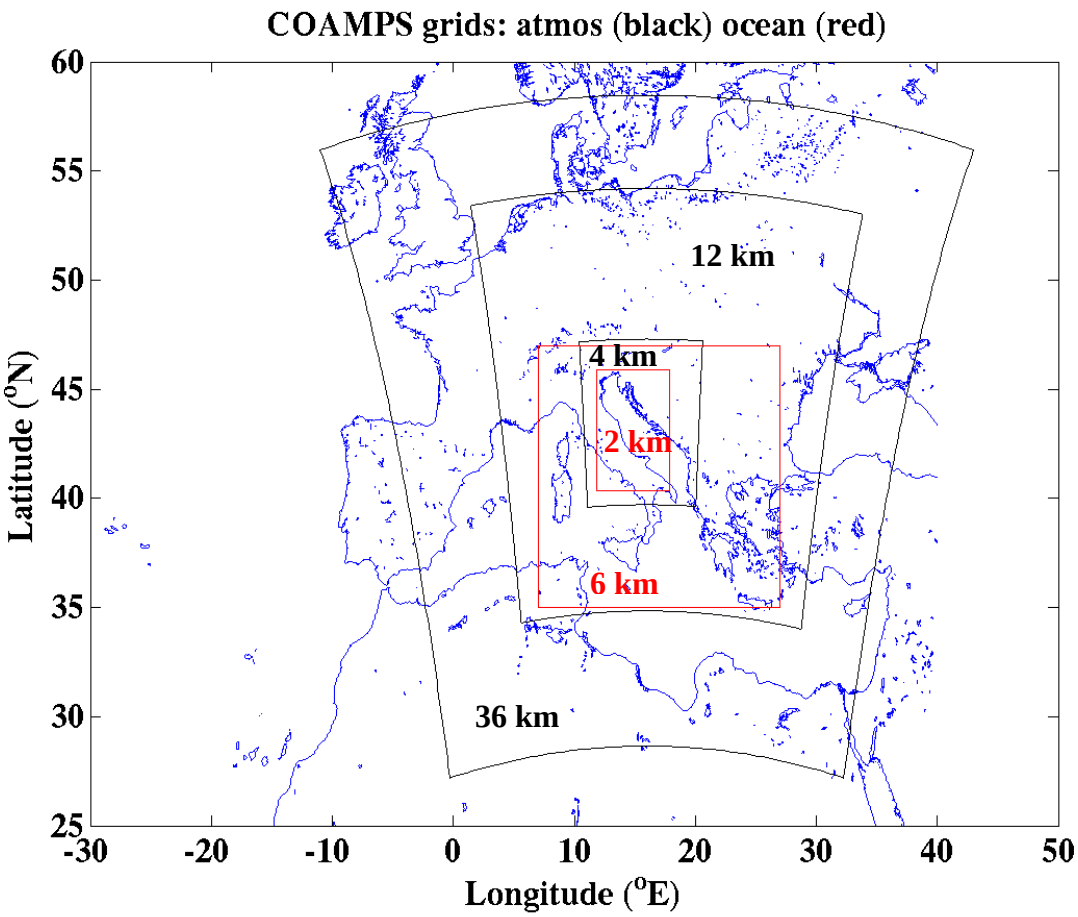

Figure 1-5: Atmospheric and ocean grid setup for the Adriatic Sea. The resolution for the atmospheric nests (black) and the ocean nests (red) are indicated.

3.1.3 Results

3.1.3.1 Atmospheric Model Validation

As discussed in the introduction, the ESMF two-way coupled run was compared to an uncoupled run and to the observational data at several stations in the northern Adriatic. For the uncoupled run, the ocean-to-atmosphere interaction was shut off, i.e. there was no heat flux feedback to the atmosphere from the NCOM SSTs. The uncoupled run, labeled [u] in the tables, is considered the control and is similar to the Pullen et al., (2007) control. The [c] in the tables represents a two-way coupled run. The tables below represent the coupled and uncoupled COAMPS statistics for the four gas platforms in the northern Adriatic for wind stress, net heat flux, sensible heat flux, and latent heat flux. Statistics shown in each of the tables below are the mean, standard deviation (STD), correlation coefficient (CC), mean bias (MB) and the root mean square error (RMSE) for both coupled and uncoupled runs.

3.1.3.1.1 Veli Rat and Acqua Alta Platforms

In terms of wind stress, Veli Rat and Acqua Alta (Venice) are the stations closest in proximity to a bora jet flow (Fig. 1-3) and have the largest wind stresses in both the observations and in COAMPS. When compared to the observations, the mean wind stress in COAMPS was larger at Veli Rat and smaller at Acqua Alta in both the coupled and uncoupled runs. However, the smaller wind stresses at Acqua Alta in COAMPS may be attributed to the intensity and positional differences of the Trieste bora jet compared to the observations. Pullen et al. (2007) COAMPS runs show a Trieste jet that is stronger at the surface and located further to the north of the COAMPS runs in this report. Further investigation of the COAMPS results revealed that strong winds were located just above the surface in relation to the Trieste jet (Fig. 1-6). This may be indicative of an issue with the stronger winds not mixing down to the surface in the newest version of the atmospheric component in COAMPS. Testing involving the terrain height fields from Pullen et al. (2007) did not make any appreciable differences.

The variations in the wind stresses between the coupled and uncoupled COAMPS run were small, e.g., the RMSE for wind stress was slightly smaller in the coupled run compared to the uncoupled run. Inspection of the wind stress time series showed good agreement, especially at Veli Rat (Table 1-1, Fig. 1-7). However, the Acqua Alta wind stress agreement was less, due to the differences in the Trieste jet strength and position (Table 1-2, Fig. 1-8). The sensible heat flux comparisons showed an improvement in the coupled run at both of the stations, while the latent heat flux MB was much lower at Acqua Alta in the coupled run.

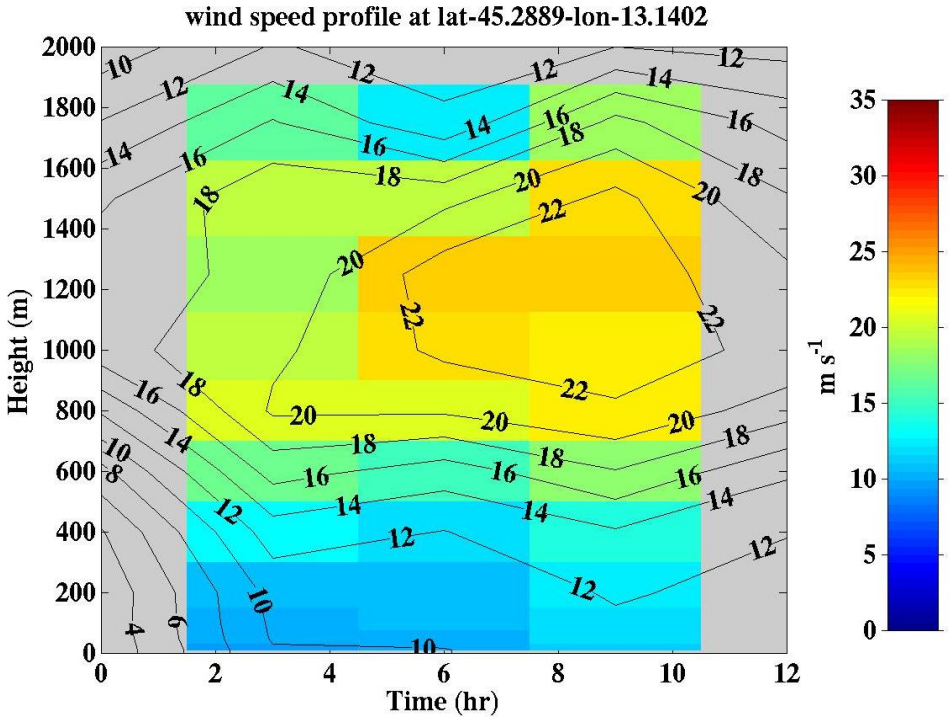

Figure 1-6: Vertical profile of wind speed (m/s) for the Trieste bora jet near Acqua Alta.

Table 1-1: COAMPS atmospheric parameter comparisons to observations at Veli Rat Gas Platform. N=276.

Variable	Obs mean/STD	COAMPS mean/STD [c]	COAMPS mean/STD [u]	CC [c]	CC [u]	MB [c]	MB [u]	RMSE [c]	RMSE [u]
Net Heat Flux (W/m^2)	280/296	197/208	228/207	0.95	0.91	83	51	144	145
Wind Stress (N/m^2)	0.092/0.070	0.147/0.077	0.154/0.079	0.74	0.74	-0.05	-0.06	0.076	0.082
Latent Ht. Flux (W/m^2)	242/74	188/48	206/50	074	0.74	54	37	74	62
Sensible Ht. Flux (W/m^2)	88/32	130/42	142/44	0.81	0.80	-42	-54	49	60

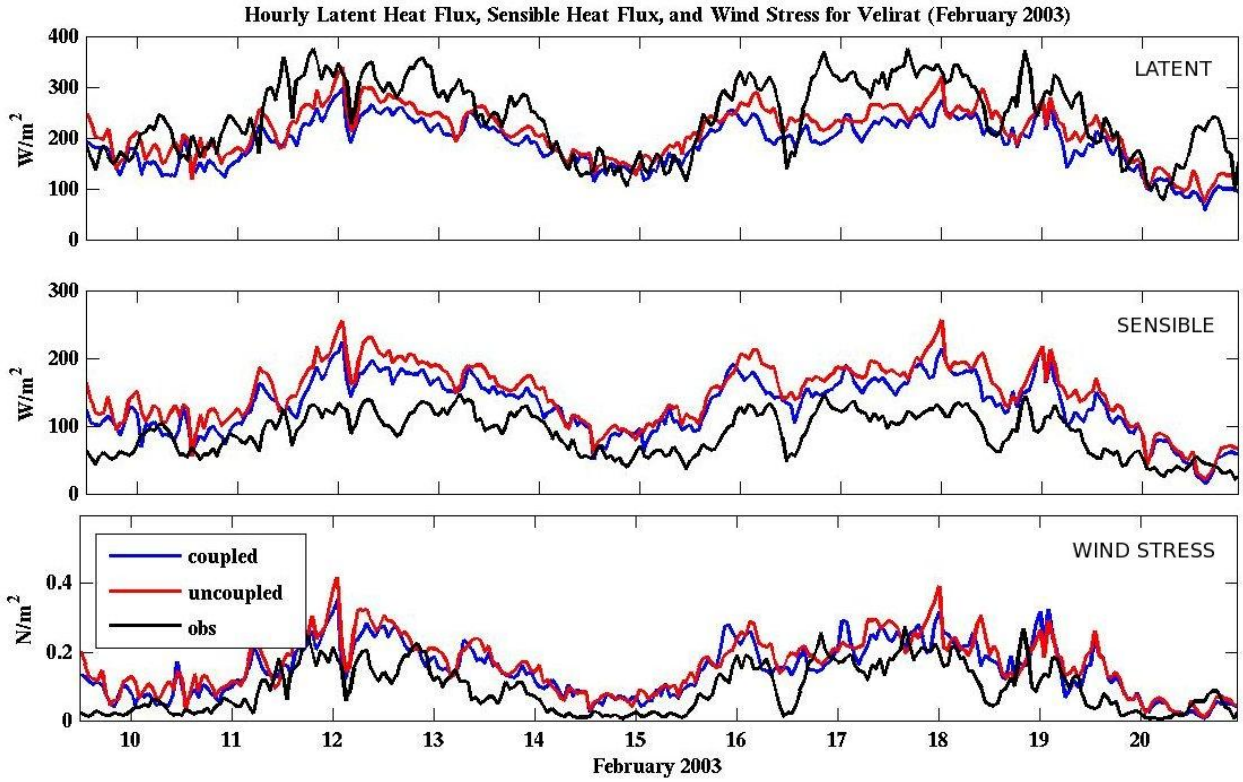

Figure 1-7: Hourly latent and sensible heat fluxes (W/m^2) and wind stress (N/m^2) for the fully-coupled COAMPS run and observations at Veli Rat.

Table 1-2: COAMPS atmospheric parameter comparisons to observations at Acqua Alta (Venice) Gas Platform. N=480.

Variable	Obs mean/STD	COAMPS mean/STD [c]	COAMPS mean/STD [u]	CC [c]	CC [u]	MB [c]	MB [u]	RMSE [c]	RMSE [u]
Net Heat Flux (W/m^2)	62/190	49/167	131/179	0.83	0.82	12	-69	108	130
Wind Stress (N/m^2)	0.151/0.168	0.118/0.101	0.135/0.111	0.79	0.78	0.03	0.02	0.112	0.108
Latent Ht. Flux (W/m^2)	71/41	88/38	135/47	0.78	0.76	-17	-64	31	71
Sensible Ht. Flux (W/m^2)	13/15	59/34	93/44	0.55	0.53	-46	-79	54	88

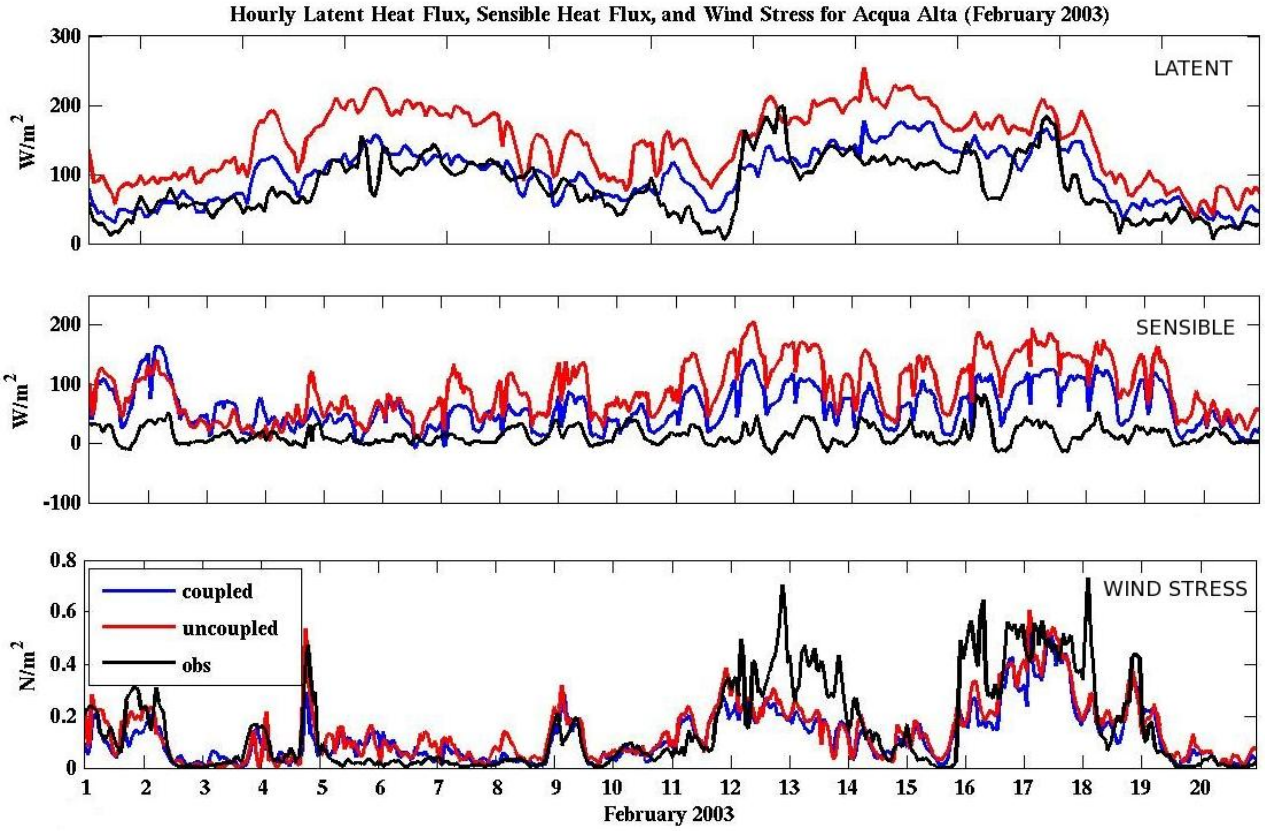

Figure 1-8: Hourly latent and sensible heat fluxes (W/m^2) and wind stress (N/m^2) for the fully-coupled COAMPS run and observations at Acqua Alta (Venice).

3.1.3.1.2 Ancona and Azalea Platforms

The Ancona and Azalea stations located near the eastern coast of Italy are far removed from the strongest winds of the bora jet flows. Both the coupled latent and sensible heat fluxes showed improvement over the uncoupled run, i.e., the mean bias and RMSE were significantly lower at both Ancona and Azalea (Tables 1-3 and 1-4). The time series at both Ancona and Azalea

(Figs. 1-9 and 1-10) illustrate the improvements of the coupled run over the uncoupled run with respect to latent and sensible heat fluxes, while the wind stress time series did not show such an improvement. The improvements in the latent and sensible heat fluxes are attributed to the more realistic SSTs provided by NCOM rather than just NCODA SST analyses.

Table 1-3: COAMPS atmospheric parameter comparisons to observations at Ancona Gas Platform. N=480.

Variable	Obs mean/STD	COAMPS mean/STD [c]	COAMPS mean/STD [u]	CC [c]	CC [u]	MB [c]	MB [u]	RMSE [c]	RMSE [u]
Net Heat Flux (W/m^2)	101/112	-19/125	151/134	0.57	0.55	120	-50	163	129
Wind Stress (N/m^2)	0.085/0.075	0.057/0.063	0.088/0.079	0.52	0.50	0.03	0.00	0.074	0.077
Latent Ht. Flux (W/m^2)	71/33	40/24	138/43	0.45	0.42	31	-66	44	79
Sensible Ht. Flux (W/m^2)	27/21	16/21	86/37	0.40	0.37	11	-59	25	68

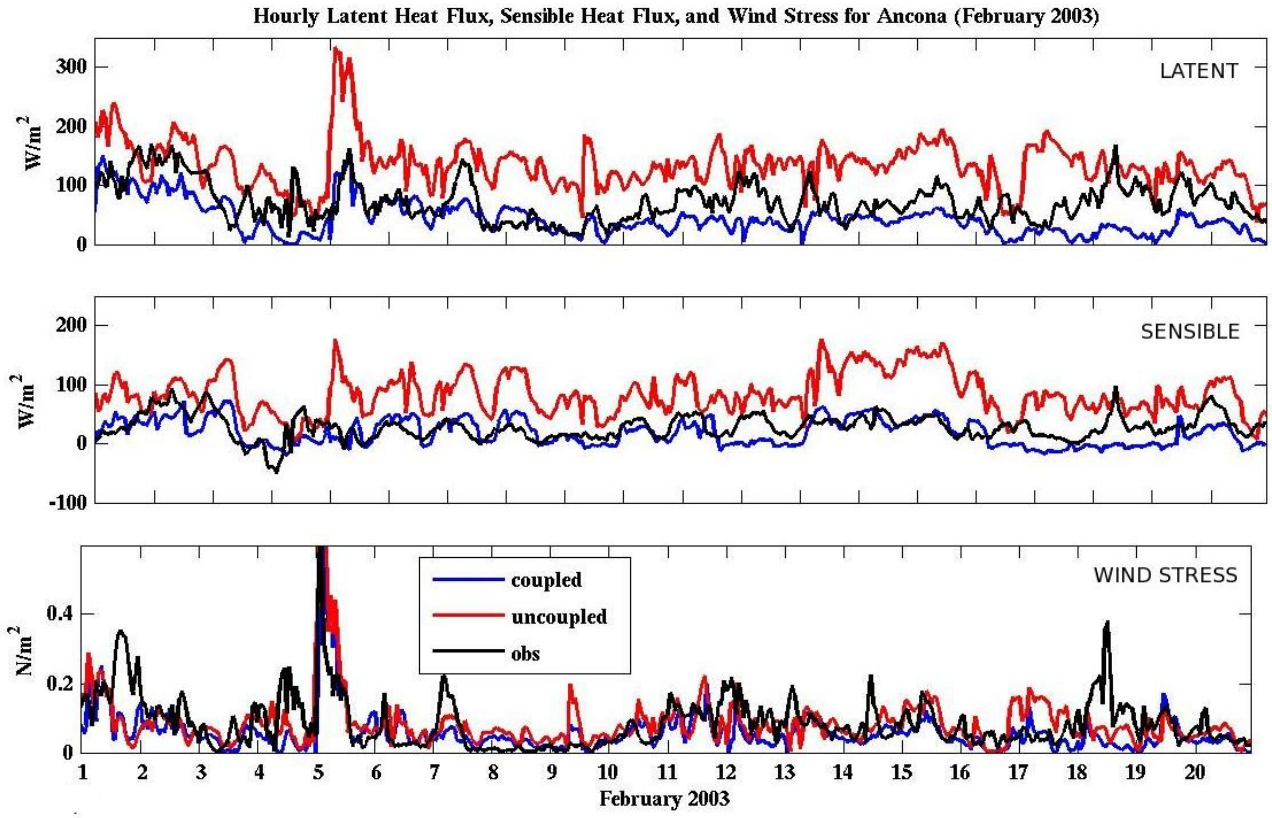

Figure 1-9: Hourly latent and sensible heat fluxes (W/m^2) and wind stress (N/m^2) for the fully-coupled COAMPS run and observations at Ancona.

Table 1-4: COAMPS atmospheric parameter comparisons to observations at Azalea Gas Platform. N=288.

Variable	Obs mean/STD	COAMPS mean/STD [c]	COAMPS mean/STD [u]	CC [c]	CC [u]	MB [c]	MB [u]	RMSE [c]	RMSE [u]
Net Heat Flux (W/m^2)	15/164	41/117	152/134	0.82	0.77	-25	-137	99	172
Wind Stress (N/m^2)	0.063/0.057	0.106/0.061	0.120/0.071	0.51	0.53	-0.04	-0.06	0.072	0.085
Latent Ht. Flux (W/m^2)	47/30	76/28	141/41	0.62	0.62	-29	-95	38	99
Sensible Ht. Flux (W/m^2)	-1/7	40/29	87/38	0.34	0.36	-42	-88	50	95

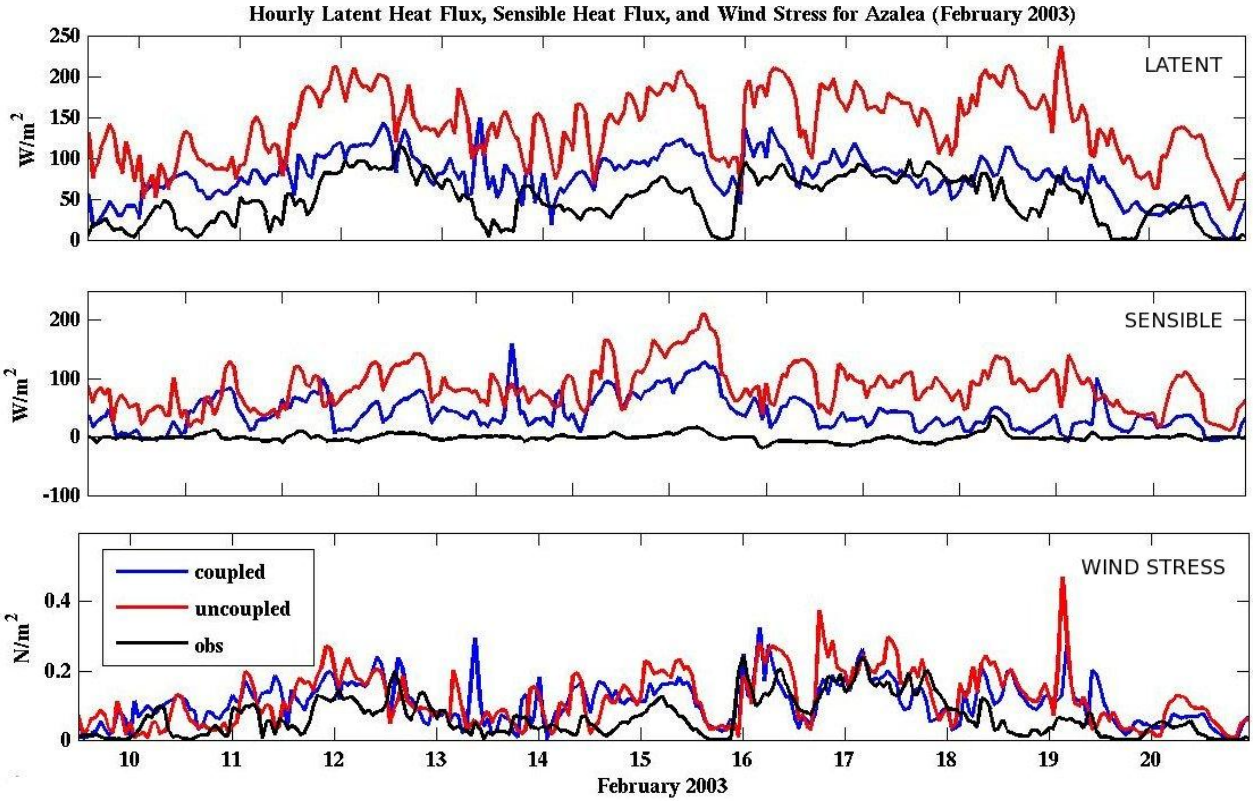

Figure 1-10: Hourly latent and sensible heat fluxes (W/m^2) and wind stress (N/m^2) for the fully-coupled COAMPS run and observations at Azalea.

Overall, the sensible, latent, and net heat fluxes show some improvement in the coupled run compared to the uncoupled run. The mean bias was almost uniformly smaller for the coupled run for both the latent and sensible heat fluxes at all four Adriatic stations. The RMS errors for the heat fluxes primarily improved in the coupled run. Additionally, the correlation coefficients were quite high for the latent heat fluxes at most of the stations and the correlation coefficient for the sensible heat flux was very high for Veli Rat, the station closest to a bora jet. Overall,

the heat flux correlation coefficients were slightly higher in the coupled run compared to the uncoupled run. As shown in the time series for heat fluxes, COAMPS tended to overestimate the total heat flux, while the sensible heat fluxes in COAMPS showed an overall consistent bias throughout the simulation at Veli Rat and Acqua Alta (Figs. 1-7 and 1-8).

3.1.3.1.3 Comparisons of Adriatic Sea COAMPS and Observational SST

The importance of using the fully-coupled air/sea COAMPS model should not be underestimated for the Adriatic Sea. Even though there are only slight improvements (although not significant) with respect to the latent and sensible heat flux correlation coefficients in the fully-coupled run, there *is* significance in the mean bias and standard deviation at each of the coastal stations (Azalea, Ancona, Acqua Alta, and Veli Rat). Due to the complex nature of the surface currents, river inflows, and ubiquitous atmospheric intermittent bora jet flows, it is imperative that realistic SSTs are represented in both deep ocean and coastal regions to accurately assess the air/sea interactions associated with the bora winds. As such, NCODA SSTs (Fig. 1-11) associated with the uncoupled COAMPS simulation are insufficient in resolution to accurately characterize the SSTs for the Adriatic Sea, especially along the coastal regions. In reality, much colder waters from the northern Adriatic flow southward along the narrow Western Adriatic Current to Azalea and Ancona, a feature that NCODA cannot resolve.

The time series of SSTs for each of the four Adriatic Sea stations (Fig. 1-12) reveal that the SSTs in the fully-coupled simulation were significantly more accurate using NCOM SSTs (Fig. 1-13) over NCODA SSTs. As a result, the latent and sensible heat flux calculations were greatly improved over the uncoupled simulation. These improved heat fluxes are pertinent in understanding the air/sea interaction associated with the bora jet flows. Therefore, the fully-coupled model is necessary to accurately depict the heat fluxes associated with this phenomenon.

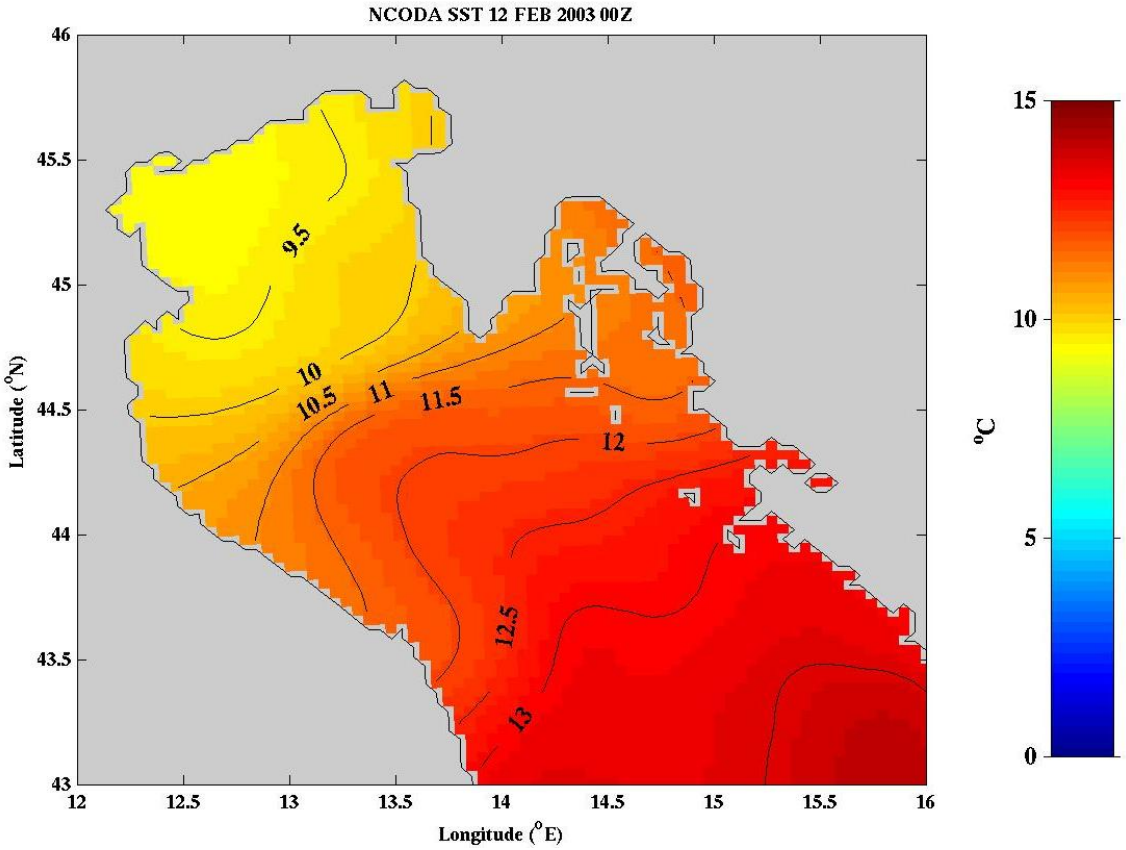

Figure 1-11: NCODA SST for 12 February 2003 00Z.

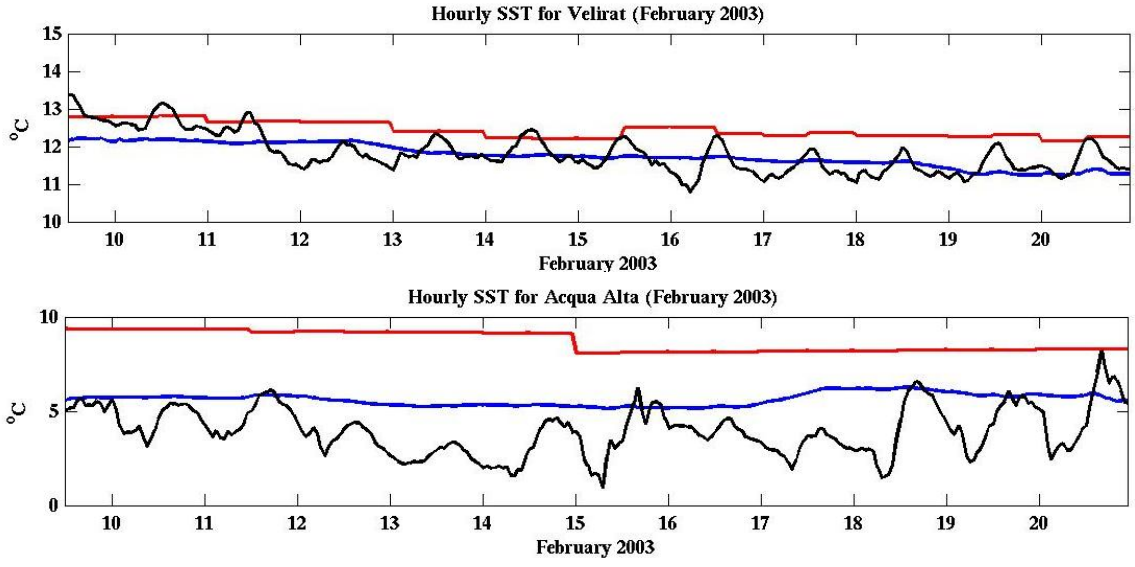

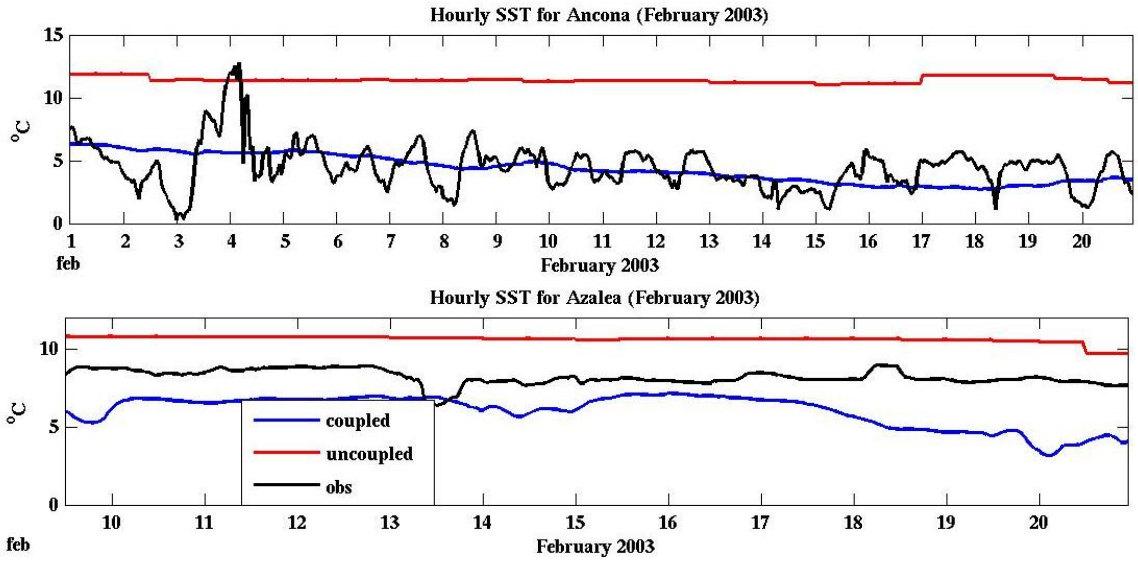

Figure 1-12: Time series of SST (°C) for Veli Rat, Acqua Alta, Ancona, and Azalea platforms. The black line represents observations, blue is coupled COAMPS, and red is uncoupled COAMPS.

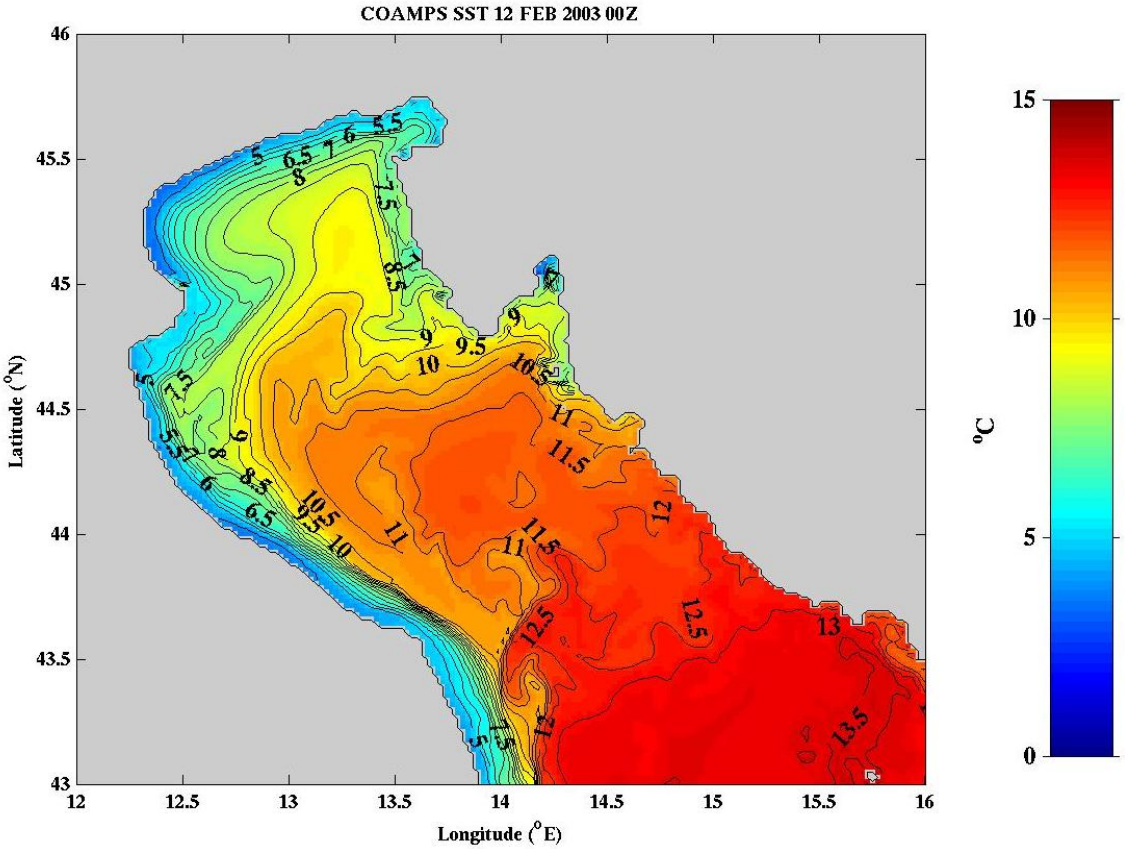

Figure 1-13: NCOM SST for 12 February 2003 00Z.

3.1.3.1.4 Gulf of Trieste Buoy Winds

In addition to the data at the four Adriatic stations, Jacopo Chiaggato of NURC provided 5 m wind data for February 2003 from a mooring located at 13.55°E and 45.55°W in the Gulf of Trieste for validation studies of the Trieste bora jet (Fig. 1-14). The comparison of 10 m COAMPS winds to the buoy data confirmed that COAMPS is underestimating the strength and/or spatial position of the Trieste bora jet near the surface. The u and v components of the wind, as well as the total wind, were underestimated in COAMPS (Table 1-5). The total wind for the coupled run was underestimated nearly 2.3 m/s, while the uncoupled run showed a slight improvement of 1.8 m/s underestimation (mainly in the u component of the wind). However, the correlation coefficient was quite high for the winds, indicating that COAMPS was capturing the onset and offset of the Trieste bora jet to quite a high degree.

Table 1-5: Gulf of Trieste Buoy Winds (m/s) from 1-21 February, 2003. Location: 45.55°W, 13.55 °E. N = 480.

Variable	Obs mean/STD	COAMPS mean/STD [c]	COAMPS mean/STD [u]	CC [c]	CC [u]	MB [c]	MB [u]	RMSE [c]	RMSE [u]
U-wind	-6.14/4.97	-4.10/3.11	-4.51/3.33	0.72	0.73	-2.04	-1.64	4.05	3.77
V-wind	-3.20/3.30	-2.33/2.71	-2.32/2.89	0.54	0.47	-0.87	-0.88	3.04	3.32
Total Wind	7.94/4.52	5.66/2.67	6.10/2.81	0.67	0.65	2.29	1.84	4.07	3.87

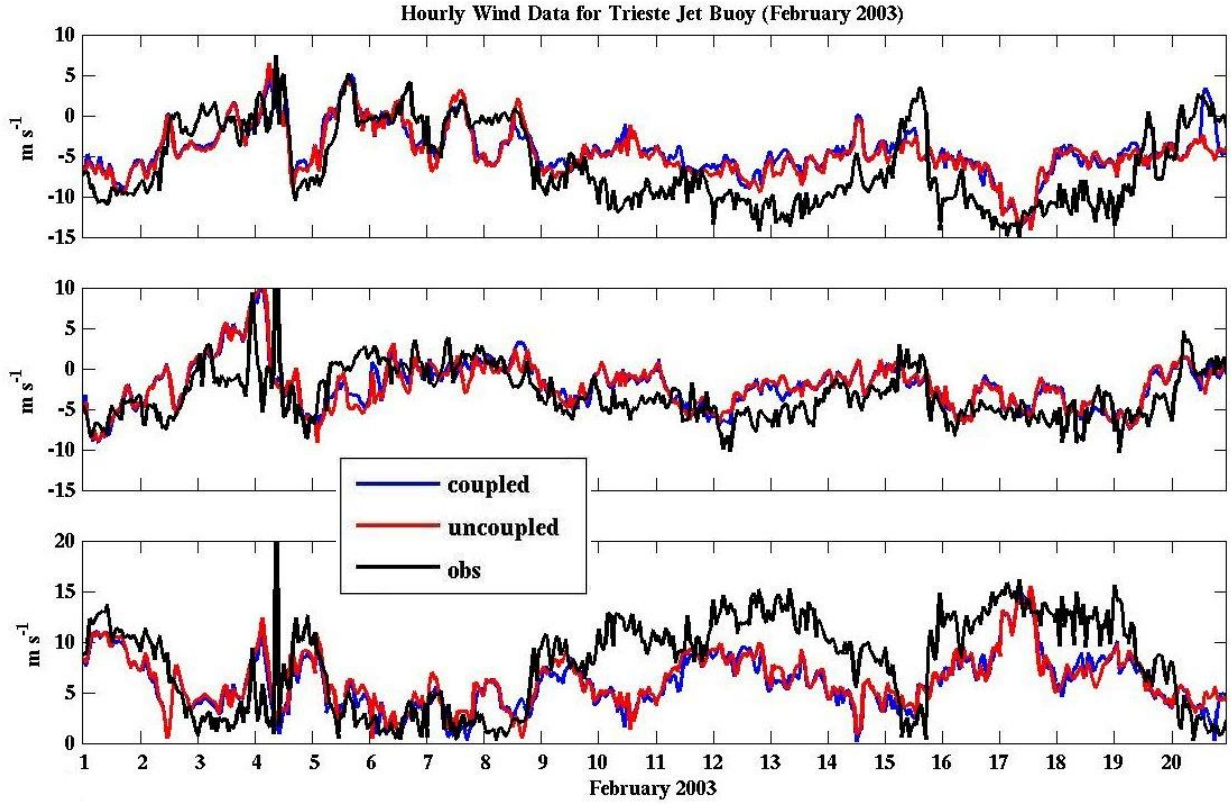

Figure 1-14: Hourly U-wind (top plot), V-wind (middle plot), and total wind (bottom plot)

comparisons for the fully-coupled COAMPS run (blue), uncoupled (red) and Gulf of Trieste Jet Buoy observations (black).

3.1.3.1.5 R/V *KNORR* Shipboard Meteorology

Ship data from the R/V *KNORR* (Fig. 1-15) was provided by Julie Pullen, formerly of NRL, for comparison of COAMPS wind stresses and heat fluxes. The *KNORR* made 10-min averaged meteorological measurements over the northern Adriatic from 31 January to 24 February 2003. For the period 1 February to 21 February 2003, COAMPS performed well with regard to estimating the wind stress (Table 1-6). The uncoupled [u] wind stresses showed an almost negligible improvement over the coupled run with regard to the MB, RMSE, and CC. The MB was very small for both the latent and sensible heat fluxes in both the coupled and uncoupled runs, while the total heat flux MB was smaller for the uncoupled run. The heat flux CC was good, but similar overall, for both the coupled and uncoupled runs. Generally, the ship data MB and RMSE were much lower than each of the station data. It is certainly possible that the instrumentation and data analysis completed on the *KNORR* was better than at the stations. Also, the ship data represent the entire northern Adriatic, while most of the stations were in coastal regions where forecasting and modeling is typically more difficult.

Table 1-6: R/V ***KNORR*** **Ship Data. 1-21 February, 2003. Number of observations = 480.**

Variable	Obs mean / STD	COAMPS mean / STD [c]	COAMPS mean / STD [u]	CC [c]	CC [u]	MB [c]	MB [u]	RMSE [c]	RMSE [u]
Wind Stress (N/m^2)	0.179/ 0.181	0.151 / 0.142	0.160 / 0.148	0.47	0.49	0.028	0.019	0.171	0.170
Net Heat Flux (W/m^2)	273/219	171/201	195/204	0.70	0.70	102	78	193	183
Sensible Heat Flux (W/m^2)	93/58	95/57	102/60	0.63	0.64	-2	-9	50	51
Latent Heat Flux (W/m^2)	185/90	167/75	181/80	0.51	0.53	18	5	85	84

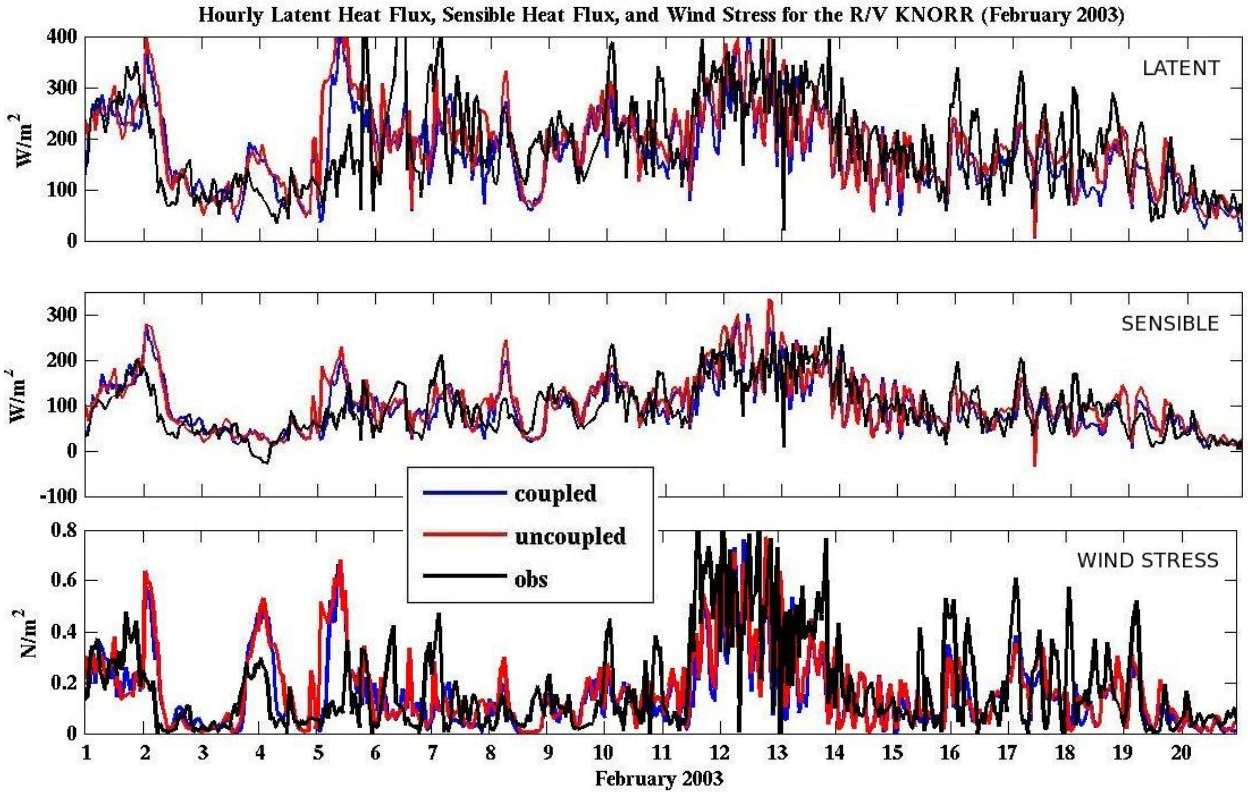

Figure 1-15: Hourly atmospheric comparisons for the fully-coupled COAMPS (blue) and uncoupled (red) run to R/V ***KNORR*** **shipboard observations (black).**

3.1.3.2 Ocean Model Validation

As noted previously, northern Adriatic oceanographic conditions are strongly influenced by the onset of bora jet flows. The shallowness of the water column combined with pronounced heat loss during the winter due to wind-induced mixing from bora events destabilizes the water column and enforces almost complete homogeneity. The presence of freshwater inflow from surrounding rivers also adds to the complexity of the oceanographic conditions.

Measurements to compare the observed gyral response to the fully-coupled COAMPS runs were evaluated using techniques used by Kuzmic et al. (2007). These include calculations of the magnitude of the complex correlation coefficient and the angular displacement, or mean directional error, between the measured ADCP and NCOM model currents following Kundu (1976):

$$\rho = \frac{\langle u_o u_m + v_o v_m \rangle + i\langle u_o v_m - u_m v_o \rangle}{\sqrt{\langle u_o^2 + v_o^2 \rangle} \cdot \sqrt{\langle u_m^2 + v_m^2 \rangle}} \tag{1}$$

$$\varphi = arctg \frac{\langle u_o v_m - u_m v_o \rangle}{\langle u_o u_m + v_o v_m \rangle}, \tag{2}$$

where u and v are the east-west and north-south, observed (o) or modeled (m), demeaned velocity components. The brackets represent time average. The complex correlations were computed for each ADCP station as a function of depth based on the closest corresponding NCOM level to each ADCP bin. It is important to note that the complex correlation coefficients take into account *both* the current speed and direction.

Eight ADCP sites were chosen to evaluate the Adriatic Sea response to the bora flow for 1 to 21 February, 2003. VR1, VR2, VR4, VR5, and VR6 were used to compare COAMPS to the double gyre current formation resulting from the bora winds (Fig. 1-2). This double gyre formation is dependent upon the strength and position of the Trieste and Senj bora jets (Fig. 1-3). As stated in the atmospheric validation section, the Trieste jet was found to be weaker in COAMPS, with a southward displacement of the bora jet axis, when compared to observations. Therefore, the resultant wind stress curl field was also displaced southward, ultimately shifting the double gyre current pattern southward (Fig. 1-16). It is also important to note that uncertainties in the current speed and direction from the observational data have been calculated to be +/- 0.5 cm/s and +/- 10 degrees for 300 kHz ADCP sites and +/- 0.3 cm/s and +/- 4 degrees for higher-frequency ADCP sites such as SS2, VR1, and VR4 (Book et al., 2007). Also, individual speed uncertainties varied less than 0.1 cm/s from these medians, but individual directional uncertainties could vary more because they are inversely proportional to mean speeds.

The ADCP sites VR1 and VR2 were located on the northern flank of the cyclonic gyre in the northern Adriatic Sea. The complex correlations were quite high at VR2 (Table 1-8), while both VR1 and VR2 showed small mean directional errors in the COAMPS run (Table 1-9). The complex coefficients were fairly uniform throughout the entire column for VR1 and VR2 (and for all ADCPs shown in this study), indicating that the flow was indeed cyclonic in COAMPS with only small deviations from the mean direction of the current, especially at VR2. This is also illustrated in the compass diagrams, where the red vectors indicate the current flow during the primary bora event of 11-21 February, 2003 (Figs. 1-17 through 1-24). There was good agreement with respect to the observations at VR1 (Fig. 1-17, Table 1-9) and fair agreement at VR2 (Fig. 1-18, Table 1-9), where mean directional errors were generally less than 10-15 degrees. However, there seems to be more tidal influence in the observations at VR2 than at VR1.

The ADCP stations VR4, VR5, and VR6 were crucial to determining whether the model was accurately representing the double gyre current pattern. In this region of the Adriatic Sea the inflection of the double gyre current develops with the northern primary cyclonic gyre encompassing a much larger area than the smaller, yet distinct, anticyclonic gyre positioned just to the east or southeast of the cyclonic gyre (Fig. 1-16). The complex correlations at these sites were generally quite low when compared to the observations, confirming the notion that the double gyre pattern, albeit present in the COAMPS run, was shifted relative to the true observations. In general, the mean directional errors show a 20-40 degree difference between the COAMPS run and observations and the negative signs indicate a circulation pattern that must be shifted south and east to obtain the directions indicated by the errors. These errors are also shown quite well in the compass diagrams at each of the ADCP sites (Figs. 1-17 through 1-

24). The errors iterate the fact that small and subtle differences in the juxtaposition of the bora jets may induce large errors in the model output when compared to the observational data. However, it is important to note that even though COAMPS did produce errors in the position of the double gyre, the model is performing as expected by shifting the double gyre southward based on the southward displacement of the Trieste bora jet axis.

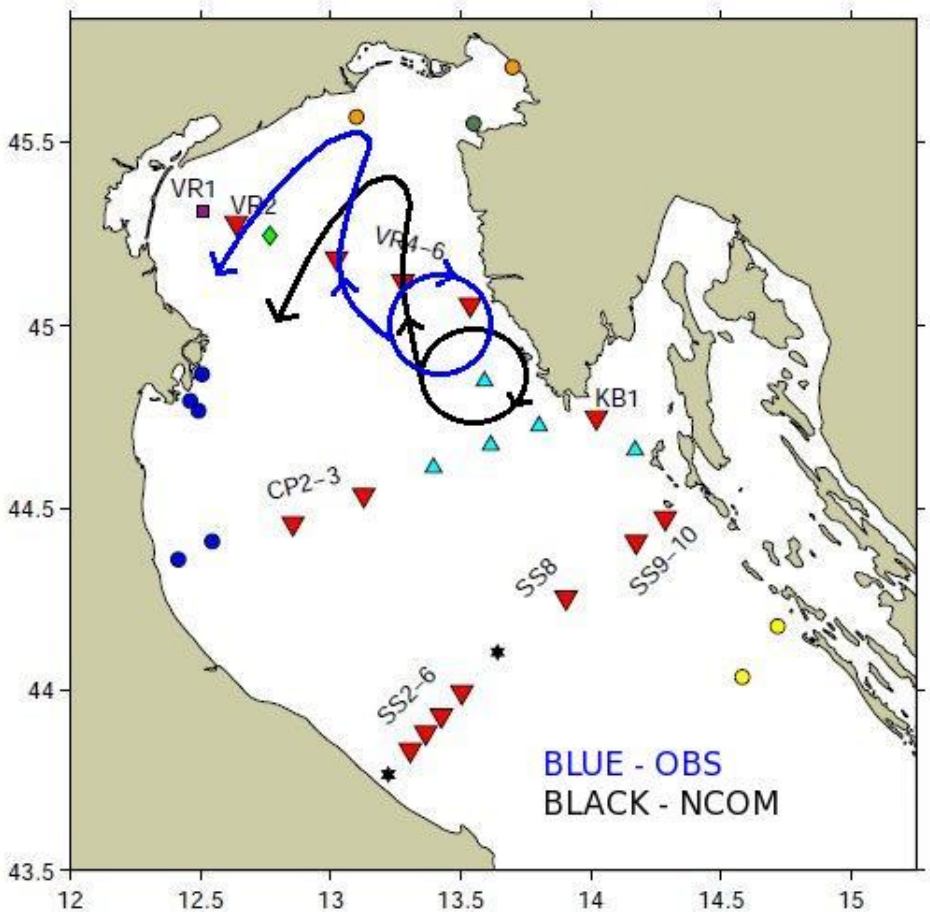

Figure 1-16: Adriatic currents in the coupled model (black line) versus the observations (blue line) showing the southward shift of the double gyre.

Further south in the northern Adriatic Sea, the ADCP sites at CP2, CP3, and KB1 were closely associated with the Senj bora jet. The currents can be quite variable at these sites depending on the strength and position of the Senj bora jet and its axis during the winter months. In terms of the complex correlation coefficient, the values at CP2 were quite low compared to the values at CP3, which can be attributed to the differences in extent and intensity of the Senj bora jet in the COAMPS run. The mean directional errors were quite small at CP3, generally less than 15 degrees throughout the depth of the column, while the mean directional errors were quite large at CP2 (Table 1-9). KB1, which was located just offshore of the Istrian Peninsula and in close proximity to the origin of the Senj jet, had a mean directional error throughout the column of less than 15 degrees, which can be considered good agreement, and a complex correlation that was only slightly higher than the values at VR4, VR5, and VR6 (Table 1-8).

Comparison of the uncoupled and coupled runs yielded mixed results with regard to the ADCP data (Tables 1-10 and 1-11). There was an overall slight improvement in the coupled runs; however, since the ocean was still being forced by the atmospheric winds of COAMPS, there was an oceanic current pattern similar to the coupled run. The mean directional error at VR4 was much improved in the coupled run (by approximately 30 degrees); however, there were no real improvements at VR5 and VR6 in the coupled run. An additional run, the pseudo "one-way coupled" run, was also statistically compared to the coupled and uncoupled runs ("pseudo" means that the initial NCOM SSTs were used to compute the fluxes throughout the 12-hour forecast integration without any changes or updates to the initial NCOM SSTs throughout the coupled forecast). NOTE: The "pseudo" one-way run is not the same as the one-way coupled run featured in Pullen et al. (2007). In general, holding the initial NCOM SSTs fixed showed some small improvements over the uncoupled run (Fig. 1-25), but the fully-coupled run (12-minute coupling and SST updates) was superior overall.

3.1.3.3 Coupling Interval

Sensitivity testing involving the coupling interval was performed and compared to two ADCP sites (VR2 and VR5). The fully-coupled run results shown throughout this report consisted of a 12-minute coupling interval. Subsequently, the coupling interval was changed to 1 hour, 3 hours, and 6 hours to investigate whether a shorter coupling interval made any appreciable differences in the overall results. Table 1-7 shows the depth-averaged complex correlation coefficient for both VR2 and VR5 for each of the coupling intervals. It appears that a shorter coupling interval resulted in some slightly better results, especially over the 6-hour coupling interval and uncoupled cases. However, differences were nearly negligible in the 12 minute and 1 hour coupling interval simulations. More testing is necessary to fully evaluate the results by changing the coupling interval.

Table 1-7: Two-way complex correlations for VR2 and VR5 for each coupling interval. Green indicates improved results.

CC	12 min	1 hr	3 hr	6 hr	uncoupled
VR2	0.560	0.554	0.519	0.513	0.461
VR5	0.242	0.246	0.232	0.228	0.210

Table 1-8: Two-way complex correlations for COAMPS for eight Adriatic Sea moorings (VR1, VR2, VR4, VR5, VR6, CP2, CP3, and KB1). Green indicates the best results.

NCOM level (m)	Mooring level (m)	CC							
		VR1	VR2	VR4	VR5	VR6	CP2	CP3	KB1
1.762	1.708	0.17							
2.554	2.708	0.18	0.62	0.15		0.10			
3.477	3.708	0.22	0.60	0.23	0.16	0.17	0.19	0.32	0.29

NCOM level (m)	Mooring level (m)	CC							
		VR1	VR2	VR4	VR5	VR6	CP2	CP3	KB1
4.552	4.708	0.27	0.59	0.22	0.17	0.16	0.14	0.26	0.30
5.806	5.708	0.32	0.59	0.18	0.21	0.16	0.14	0.25	0.29
7.268	7.208	0.36	0.58	0.18	0.22	0.17	0.14	0.24	0.29
8.971	8.708	0.40	0.57	0.22	0.24	0.17	0.12	0.23	0.29
10.957	10.708	0.47	0.54	0.21	0.26	0.16	0.08	0.23	0.28
13.271	13.208	0.46	0.52	0.23	0.28	0.16	0.05	0.20	0.27
15.968	16.4287		0.51	0.26	0.28	0.16	0.09	0.22	0.25
19.112	19.4287		0.48	0.26	0.28	0.16	0.15	0.22	0.21
22.777	22.5481			0.28	0.27	0.19	0.22	0.22	0.27
27.049	27.0481			0.30	0.31	0.17	0.24	0.30	0.31
32.027	32.3767						0.27	0.33	0.28
37.831	37.3767						0.29	0.33	0.15
44.595	44.8471								0.17

Table 1-9: COAMPS (two-way coupled) current directional errors (in degrees) compared to observation moorings (1-21 February, 2003). Green indicates improved results.

NCOM level (m)	Mooring level (m)	VR1	VR2	VR4	VR5	VR6	CP2	CP3	KB1
1.762	1.708	4.71							
2.554	2.708	-4.42	-5.98	-32.50		-61.34			
3.477	3.708	-11.93	-5.03	-27.85	-29.22	-33.41	76.79	7.22	6.74
4.552	4.708	-11.00	-2.92	-31.64	-25.62	-21.37	-74.96	-5.18	7.94
5.806	5.708	-8.61	-0.84	-36.43	-32.89	-29.21	-64.93	-9.29	5.07
7.268	7.208	-3.98	1.94	-38.39	-32.31	-19.39	-66.76	-6.15	3.35
8.971	8.708	1.81	2.36	-33.85	-35.40	-20.94	-57.50	0.58	-2.47
10.957	10.708	5.53	6.90	-36.15	-34.90	-16.41	-65.70	0.35	-2.13
13.271	13.208	1.41	10.51	-31.02	-35.89	-18.63	85.57	2.92	-2.00
15.968	16.4287		15.21	-30.82	-38.48	-18.30	4.64	9.54	-1.07
19.112	19.4287		22.69	-28.34	-39.95	-21.45	-9.76	5.79	9.98
22.777	22.5481			-31.63	-33.63	-25.52	7.31	12.45	9.42
27.049	27.0481			-27.20	-45.31	-28.56	10.66	17.53	10.66
32.027	32.3767						-0.18	23.90	8.29
37.831	37.3767						-0.55	35.76	8.04
44.595	44.8471								7.76

Table 1-10: Uncoupled complex correlation coefficients for eight Adriatic Sea moorings (VR1, VR2, VR4, VR5, VR6, CP2, CP3, and KB1). Green indicates better results.

NCOM level (m)	Mooring level (m)	CC							
		VR1	VR2	VR4	VR5	VR6	CP2	CP3	KB1
1.762	1.708	0.17							
2.554	2.708	0.18	0.53	0.16		0.11			
3.477	3.708	0.22	0.51	0.22	0.16	0.16	0.17	0.35	0.35
4.552	4.708	0.27	0.50	0.21	0.16	0.17	0.12	0.31	0.36
5.806	5.708	0.32	0.50	0.17	0.19	0.17	0.13	0.28	0.34
7.268	7.208	0.37	0.49	0.15	0.20	0.17	0.15	0.29	0.34
8.971	8.708	0.47	0.47	0.21	0.21	0.16	0.14	0.27	0.35
10.957	10.708	0.46	0.44	0.20	0.23	0.15	0.11	0.27	0.35
13.271	13.208	0.24	0.42	0.21	0.25	0.15	0.06	0.24	0.36
15.968	16.4287		0.39	0.23	0.24	0.14	0.01	0.26	0.34
19.112	19.4287		0.36	0.24	0.22	0.16	0.08	0.24	0.26
22.777	22.5481			0.26	0.21	0.16	0.13	0.23	0.22
27.049	27.0481			0.29	0.25	0.17	0.18	0.27	0.22
32.027	32.3767						0.20	0.24	0.23
37.831	37.3767						0.20	0.25	0.19
44.595	44.8471								0.20

Table 1-11: Uncoupled mean directional error for eight Adriatic Sea moorings (VR1, VR2, VR4, VR5, VR6, CP2, CP3, and KB1). Green indicates improved results.

NCOM level (m)	Mooring level (m)	VR1	VR2	VR4	VR5	VR6	CP2	CP3	KB1
1.762	1.708	5.67							
2.554	2.708	-6.25	-4.49	-62.45		-55.16			
3.477	3.708	-13.34	-5.79	-52.98	-15.81	-32.69	-84.98	10.14	25.62
4.552	4.708	-12.24	-2.98	-48.51	-20.00	-19.41	63.20	-1.13	25.26
5.806	5.708	-8.61	-1.41	-55.93	-23.48	-20.17	-47.47	-1.29	24.55
7.268	7.208	-5.67	1.38	-58.13	-24.59	-20.00	35.07	-0.27	23.36
8.971	8.708	3.26	0.40	-50.32	-28.42	20.71	-22.83	7.61	21.42
10.957	10.708	6.65	4.81	-50.13	-24.61	-18.30	-8.69	10.09	23.93
13.271	13.208	2.54	7.97	-44.41	-26.57	-18.92	5.81	11.63	19.07
15.968	16.4287		20.68	-45.13	-29.90	-20.12	-21.59	15.54	11.39
19.112	19.4287		33.34	-40.51	-33.68	-13.90	-16.98	14.35	3.13
22.777	22.5481			-42.98	-33.71	-11.52	14.64	14.95	-2.69
27.049	27.0481			-34.78	-39.20	-10.32	24.37	16.33	-8.77
32.027	32.3767						11.57	15.87	-16.59
37.831	37.3767						9.23	20.63	-26.71

NCOM level (m)	Mooring level (m)	VR1	VR2	VR4	VR5	VR6	CP2	CP3	KB1
44.595	44.8471								-27.70

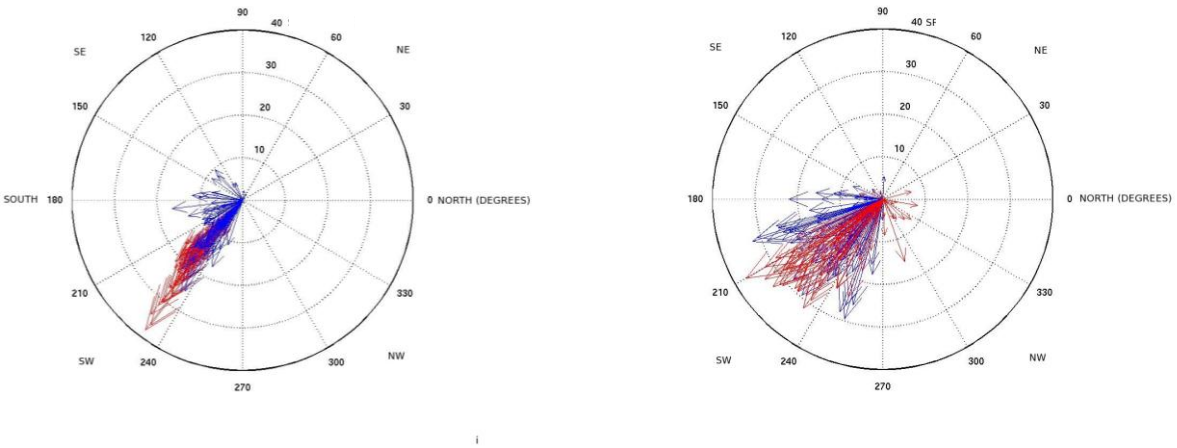

Figure 1-17: Compass diagrams indicating speed (cm/s) and direction (degrees) of currents at VR1 for 1-21 February, 2003. Red vectors indicate the period 11-21 February, 2003. Vectors are pointing in the direction of the current flow. Left: Two-way coupled COAMPS, Right: Observations.

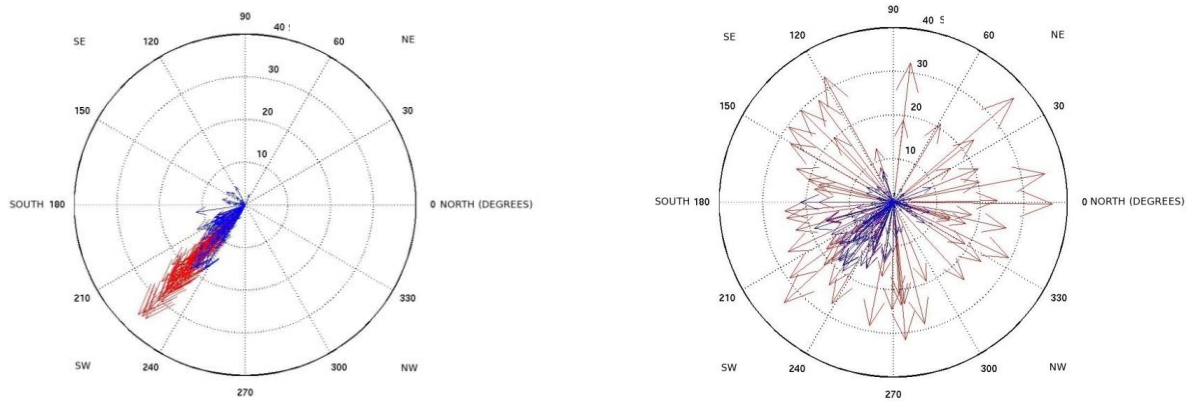

Figure 1-18: Compass diagrams indicating speed (cm/s) and direction (degrees) of currents at VR2 for 1-21 February, 2003. Red vectors indicate the period 11-21 February, 2003. Vectors are pointing in the direction of the current flow. Left: Two-way coupled COAMPS, Right: Observations.

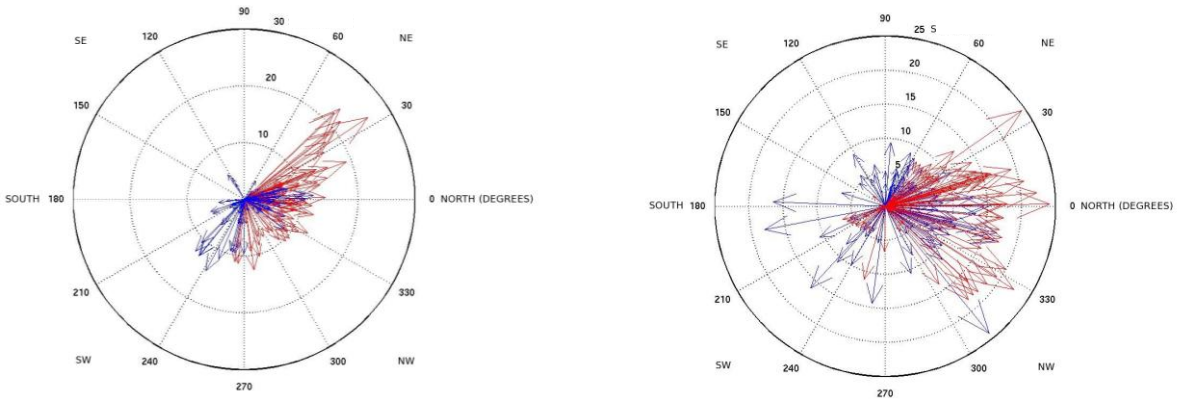

Figure 1-19: Compass diagrams indicating speed (cm/s) and direction (degrees) of currents at VR4 for 1-21 February, 2003. Red vectors indicate the period 11-21 February, 2003. Vectors are pointing in the direction of the current flow. Left: Two-way coupled COAMPS, Right: Observations.

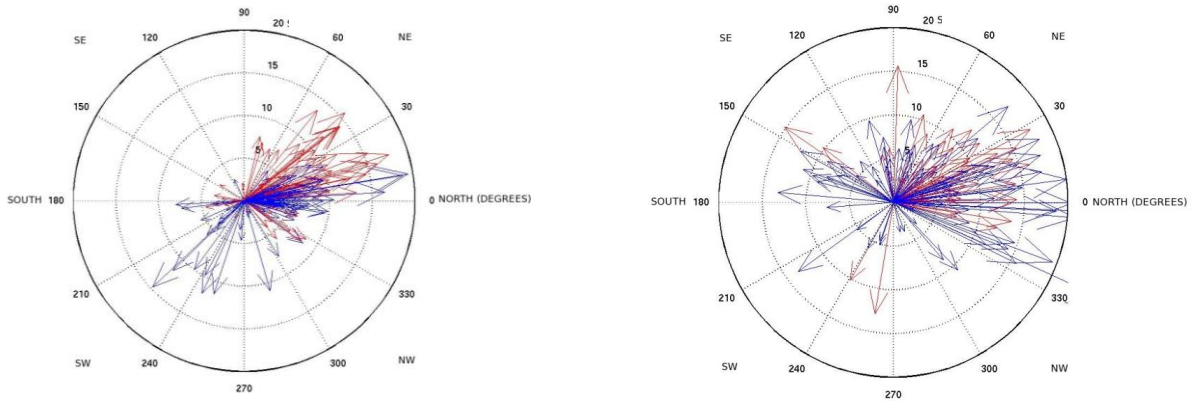

Figure 1-20: Compass diagrams indicating speed (cm/s) and direction (degrees) of currents at VR5 for 1-21 February, 2003. Red vectors indicate the period 11-21 February, 2003. Vectors are pointing in the direction of the current flow. Left: Two-way coupled COAMPS, Right: Observations.

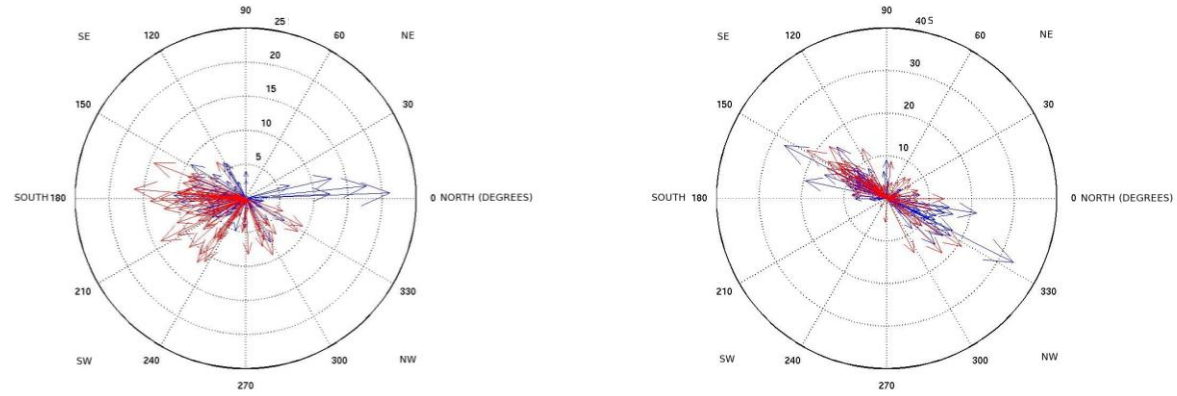

.

Figure 1-21: Compass diagrams indicating speed (cm/s) and direction (degrees) of currents at VR6 for 1-21 February, 2003. Red vectors indicate the period 11-21 February, 2003. Vectors are pointing in the direction of the current flow. Left: Two-way coupled COAMPS, Right: Observations.

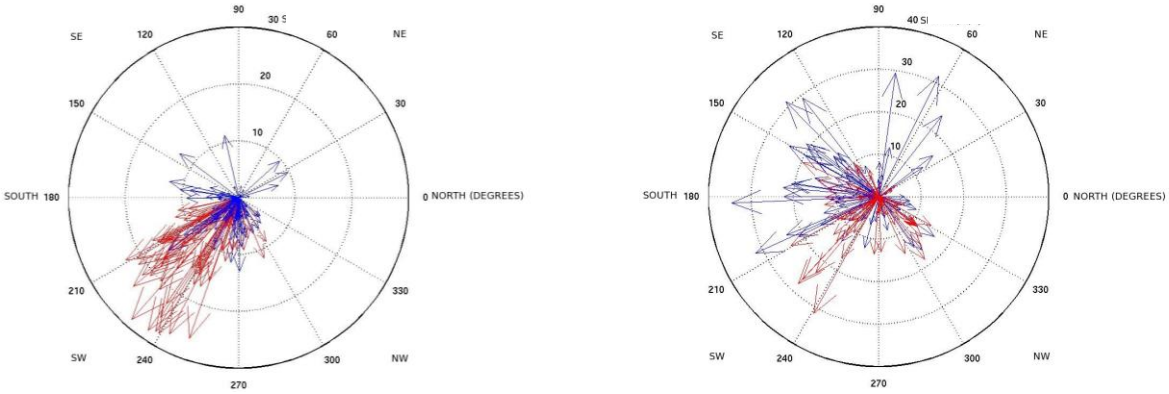

Figure 1-22: Compass diagrams indicating speed (cm/s) and direction (degrees) of currents at CP2 for 1-21 February, 2003. Red vectors indicate the period 11-21 February, 2003. Vectors are pointing in the direction of the current flow. Left: Two-way coupled COAMPS, Right: Observations.

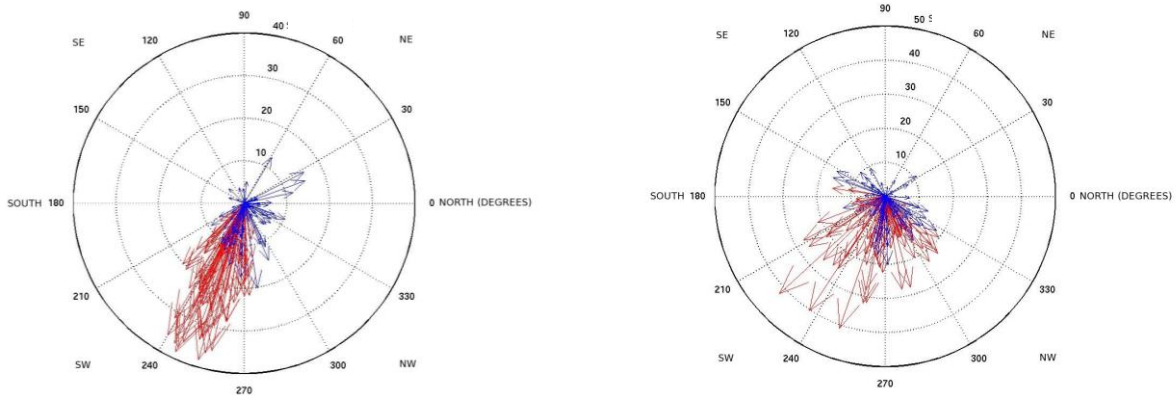

Figure 1-23: Compass diagrams indicating speed (cm/s) and direction (degrees) of currents at CP3 for 1-21 February, 2003. Red vectors indicate the period 11-21 February, 2003. Vectors are pointing in the direction of the current flow. Left: Two-way coupled COAMPS, Right: Observations.

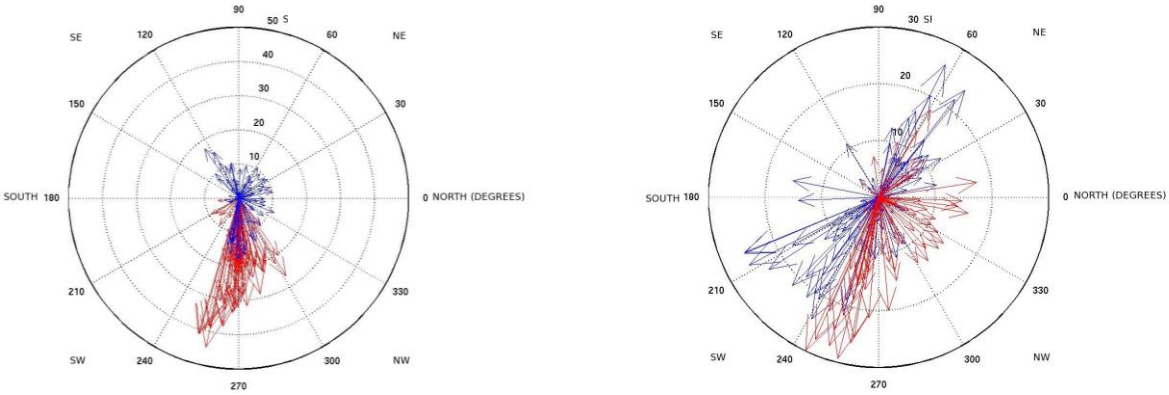

Figure 1-24: Compass diagrams indicating speed (cm/s) and direction (degrees) of currents at KB1 for 1-21 February, 2003. Red vectors indicate the period 11-21 February, 2003. Vectors are pointing in the direction of the current flow. Left: Two-way coupled COAMPS, Right: Observations.

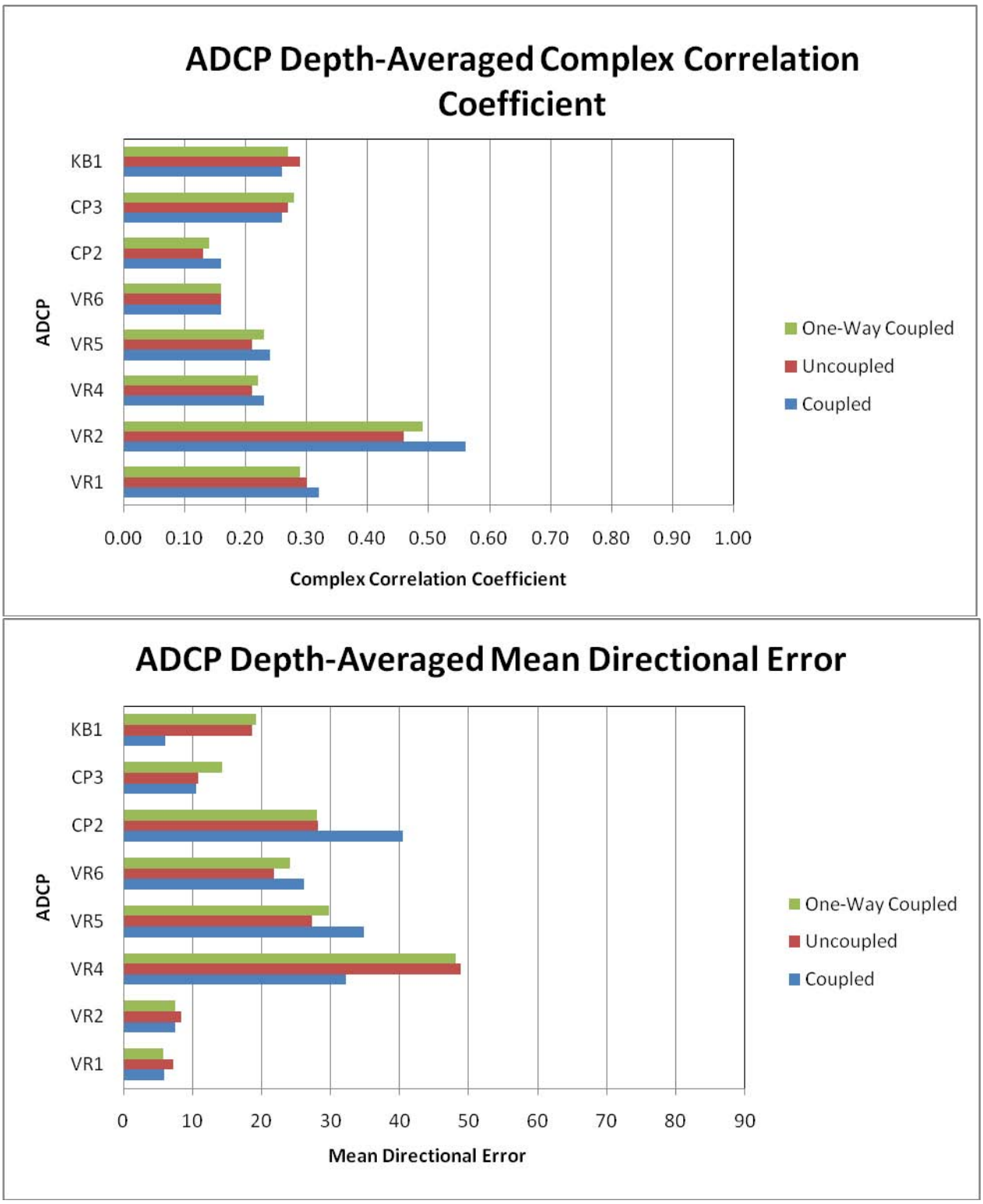

Figure 1-25: Summary of ADCP statistics for (a): depth-averaged complex correlation coefficient and (b): depth-averaged mean directional error for fully-coupled, uncoupled, and one-way coupled runs.

3.1.3.4 Ocean Model Validation with High Resolution Bathymetry

The plots (Fig. 1-26) and tables (Tables 1-12 and 1-13) below are COAMPS coupled and uncoupled simulation results obtained in the late stages of the VTR evaluations utilizing high-resolution 7.5 second bathymetry (versus the DBDB2 default bathymetry) for the Adriatic Sea. Overall, the ocean currents were much better simulated when compared to DBDB2 bathymetry (Sections 3.1.3.2 and 3.1.3.3), especially in the region of the double gyre surface current pattern (VR4, VR5, and VR6). Complex correlation coefficients and mean directional error were drastically improved upon at these ADCP sites. However, it is important to note that the small southward shift of the double gyre pattern due to southward shift and weaker Trieste bora jet (based on observations) was still present, but the currents were better defined using the high-resolution bathymetry. It is recommended that higher-resolution bathymetry be used in COAMPS if the data is available for the region of interest. There was an overall slight improvement in the correlation coefficient using the coupled model for the ocean currents; however, there was very little difference in the wind forcing between the coupled and uncoupled simulations.

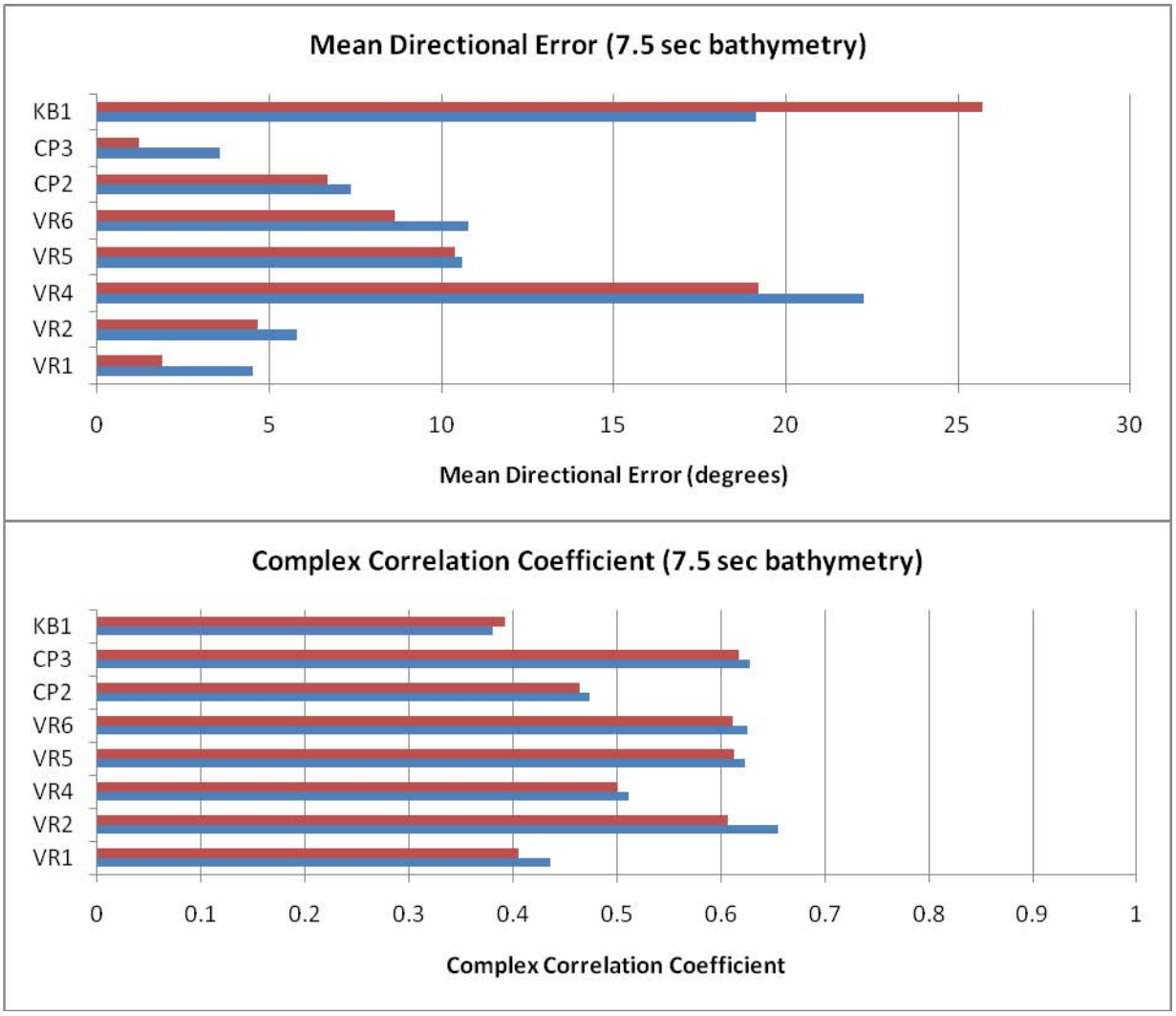

Figure 1-26: Mean directional errors and complex correlation coefficients for each ADCP site for February 1-23, 2003. Blue is coupled and red is uncoupled (no ocean feedback).

Table 1-12: Coupled mean directional errors and complex correlation coefficients with depth based on NCOM and ADCP levels using 7.5 second bathymetry dataset.

COAMPS current directional errors (degrees) compared to observation moorings (February 1-21, 2003)									
NCOM level (m)	Mooring level (m)	VR1	VR2	VR4	VR5	VR6	CP2	CP3	KB1
1.762	1.708	-2.28							
2.554	2.708	-3.65	-12.30	-26.58		-8.28			
3.477	3.708	-8.84	-11.76	-24.87	-8.28	-11.35	11.51	-4.97	23.88
4.552	4.708	-9.18	-8.92	-26.67	-11.35	-10.87	5.09	-8.45	26.09
5.806	5.708	-6.27	-8.04	-21.23	-10.87	-12.31	-0.73	-8.14	23.74
7.268	7.208	-9.82	-5.70	-22.30	-12.30	-11.80	-6.86	-6.51	23.21
8.971	8.708	-1.70	-5.79	-22.37	-11.79	-12.34	-8.69	-7.20	20.44
10.957	10.708	-0.38	-4.14	-21.45	-12.34	-14.26	-10.89	-5.63	21.53
13.271	13.208	-0.50	-2.74	-22.37	-14.23	-11.65	-12.50	-5.28	19.98
15.968	16.4287		-1.43	-21.77	-11.65	-9.88	-13.40	-4.28	17.88
19.112	19.4287		2.93	-19.91	-9.87	-5.24	-17.15	-3.91	17.41
22.777	22.5481			-18.62	-5.24	-8.59	-15.21	-1.74	14.14
27.049	27.0481			-19.02	-8.60	-12.54	-9.83	-0.51	16.40
32.027	32.3767						-10.20	3.64	16.92
37.831	37.3767						-6.65	6.70	14.49
44.595	44.8471								11.79
Complex Correlation coefficients compared to observation moorings (February 1-21,2003)									
NCOM level (m)	Mooring level (m)	CC							
		VR1	VR2	VR4	VR5	VR6	CP2	CP3	KB1
1.762	1.708	0.31							
2.554	2.708	0.34	0.65	0.25		0.57			
3.477	3.708	0.39	0.67	0.45	0.57	0.58	0.35	0.60	0.32
4.552	4.708	0.42	0.66	0.44	0.58	0.60	0.36	0.61	0.35
5.806	5.708	0.44	0.66	0.52	0.60	0.61	0.35	0.62	0.34
7.268	7.208	0.47	0.67	0.53	0.61	0.62	0.39	0.62	0.35
8.971	8.708	0.50	0.67	0.56	0.62	0.64	0.41	0.62	0.34
10.957	10.708	0.53	0.66	0.57	0.64	0.65	0.41	0.62	0.35
13.271	13.208	0.52	0.65	0.56	0.65	0.63	0.48	0.60	0.37
15.968	16.4287		0.64	0.56	0.63	0.64	0.52	0.62	0.38
19.112	19.4287		0.62	0.56	0.64	0.66	0.53	0.62	0.38
22.777	22.5481			0.56	0.66	0.65	0.58	0.63	0.41
27.049	27.0481			0.57	0.65	0.65	0.59	0.67	0.42
32.027	32.3767						0.59	0.67	0.44
37.831	37.3767						0.59	0.66	0.41
44.595	44.8471								0.46

Table 1-13: Uncoupled mean directional errors and complex correlation coefficients with depth based on NCOM and ADCP levels using 7.5 second bathymetry dataset.

COAMPS current directional errors (degrees) compared to observation moorings (February 1-21, 2003)									
NCOM level (m)	Mooring level (m)	VR1	VR2	VR4	VR5	VR6	CP2	CP3	KB1
1.762	1.708	2.92							
2.554	2.708	0.26	-11.88	-18.58		-17.38			
3.477	3.708	-7.46	-10.66	-20.58	-7.57	0.02	11.21	-0.20	34.03
4.552	4.708	-7.54	-7.69	-23.04	-11.04	1.21	4.71	-4.71	35.17
5.806	5.708	-4.21	-6.90	-18.72	-10.16	3.41	-1.36	-3.63	33.20
7.268	7.208	-3.09	-4.78	-19.77	-11.57	0.04	-7.07	-1.88	32.91
8.971	8.708	-0.19	-4.26	-20.29	-11.32	-3.73	-9.81	-1.93	30.33
10.957	10.708	1.44	-2.76	-19.18	-12.11	-2.67	-11.17	-1.04	31.48
13.271	13.208	1.02	-1.34	-20.26	-13.99	-8.18	-12.70	-0.90	29.39
15.968	16.4287		-0.47	-19.55	-11.69	-6.73	-12.09	-0.62	27.55
19.112	19.4287		4.16	-17.64	-9.98	-16.41	-14.59	-1.52	25.93
22.777	22.5481			-16.21	-5.88	-22.89	-13.01	-1.35	22.58
27.049	27.0481			-16.71	-8.82	-30.25	-7.71	-2.16	21.78
32.027	32.3767						-8.43	0.84	18.91
37.831	37.3767						-5.11	3.50	10.88
44.595	44.8471								5.85
Complex Correlation coefficients compared to observation moorings (February 1-21,2003)									
NCOM level (m)	Mooring level (m)	CC							
		VR1	VR2	VR4	VR5	VR6	CP2	CP3	KB1
1.762	1.708	0.26							
2.554	2.708	0.30	0.62	0.24		0.56			
3.477	3.708	0.35	0.63	0.43	0.57	0.57	0.31	0.59	0.33
4.552	4.708	0.38	0.63	0.42	0.57	0.59	0.37	0.60	0.36
5.806	5.708	0.42	0.62	0.51	0.59	0.60	0.35	0.61	0.35
7.268	7.208	0.45	0.62	0.52	0.60	0.60	0.40	0.62	0.36
8.971	8.708	0.48	0.61	0.55	0.61	0.62	0.41	0.61	0.35
10.957	10.708	0.51	0.60	0.56	0.63	0.63	0.42	0.62	0.37
13.271	13.208	0.50	0.59	0.55	0.64	0.62	0.48	0.59	0.39
15.968	16.4287		0.59	0.55	0.62	0.63	0.53	0.61	0.40
19.112	19.4287		0.56	0.56	0.63	0.64	0.53	0.61	0.40
22.777	22.5481			0.56	0.64	0.64	0.57	0.62	0.41
27.049	27.0481			0.56	0.64	0.64	0.56	0.65	0.41
32.027	32.3767						0.55	0.66	0.44
37.831	37.3767						0.55	0.64	0.43
44.595	44.8471								0.50

3.2 Test Case 2: Ligurian Air-Sea Interaction Experiment (LASIE07)

3.2.1 Purpose

The goals of Test Case 2 were to validate COAMPS against data from the Ligurian Sea Air-Sea Interaction Experiment of June/July 2007 (LASIE07). LASIE07 focused on the coincident measurement of oceanic and atmospheric boundary layer properties through the gathering of concurrent atmospheric and oceanic soundings. The atmosphere provides strong forcing (buoyancy and stress) on the ocean in this region, in winter and to a slightly lesser extent in summer. However, in the summer the SST response to wind events can be potentially larger, due to the 8ºC difference between the mixed layer (top 10-20 m) temperature and the temperature at around 50 m just below the seasonal thermocline. Hence, in the summer it is likely that much larger SST changes can be induced by atmospheric forcing. An interesting question is whether the ocean response in summer provides any feedback to the atmosphere and if fully coupled processes are involved. The first objective was to validate the coupled model against a detailed dataset of atmospheric and oceanic measurements. The second objective was to investigate the feedbacks from the ocean in synoptic events in summer in the Ligurian Sea, using fully coupled simulations and an uncoupled system where the atmospheric model receives no feedback from the ocean model. The model simulations for Test Case 2 must resolve strong summer Mistral winds due to steep land topography, specifically demonstrating their effect on the ocean (mixed layer cooling and eddy response) and feedback to the atmosphere (impacts on clouds, heat fluxes and wind stress).

A comprehensive report has been written that details the LASIE07 test area, observations, model configuration and results (Small et al., 2010). Please refer to this document for an in depth discussion of Test Case 2. A summary is provided below.

3.2.2 Test Case Characteristics

3.2.2.1 Test Area and Observations

The Ligurian Sea in the northwestern Mediterranean comprises a relatively shallow region (500m or less) northeast of the island of Corsica, and deeper water (over 2000m) to the northwest. It is characterized by a permanent cyclonic circulation involving both the surface and intermediate waters. More specifically, the Western Corsica Current and the East Corsica Current flow northwards on either side of Corsica, joining along the eastern periphery of the basin and forming the Northern Current, which flows westward along the coast of Provence, completing the cyclonic loop. The summer climatology of SST (Fig. 2-1) shows the dominant influence of wind stress on SST distribution. Relatively cool SST is seen in the deep Ligurian Sea and east of the Strait of Bonifacio, where winds are strong (Fig. 2-2). Warmer SST is found in the lee of the islands and in shallow water. Cold filaments extending east of the Strait of Bonifacio have been previously observed by Artale et al (1994), Perilli et al. (1995), Salusti (1998), and Bignani et al. (2008). Artale et al. and Perilli et al. suggest that the filament is related to a north/south cyclonic/anticyclonic gyre couplet driven by the strong winds through

the Strait of Bonifacio and the consequent Ekman pumping. As summer progresses from June to July, the SST increases by about 3ºC over the whole region in response to strong solar insolation and generally light winds (note different color scales in Figs. 2-1a, b).

In summer, surface winds are light except during occasional Mistral events which are often associated with cyclogenesis in the lee of the Alps (Drobinski et al., 2005). The mean wind picture (Fig. 2-2a, from QuikSCAT) shows the influence of the Mistral and Tramontane winds, with strong northwesterly winds emanating from the Gulf of Lions and turning cyclonically in the Ligurian Sea to southwesterly (Place names are marked on Fig. 2-1). Winds are weaker in the Gulf of Genoa and in the lee of the islands of Corsica and Sardinia, whereas a strong corner jet exists at the northwest tip of Corsica. There is also a jet in the Strait of Bonifacio between the two islands. Off the west coast of Italy, strong southwesterly winds are known locally as 'libeccio', while southeasterly winds are also frequent, known as 'sirocco'.

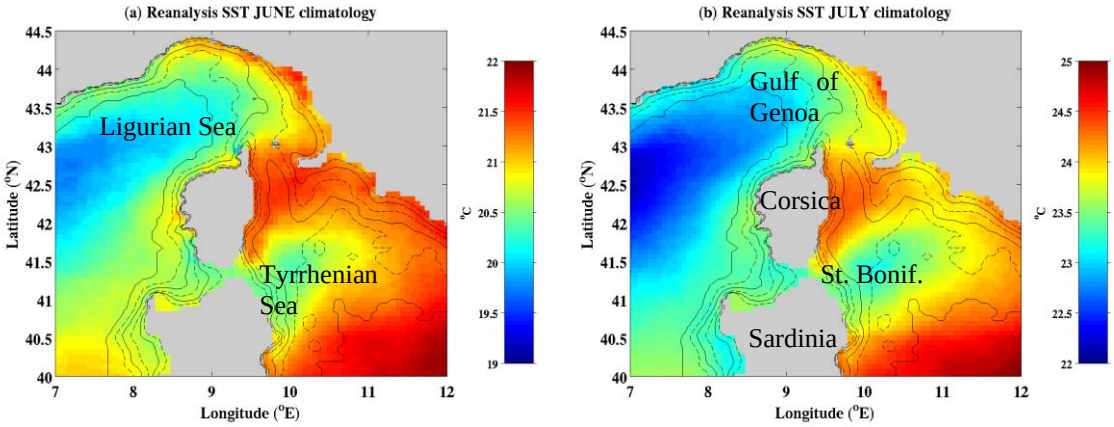

Figure 2-1: Climatological mean SST and bathymetry for the Ligurian and Tyrrhenian Sea for (a): June and (b): July. SST comes from the Consiglio Nazionale delle Richerche (CNR), Gruppo di Oceanografia da Satellite (GOS) reanalysis products. Bathymetry is contoured at 2000m, 500m, 100m (solid) and 1000m, 200m, 50m (dash). Names mentioned in the text are labeled in (a) and b) St. Bonif. refers to the Strait of Bonifacio.

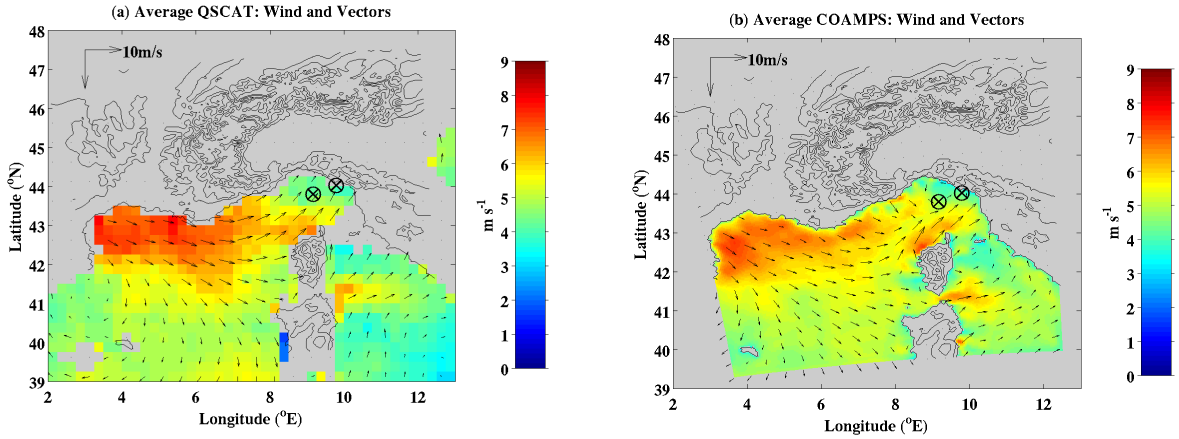

Figure 2-2: Near-surface winds over the Ligurian Sea. (a): Monthly average of neutral

equivalent 10 m winds from QuikSCAT. (b): monthly average of 10 m winds from COAMPS. These are averaged from 10 June to 9 July 2007 using model data only at times of the QuikSCAT swath (6am, 6pm local time). The topography of the Alps and Massif Central is contoured. The location of the ODAS (offshore) and METEO (coastal) moorings is shown in circles.

The two main regions of interest in the Ligurian Sea are shown in Fig. 2-3. These regions are i) the shallow water, the Gulf of La Spezia and Palmaria Islands, and the inner shelf, and ii) a deep water region. These areas are located by the pink circle in Fig. 2-3 and referred to by the i) Italian ENEA or METEO buoy and the ii) permanent Ocean Data Acquisition System (ODAS) buoy.

The Test Case 2 simulations, as well as the collection of meteorological and oceanographic observations, covered the time frame of 15 June to 10 July, 2007. During LASIE07 a combination of moorings, ship surveys (atmosphere and ocean), drifters, and gliders were used to gather *in situ* information, supported by satellite imagery of SST as well as Synthetic Aperture Radar (SAR) images. The Consiglio Nazionale delle Richerche (CNR) Research Vessel (R/V) *URANIA* and NATO Undersea Research Centre (NURC) ship R/V *LEONARDO* were employed, as well as the FWG vessel *PLANET*.

Comprehensive ocean profile data were gathered, including CTDs on *LEONARDO* and *PLANET*, and over 300 turbulence profiles. In the atmosphere over 100 radiosonde profiles were collected. Near-surface meteorological data and sub-surface thermistor data were collected from the ODAS buoy. Current and near-surface temperature measurements came from the nearby Shallow-water Environmental Profiler in Trawl-safe, Real-time configuration (SEPTR) and meteorological and wave data were collected at the METEO buoy near ENEA. Bathymetry comes from DBDB2.

This validation test mainly uses the following datasets and variables: satellite vector wind data, winds at the METEO and ODAS moorings, solar and longwave radiation at ODAS, near surface temperature and humidity, SST, and surface fluxes at METEO and ODAS, subsurface temperature at ODAS, radiosonde data from R/V *PLANET* for atmospheric boundary layer structure, and CTD data from *PLANET* for mixed layer depth and upper ocean structure (Teixeira, 2007).

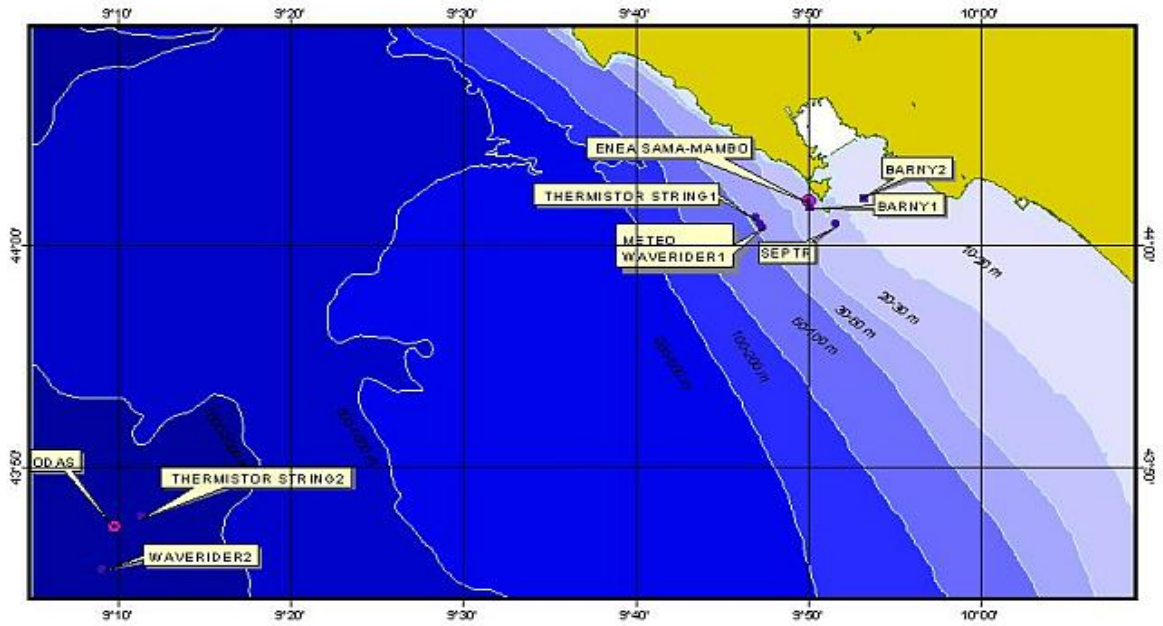

Figure 2-3: Test Case 2 model domain with bathymetric contours shown and LASIE07 deployed instrumentation marked.

3.2.2.2 Model Setup

The COAMPS Ligurian Sea configuration consisted of three nests of horizontal spacing 36 km, 12 km and 4 km, respectively (see Fig. 2-4 for the nest locations), with each nest having 40 vertical layers (with 14 layers in the lowest 1000 m and four in the lowest 100 m). Explicit microphysics were switched on in the inner nest to model cumulus convection, which was parameterized in the outer nests using the Kain and Fritsch (1993) scheme. Lateral boundary conditions for the atmospheric model came from the operational NOGAPS 1° model with 6-hourly output.

The NCOM had a 6 km horizontal resolution course mesh grid and a 2 km inner nest with 50 vertical levels, 35 sigma layers in the top 550 m, and 15 *z* levels below that. Initial and boundary conditions came from NOGAPS 1° resolution (6-hourly) and global NCOM (1/8°). The model was initialized on 10 June, five days before the main observation-model comparison began. The reason for this short spin-up was that the ocean model had no data assimilation, and a longer spin-up would have possibly allowed a large drift away from observed conditions. A 12-minute coupling interval was used in the simulations. At every coupling interval, SST from the ocean model was passed to the atmospheric model, formulating the bulk fluxes from the near-surface atmospheric variables (temperature, humidity, and wind velocity) with the modified Louis (1979) scheme. The fluxes were then passed back to the ocean. In COAMPS, the atmospheric model and then the ocean model were run in sequence. Time steps for the outer ocean and atmospheric grids were both 90 seconds. The system ran using MPI. The initial ocean condition was taken from a data-assimilating run of the global NCOM.

Two main experiments were performed for this study. The first was a fully coupled run using the model as described above. For the second experiment, we ran the atmosphere and ocean components, but the SST from the ocean was not passed to the atmosphere. Instead the atmospheric model used SST from an analysis of observations (through NCODA; Cummings, 2005) to compute the bulk fluxes. These fluxes were then used within the atmosphere and ocean model. We refer to this as the 'Uncoupled run', wherein the ocean was forced by the atmospheric component but there was no feedback from ocean to atmosphere. Note that this experiment was referred to as the 'Control' in Pullen et al. (2007). It differs from the 'one-way coupled' case of Pullen et al., (2007), which modified the fluxes for the ocean component to include the NCOM SST. The fluxes felt by the atmosphere were not modified in that case.

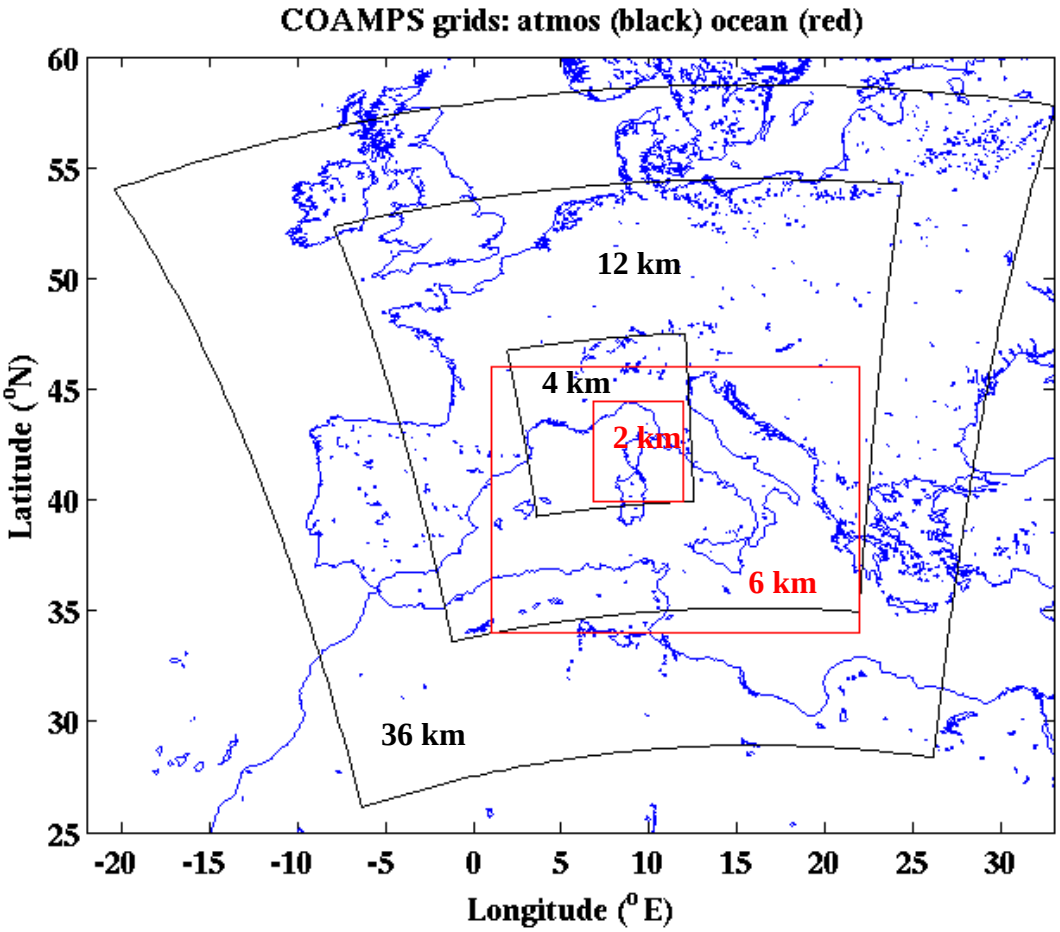

Figure 2-4: Map showing model nests for the atmosphere (in black) and ocean (red). Corresponding grid resolutions are annotated. The coastline data are from the outer (coarse) atmospheric nest.

In addition to the month-long simulations described above, a case study was performed for one Mistral event, namely a 72-hour forecast-type run with no assimilation after the initial time.

This case study helped explain why the coupled and uncoupled runs exhibited very small differences at the LASIE07 deep location, as discussed below.

3.2.3 Results of Month-Long Validation

Comparisons of measurements of near-surface variables from the ODAS and METEO moorings and estimates of surface fluxes at ODAS are made in the following sections, with the COAMPS model in a coupled and uncoupled mode. The fluxes for COAMPS are computed within the model, as described above, using ocean model SST (coupled case) or NCODA SST (uncoupled case) and atmospheric near-surface variables, using the modified Louis et al. (1979) scheme. For the ODAS mooring, fluxes were estimated from the wind measurements at 14.5 m and temperature and humidity at 13 m, using the Fairall et al. (1996) algorithm. Table 2-1 provides statistics for comparisons of ODAS and METEO buoy observations to COAMPS fully coupled [c] and uncoupled [u] simulations at the 4 km resolution. The statistics include CC, MB, and RMSE. Note that, while other data are assimilated into COAMPS, LASIE07 data are not.

Table 2-1: ODAS buoy vs. COAMPS 4 km grid simulation for June to 9 July, 2007, nearest grid point from 15. Wind speed statistics for the METEO buoy for one month are also included, while the statistics of air temperature, relative humidity, wind stress, and sensible heat fluxes at METEO are derived from just 10 days of data.

Variable	CC [c]	CC [u]	MB [c]	MB [u]	RMSE [c]	RMSE [u]
Wind Stress (N/m^2)	0.74	0.72	0.0057	0.0068	0.0460	0.0480
Wind Speed (m/s)	0.68	0.63	0.54	0.62	2.36	2.54
Downwelling solar flux (W/m^2)	0.93	0.94	-17	-21	122	121
Long-wave radiation (W/m^2)	0.59	0.59	-1.90	-1.00	24.41	24.28
Near surf. Air Temp (°C)	0.63	0.61	-0.23	0.14	1.04	1.01
Near surf. rel. humidity (%)	0.62	0.64	2.16	0.83	8.62	8.52
Sensible Heat Flux (W/m^2)	0.53	0.44	-3.81	-3.34	7.01	6.97
Latent Heat Flux (W/m^2)	0.61	0.64	-23.87	-18.72	46.93	46.00
METEO Buoy	**CC [c]**	**CC [u]**	**MB [c]**	**MB [u]**	**RMSE [c]**	**RMSE [u]**
Wind Speed (m/s)	0.43	0.42	-0.74	-0.63	2.40	2.40
Wind Stress (N/m^2)	0.34	0.29	-0.007	-0.004	0.02	0.05
Near surf. Air Temp (°C)	0.50	0.09	1.13	2.05	3.12	2.76
Near surf. rel. humidity (%)	0.54	0.50	-6.79	-6.69	11.80	11.92
Sensible Heat Flux (W/m^2)	0.60	0.57	-4.27	2.79	6.49	9.05
Latent Heat Flux (W/m^2)	0.72	0.76	-4.29	25.55	39.90	47.24

3.2.3.1 Wind Speed

Typically, wind speeds in the LASIE07 trial area were light, with a monthly average about 4-5 m/s (Fig. 2-2a). Stronger winds were observed emanating from the Gulf of Lion (Fig. 2-2a),

probably associated with occasional alpine lee cyclogenesis over the Gulf of Genoa and the summer Mistral. Other regions of strong winds include the strait of Bonifacio between Sardinia and Corsica (mean wind up to 7 m/s) and the northwest coast of Corsica. These features are seen both in QuikSCAT (Fig. 2-2a) and in COAMPS (Fig. 2-2b) and it is noteworthy that the COAMPS winds add more detail and finer structure and better resolve the Corsica/Sardinia Strait jet (QuikSCAT data are not assimilated into COAMPS in this experiment).

Transient variability of the winds can be seen in LASIE07 mooring data from a location just offshore of La Spezia (METEO buoy close to West Palmyra Island, Fig. 2-5) and at the ODAS buoy, (Fig. 2-6a, for locations see Fig. 2-3). In particular, observed wind speeds approached 10 m/s or more on 26-27 June and 3-4 July at ODAS and METEO (Figs. 2-5, 2-6a, black lines) and on 23 June, and at ODAS only on 9-10 July (Fig. 2-6a). These events were associated with Mistral winds off the Gulf of Lion, with wave heights greater than 2 m at the METEO buoy.

COAMPS coupled model data at the closest grid point to the moorings (Figs. 2-5, 2-6a; blue lines) reproduced the main features of these wind events, but a close inspection reveals some differences. The overall correlation between the fully coupled model and observations at the METEO buoy was 0.43 (from hourly data), and at ODAS it was 0.68 for the coupled model (3-hourly averages). The mean bias was rather small, around 0.5 m/s, while the RMSE was about 2.4 m/s for both locations. The correlation at ODAS was significant at 99% and at METEO it was significant at 95%, using a standard two-sided test. The uncoupled run produced fairly similar wind speeds (Figs. 2-5, 2-6; red line) but had slightly lower correlations: 0.42 and 0.63 at METEO and ODAS, respectively. These differences in CC between the coupled run and uncoupled run were not significant at 95% using standard tests.

Poorer correlations at the METEO location related to difficulties in getting near coastal winds correct, being subject to fine-scale aspects of topography, coastline and possibly land use and vegetation. In particular it can be noted that the COAMPS model produced a strong diurnal wind in the morning (land breeze with a northerly direction) at METEO (Fig. 2-5), which was less prominent and more irregular in the observations. The coupled model overpredicted the strong wind events of 26 June and 4 July (day 34) at METEO (Fig. 2-5) but slightly underpredicted the same events at ODAS (Fig. 2-6a).

A comparison of wind stress from COAMPS and ODAS observations is shown in Fig. 2-6b. (Wind stress at METEO is discussed in Section 3.2.3.5.2 and Fig. 2-17a). As expected, the wind stress tended to exaggerate the model-observation differences seen in the wind speed (Fig. 2-6a). For the high wind events of 16, 23, and 26 June, the model wind stress was typically between ½ and ⅔ of the observed value, but agreement was nearly perfect on 4 July (with a small temporal lag).

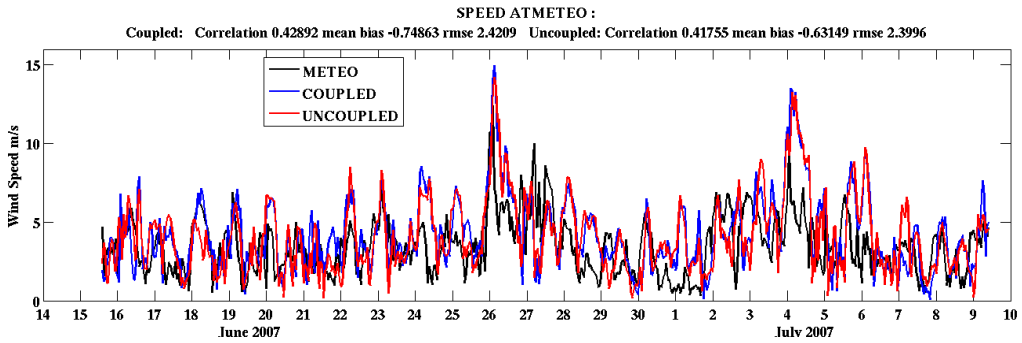

Figure 2-5: Wind speed measurements from LASIE07 mooring data and from COAMPS. Observations (black line) from the METEO buoy (West Palmyra Island, see Figure 2-3). The model 10 m wind is from COAMPS inner (4 km) grid, nearest grid point: coupled (blue), uncoupled (red). Data are from 15 June to 9 July.

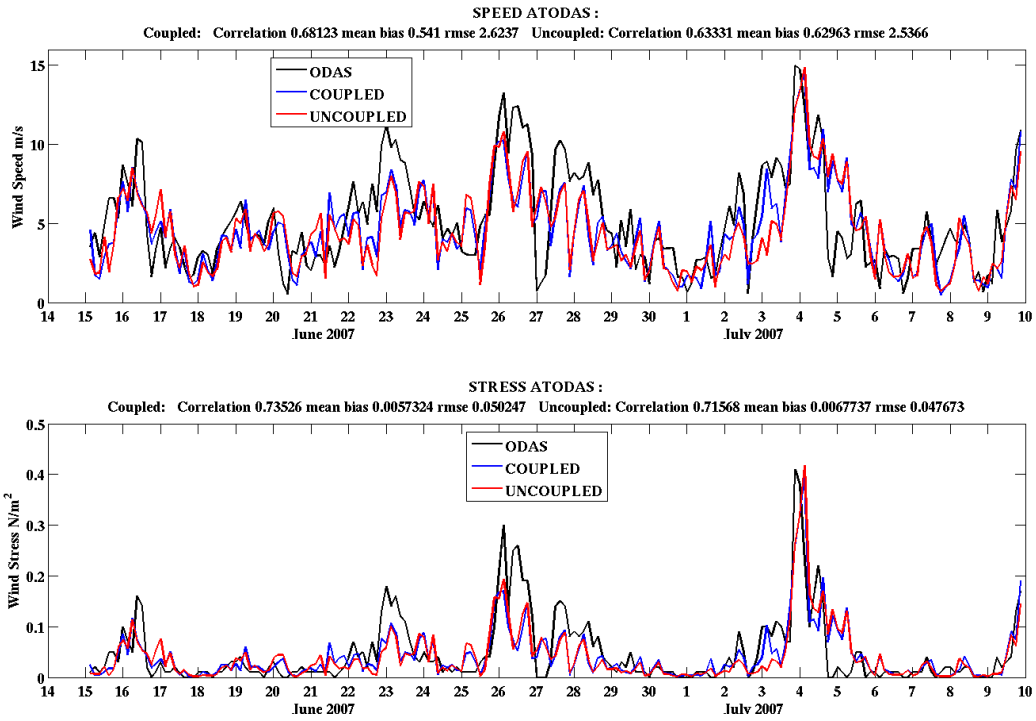

Figure 2-6: (Top) Wind speed measurements and (Bottom) wind stress from LASIE07 mooring data (black) and from COAMPS. Observations are from the ODAS buoy (see Figure 2-3). The model 10 m wind is from COAMPS inner (4 km) grid, nearest grid point: coupled (blue), uncoupled (red). Data are from 15 June to 9 July. COAMPS hourly data were averaged onto the 3-hour average period of ODAS.

The land-sea breeze simulation in the model can be compared against satellite wind data from QuikSCAT. The QuikSCAT swaths are twice daily, at local early morning and early evening. Maps of the difference between morning winds (6 am local time) minus early evening winds (6 pm local time) from QuikSCAT and COAMPS show the land-breeze minus sea-breeze difference, referred to here as the 'diurnal wind' (Fig. 2-7). It can be seen that COAMPS has a

larger diurnal wind, although the spatial distribution is similar. In particular, the model shows a large diurnal wind in the Gulf of Genoa, the region of the LASIE07 experiment (Fig. 2-7b), and extending as far as the ODAS mooring, but there was a stronger diurnal wind at the METEO location, reaching 2 to 3 m/s. This contrasted with corresponding values of 1 m/s or less in the QuikSCAT data (Fig. 2-7a). Although it may be argued that QuikSCAT is not suitable to examine near-to-coast effects (because of land contamination within 25 km of the coast), this figure strongly suggests that the diurnal wind in COAMPS was much too large. This may possibly relate to larger SST in the model than observed (see Section 3.2.3.3), which would exaggerate the land breeze but diminish the sea breeze. It may also relate to cooler nighttime ground temperatures due to a lack of cloud cover.

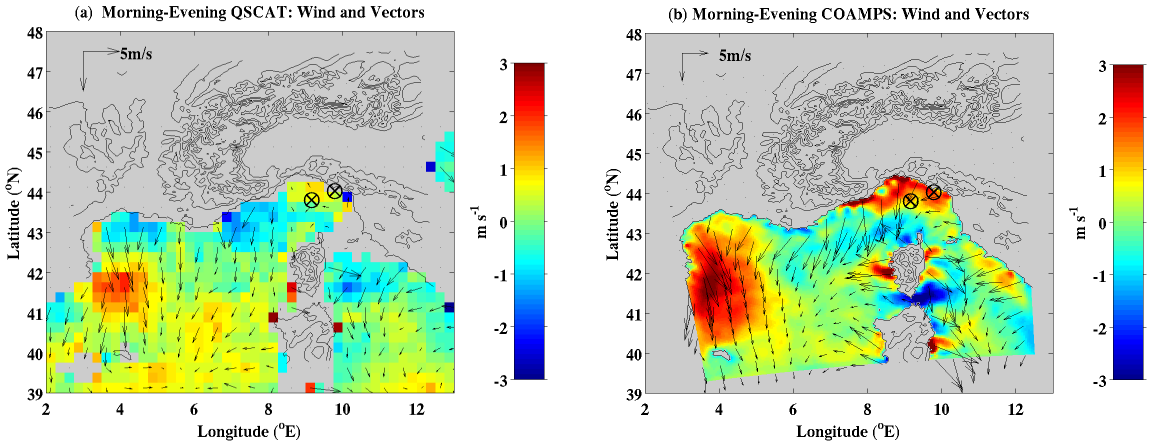

Figure 2-7: Near-surface land-sea breeze over the Ligurian Sea. (a): the average difference of ascending (6 am) minus descending (6 pm) swath data from QuikSCAT. (b): corresponding average of 6 am minus 6 pm forecasts from COAMPS. The topography of the Alps and Massif Central is contoured. The location of the ODAS (offshore) and METEO (coastal) moorings are shown in circles.

3.2.3.2 Radiation

Downwelling solar irradiance comparisons from ODAS and COAMPS are seen in Fig. 2-8a. There was very good agreement on the clear sky days, which lead to a good overall correlation of 0.93 and 0.94 for fully coupled and uncoupled runs, respectively. However, on non-clear-sky days, such as from 17-21 June and 25-26 June, agreement was not as good, with COAMPS usually overpredicting solar flux. This suggests that some aspect of cloud cover was missing in COAMPS on these days. The virtual agreement of the coupled and uncoupled runs (the red and blue curves mostly overlie) showed that coupled processes were not important to cloud cover in this model and at this location. Specifically, the SST differences between the two models, shown below, did not appear to have an effect on clouds (21 June is an exception, a day when the surface latent heat flux was larger in the coupled run than in the uncoupled or the observations – see Fig. 2-13b). Further analysis of the cloud fields (not detailed here) showed that the reason for overprediction of solar radiation in COAMPS on certain days was not a simple case of no clouds being predicted but rather that COAMPS clouds may have been too

diffuse or occurred at wrong times of day, such as early morning, and evaporated or moved away before the mid-day.

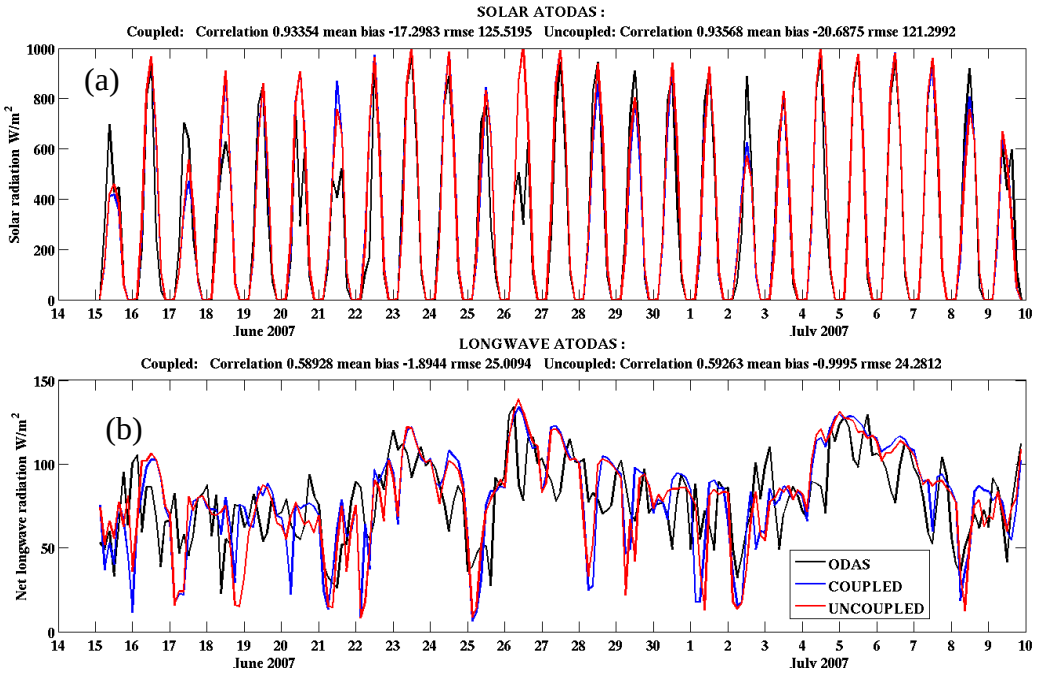

Figure 2-8: (a): Downwelling solar flux measurements from LASIE07 mooring data and from COAMPS. (b): Long-wave radiation at ODAS. The ODAS downwelling measurements are subtracted from an estimate of upwelling IR, given by $\varepsilon\sigma T^4$, where ε is the emissivity of sea water (set to 0.98 here), σ is the Steffan-Boltzmann constant, and T is surface temperature, estimated here by the 1 m ocean temperature.

The net long wave radiation (Fig. 2-8b) showed a similar multi-day oscillation in model and observations that explained the high correlations (Table 2-1), but there were some differences on sub-daily timescales. Near-zero radiation denoted times when long wave forcing down from clouds and water vapor nearly balanced that forcing upward from the sea surface, but large positive values denoted periods of great unimpeded upward radiation. Small near-zero values were recorded in both model and observations on 21 and 25 June and 2 and 8 July, when the relative humidity was high (Fig. 2-11b) and clouds were present in the boundary layer of the model. However, COAMPS appears to have too many instances of early morning near-zero longwave radiation (16, 17, 20, 22, 28, 29 June and 1 July), indicating either the cloud and water vapor were not distributed correctly in the model or the radiative transfer function was in error.

3.2.3.3 Sea surface temperature at ODAS

The sea surface temperature is a very important ocean variable for air-sea interaction. Because the upper few meters of the ocean are very sensitive to diurnal warming by solar radiation and longwave cooling, there can be a strong vertical gradient of temperature near the surface. Therefore, as different instruments (satellite and *in situ*) measure the SST at different near-

surface depths, they often produce diverse SST values (Fairall et al., 1996a). However, it is expected that measurements of SST from these different instruments would agree the most during nighttime, to within about 0.3ºC (Marullo et al., 2007). For this reason, several of these comparisons are made with nighttime-only data. Further discussion of this can be found in Small et al., 2010.

A timeseries of near-surface ocean temperature from the ODAS mooring (at 1 m) and the NCOM component of the coupled COAMPS (at 0.25 m) is shown in Fig. 2-9a. The uncoupled COAMPS has SST fixed for the duration of the forecast, only changing every 6 or 12 hr, depending on the NCODA data assimilation cycle. The coupled model showed similar trends to the observations, with comparable cycles of warming and cooling over several days (on synoptic timescales). However, the COAMPS model produced a stronger diurnal SST cycle on some days and a bias of warmer temperature (by about 1ºC) after 25 June (10 days into the run; the first five days are not shown). Further, the SST from the ocean part of the uncoupled run (red line) exhibited larger diurnal cycles than the coupled run, but had a similar overall change.

To identify whether the offset between model and observation is due to model error or observation calibration, drift or both, we compared against different, independent datasets. Firstly, CTD profiles collected from within a 10 nautical mile radius of ODAS and at a similar total water depth were identified. For CTD profiles that showed a clear mixed layer (~10 m deep), the mixed layer temperatures were plotted on Fig. 2-9a as crosses, and they showed values similar to or lower than the ODAS temperature. The fact that no CTD value was higher than the ODAS temperature suggests that the model was exhibiting a warm bias (Note that CTD values that were lower than ODAS may be due to spatial heterogeneity on small sub-10 nm scales).

COAMPS and ODAS may also be compared with nighttime satellite data when the various SST measurements should be most similar. ODAS comparisons were made to NCODA SST (00Z), which is based on satellite and *in situ* data, to the coupled model at 06Z and to nighttime satellite SST data from the Italian CNR Gruppo di Oceanografia da Satellite (GOS) (Marullo et al. 2007; Fig. 2-9b). The comparisons revealed that the coupled model had a warm bias in nighttime SST. The biases relative to ODAS for both the NCODA analysis and the CNR GOS SST were generally less than those for COAMPS, especially after 26 June. Taken together, Fig. 2-9 (a and b) showed that the model had a warm error bias which developed about 10 days into the run but stayed fairly constant after that.

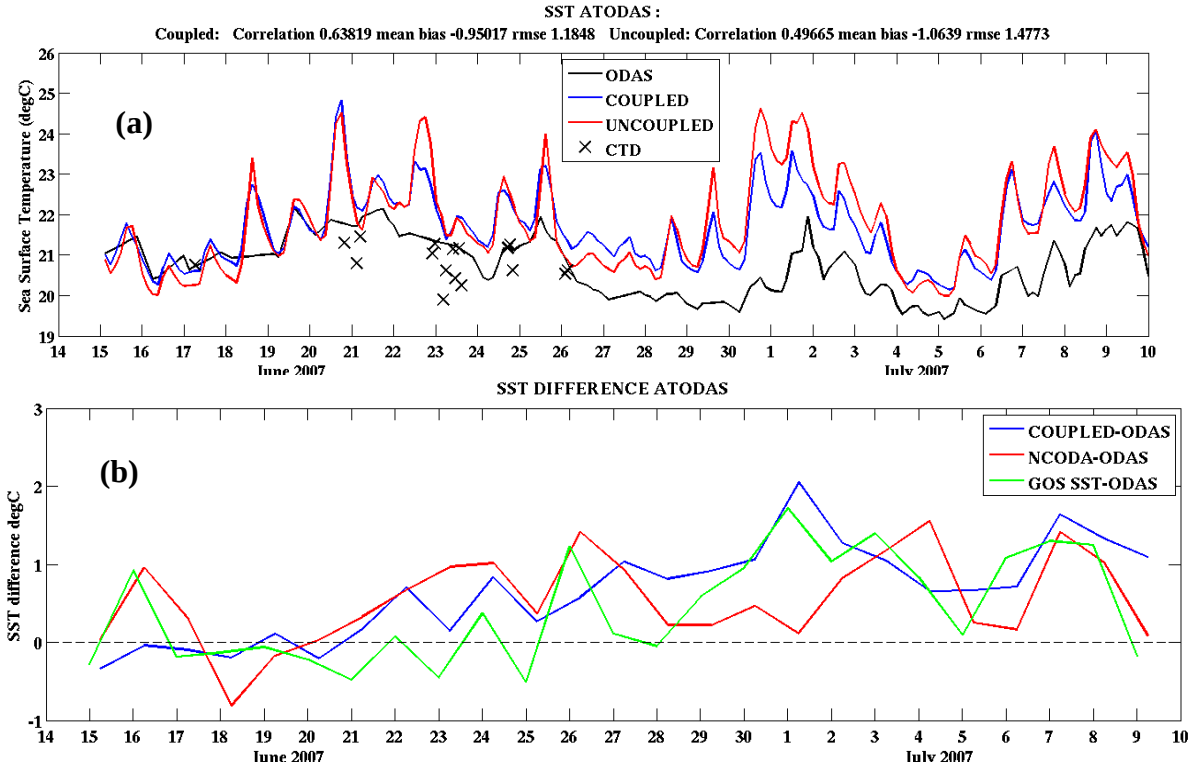

Figure 2-9: Timeseries of SST at the ODAS location. (a): Curves show (see legend) the ODAS 1 m ocean temperature, the fully coupled run upper level temperature (0.25 m) from NCOM, the uncoupled run upper level temperature (0.25 m), and mixed layer temperatures derived from selected CTD data. (b): using nighttime values only, differences with the corresponding ODAS 1 m temperature. Curves show (see legend) the coupled run at 06Z, the NCODA analysis 0Z SST, and the delayed time satellite SST products from GOS (using all available infrared sensors). ODAS data are interpolated where SST measurements are missing.

Another notable discrepancy between model and observations is in the daytime (diurnal) warming of SST. The ODAS temperature was nominally measured at around 1 m depth, whereas the model temperature is taken from the middle of the upper layer at about 0.25 m depth. Further, the near-surface temperature data from ODAS had many data gaps which degraded the analysis of diurnal cycle. This is clearly illustrated in Fig. 2-10a for the period of 16-22 June, showing the original (non-interpolated) ODAS near-surface data as a black dashed line. The ODAS data gave a reasonably full record of the diurnal cycle on just one day, the 21st.

A few days of near-surface temperature data were also available from a free-falling turbulence microstructure probe deployed from R/V *URANIA*. They were acquired while the ship was drifting with engines off, beginning at the ODAS buoy location. For each profile the temperature data have been averaged into 0.5 m bins, and are displayed for depths centered at 2 m, 3 m and 4 m. The probe was deployed for multiple profiles (series), with 6-8 profiles per series and each profile lasting about 15 minutes. The data were further averaged into mean

values for each series, together with their standard deviations. The mean values are shown in Fig. 2-10a as solid lines, with different colors denoting the different depths (see legend), while the +/-1 standard deviations are shown as small colored dots. A diurnal cycle is quite visible at each of the depth levels, with an amplitude (maximum evening temperature minus minimum morning temperature) of up to 1ºC at 2 m depth and about 0.5ºC at 4 m depth. The temperature variability at a fixed depth within each series, represented by the +/-1 standard deviation dots, possibly relates to patches of different waters encountered during each series of acquisition (between the start/end of each series the R/V URANIA covered a distance of about 1.5 nautical miles).

The corresponding coupled model near-surface temperatures reveal several notable features. Firstly, the diurnal cycle at 1 m (Fig. 2-10b, black line) is much larger than at subsequent depths, as expected from typical solar absorption curves. The diurnal range at 2 m is 0.5-1ºC, slightly less than observed. The diurnal range at 3 m and 4 m (Fig. 2-10b, red and green lines) appears to be fairly small compared to observations (Fig. 2-10a), and there appears to be dissimilar frequency components (i.e., between 19 and 20 June there are three peaks in temperature at 4 m; the second peak is out of phase with the 1 m temperature). Further, the observed temperatures at the different depths typically collapse to similar values at nighttime (see discussion above) but the model temperatures do not.

Differences between the observed and model-predicted near-surface temperature may be due to measurement uncertainties, limitations of mixed layer physics in the model, poor prediction of advective processes, or incorrect fluxes. Regarding measurement uncertainties, it should be noted that the turbulence data were consistent with the limited ODAS temperature data from 17-20 June. The model's mixed layer physics could show limitations, as the Jerlov Type IA solar absorption used in the model may be absorbing too much solar radiation in the upper 1 m or so and not enough in the next few meters. Regarding the fluxes, the winds and wind stresses during 17-20 June were similar in both model and observations, with wind speed errors typically less than 2 m/s (Fig. 2-6), but solar radiation had large errors of over 200 W/m^2 (averaged over daylight hours). The model had significantly larger solar radiation flux into the ocean on 18, 20 and 21 June (Fig. 2-8).

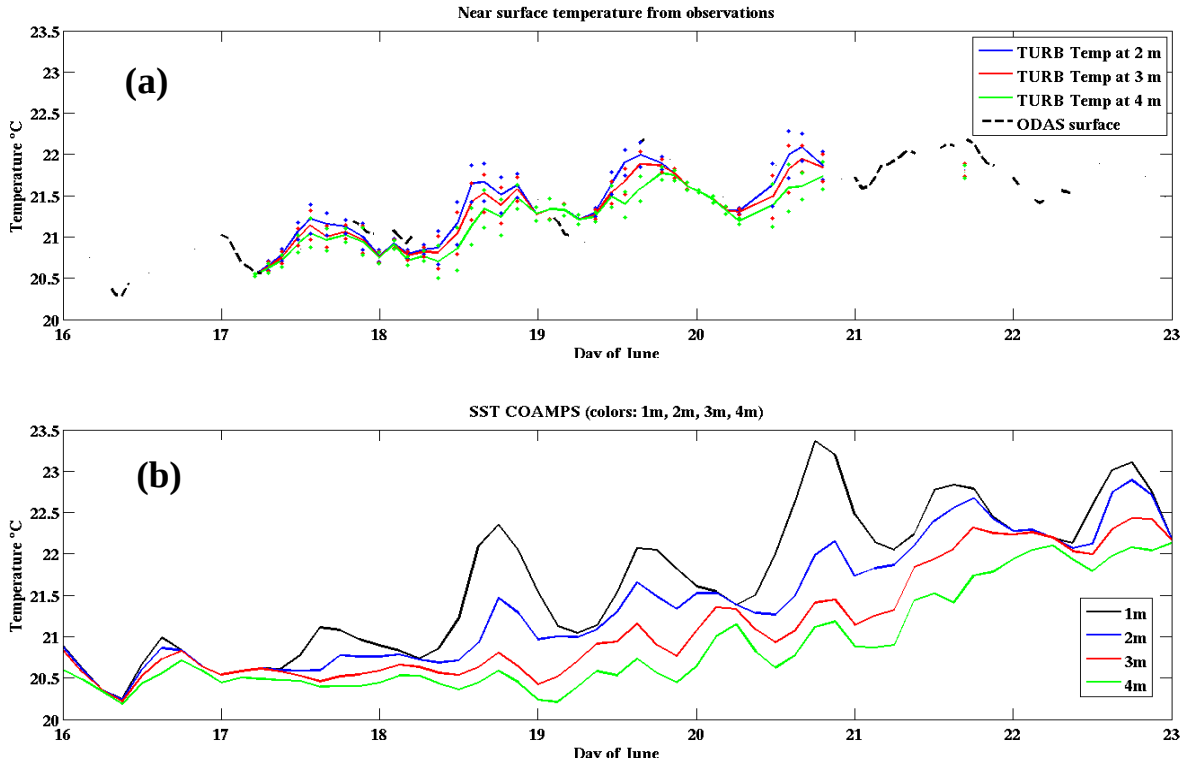

Figure 2-10: SST diurnal cycle. (a): Near-surface temperature data from turbulence microstructure probes (thick solid lines and small colored dots), deployed from R/V URANIA, and original ODAS data (blue dashed line). The thick solid lines denote mean values from a series of casts, with different colors denoting different depths (see legend), while the +/-1 standard deviation is shown as small colored dots. (b): near-surface temperatures from the NCOM component of the coupled model. Different colors denote different depth cells, as noted in legend.

3.2.3.4 Near surface atmospheric parameters

Both the near-surface air temperature and near surface relative humidity in the model were well correlated (0.6 or above) with their observed counterparts (Fig. 2-11a, b), but, as with the wind speeds, there were significant differences on daily and sub-daily scales. For example, large amplitude, cold, dry intrusions often occurred in the early morning in the model (e.g., 16, 17, 20, 22 June) that were absent or weak in the observations. They occurred in both the coupled and uncoupled runs. A profile comparison of temperature and humidity with radiosonde data (Section 3.2.3.7) in the lowest 2 km revealed that the model had an overly large 'atmospheric tide' due to thermal heating or possibly to the land-sea breeze (Fig. 2-7), such that in the early morning cold, dry air from the high land mass to the north and east was advected over the mooring location.

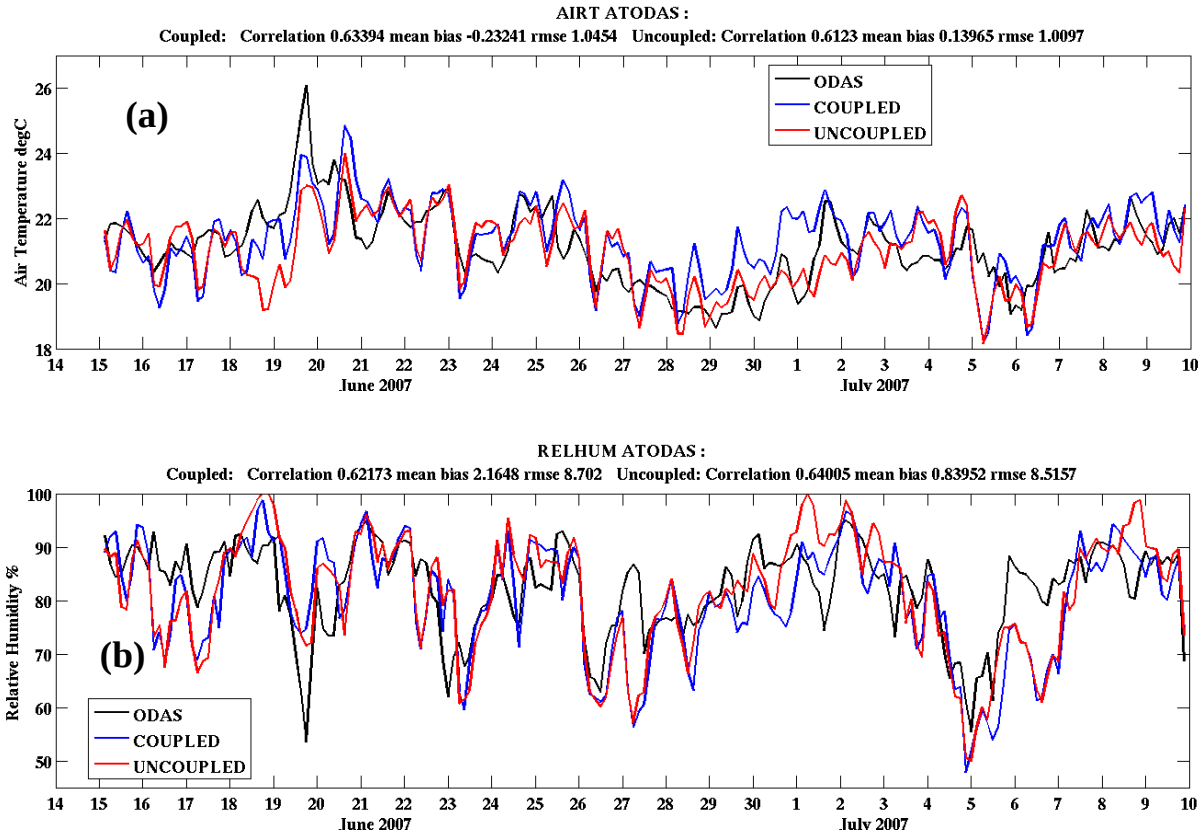

Figure 2-11: As Fig. 2-6a, but for (a): near-surface air temperature and (b): near-surface relative humidity. Air temperature and relative humidity were at 10 m in the model and 13 m at ODAS.

The turbulent heat fluxes depend on 1) wind speed, 2) the sea-minus-air temperature difference (for sensible heat), and 3) the difference between the near surface air humidity (q_a) and the saturation specific humidity for the SST value q_s (for latent heat). The sensible heat flux plot (Fig. 2-12b) shows that COAMPS often predicted large, positive (unstable) heat fluxes not seen at ODAS. For example, on the mornings of 16, 17, 26, 27, and 28 June and 5 July, the wind speed was reasonably high in the model (>5 m/s; Fig. 2-6a) and the model air temperatures were too cool (Fig. 2-11a) compared to ODAS. This, combined with the general tendency for COAMPS SST to be too high (Fig. 2-9), lead to a large sea-air temperature difference (Fig. 2-12a) and sensible heat fluxes that were too large (Fig. 2-12b). On other occasions COAMPS–ODAS differences were partly due to weak winds in the model.

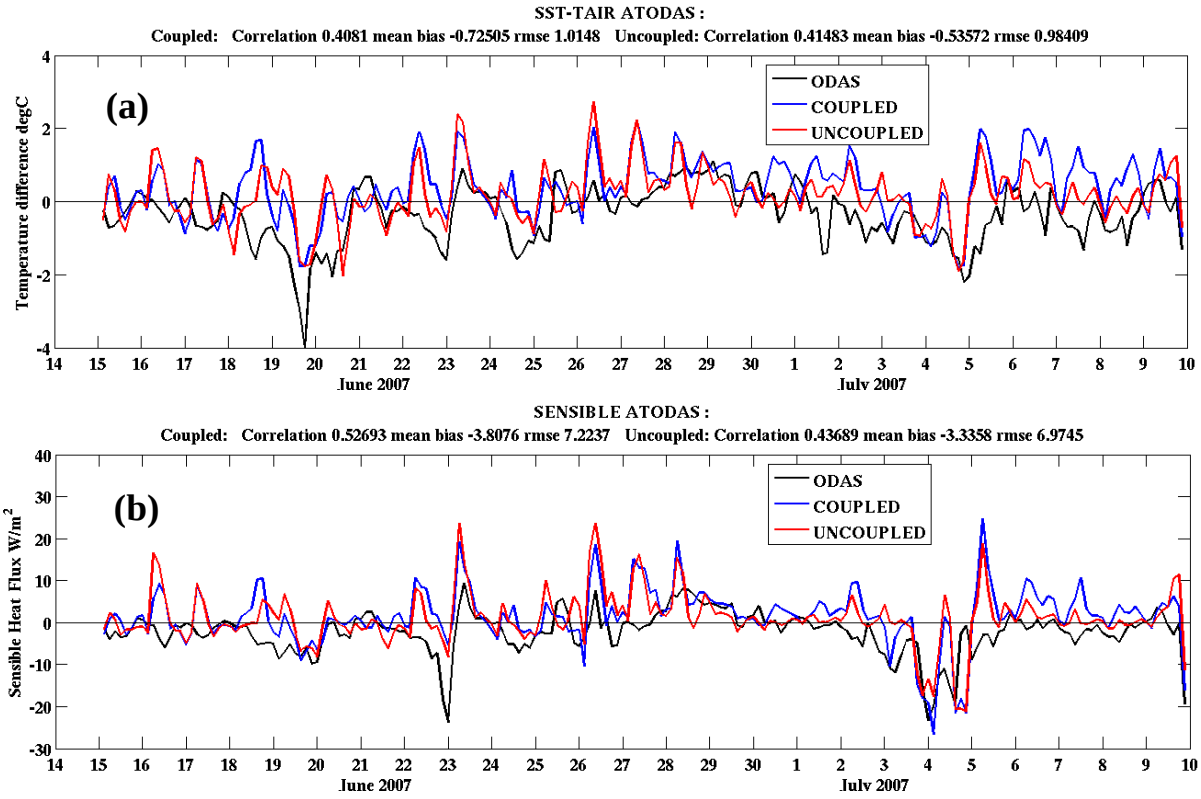

Figure 2-12: As Fig. 2-6a, but for SST minus near-surface air temperature (a) and sensible heat flux (b).

The latent heat flux plot (Fig. 2-13b) shows that COAMPS had skill in reproducing some of the large 150-200 W/m^2 strong wind events of 23 and 26 June and early on 4 July. On these days COAMPS slightly underpredicted relative humidity (Fig. 2-11b) and wind speed (Fig. 2-6a). The low air relative humidity in the model lead to large values of q_s- q_a (Fig. 2-13a), thus cancelling the effect of the low wind speed error on latent heat flux so that the model and observed latent heat fluxes tended to agree on those days (Fig. 2-13b). On other days agreement was poor, and the inflated latent heat fluxes in the model on 16, 17, and 27 June and 5 July were due to lower air humidities (Fig. 2-11b) and larger wind speeds than observed (early 27 June and 5 July, Fig. 2-6a), somewhat related to the land breeze problem (Fig. 2-7).

Despite the biases in sensible and latent heat flux, the CC between model and observations was high: 0.53 for sensible and 0.62 for latent, significant at 99%. The corresponding correlations for the uncoupled run were 0.44 and 0.64, respectively. Again, the differences between uncoupled and coupled heat fluxes were not significant at 95% following standard tests.

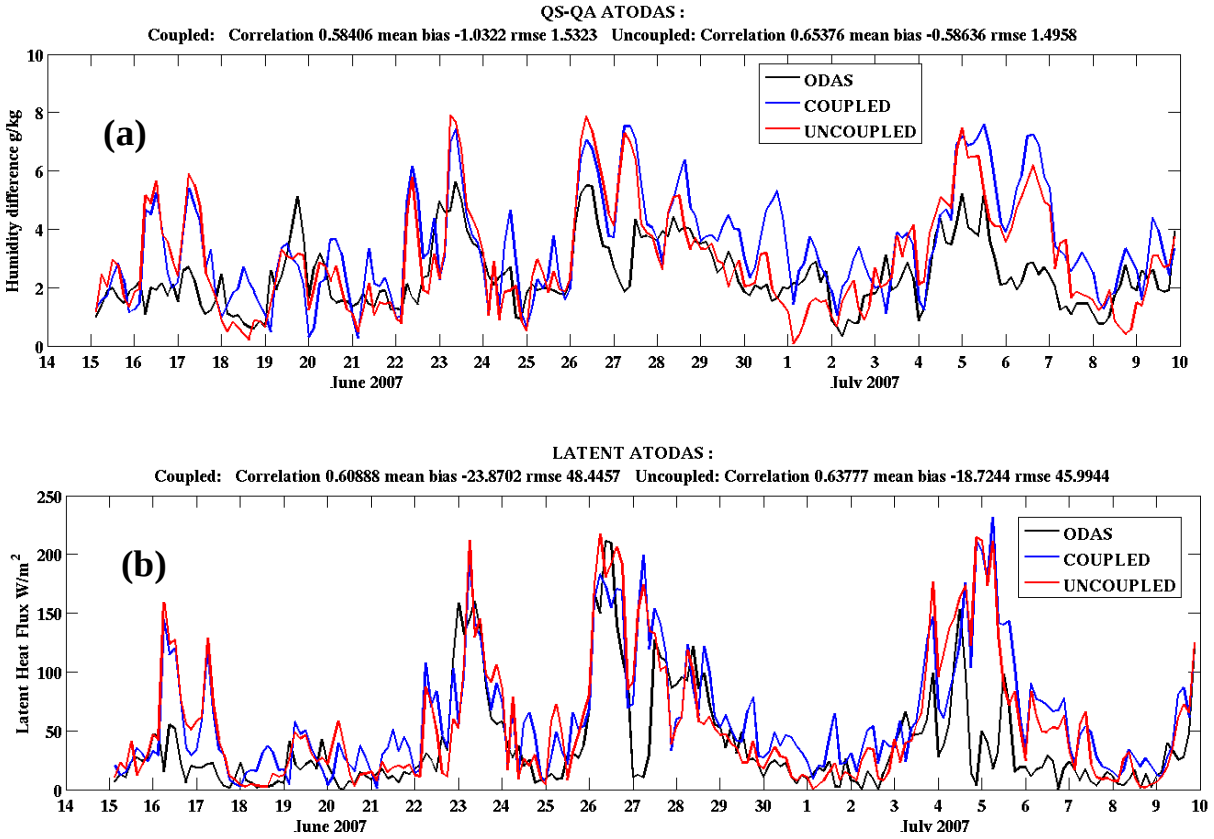

Figure 2-13: As in Fig. 2-6a, but for the difference between the saturation specific humidity at the SST and the near-surface air specific humidity (a) and latent heat flux (b).

3.2.3.5 Effects of Coupling on COAMPS Ocean/Atmosphere Evolution in the Coastal Zone

In this section the analysis of LASIE07 data, previously confined to the deep-water ODAS site, is extended to include the coastal zone off La Spezia. Coastal data used in the comparison includes current and near-surface temperature measurements from the SEPTR and the METEO buoy observations.

3.2.3.5.1 SST at the SEPTR Site

In addition to the deep water ODAS site, fluxes were estimated at the METEO buoy location, located in shallow water (between 30 and 50 m deep) southwest of West Palmaria island (See Fig. 2-3 for locations). The METEO buoy records wind speed, air temperature and humidity at a height of about 2.5 m above the surface. Unfortunately no coincident SST data was available, so near-surface temperature measurements were obtained from the nearby Shallow-water Environmental Profiler in Trawl-safe, Real-time configuration (SEPTR), located 20 to 30 m deep (the buoy and the profiler were separated by about 5 km). SEPTR consists of a "BARNY" bottom-mounted ADCP with an additional autonomous profiling instrument that rises to the surface once every four hours to transmit data via satellite communication and then re-descends (Rixen et al., 2009). Data is taken from the descending portion of the profile. The SEPTR also

includes a CTD, with temperature profiles divided into 0.5 m bins, with the upper bin representing SST (mid-depth was 0.25 m). Data was acquired from 15-26 June 2007, which defines the limits of the flux comparison.

The SEPTR SST data is compared against model data in Figure 2-14a. Even with only ~4 hourly sampling, the diurnal SST cycle is clearly evident in the SEPTR data (black line). In addition, the nighttime SST rose from just above 22ºC on the 16th to about 24ºC on 25 June, with most of the rise occurring from 15-19 June when winds were fairly calm. The coupled model SST (blue line in Fig. 2-14a, representing 0.25 m temperature) showed similar features, except that it was too cold (by about 1-1.5ºC) at the beginning of the record and possibly had a larger diurnal range. It should be noted that the 1 hr COAMPS data better resolved the diurnal cycle. In contrast, the NCODA SST (Figure 2-14a red line) had a very large cold bias of 2ºC or more throughout the record, with a maximum difference of over 4ºC occurring on 18 June (NCODA minus SEPTR SST).

An inspection of the NCODA SST maps (Fig. 2-15a, b) revealed the presence of a relatively cool band of water near the METEO site on 17 June (Fig. 15a) followed by the formation of a cold eddy on 18 June (Fig. 2-15b). In contrast the coupled model showed a narrow band of warm water near the METEO site (Fig. 2-15c), consistent with the CNR GOS satellite analysis (Fig. 2-15d) and with the SEPTR data (evidence for the lack of a cool eddy is also seen in the AVHRR image of 20 June, Fig. 2-14c). Thus, the fact that the cold eddy in NCODA does not appear in the *in situ* data or other satellite analyses, suggests that the eddy is erroneous. The NCODA analysis utilized satellite and *in situ* data and at present the source of the error is unknown (possibilities include incorrect cloud masking of satellite data, satellite data heavily affected by cloud that day, or poor quality profile data).

It is worth noting that the NCODA temperatures were too cool, not just during the time of the cold eddy (18-20 June), but also before 18 June (see Figs. 2-14 and Fig. 2-15a) and after 20 June (Fig. 2-14). Errors in the uncoupled run's fluxes were also significant outside of the period of the cold eddy (shown in Section 3.2.3.5.2). Figure 2-14a displays nighttime temperature readings from the CNR GOS satellite product. Until 20 June the CNR GOS data performed better than NCODA (Figs. 2-14 and 2-15d), but a cool bias in the GOS data relative to SEPTR SST after 20 June was also seen. It is likely that the NCODA and GOS analyses had a cool bias for similar reasons: firstly, the analyses did not resolve narrow coastal features, due to coarse resolution and over-smoothing, and secondly, the analyses were not designed to show the very-near surface temperatures (the 0.25 m temperature, or "skin" temperature). Specifically, the CNR GOS analysis estimates the foundation temperature, defined as the ocean temperature just below the influence of the diurnal warm layer, while NCODA estimates the "bucket" or bulk temperature and is not designed to incorporate diurnal warm layer effects (J. Cummings, pers. comm., 2009).

Unfortunately the SEPTR data ended on 26 June, so it is not possible to accurately validate the model SST after that time. However, a satellite image from the afternoon of 29 June (Fig. 2-14d) showed warm temperatures of over 24ºC near the LASIE07 coastal location (blue circle), much closer to the coupled model SST than the NCODA SST.

Due to the large differences in the NCODA and coupled model SST in this coastal location, the turbulent surface heat fluxes and stress were significantly different between coupled and uncoupled models. This gave rise to differences in the uncoupled ocean model SST relative to the coupled model at the SEPTR location, as seen in Fig. 2-14b. Here the uncoupled ocean model SST was generally warmer than the coupled model SST, particularly after 26 June, when differences were up to 2ºC or more. This will be addressed in more detail in Section 3.2.3.5.3 below.

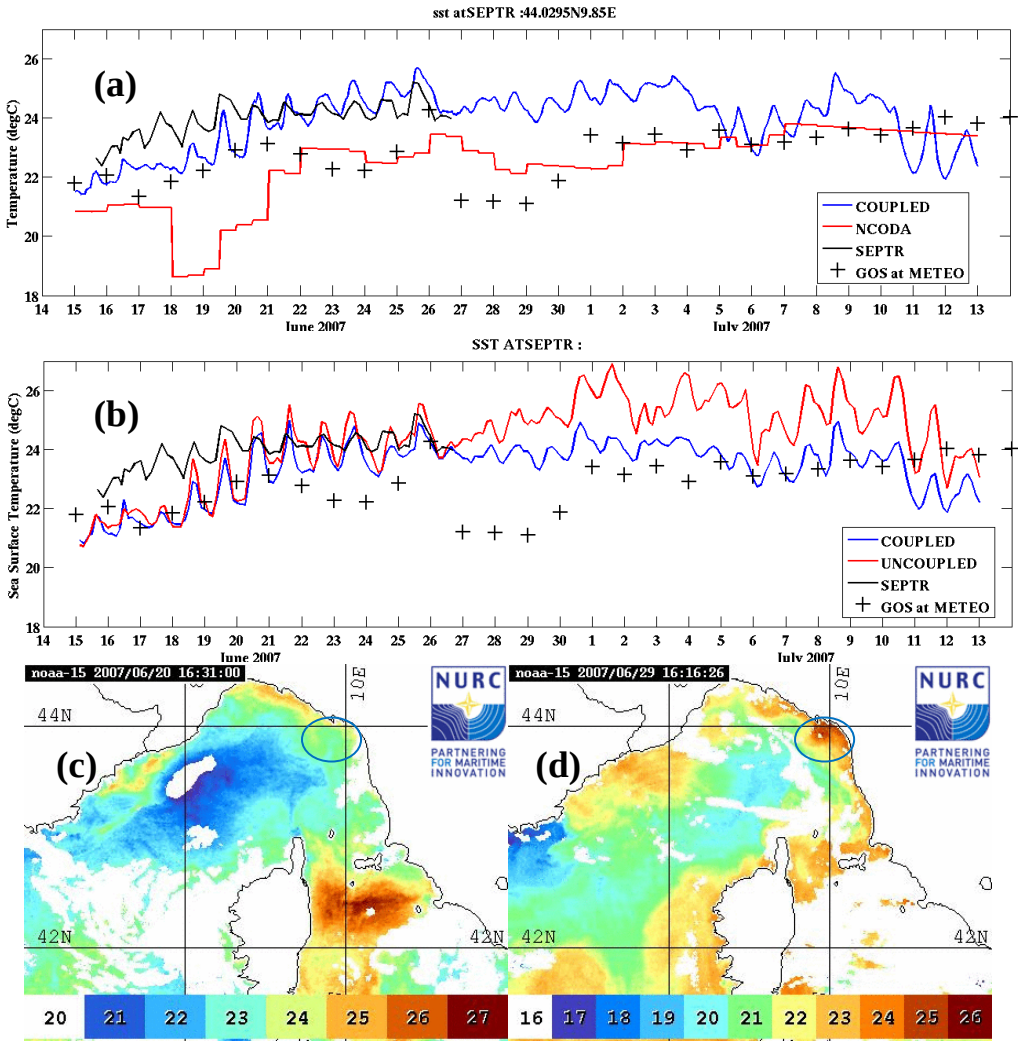

Figure 2-14: (a): SST at the LASIE07 coastal location. The black line is 0.25 m temperature from the SEPTR instrument. The blue line is 0.25 m coupled model temperature at the nearest grid point to SEPTR. The red line is NCODA SST analysis at the nearest grid point to SEPTR. Crosses are SST analysis from the CNR GOS product for the nearby METEO location. (b): As a), but now showing the uncoupled model 0.25 m temperature in red. (c): NOAA infrared satellite image for 1631 hours on 20 June, 2007. d) NOAA infrared satellite image for 1616 hours on 29 June, 2007. Note the warm temperatures of above 24°C near La Spezia (circled in blue). The image is from the LASIE07 website. Note the different color bars on the satellite images.

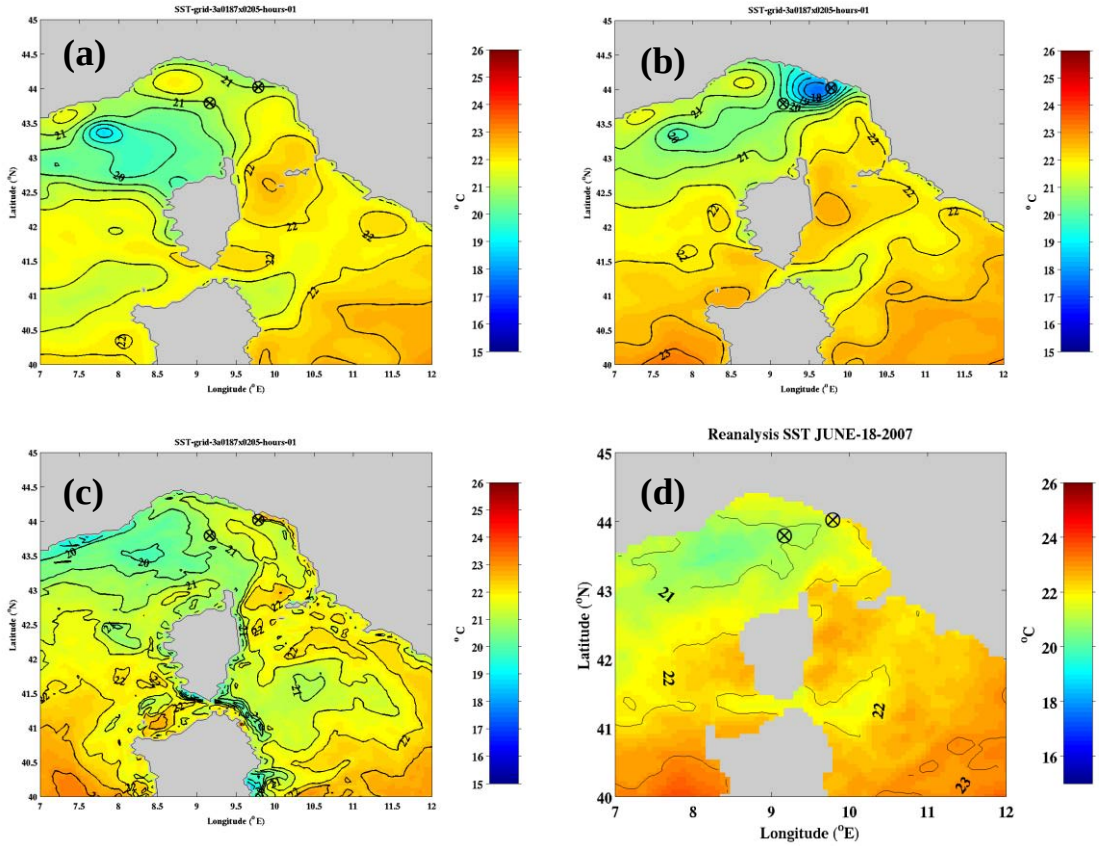

Figure 2-15: SST maps from model and analysis of satellite data. (a): Analysis of NCODA SST for 17 June (00Z), (b): analysis of NCODA SST for 18 June (00Z), (c): coupled model SST from 18 June, 01Z, and d) analysis of CNR GOS satellite SST data from 18 June.

3.2.3.5.2 Fluxes at the Coastal METEO Site

The large differences in SST between the coupled model and NCODA are likely to affect near-surface atmospheric variables and surface fluxes. Fig. 2-16b shows the 2 m air temperatures from both the model and the METEO buoy, sampled concurrently with the SEPTR profiles. For comparison, the SST for the same data range and sampling interval is shown in Fig. 2-16a. The 2 m air temperature from the coupled model was significantly warmer than that in the uncoupled model during the first half of the record. The coupled model air temperature was also closer to the observed temperature, although it still had a cool bias up to 20 June due to the cool SST bias during those days. As well as an improved MB, the coupled model had a much higher correlation (0.5) with observations relative to the uncoupled model (0.1), although this was only marginally statistically significant at 90% due to the small number of independent samples in this short, ~10 day record.

Despite the improvement in SST and air temperature in the coupled model relative to uncoupled, the sea-air temperature difference (not shown) was not particularly improved in the coupled model. This was expected because the coupled model SST and air temperature were both warmer than the uncoupled model counterparts, leading to some compensation when the

difference was taken. As a result, accounting for the fact that the model wind speeds (Fig. 2-16d) were similar in both the coupled and uncoupled model, the sensible heat flux timeseries (Fig. 2-17b) did not show a clear winner between models: the coupled model had higher correlation and lower RMSE but the uncoupled model had a lower absolute bias.

In contrast to the sensible heat flux, the latent heat flux was perhaps more directly dependent on SST through its reliance on q_s, the saturation specific humidity at the surface temperature. The variable q_s is an exponential function of SST and was significantly biased low in the uncoupled run because of its cool SST. It became so low on 18 June that the specific humidity of the air exceeded that of the SST, resulting in negative latent heat flux (Fig. 2-17c). This is a situation that is equivalent to droplets of water being transferred from the air to the ocean. The coupled model latent heat flux had a greatly improved MB and RMSE (Fig. 2-17c). The impact of the cool SST in NCODA could also be seen in the relative humidity timeseries (Fig. 2-16c), where on 18, 20 and 21 June the uncoupled model had periods when the near-surface was saturated or above 98% relative humidity, a phenomenon not observed in the METEO timeseries. The coupled model performed slightly better with respect to relative humidity, although the differences in CC, MB and RMSE were not significant.

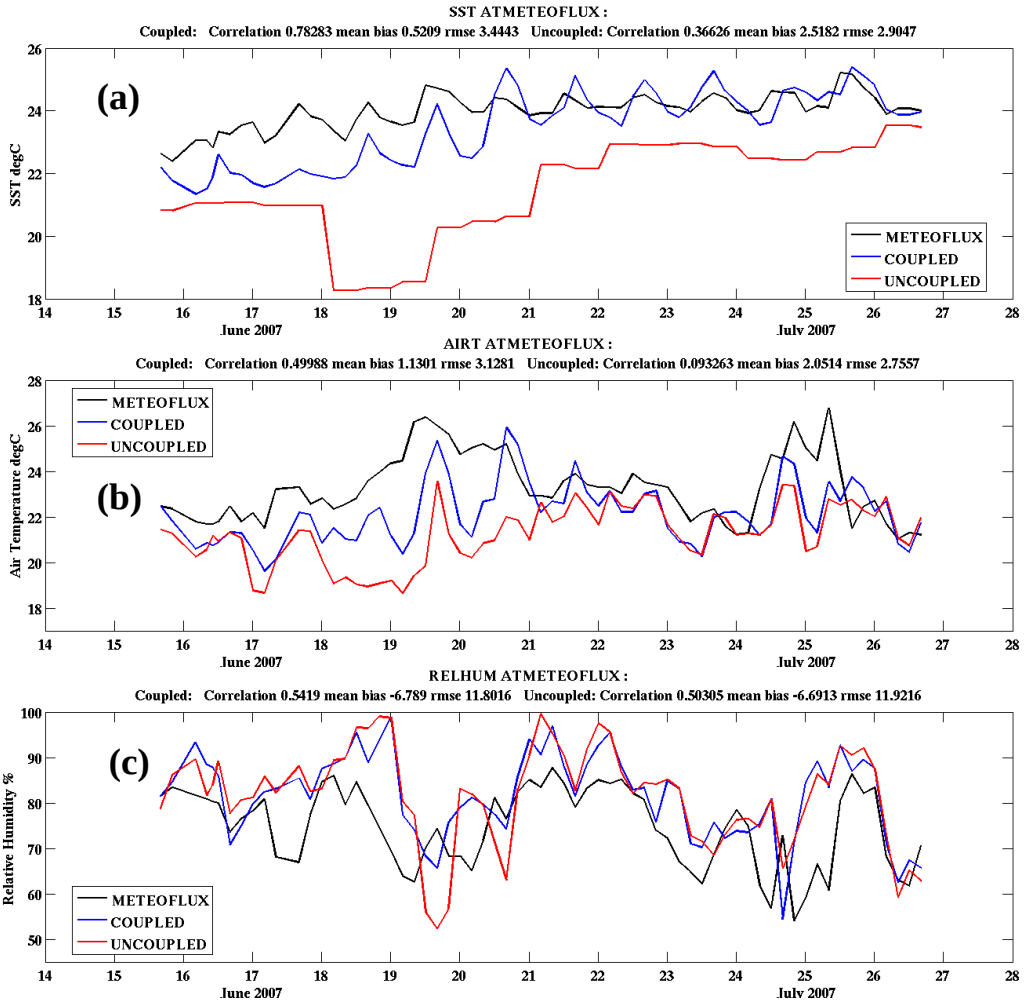

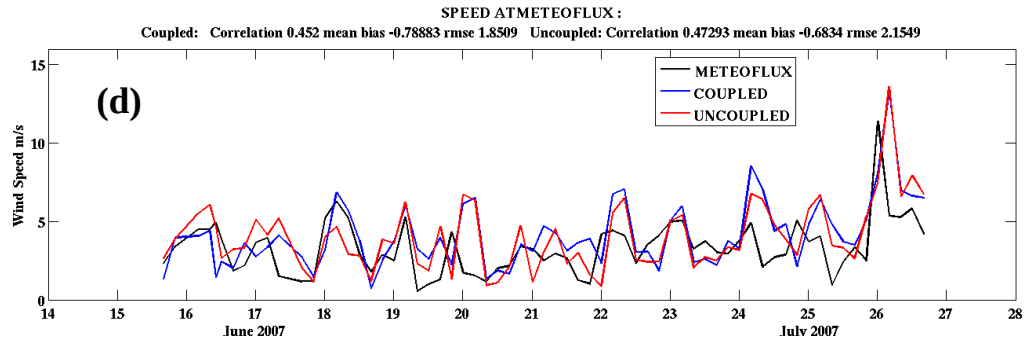

Figure 2-16: Time series of variables at the METEO location: observations (black), coupled model (blue), and uncoupled (red). Data from observations and models were sampled about every 4 hours. (a): SST (using SEPTR for observed values), (b): air temperature at 2 m, (c): relative humidity at 2 m, d) wind speed at 2 m (observations) and 10m (model).

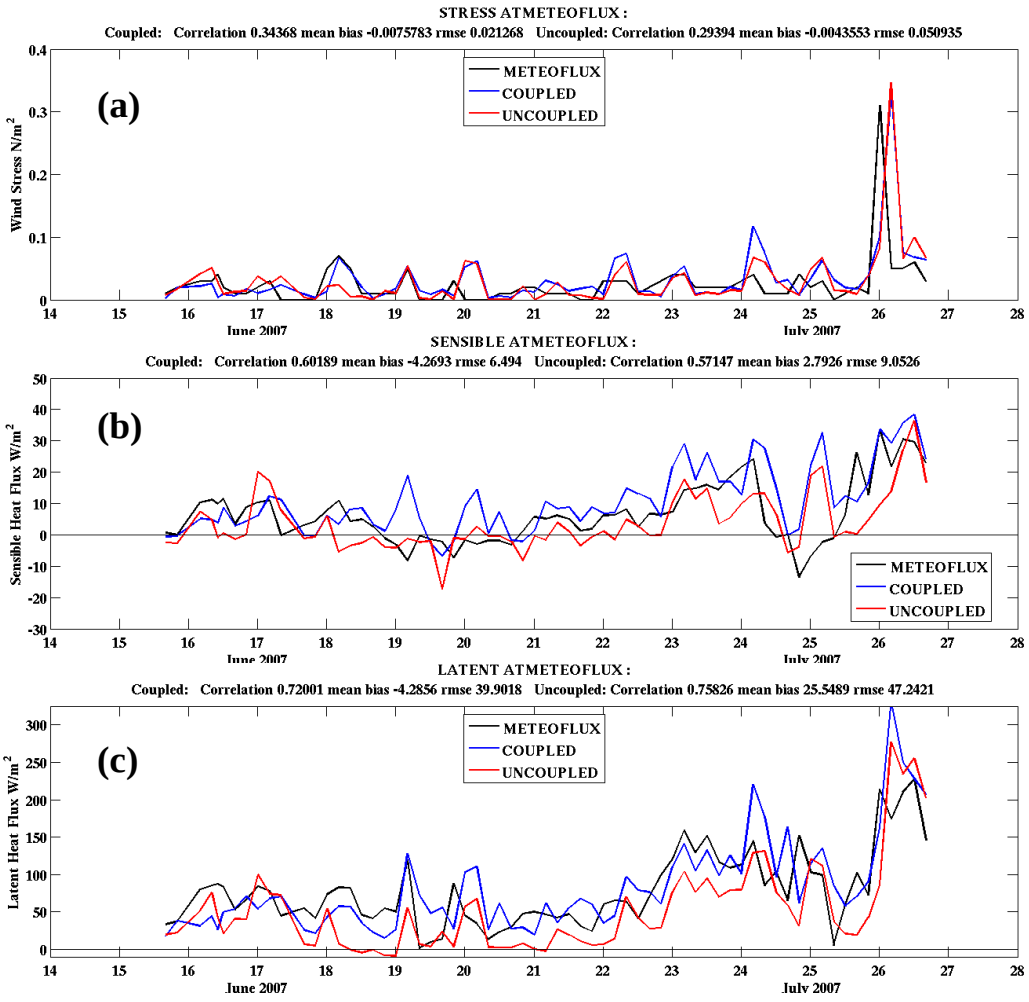

Figure 2-17: Time series of variables at the METEO location: observations (black), coupled model (blue), and uncoupled (red). Data from observations and models were sampled about every four hours. a) wind stress, (b): sensible heat flux, (c): latent heat flux.

3.2.3.5.3 Spatial Variability of Flux Changes Due to Coupling

In order to see what effects changes in surface fluxes have on oceanic and atmospheric fields, the flux analysis of METEO station data was expanded to a wider area in the model. As a starting point, a warm coastal band of SST was identified as a dominant feature throughout the month long simulation, as seen in the time-average of SST from the coupled model (Fig. 2-18a) for the period 15 June to 12 July, 2007 (referred heretofore as a "month-average"). The warm band occurred in the northeast Ligurian and Tyrrhenian Seas, including off the La Spezia coast and further south towards Pisa (Fig. 2-18a, area circled). The corresponding time average from NCODA (Fig. 2-18b) showed a much weaker feature near the coast, while the CNR GOS SST had a coastal temperature signal somewhat closer to the coupled model (Fig. 2-18c). The difference between the time-averaged coupled model SST and NCODA SST (Fig. 2-18d) increased up to 2ºC in the narrow coastal band. As discussed above, the LASIE07 *in situ* data suggested that the coupled model SST was more accurate than NCODA in this coastal region. Conversely, the coupled model also showed much cooler temperatures around the east coast of Corsica and Sardinia than seen in either of the satellite data products, suggesting that the coupled model is not predicting well in these regions.

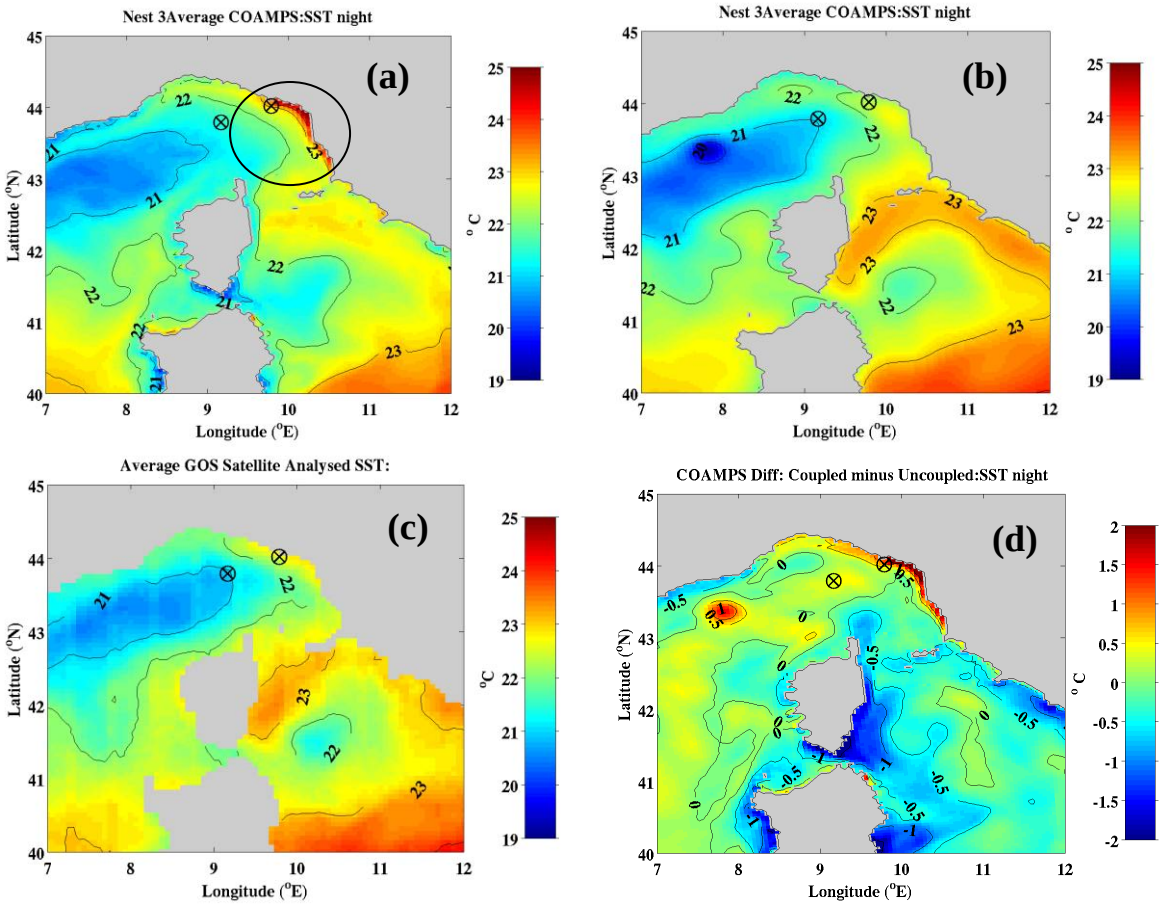

Figure 2-18: Month-long (15 June to 12 July) averages of nightime SST, (a): from the

coupled COAMPS model, (b): from the NCODA analysis, (c): from the CNR GOS product, and d) the difference between a) and b). The coastal area of interest is circled in Fig. 2-18a.

Because of the warmer SST in the LASIE07 coastal region, the turbulent surface heat fluxes (sensible and latent) were high, combining to nearly 150 W/m^2 (out of the ocean) in the coupled model (Fig. 2-19a). This is an almost 100% change in heat flux relative to the uncoupled model (Fig. 2-19b) (The percentage difference used here and in all subsequent plots is 100x(P_c-P_{uc})/|P_{uc}|, where P_c is the relevant variable in the coupled model and P_{uc} is that in the uncoupled model). There were also enhancements in the coastal zone wind stress. These were difficult to see in the map from the coupled model (Fig. 2-19c), but they reached nearly 25% of the uncoupled model value (Fig. 2-19d).

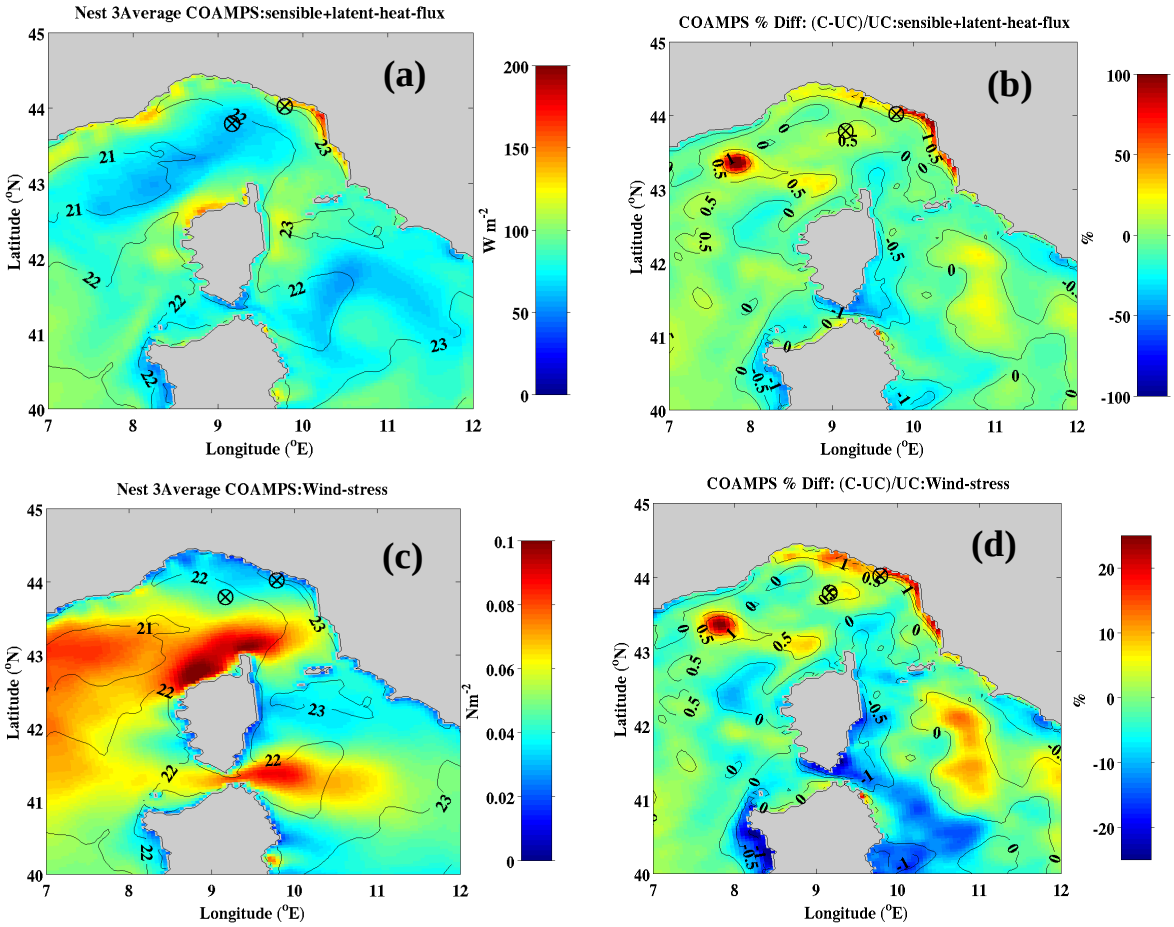

Figure 2-19: (a): Month long average of combined sensible and latent heat flux from the coupled model. Positive values denote ocean losing heat, (b): The percentage difference for combined heat flux between coupled and uncoupled model, (c): month-long average of wind stress from the coupled model, d) the percentage difference in wind stress between the coupled and uncoupled model.

To investigate in detail the effect of coupling on ocean model SST evolution, we studied the total heat flux into the ocean and how that is modified by coupling. The total heat flux comprises sensible and latent heat flux and longwave (net) and absorbed solar radiation (where a constant albedo of 0.04 is used to compute the reflected part). Using the convention of mean positive heat flux out of the ocean, the month-long average of total heat flux in the coupled run was negative everywhere (not shown), meaning the ocean was gaining heat due to very large solar fluxes at this location and time of year. The ocean region of minimum heat gain was actually in the same coastal zone, because of the large sensible and latent heat flux out of the ocean. The difference (coupled minus uncoupled) was between 50 and 100 W/m^2 in this coastal zone (see Fig. 2-20a and a close-up in Fig. 2-20b). Expressed as a percentage, the heat flux changed by 50-100% in this region.

An estimate of the effect of this total heat flux change on SST can be made as follows. Assuming a mixed layer depth, H, over which all the surface heat flux is distributed, the temperature change, ΔT, averaged over the mixed layer in time Δt is given by

$$\Delta T = \frac{Q.\Delta t}{H\rho c_p},$$

where Q is the average total heat flux, ρ is ocean density and c_p is the specific heat capacity of water. It follows that the difference in temperature change between coupled and uncoupled ocean models, δT, is given by

$$\delta T = \frac{\delta Q.\Delta t}{H\rho c_p}, \qquad (1)$$

where δQ is now the difference in total heat flux between coupled and uncoupled runs. Using values of δQ=50 W/m^2 from Fig. 2-20b and approximating ρ=1000 kg/m^3 and c_p=4000 J/kg^3, a typical mixed layer depth of H=10 m gives $\delta T \sim$=3.2ºC. This may be compared with the change in ocean model SST between the coupled and uncoupled run (Fig. 2-20c). When averaged over a full month, the SST change was up to 1º to 2º C of cooling in the coastal zone of interest (Fig. 2-20d). There is close spatial correspondence between Fig. 2-20c and Fig. 2-20a (with a reversal of sign), suggesting that surface fluxes caused the change in SST. The difference in time-averaged SST did not exactly correspond to the estimate in (1), which is the difference in SST change over the length of the run. Therefore, we demonstrate in Figs. 2-20e and f the difference (coupled minus uncoupled) in $\delta T \sim T_f - T_i$, where T_i is the average SST of the simulation's first week and T_f is the final week's average SST (This field was more affected by transients than the month-long average and did not show such close correspondence with Fig. 2-20a). It can be seen that this quantity reached 3ºC of cooling in the LASIE07 coastal area (Fig. 2-20f), consistent with the estimate (1).

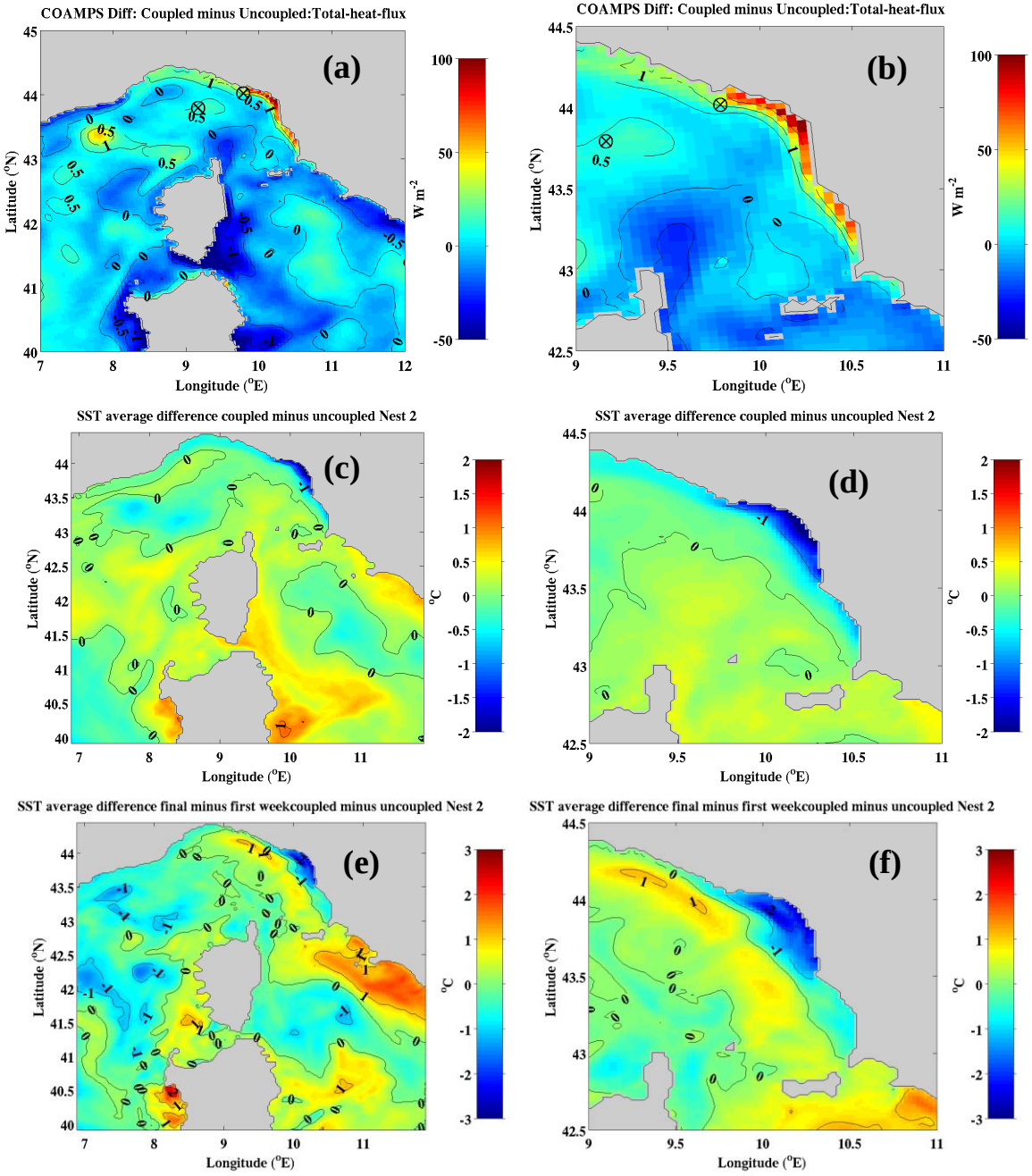

Figure 2-20: (a): The total heat flux difference between the coupled and uncoupled model, averaged over a month (Positive values of total heat flux difference denote ocean losing more heat in the coupled model), (b): close up of a) showing the LASIE07 region, (c): difference in one month average SST for the coupled model minus uncoupled ocean model, d) close-up of c) showing LASIE07 region, (e): difference (coupled minus uncoupled) in the term T_f-T_i, where T_i is the first week average SST, and T_f is the final week average SST. The lower panels have more structure due to transients but they highlight the temporal change of the SST field, f) close-up of e).

3.2.3.5.4 Effects on Oceanic and Atmospheric Boundary Layers

For operational purposes, knowledge of the SST and the diurnal warm layer in the ocean is important for sonar applications. Changes in SST due to coupling are likely to affect the vertical sound speed gradient in the warm layer (upper 5 m or so) and thus affect acoustic propagation. This is evident in Fig. 2-21, which shows the COAMPS time-average sound speed profile at the approximate SEPTR location for the afternoons of 1-12 July, 2007, a period when the coupled and uncoupled model SST were very different (Fig. 2-14b). The uncoupled COAMPS had a profile leading to a much stronger downward refraction throughout most of the water column (the water depth is about 25 m) when compared against the coupled model (Fig. 2-21). This allows for an exaggerated 'afternoon effect'.

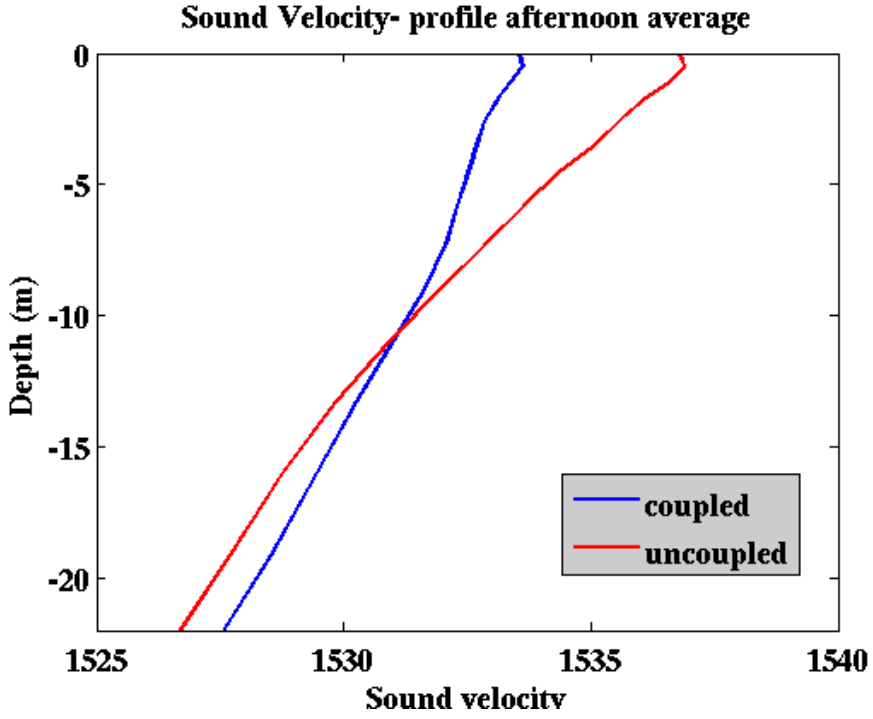

Figure 2-21: Sound velocity profiles averaged between 1500 and 1800Z for 1-12 July, 2007 from the coupled COAMPS (blue) and the uncoupled COAMPS (red) at the approximate location of SEPTR.

Finally, Fig. 2-22 shows how coupling affects the interior atmospheric and oceanic boundary layers, as measured by planetary boundary layer height (PBL) and mixed layer depth (MLD), respectively. The PBL, averaged over a month of the coupled run (Fig. 2-22a), bore some resemblance to the mean SST field (Fig. 2-18a) and turbulent heat fluxes (Fig. 2-19a), with deeper PBLs (300-500 m) appearing over the warmer waters of the Gulf of Genoa coast. It is also clear that shallow PBLs (~200 m) occurred downstream of the islands of Corsica and Sardinia. When taking the difference between coupled and uncoupled runs (Fig. 2-22b), there was an increase in PBL in the coupled COAMPS along the Gulf of Genoa coast and in other regions where the coupled model SST was higher than NCODA (contours on Fig. 2-22b are of

SST difference: compare these with Fig. 2-18d). Conversely, the PBL was shallower in the coupled model where SST was cooler, such as to the east of Corsica and Sardinia (Fig. 2-18d, Fig. 2-22b). The differences in PBL height between coupled and uncoupled COAMPS reached +/-50 m or more, corresponding to percentage differences of up to +/-20% (Fig. 2-22e).

In the ocean, the spatial distribution of mean MLD (Fig. 2-22c) is dependent on the spatial distribution of wind stress (e.g., Fig. 2-26b) and of wind stress curl (Fig 2-27c shows the related quantity, Ekman pumping), such that deep mixed layers occurred around the northeast tip of Corsica where wind stress was high, and off the northeast coast of Sardinia where wind stress curl induced downwelling. These deep mixed layers reached 15 to 20 m compared to average values of around 10 m (See Fig. 2-22c, where the Kara et al., (2000) mixed layer depth algorithm was used. The algorithm begins searching for MLD at 7 m to avoid diurnal warming effects, so an MLD identified as shallower than ~10 m may not be a true mixed layer because there are insufficient vertical levels between 7 and 10 m to determine one). When taking the difference of coupled minus uncoupled MLD, averaged over a month, the differences ranged from +/- 1 to 2 m (Fig. 2-22d). These values were quite small in absolute terms, and when expressed as a percentage difference relative to the uncoupled run, they were equivalent to a +/-10% change in MLD (Fig. 2-22f). Note that the spatial distribution of MLD percentage difference (Fig. 2-22f) resembles the maps of SST difference (Fig. 2-18d), heat flux difference (Fig. 2-19b) and wind stress difference (Fig. 2-19d). Generally, areas of positive (negative) SST anomalies, heat flux anomalies, and particularly wind stress anomalies correspond to areas of increased (reduced) MLD. By showing the differences in month-long averages of MLD, the effect is somewhat underestimated. If instead the coupled minus uncoupled change in MLD_f-MLD_i was computed (using the same terminology as for SST above), MLD differences of 2 to 3 m, or 20%, would appear in the coastal zone (not shown).

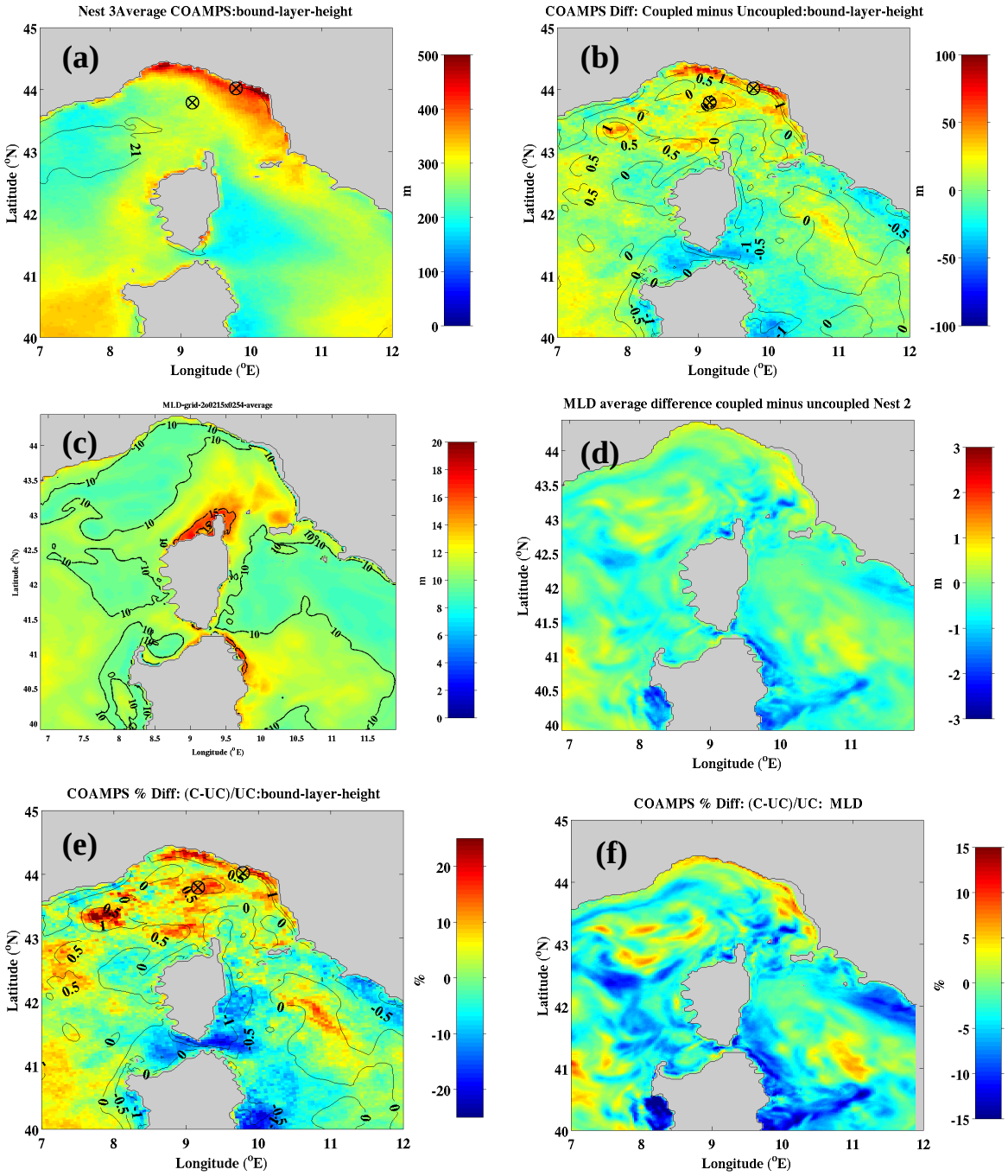

Figure 2-22: Left panels: Planetary boundary layer height. Right panels: Ocean mixed layer depth. (a) and (b): Averaged over one month of the coupled run, (c) and (d): the difference (coupled minus uncoupled) in the month-average, (e) and (f): the percentage difference ((coupled minus uncoupled)/uncoupled) in the month-average.

3.2.3.6 Summer Mistral Event Case Study

In order to further examine air-sea interaction in the Ligurian Sea, a case study was performed for the Mistral wind period of 26-28 June, focusing on the differences between an uncoupled and a coupled simulation. In this experiment, the initial SST for both the coupled run and the uncoupled run was identical and was set equal to the global NCOM field for 00Z, 26 June. The coupled run then proceeded for three days with 12-minute coupling in free mode (with no data assimilation after the initial time), while the uncoupled run kept the SST for the atmosphere fixed at its initial value for the entire 72-hour run (this design mimics a standard 72 hr atmospheric forecast). Hence, differences were only due to coupling, not to initial biases in the SST field, or the influence of assimilation.

The 3-day average wind speed and velocity at 10 m for 26-28 June from QuikSCAT revealed strong winds of 12 to 13 m/s over the Ligurian Sea associated with the Mistral (Fig. 2-23a). The COAMPS winds were slightly weaker but reproduced the main features of the flow (Fig. 2-23c). The magnitude of the wind speed difference, about 1 m/s, was similar to that found in ODAS timeseries data during this period (Fig. 2-6a). The model added more detail by resolving the Mistral and Tramontane winds in the Gulf of Lions, the jet through the Strait of Bonifacio, and the corner jet around the northern coast of Corsica (Fig. 2-23c).

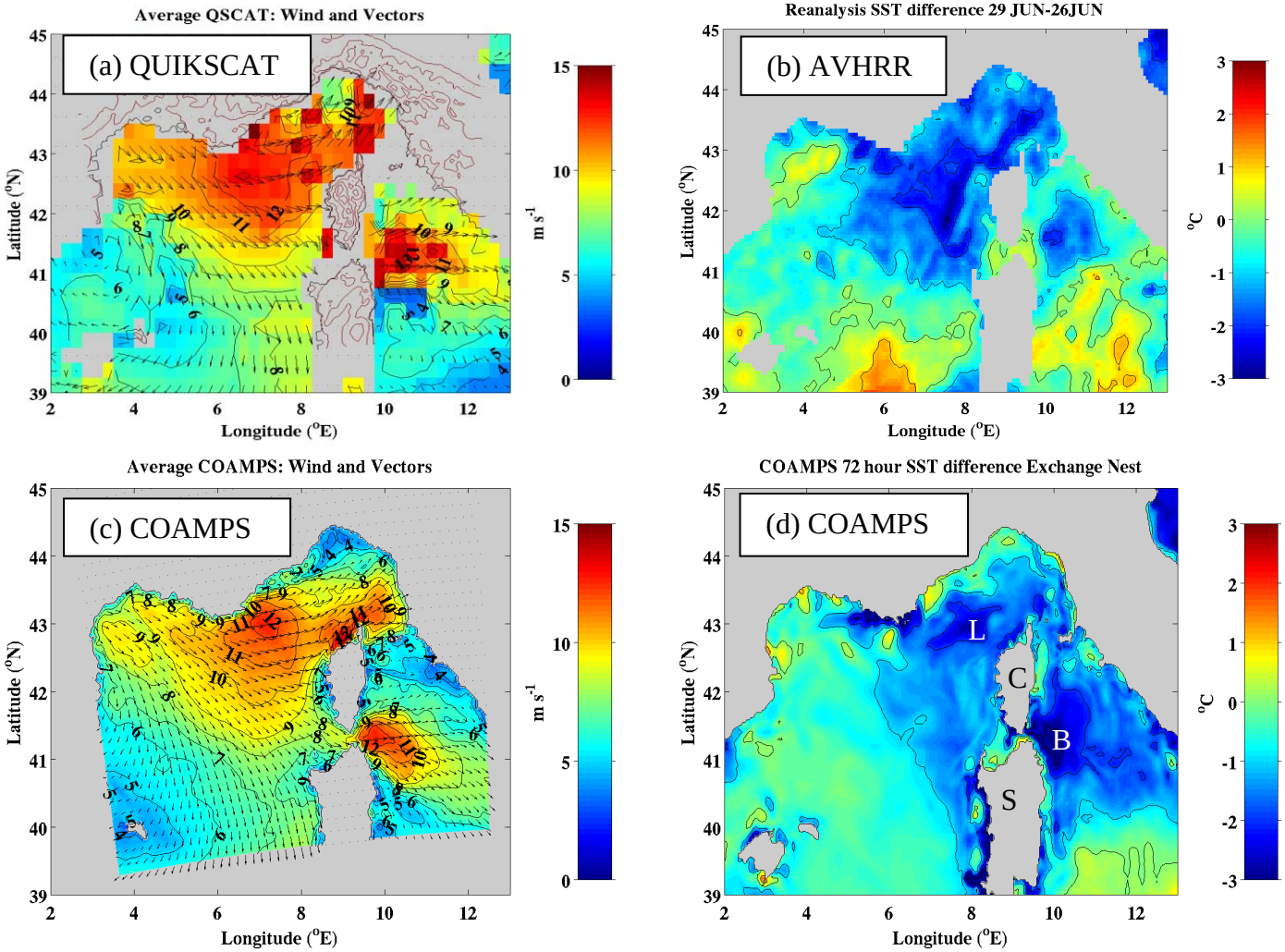

Figure 2-23: Mistral winds and ocean response during LASIE07. Left: average 10 m wind speed and vectors, 26 to 29 June 2007 during Mistral winds. Right: SST change, 29 June minus 26 June. The top panels show observations from QuikSCAT scatterometer and from an optimally interpolated AVHRR composite (from CNR GOS data). The bottom panels show results from the COAMPS coupled model. The labels L, B, C and S at bottom right refer to Ligurian Sea, Strait of Bonifacio, Corsica and Sardinia, respectively.

The ocean response to the winds was illustrated by the difference in SST between 26 and 29 June from analyzed infrared satellite SST data (Fig. 2-23b). The ocean cooled by over 1°C over 72 hours in most of the Ligurian Sea and northern Tyrrhenian Sea, with the strongest cooling to the north and west of Corsica and east of the Strait of Bonifacio, where the cooling was between 2°C and 3°C. Clearly, the greatest cooling occurred in the regions of strongest winds, with the exception of the western Gulf of Lion, where there was weak warming. East of the Strait of Bonifacio, the cooling was reminiscent of the filaments identified by Salusti (1998) and Perilli et al. (1995).

The coupled COAMPS model resolved most of the ocean response to the strong winds (Fig. 2-23d). A zoomed view of the second nest SST difference (Fig. 2-24a) shows cooling of over 2°C in parts of the Ligurian Sea and up to 3°C cooling east of the strait. Because the atmospheric model of the uncoupled run did not see this SST change (the SST was kept fixed in time), a large difference in the fluxes between the two experiments was expected. Especially in the regions of cooling SST in the coupled run, a more negative (i.e., more stable) value of sea-air temperature difference T_s-T_a was likely due to the T_s reduction. Indeed, plots of the sea-air temperature difference from the runs (Fig. 2-25) indicated that T_s-T_a was reduced by up to 1°C in the coupled run compared to the uncoupled run in the regions of strong SST cooling (Fig. 2-25c). These differences suggested that the air-sea fluxes would be very different between the runs, as indeed turned out to be the case.

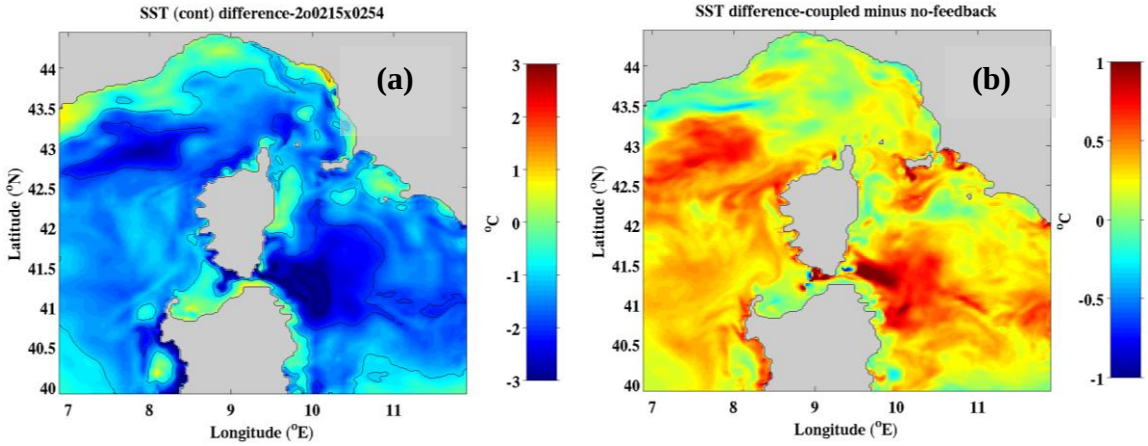

Figure 2-24: (a): The 72-hour SST difference (29 June 00Z minus 26 June 00Z) from the fully coupled run, T'_{couple}. (b): The difference in SST evolution between the coupled and uncoupled run (i.e. T'_{couple}-$T'_{uncouple}$). The ocean model SST is used for the uncoupled run.

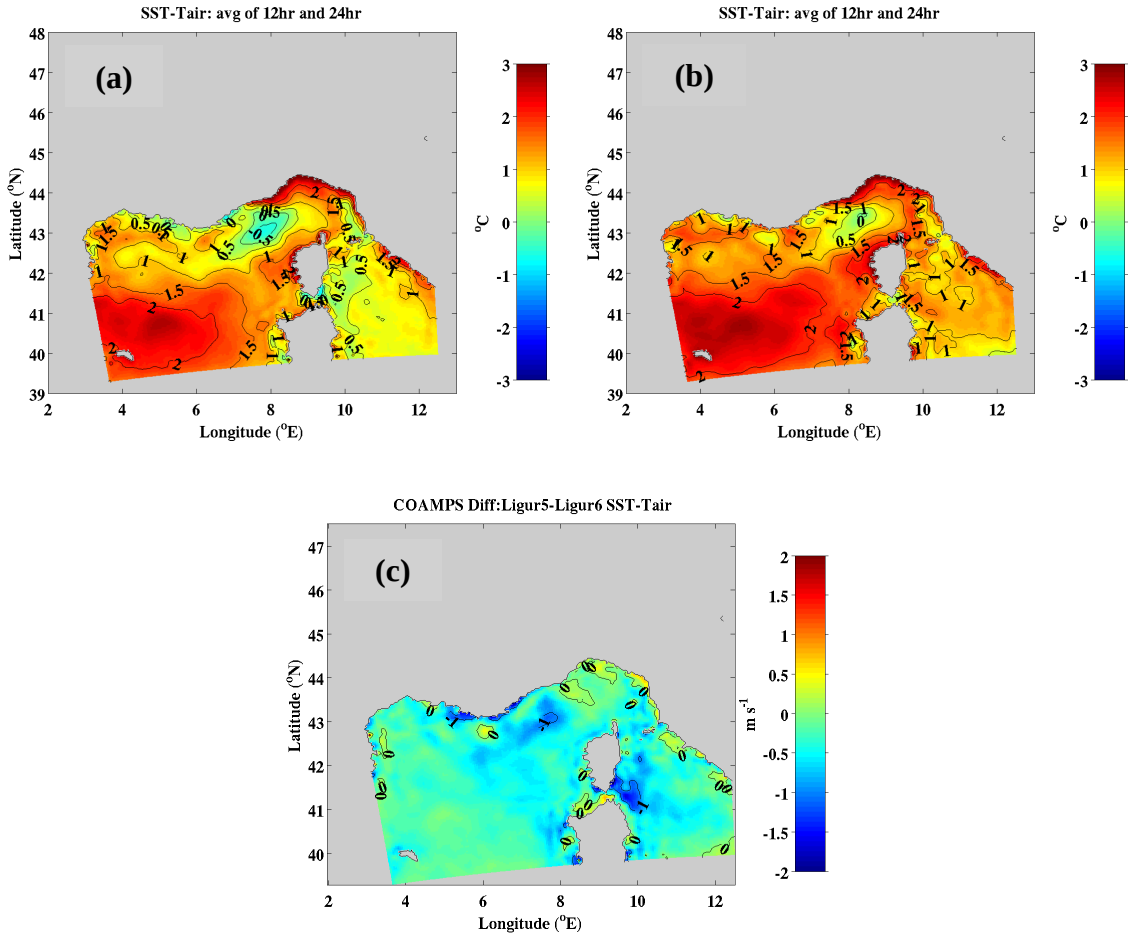

Figure 2-25: SST minus 2 m air temperature, averaged over 3 days. (a): From the coupled run, (b): from the uncoupled run, and (c): the coupled-uncoupled difference.

The surface latent heat flux averaged over the three day coupled run showed large fluxes over 200 W/m^2, where the winds are strong (Fig. 2-26a) and the surface stress reaches up to 0.25 N/m^2 in these regions (Fig. 2-26b). Taking the difference between coupled and uncoupled, the latent heat flux was reduced by up to 100 W/m^2, or 50% (Fig. 2-26c, contours). The stress was reduced by up to 0.05 N/m^2, or 20% (Fig. 2-26c), in the regions of strong SST cooling (Fig. 2-24a). The sensible heat fluxes showed similar differences of up to 30 W/m^2 (not shown). The heat flux differences were due to a combination of the change in stability between experiments, directly affecting air-sea temperature difference and indirectly impacting the turbulent exchange coefficients, and wind speed differences between runs. A cooler SST in the coupled run meant a smaller saturation specific humidity at that value of SST (q_{sat}(SST)), so the difference between air humidity and q_{sat}(SST) was likely to decrease and contribute to a lower latent heat flux in the coupled run. A change in stability (i.e., air-sea temperature difference) of 1ºC between the experiments was comparable to the magnitude of the actual air-sea temperature difference in the runs, potentially leading to 100% changes in sensible heat flux. The wind speed differences reached up to +/-0.5 m/s (~ 5% of the average wind speed) and were not likely to greatly impact the heat fluxes. In contrast, changes in the stress were due both to the wind speed and stability fluctuations (the latter affects stress via the drag

coefficient). At wind speeds of 10 m/s, the effect of a 1ºC change of stability on drag coefficient is less than 10% (see Liu et al., 1979, their Fig. 12), while a wind speed change of 0.5 m/s would create about a 10% change in stress.

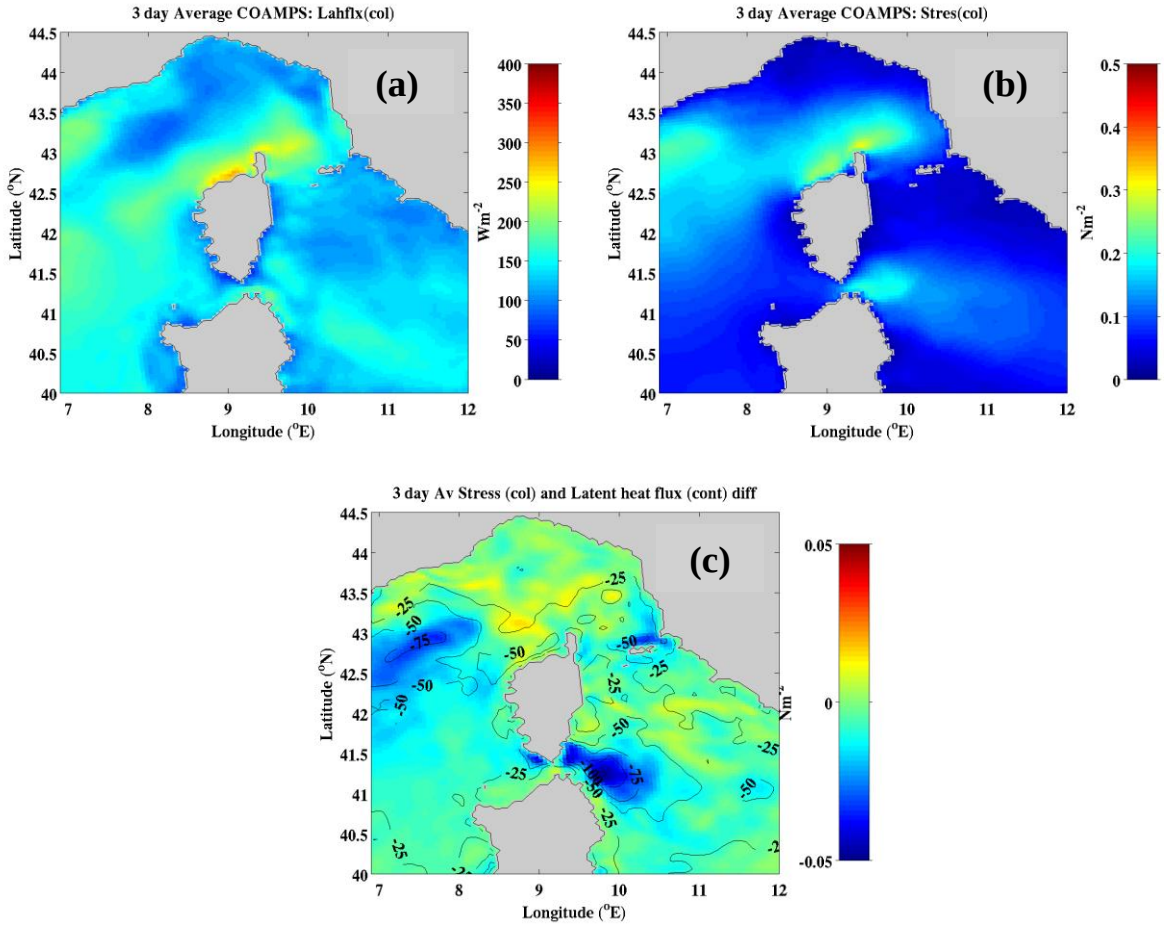

Figure 2-26: Three-day averages (26-28 June) from the coupled model of (a): surface latent heat flux (W/m^2) and (b): surface stress (N/m^2). (c): The difference of 3-day average latent heat flux (contour) and stress (color) between the coupled run minus the uncoupled run.

When the reduced fluxes (heat flux, stress) in the coupled run acted on and interacted with the ocean model, the resultant cooling of SST was diminished relative to the uncoupled simulation, where the fluxes were not modified by changes in SST. The difference, which approached 1ºC, is shown in Fig. 2-24b. In other words, the coupling provided a negative feedback on the surface forcing under strong winds.

In the regions of largest SST cooling (Fig. 2-24a), the initial MLD in the model was shallow (10 m or less, Fig. 2-27a) and winds were strong, suggesting cooling was caused by entrainment or upwelling. This is confirmed by estimates of the near surface heat flux into the ocean in the model, which were always positive in daytime throughout the experiment due to the strong solar radiation (not shown) and despite evaporative cooling.

The upper ocean stratification changed significantly during the wind event. After the three-day period of strong winds, the MLD increased by 10-20 m or more in some regions (Fig. 2-27b). The largest increases of MLD occurred to the north and east of the northern tip of Corsica, and south and east of the Strait of Bonifacio. Interestingly, estimates of the Ekman pumping (Fig. 2-27c; note the convention that positive values denote downwelling) from the wind stress fields showed the largest downwelling in these same regions. We can speculate that the increase in MLD is due to a combination of the entrainment due to the stress acting on the surface (Fig 2-26b) and downwelling caused by Ekman pumping. Further analysis of this is included in Small et al., 2010. Mixed layer depth differences between the coupled and uncoupled runs were typically of the same sign as the stress and heat flux differences, reaching up to 10 m (Fig. 2-27d). In other words, the coupled model showed mostly a reduced mixed layer deepening in response to the diminished stress and heat fluxes. However, the spatial correspondence between changes in MLD among the experiments and changes in the stress, heat flux, and Ekman pumping was less clear than the changes in SST (Small et al., 2010).

It may be argued that the experimental design for the pair of runs in this case study could exaggerate the impact of coupling by fixing the uncoupled run's SST for 72 hours, compared to typical update cycles of every 12 or 24 hours. Indeed, the differences in these twin experiments grew with time and would have been less at 12 or 24 hours. However, much of the change took place in the first 24 hours, as noted from the SST evolution at ODAS (Figs. 2-9a). A significant advantage of the current experiment was its use of identical initial SST fields in the coupled run and in the uncoupled atmospheric simulation. In another experiment the atmospheric model SST was kept fixed at the initial NCODA SST for 72 hours. Here, large differences arose between the coupled and uncoupled runs due to biases in the initial NCODA SST and the global NCOM SST. The biases were often larger than any differences that would be expected from the impact of coupling alone. Perhaps the best way to examine coupling impacts would be to use the same initial SST but vary the coupling interval between the existing 12-minutes to 12- or 24-hours in order to mimic the impact of updating SST at analysis times. Some of these experiments were performed for Test Case 1 in the Adriatic Sea.

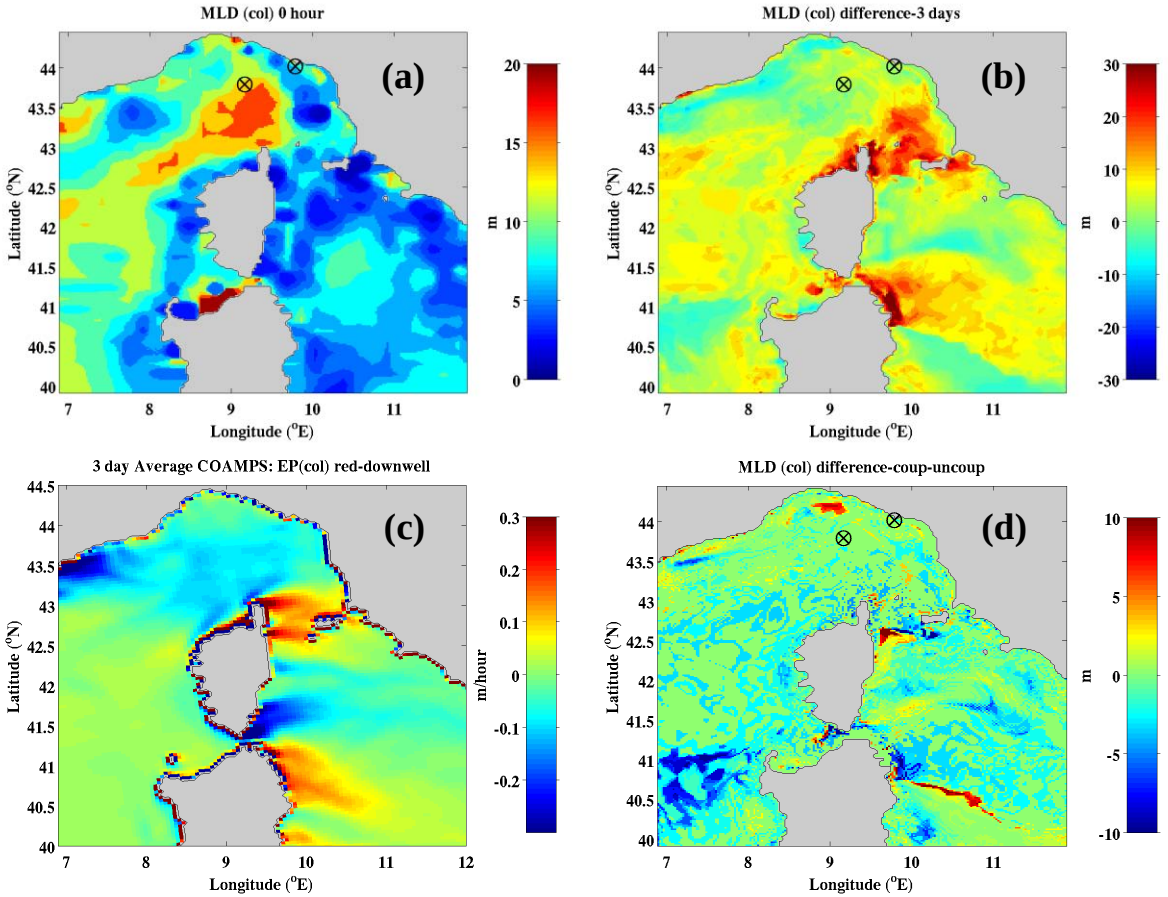

Figure 2-27: (a): Initial mixed layer depth from the coupled model. (b): Mixed layer depth change over 69 hours from coupled run. (c): The three-day average of Ekman pumping velocity (m/hr), with positive downwards convention such that red areas denote downwelling. (d): The mixed layer depth difference between the coupled run and the uncoupled run at the end of the three-day simulation.

Finally, this case study can be used to show why the differences in near-surface atmospheric and oceanic fields between the coupled and the uncoupled run at the LASIE07 location were so small (as discussed in sections 3.2.3.1 to 3.2.3.6). From Fig. 2-26c it is evident that the differences in heat flux and stress at ODAS due to coupling were negligible, in contrast to the large differences in the strong wind regions of the central Ligurian Sea and to the east of the Strait of Bonifacio. This, in turn, is due to the small change in T_s-T_a that occurred at the LASIE07 location (Fig. 2-25c) because of the relatively small SST cooling there (about 1ºC or less compared to 2ºC to 3ºC cooling in the strong wind regions, Fig. 2-24a). The rather small changes in surface fluxes that occurred due to coupling at the LASIE07 location lead to relatively slight changes in SST evolution (Fig. 2-24b) and negligible differences in the structure of the atmospheric boundary layer and the upper ocean (see the following sections 3.2.3.7 and 3.2.3.8). It can be hypothesized that the impact of coupling will be much larger in strong wind regions, but unfortunately a lack of experimental data in those regions currently precludes validation of this hypothesis.

3.2.3.7 Radiosonde to COAMPS Comparison

Figures 2-28 through 2-30 show comparisons of atmospheric profiles from R/V *PLANET* radiosonde data to COAMPS profiles. The plots are displayed as time series vs. height (for temperature and relative humidity) and time series vs. pressure (for potential temperature). Radiosonde data primarily came from a survey area within 10 nm of the ODAS buoy and model data were for a single point closely matching the ODAS location, so differences that arose due to spatial displacement with the model data were likely to be small.

The overall characteristics of air-mass and boundary layer from the radiosonde data were qualitatively reproduced in the fully coupled model. For example, on 19 June there was warm dry air in the lowest 2 km, while from 17-18 and 21 to 22 June, a moist cool boundary layer developed in the lowest 1 km. A moist boundary layer developed again on the 25th just before the Mistral winds of 25-26 June (Figs. 2-28 through 2-30).

Quantitative differences between model and observation were also apparent, in the form of a large diurnal signal in temperature and potential temperature in the model, with cold air in the early morning and warm air in the afternoon. These were possibly due to an ‘atmospheric tide’ caused by solar heating and absorption by water vapor or due to the large land breeze circulation discussed in Section 3.2.3.1. There were some hints of this in the radiosonde data, but the amplitude and phase were not well defined.

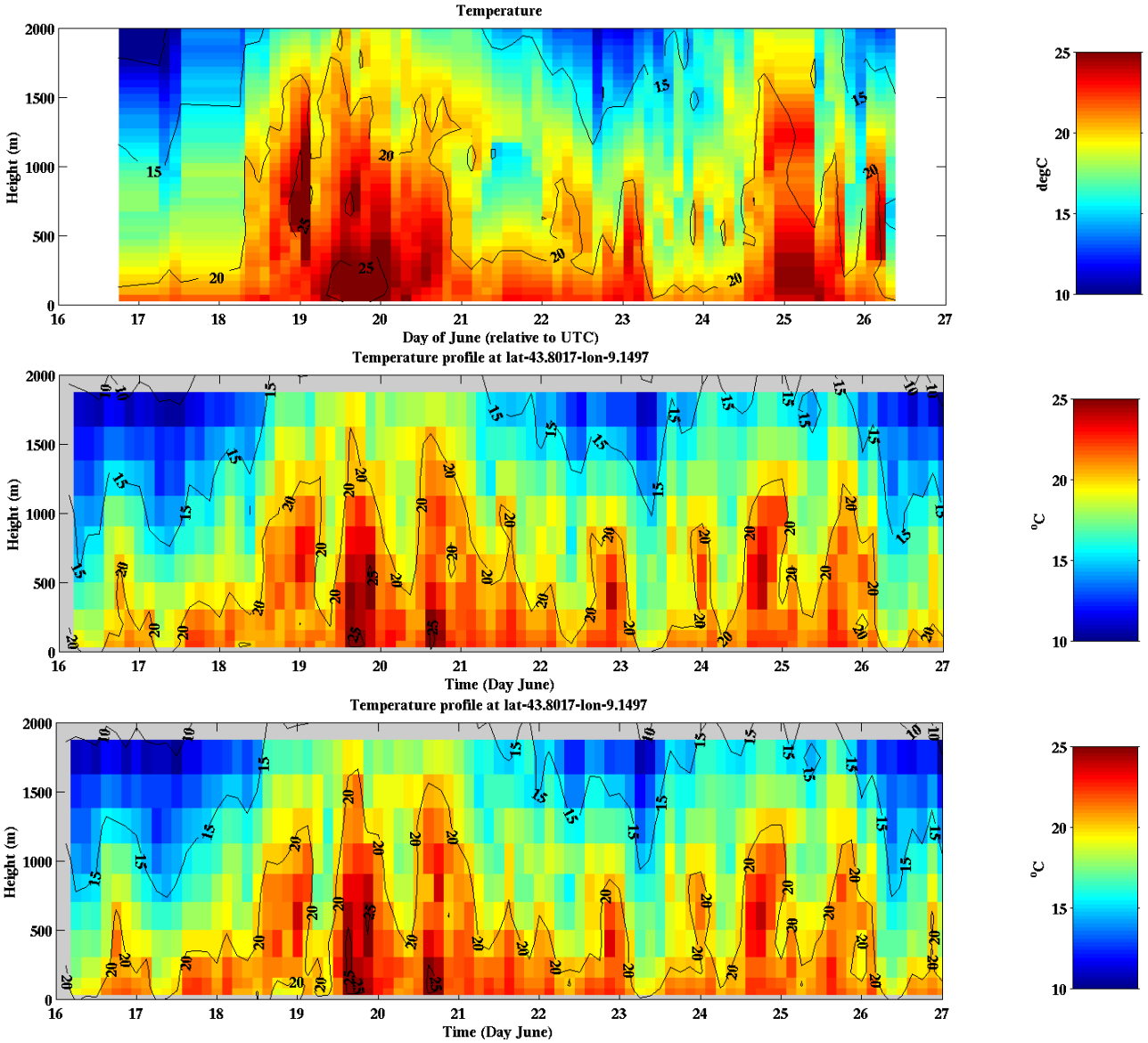

Figure 2-28: Atmospheric boundary layer profiles of temperature. Top: Radiosonde data from various locations near ODAS, plotted as time vs. height. Middle: Corresponding results from the fully coupled run taken at the ODAS location. Bottom: Results from the uncoupled run.

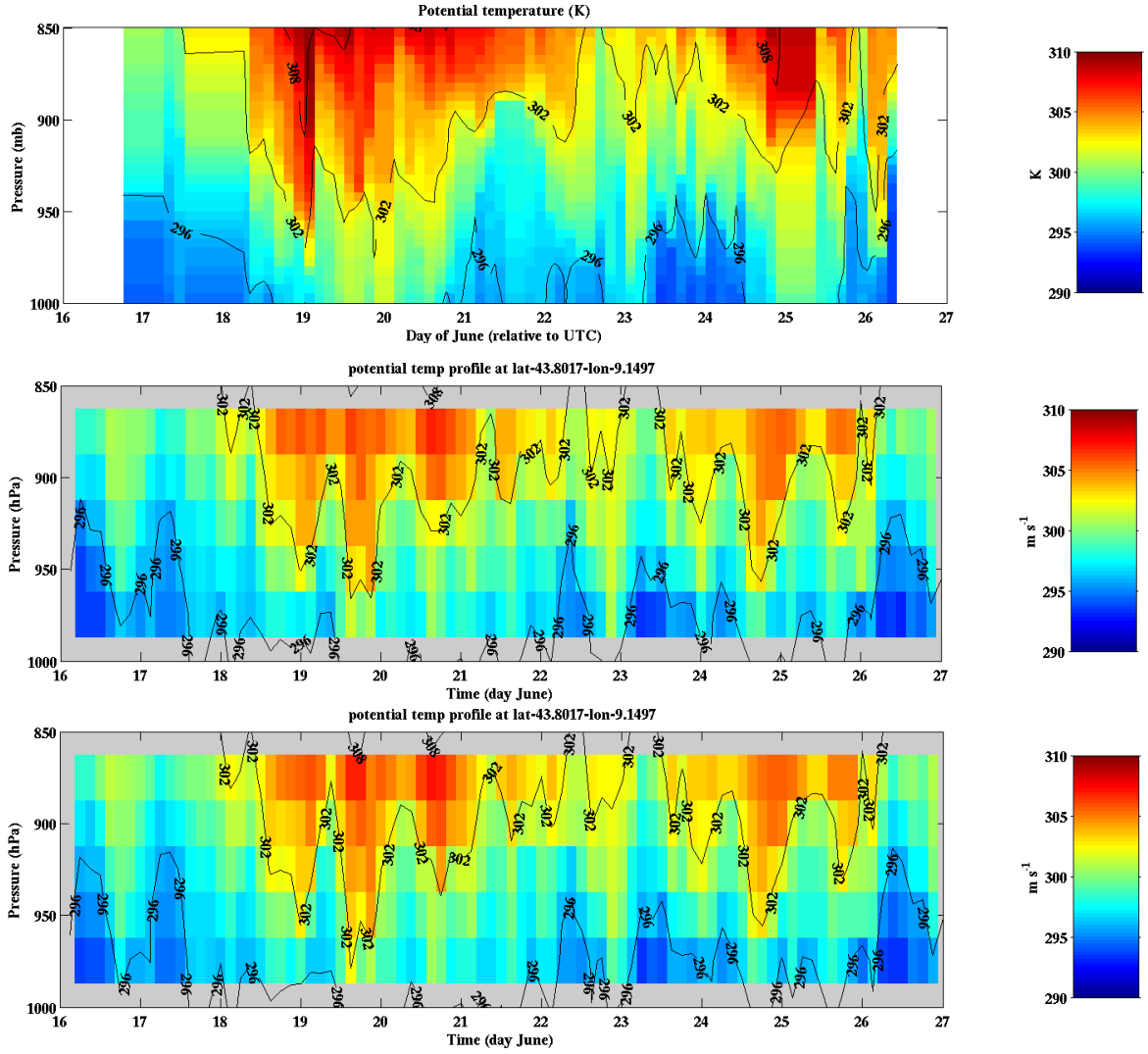

Figure 2-29: Atmospheric boundary layer profiles of potential temperature. Top: Radiosonde data from various locations near ODAS, plotted as time vs. pressure. Middle: Corresponding results from the fully coupled run taken at the ODAS location. Bottom: Results from the uncoupled run.

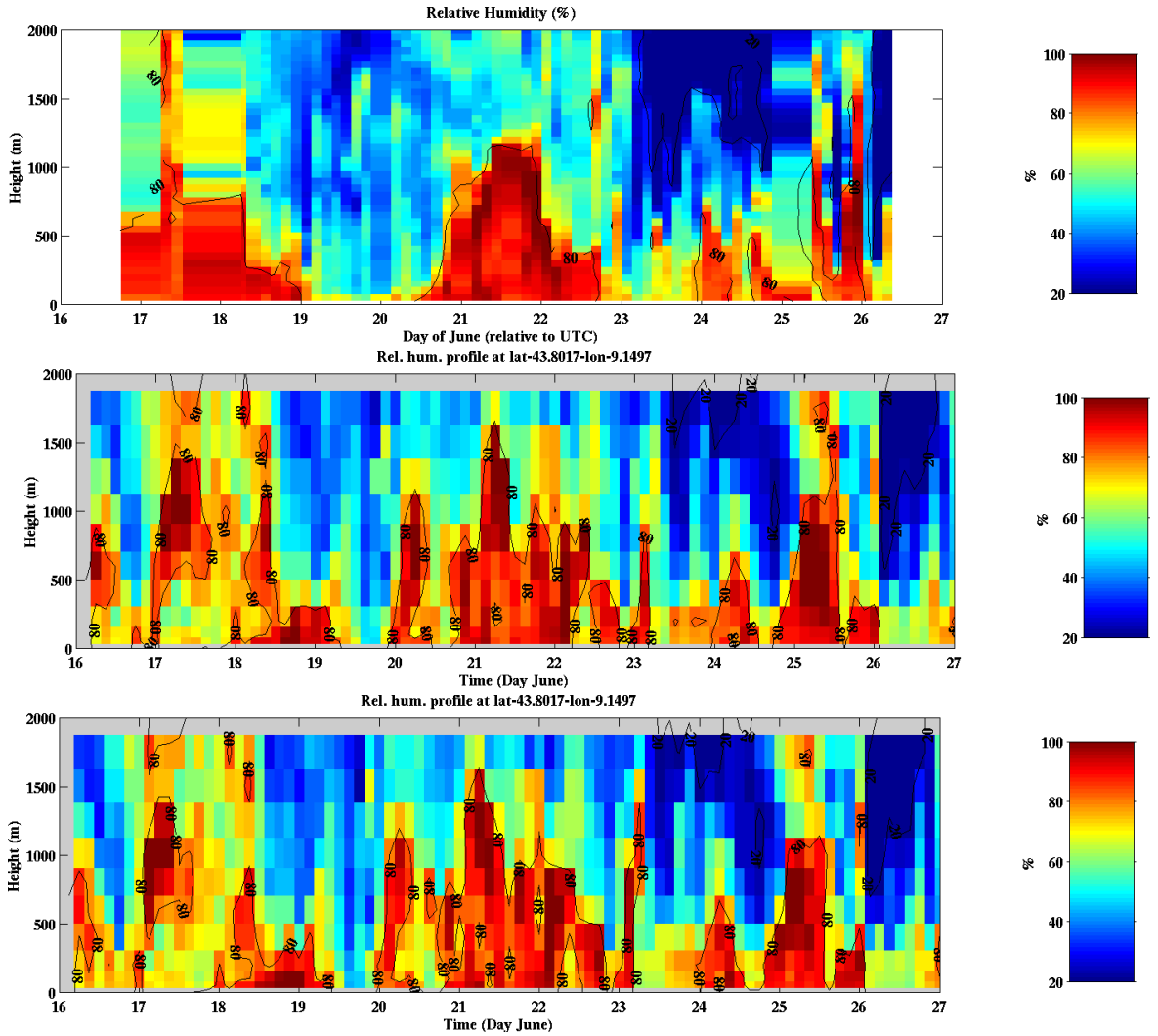

Figure 2-30: Atmospheric boundary layer profiles of relative humidity. Top: Radiosonde data from various locations near ODAS, plotted vs. time and height. Middle: Corresponding results from the fully coupled run taken at the ODAS location. Bottom: Results from the uncoupled run.

3.2.3.8 Mixed layer depth and CTD data analysis

During LASIE07 CTD data were gathered in the coastal region by R/V *LEONARDO* and in the deep water region (mostly near the ODAS buoy) by R/V *PLANET*. The focus of this analysis was on deep water CTD data. Figure 2-31 shows the CTD survey region of R/V *PLANET* with the analyzed data taken from within the black rectangle near the ODAS mooring. The nearest COAMPS output in space and time was matched to each CTD cast (based on the 3-hourly output of nest 2 COAMPS profile data).

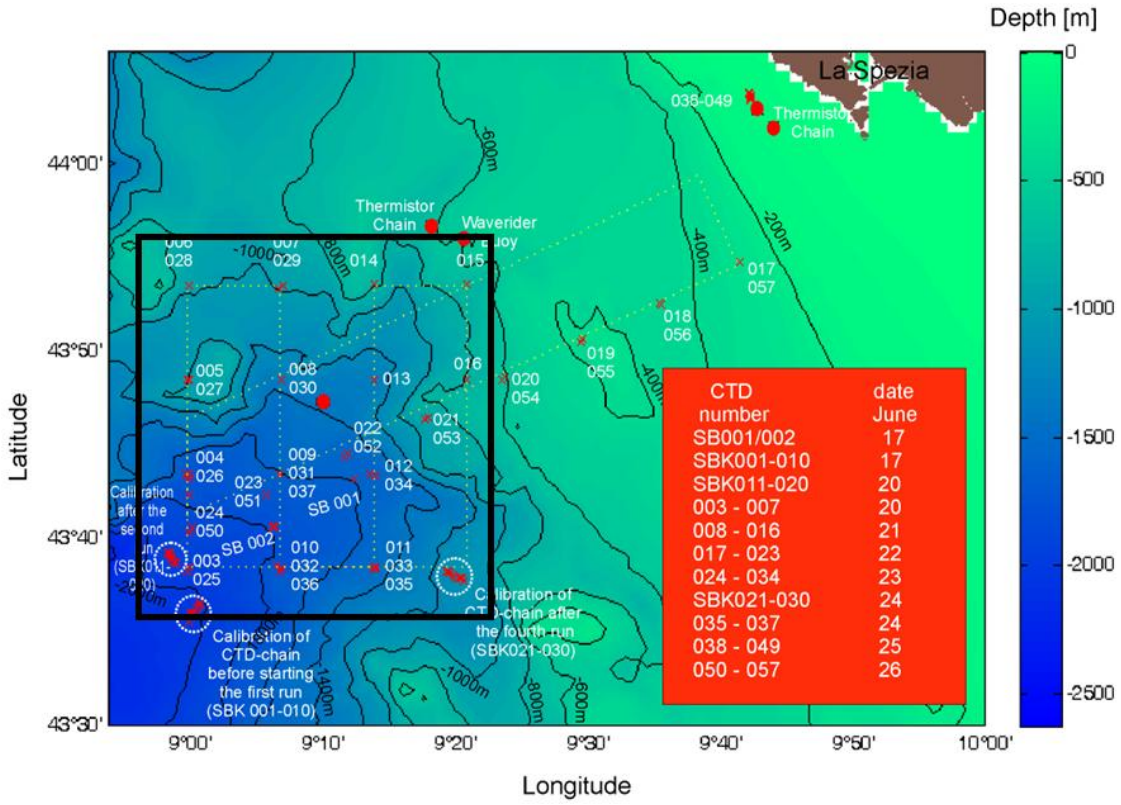

Figure 2-31: The R/V *PLANET* CTD survey region. Individual CTDs are marked by numbers with a key in the red box showing dates. Ship track is shown as dashed lines. CTD data analyzed in this project is contained within the black rectangle.

For each profile, the MLD was found using a temperature-threshold method modified from Kara et al., (2000). Here we searched for a temperature change of 0.1ºC from the temperature at 7 m, an initial depth chosen to avoid complications due to diurnal warming occurring in the first few meters. The small value of 0.1ºC temperature change was chosen because the CTD and model data had high vertical resolution and very strong temperature gradients at the base of the mixed layer. (Note that if a mixed layer is identified between 7 and 9 m deep it may mean that no mixed layer is present and instead it has just found the next depth level after 7 m.)

A mixed layer depth timeseries for CTD casts and COAMPS is shown in Fig. 2-32. Apart from two observations on 17 June, the observational data were mainly gathered between 20 and 26 June. The data from the 17th, 22nd, 23rd and 26th show that the observations (circles) had deeper mixed layers (often between 10 m and 18 m) than the model, which mostly had sub-10 m mixed layers. Observations on 20 and 21 June suggest an absence of a real mixed layer (as discussed above). Differences between the coupled model (blue asterisk) and uncoupled model (red cross) were small but with a slight suggestion of a deeper mixed layer on 24 and 26 June for the uncoupled run.

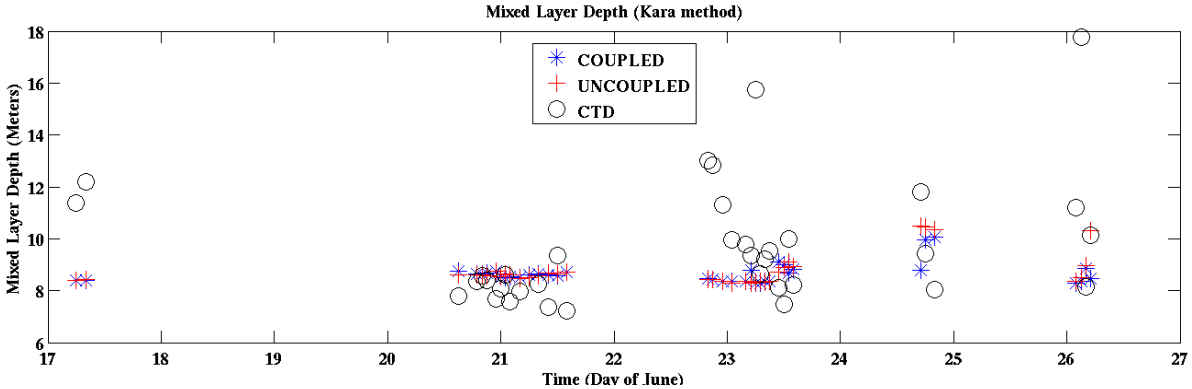

Figure 2-32: Mixed layer depths from CTD data, the coupled model, and the uncoupled model (see legend) as a function of time.

Because CTD data were sparse in time and space, an ODAS timeseries of data was studied next. ODAS has an advantage of being a continuous time record at a single location but has a disadvantage of having just three measurement depths: 1 m, 12 m and 28 m. However, ODAS can be used to infer periods when the mixed layer is 12 m or 28 m deep. This can then be compared against similar records from the coupled model. Figure 2-33b shows the ODAS thermistor records. As indicated by the vertical lines, there are sustained periods of 12 m deep mixed layer between 26 and 29 June and 4 and 5 July. There are no instances of a 28 m deep mixed layer, but on 4 July the 28 m temperature approaches the mixed layer value. Additionally, there are transient periods of 12 m-deep mixed layers on 17 and 23 June and 10 July (marked by ellipses). Compared to the wind stress timeseries in Fig. 2-33a, it can be seen that these events correspond to the strong winds of 16 and 23 June and 25-28 June, as well as 3-4 and 9-10 July.

Coupled COAMPS and uncoupled ocean-only (NCOM) results are shown in Figs. 2-33c and 2-33d, respectively. Because the model vertical levels do not exactly correspond to the ODAS thermistor depths, a selection of three levels is shown: 5 m, 11 m and 25 m. The top level was chosen at 5 m depth rather than close to the surface to avoid problems caused by the exaggerated diurnal warming in the model. The latter two levels were closest to the corresponding ODAS depths. The near-surface behavior of the coupled and uncoupled runs was very similar (Figs. 2-33c, d). The periods of sustained MLD of at least 11 m in the model were from 4-6 July and 10-12 July (marked with vertical lines). The first event was longer than the corresponding period in observations, possibly due to the stronger model winds on 5 July after the observed winds had died down (Fig. 2-33). The second event (10-12 July) in the model was also due to stronger and more prolonged winds, with the mooring data only hinting at brief mixed layer formations in this time period (Fig. 2-33b). In contrast, COAMPS did not show a sustained deep mixed layer from 26-29 June, likely because the model winds during this period were weaker than observed (Fig. 2-33a).

To summarize the MLD analysis, the results showed that there was a tendency towards shallower mixed layers in the model compared to observations, when the wind stress was weaker in the model. When the model predicted stronger wind stress than observed, the mixed

layer lasted longer in the model, but a precise comparison of the actual MLD during this period (3-5 and 10-12 July) was not possible due to a lack of available CTD data.

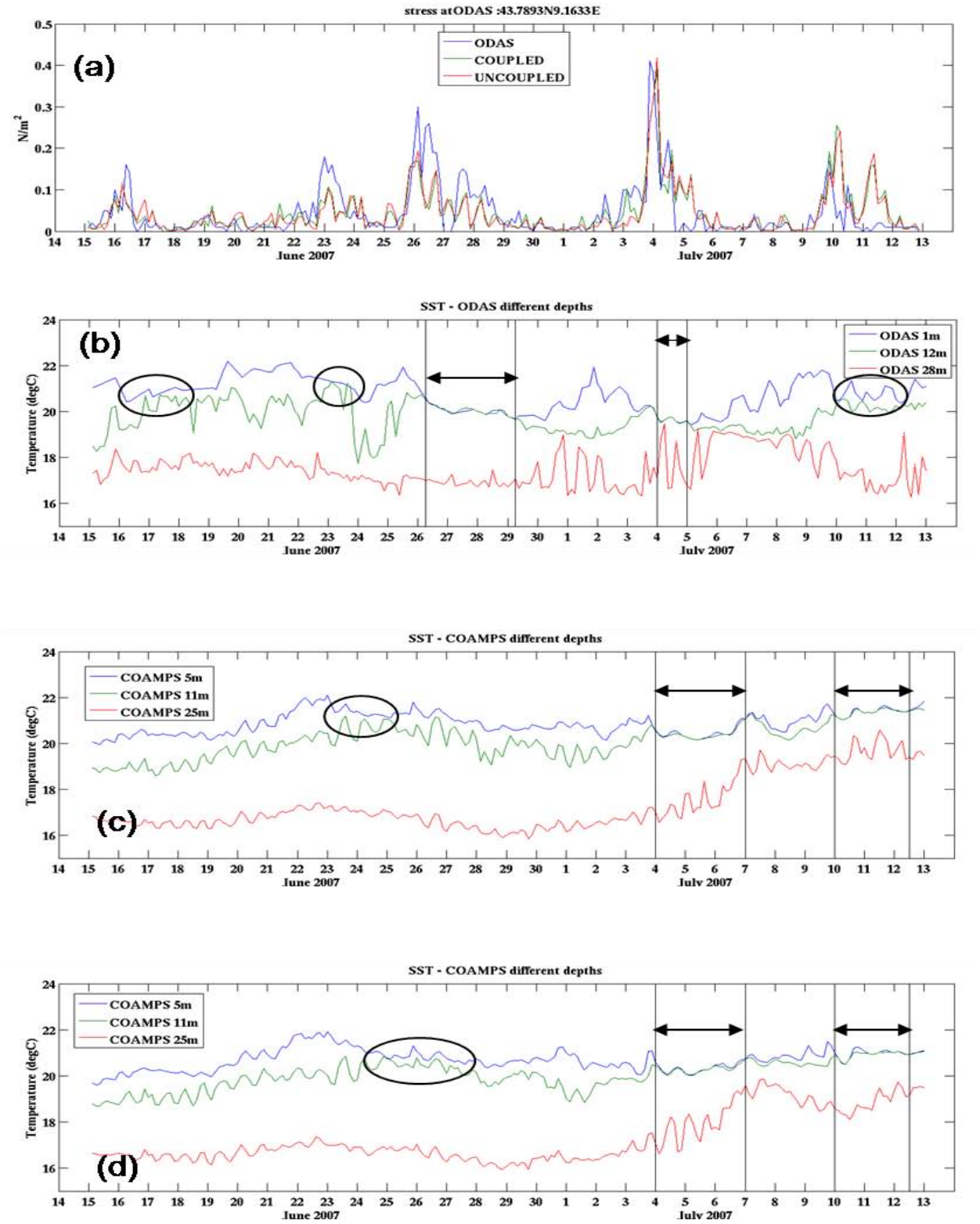

Figure 2-33: (a): Wind stress at ODAS. (b): Temperature at ODAS: 1 m (blue), 12 m (green), and 28 m (red). (c): From the coupled model run, temperature at 5 m, 11 m and

28 m. (d): From the uncoupled run, temperature at 5 m, 11 m and 28 m. Thick vertical lines connected by arrows indicate periods when a mixed layer of at least 12 m exists in the observations as in (b) and at least 11 m deep in the model- c), d). The ellipses denote periods when mixed layers of 12 m briefly exist in the observations- b) and mixed layers of between 8 m and 11 m exist in the model- c), d).

The deeper temperature and salinity structure in the Ligurian Sea is analyzed in Figs. 2-34 to 2-36, focusing on the top 200 m only (deeper processes were not considered in this report). The individual CTD profiles are shown as green lines in Fig. 2-34, and the average of all such profiles is shown in red. Note that potential temperature is used rather than actual temperature; this is the quantity output by the model (differences in the top 100 m between temperature and potential temperature are generally very small). The profiles show a typical summer seasonal thermocline (Fig. 2-34a) extending to ~100 m. The temperature predictions are from the NCOM component of the coupled system. Temperature was fixed in uncoupled COAMPS during the forecast, changing every 6 or 12 hrs depending on the NCODA data assimilation cycle. There was considerable variability between different CTDs, with thermocline displacements of over 20 m (peak-trough) occurring in the thermocline, possibly due to internal waves and frontal effects. The mean profile (Fig. 2-34a, red) showed a strong vertical gradient in the top 20 m (where the mixed layer base was generally located), and a weaker gradient between 20 and 100 m, which was the main thermocline.

Salinity profiles showed a very large variability, especially in the top 60 m (Fig. 2-34b). LASIE07 CTD chain data not included in this report showed the presence of a salinity front of around 37.6 psu in the region between onshore waters and over 38 psu in offshore waters. The front extended to at least 50 m depth.

From the temperature and salinity profiles the sound velocity and potential density were derived using the standard UNESCO algorithms. The mean sound velocity (Fig. 2-34c, red line) reveals a sound channel centered at around 100 m depth. The individual profiles display the presence of an upper mixed/sonic layer within the top 20 m (green lines) that tends to be smoothed out in the average profile, followed below by a strong downward refracting profile. The potential density profiles (Fig. 2-34d) were relatively smooth, dominated by the temperature structure in the top 100 m. A strong pycnocline was evident, extending, albeit weaker, to between 100 and 200 m due to increasing salinity at those depths (while temperature was constant).

'The temporal mean model profile from all points closely matching the CTD data times and locations is shown in Fig. 2-34 as black (coupled) and blue (uncoupled, ocean-only (NCOM) solid lines. These lines mostly overlap and cannot be distinguished visibly. A comparison of the mean errors is shown in Fig. 2-36. Both model experiments demonstrated a cool bias in the thermocline (Fig. 2-34a), resulting in lower sound velocities (Fig. 2-34c) and higher pycnocline potential density (Fig. 2-34d), compared to observations.

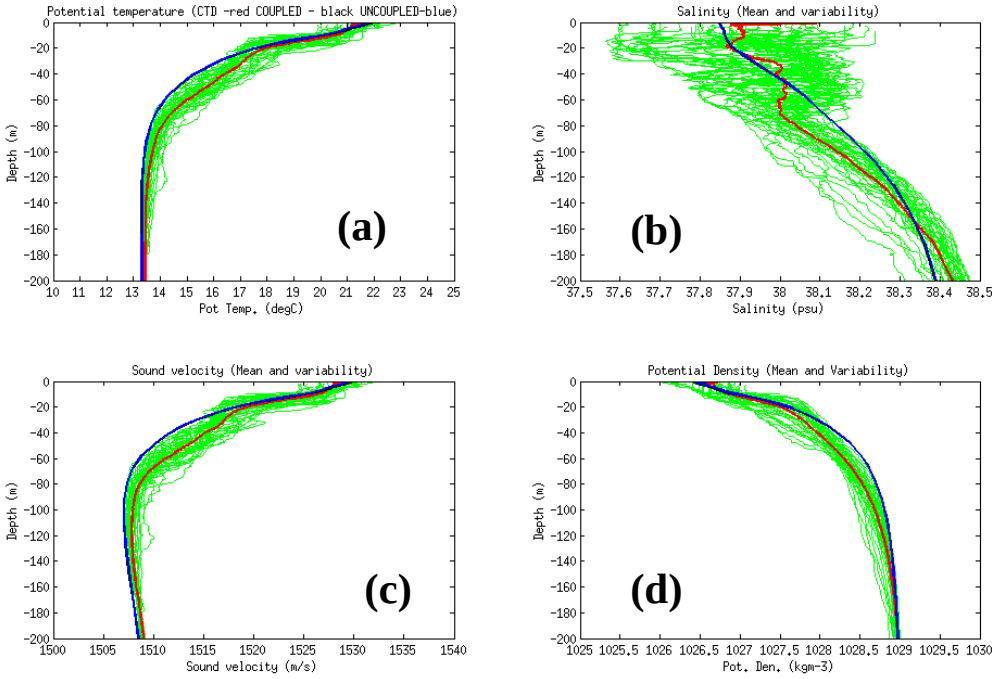

Figure 2-34: CTD and model ocean profiles. (a): Potential temperature. (b): Salinity profiles. (c): Sound velocity. (d): Potential density. Individual profiles from CTD are green, mean CTD is red, coupled model mean is black, and uncoupled model mean is blue. The model lines mostly overlap.

The differences between individual CTD profiles and their model counterparts were computed using the RMS at each depth and were compared to the STD. The RMS and STD are shown in Fig. 2-35 together with the MB, which is the difference (observed minus model) between the mean profiles of Fig. 2-34. There was a large RMS of temperature of up to 1.2ºC in the seasonal thermocline centered at 40-50 m depth, which was much larger than the observed STD (Fig. 2-35a). This indicates that COAMPS performed poorly in the main thermocline. In contrast, a RMS of over 1ºC centered between 10 and 20 m is comparable to the STD and is due to the difficulty of obtaining the MLD in the correct position (errors in MLD lead to large errors of temperature at a given depth). The mean bias profile (Fig. 2-35a, blue line) revealed that, in addition to a cool model bias in the main thermocline (mean error positive), there was a warm bias near the surface (mean error negative) consistent with the warm SST bias noted in the ODAS mooring comparisons (Figs. 2-9 and 2-10).

The sound velocity RMS and mean bias (Fig. 2-35c) followed the same pattern as in temperature, with significant differences centered around 40-60 m (up to 4 m/s mean bias and RMS). In the salinity profiles (Fig. 2-35b) the RMS was comparable to the standard deviation in the top 50 m but was much bigger than the standard deviation between 50 and 100 m, where the mean bias was also large.

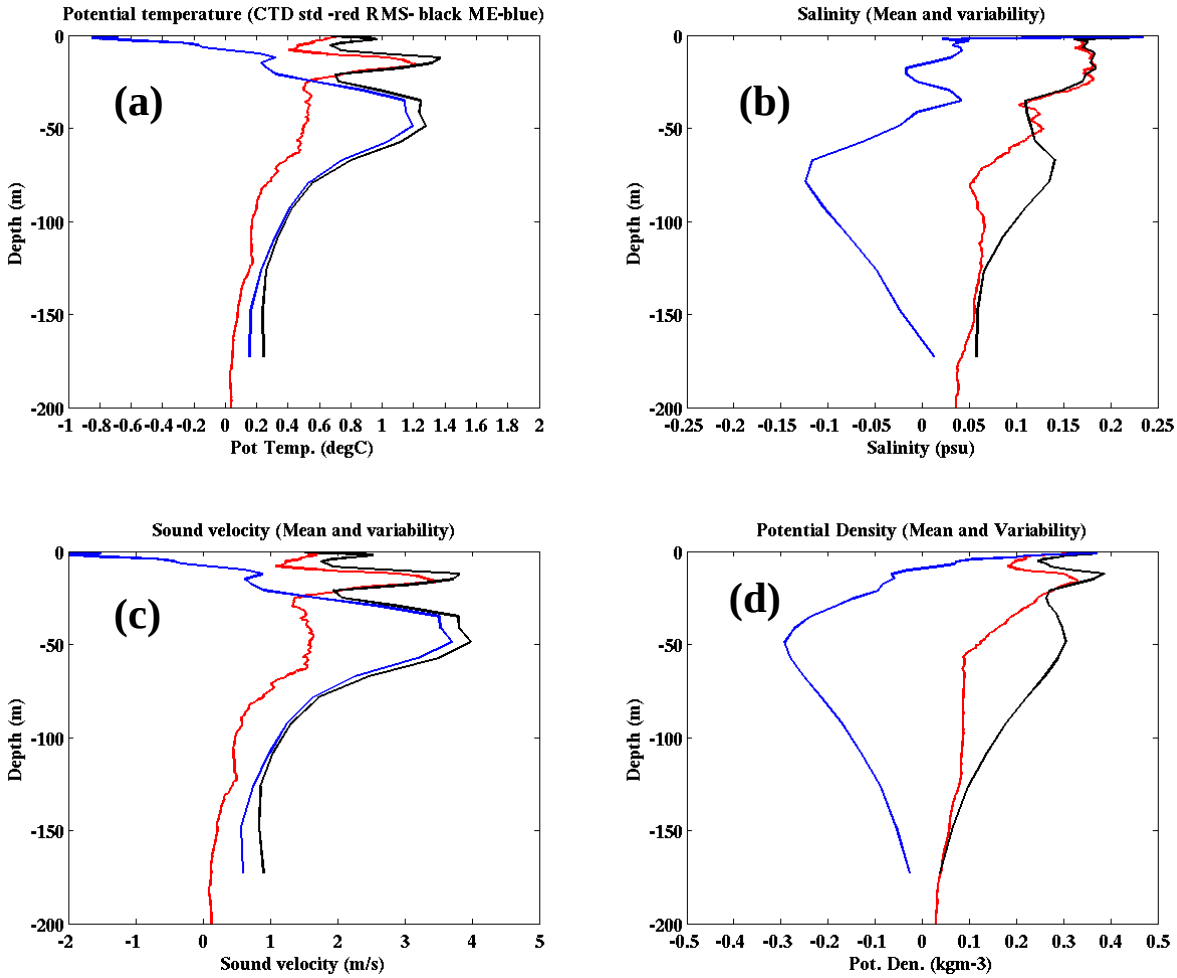

Figure 2-35: Standard deviation of CTD profiles for (a): potential temperature (°C), (b): salinity (psu), (c): sound velocity (m/s), and (d): potential density (kg/m^3). The colors represent the standard deviation of CTD data (red), the coupled run RMS difference with CTD (black), and the mean bias (obs-model) for the coupled run (blue).

Comparison of the potential temperature RMSE and mean bias computed for the coupled model (solid lines) and uncoupled model (dashed line) is shown in Fig. 2-36a. The errors were extremely close for both RMS and mean bias. For example, a careful examination of the temperature errors revealed that the differences between coupled and uncoupled reached up to 0.3ºC at the surface and were less than 0.1ºC at deeper levels, a negligible difference between the subsurface temperature structure in the coupled and uncoupled runs. The reason relates to the earlier findings that the surface fluxes were also scarcely different, either due to LASIE07 being in a location of relatively calm weather or to the short timescales (days to weeks) being considered here compared to longer timescales of some ocean responses.

The substantial mean bias in the thermocline seen in Fig. 2-35a and Fig. 2-36a in both the coupled and uncoupled models may be attributed primarily to errors in the initial condition. When comparing the month-long average temperature profile (Fig. 2-36b, black line) with the initial condition (Fig. 2-36b, red line), the differences were confined to the top 10-20 m

(presumably arising from the surface flux evolution), while the deeper thermocline (between 20 and 80 m) was mostly unchanged over the course of the month-long run.

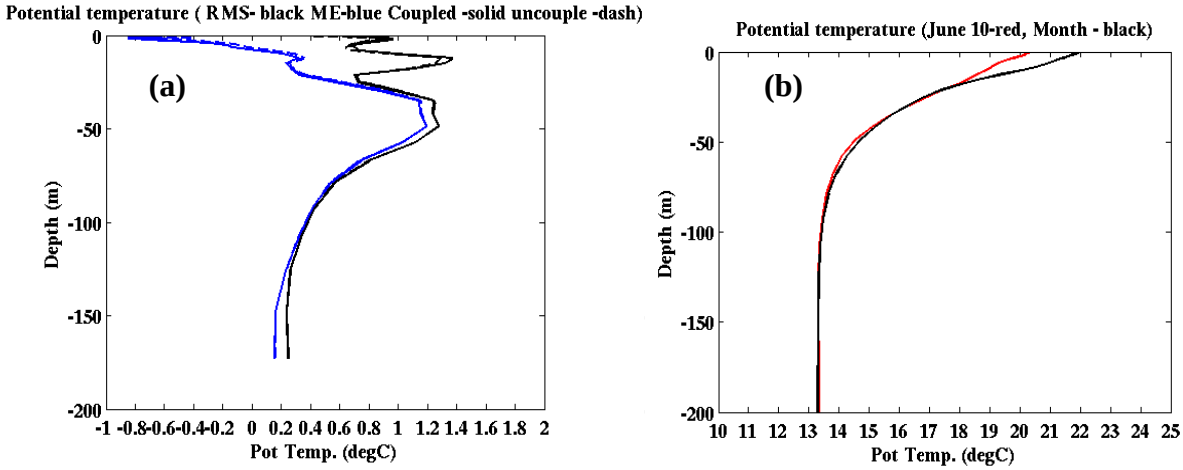

Figure 2-36: Potential temperature (°C) mean bias for the (a): coupled (blue, solid) and uncoupled run (blue, dashed), and RMS difference for the coupled (black, solid) and uncoupled run (black, dashed). (b): month-long average potential temperature profile (black line) compared to the initial condition on 10 June (red line).

3.3 Test Case 3: Autonomous Ocean Sampling Network (AOSN)

The Autonomous Ocean Sampling Network (AOSN) project combines innovative robotic vehicles with advanced ocean models to improve observational capabilities and ocean dynamics predictions (http://www.mbari.org/aosn/). The operational system includes near real-time data collection by adaptive platforms and sensors that then assimilate that information into numerical models to create four-dimensional fields and predictions of future conditions.

3.3.1 Purpose

Test Case 3 sought to gain a better understanding of the sensitivity of coupling with continuous data assimilation in the atmosphere and ocean. When the COAMPS and NCOM are fully coupled, each model's errors evolve in lock-step. It is generally unclear whether the model bias is reduced or increased from coupling. This test case also offered an opportunity to examine air-sea interaction in a weak wind regime that occurs during upwelling events. The fully coupled COAMPS was used to investigate the sensitivity of data assimilation and coupling in simulating the cold ocean upwelling and relaxation over the US west coast during summer of 2003. The upwelling and relaxation were driven by a series of alternating, prevailing, weak, southerly (4-5 August and 20-21 August) and stronger northwesterly (6-19 and 23-31 August) winds. Model-simulated parameters at the air-sea interface such as SST, 2 m air temperature and humidity, and 10 m winds were compared with the observations.

3.3.2 Test Case Characteristics

3.3.2.1 Test Area and Observations

Monterey Bay, one of the largest bays on the west coast, often has a strong land-sea breeze circulation that makes it an excellent site for air-sea interaction observations (Tseng et al., 2005; Vesecky et. al., 2001). The regional circulation is described in two distinct hydrographic states: an upwelling state (1-3 weeks) and a relaxed state (3-6 days). The two states are driven by prevailing wind patterns and scales. During the summertime upwelling periods, the typical circulation of the Monterey Bay region is comprised of four circulation patterns: 1) an upwelling front starting at Pt. Año Nuevo, 2) a cyclonic circulation inshore of the front in Monterey Bay, 3) an anti-cyclonic eddy-like circulation offshore of the upwelling front, and 4) a second upwelling region off of Pt. Sur. When the winds calm, upwelling diminishes, and the offshore eddy-like circulation pours into the Bay and mingles with the flow over the shelf (Rosenfeld et al. 1994). Monterey Bay circulation is closely related to the California Current (CC) System, a broad, weak, equatorward-flowing current. The CC dominates flow offshore. Closer to shore, the Inshore Countercurrent (IC) and the California Undercurrent (CU), each within about 100 km of the coast, serve as two narrow poleward-flowing boundary currents. The IC is a weak current, appearing in fall and winter to transport shallow, upper layer water. The CU is a narrow, relatively weak subsurface flow that transports warm, saline, equatorial water. The CU has a mean speed of about 15 cm/s and is strongest around 100-300 m depth (Pierce et al. 2000).

AOSN sampling was conducted from 3 August through 8 September, 2003. Observations were taken using 12 Slocum gliders (CTD, optical properties), five spray gliders (CTD), five autonomous underwater vehicles (AUVs) (CTD, currents, biolum, chemistry), Advanced Very High Resolution Radiometer (AVHRR), Geostationary Operational Environmental Satellite (GOES) West and Sea-viewing Wide Field-of-view Sensor (SeaWiFS) satellite data, Coastal Ocean Dynamics Applications Radar (CODAR) surface currents, QuikSCAT winds, oceanographic moorings M1 and M2, drifters (T and S), vertical profilers, bottom mounted ADCPs, and an airplane for SST, wave height, air temperature, wind strength, direction, and humidity.

The glider observations were essential components in AOSN. The NCODA assimilated the Monterey Bay glider data into the NCOM model. Glider data assimilation improves the surface temperature at both the mooring locations for the NCOM 4.0 hindcasts and nowcasts and for short-range (1–1.5 days) forecasts.

Bathymetry came from SRTM30, a near-global digital elevation model (DEM) comprised of a combination of data from the Shuttle Radar Topography Mission (SRTM) and the U.S. Geological Survey's GTOPO30 data set. The global data set is constructed and distributed in the SRTM30 grid format, which divides the Earth into 33 areas. Grid cells within each area have a 30 arcsecond latitude and longitude spacing (Becker et al., 2009). A 3D bathymetric map of the test area is shown in Fig. 3-1.

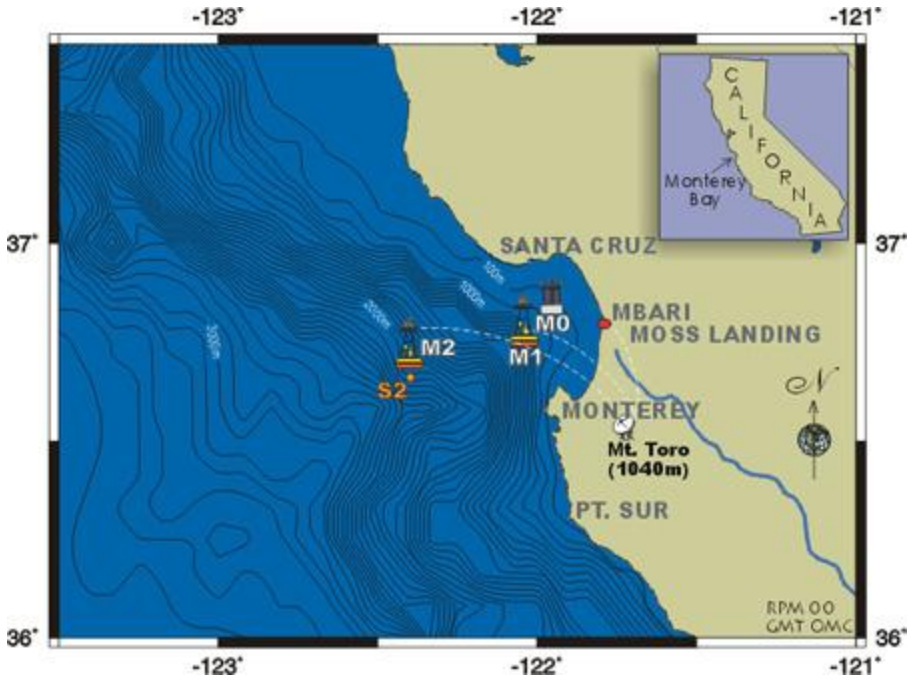

Figure 3-1: Monterey Bay test area showing M1 and M2 moorings.

3.3.2.2 Model Setup

For the testing month of 1-30 August, 2003, the control run featured a continuous data assimilation in both the atmosphere, through MVOI, and in the ocean, through NCODA 3D. The model setup included a 12-hr update cycle and a 48-hr forecast. The COAMPS model had four nested atmospheric grids: 81, 27, 9 and 3 km with 40 vertical levels. The meteorology for this time period is described by Doyle et al., (2009).

The NCOM only had one grid with a horizontal resolution of 3 km (Fig. 3-2). The NCOM vertical resolution was set at 10 sigma layers and 30 *z*-levels. The coupling interval was 12 minutes in concurrent mode. For the first sensitivity test, the coupled model ran for one month without any observations from the atmosphere and ocean. The second sensitivity test was a one-way coupled run, i.e. there was no ocean feedback to the atmosphere. The one-way coupling interval was one hour.

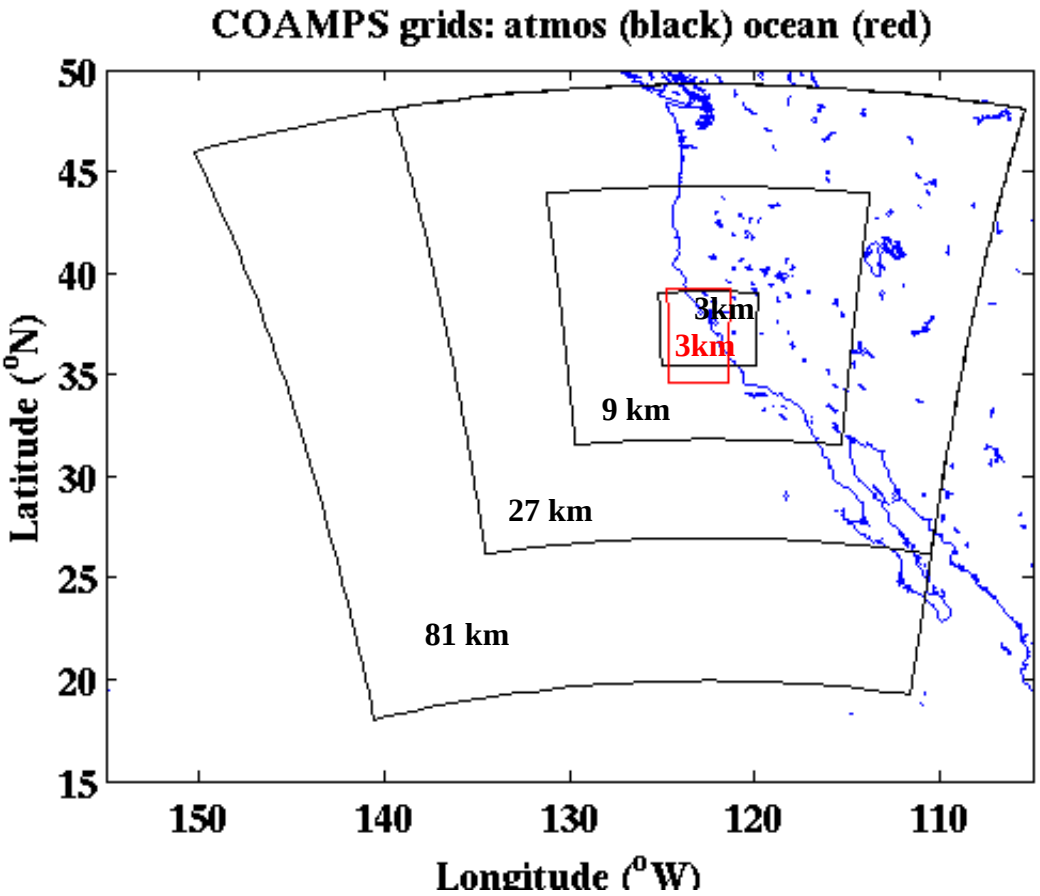

Figure 3-2: COAMPS atmospheric grid nests (81 km, 27 km, 9 km and 3 km) and the 3 km NCOM grid for Test Case 3.

3.3.3 Results

3.3.3.1 COAMPS Two-way coupled (Control) Run

There were two alternating SST relaxation and upwelling periods during August 2003, which can be clearly identified by the 10 m wind pattern observed at the M2 mooring (Fig. 3-3, from Ramp et al., 2009). The upwelling was associated with the uniform, offshore, northwesterly winds that measured around 10 m/s. The relaxation was associated with southerly winds that were usually less than 5 m/s. The first relaxation/upwelling episode began with a relaxation period from 4-6 August, followed by upwelling from 6-19 August. The second relaxation period began 20-21 August. The second upwelling began 23-31 August.

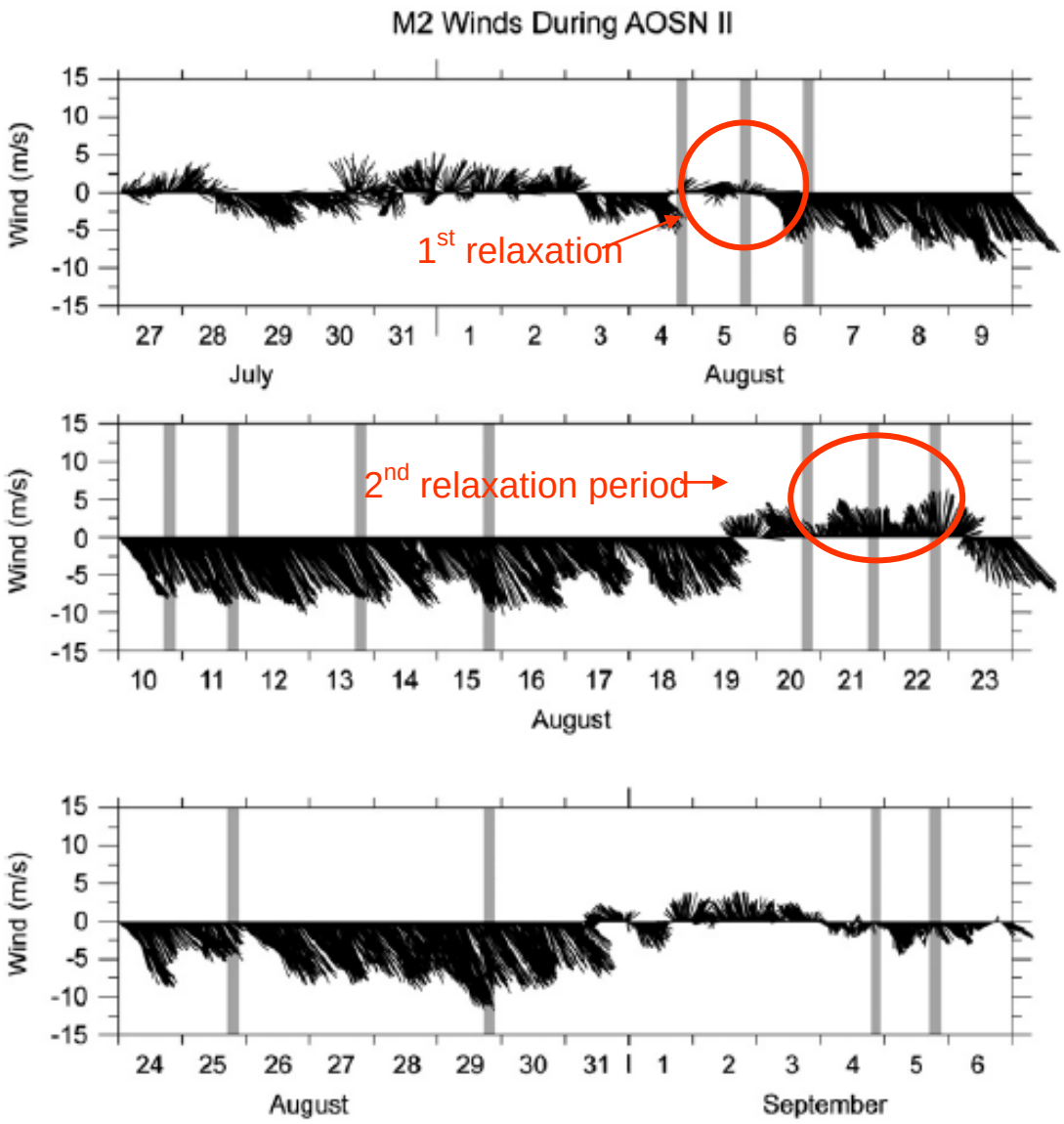

Figure 3-3: Wind measurement from the M2 mooring. Gray-shaded bars represent the available aircraft observation time frames (from Ramp et al., 2009).

The two-way coupled data-assimilated Control run was able to predict the onset of the upwelling and relaxation episodes quite well. Sea surface comparisons during the first relaxation period between the 00 UTC Control 24-hr forecast run and aircraft observations showed that the model gave warmer results than did observations. COAMPS also lacked the fine horizontal mesoscale SST structure seen in the aircraft observations. On 6 August, the model began to reveal a path of colder water west of Point Año Nuevo, which was about 2°C warmer than the observations. The COAMPS SST was about 4°C too warm south of Monterey Bay and 6°C too warm north and west of Point Año Nuevo. SST discrepancies in the model are attributed to a slower model spin-up time in the weak wind regime (Fig. 3-4). The first cold upwelling area shown from the aircraft observation on 10 August took an elongated shape that then expanded about 40 km west of Point Año Nuevo and southwest of Point Sur. Nearer Point Sur, the upwelling continued to expand westward and almost doubled its width by 15 August,

with a minimum SST of 10°C. This cold upwelling event was well captured by the two-way coupled COAMPS run. The model accurately predicted a cold upwelling center west of Point Año Nuevo and another one west of the Point Sur, which was supported by observations. The upwelling area west of Point Año Nuevo was predicted by COAMPS as much narrower than the observation (Fig. 3-5). On 15 August, the model minimum SST was about 12°C, which was ~1-2°C warmer than the aircraft observation. The warm SST center north of Monterey Bay was captured by COAMPS but was not as strong as that seen by aircraft (Fig. 3-5d). A higher horizontal grid resolution for NCOM may have helped to resolve this small-scale feature inside Monterey Bay.

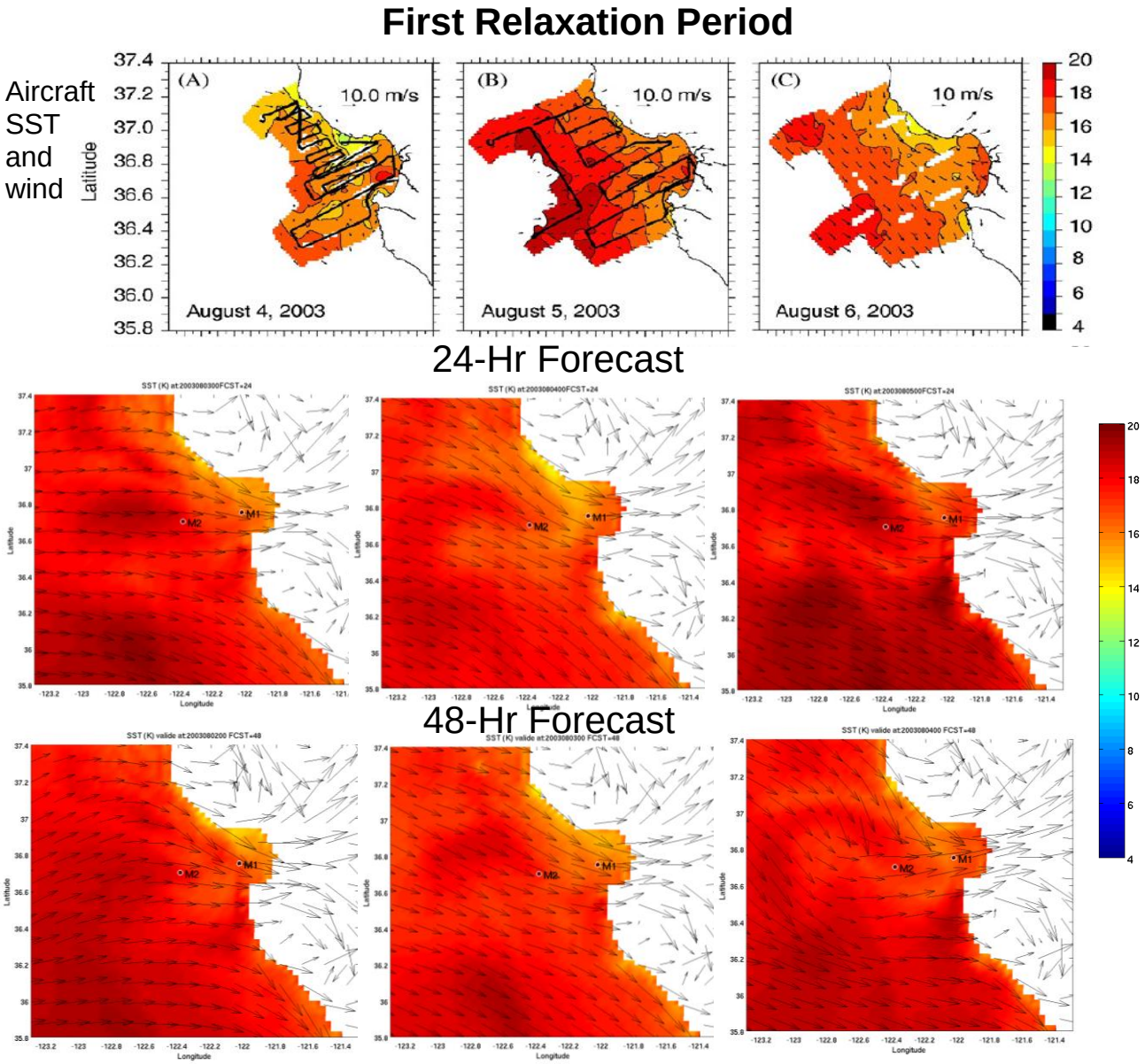

Figure 3-4: Comparison of aircraft observations and the Control 24-hr and 48-hr SST for the first relaxation period. Black lines in (A) and (B) represent aircraft flight paths. Vectors indicate wind magnitude and direction. The color scale represents SST (°C).

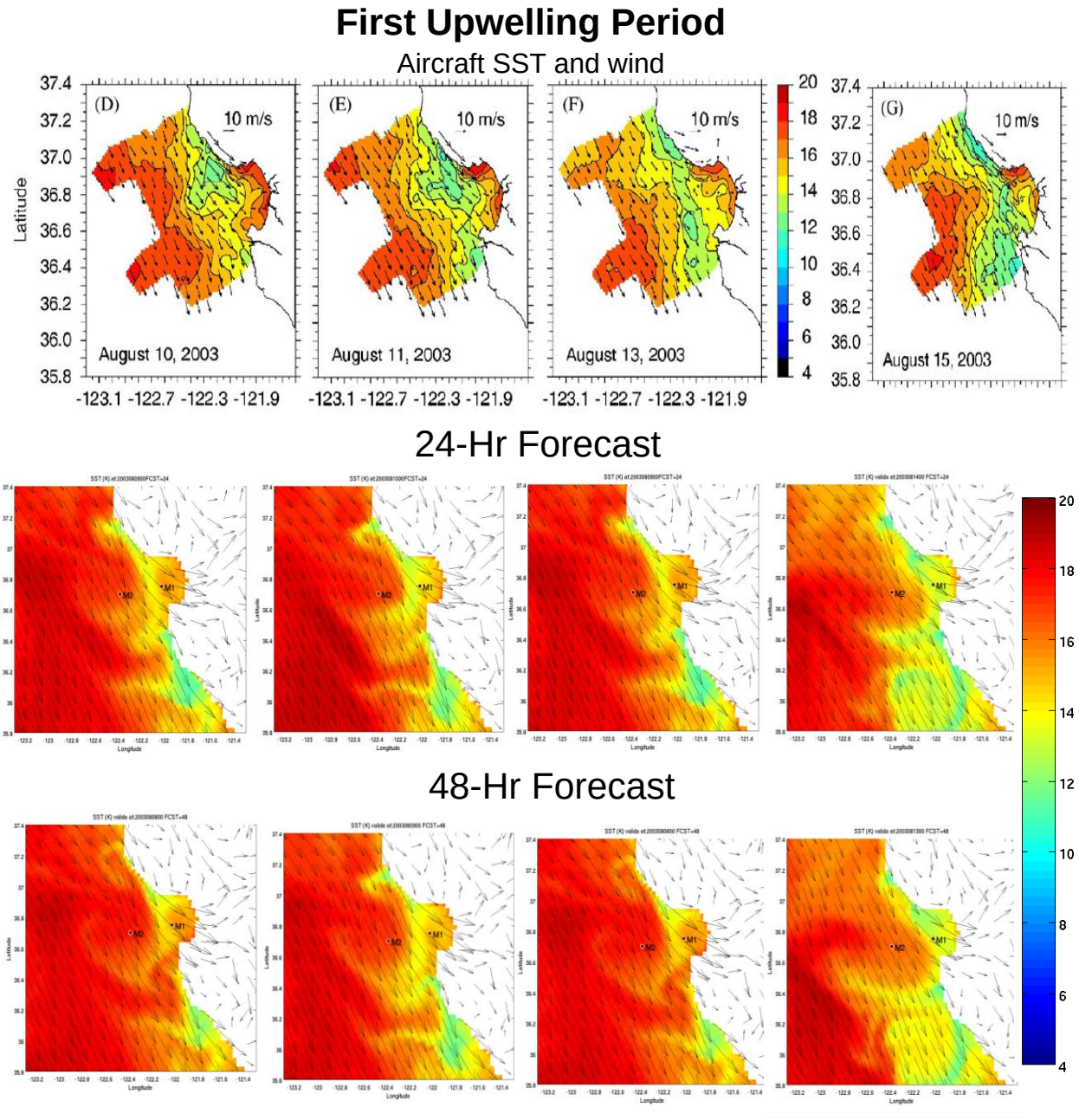

Figure 3-5: Comparison of aircraft observations and the Control SST for the first upwelling period of 10-15 August, 2003. Vectors indicate wind magnitude and direction. The color scale represents SST (°C).

During the second relaxation period from 20-22 August, the aircraft observations showed the SST warming back up to ~16°C. The upwelling area shrank back to north of Point Sur. Compared to the observations, the COAMPS SST recovery time was too fast. The upwelling area west of Point Año Nuevo and north of Point Sur had completely disappeared on 22 August (Fig. 3-6). Because the Control run did not have stronger, broader upwelling areas prior to this relaxation period, it is not surprising that the cold upwelling disappeared faster than the

observations once the wind stress forcing had subsided. The aircraft sampled the second upwelling event on 25 and 29 August (Fig. 3-7). Again, COAMPS was able to predict the 25 August onset of the upwelling center (west of Point Año Nuevo and Point Sur). However, the model upwelling area was smaller than in observations. The COAMPS SST bias from the second upwelling period was similar to the first period, and the Control 48-hr forecast of the relaxation/upwelling episodes was very similar to the 24-hr forecast. The COAMPS persistent forecast for the relaxation/upwelling was excellent for up to two days.

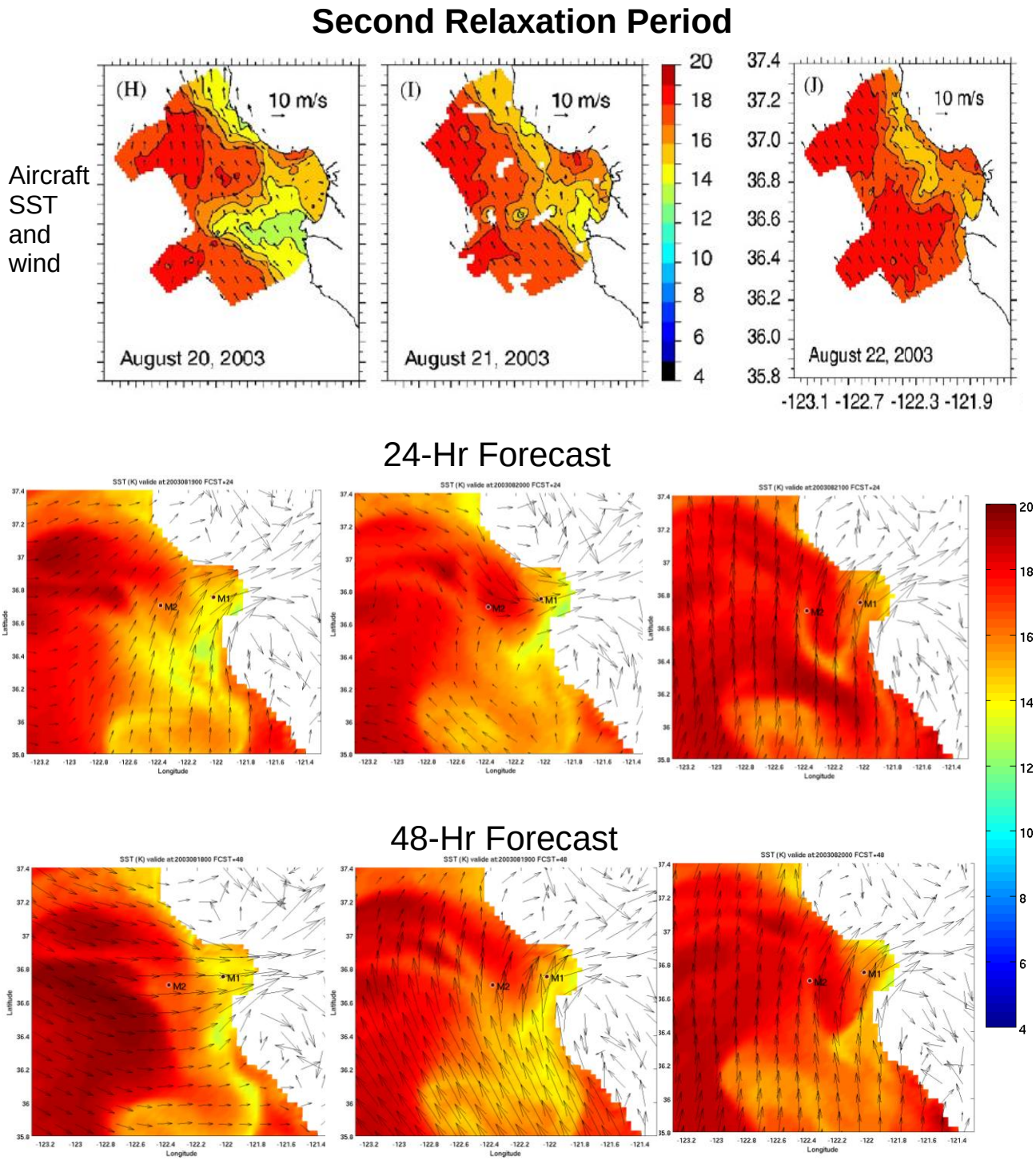

Figure 3-6: Comparison of the Control SST and aircraft observations for the second relaxation period. Vectors indicate wind magnitude and direction. The color scale represents SST (°C).

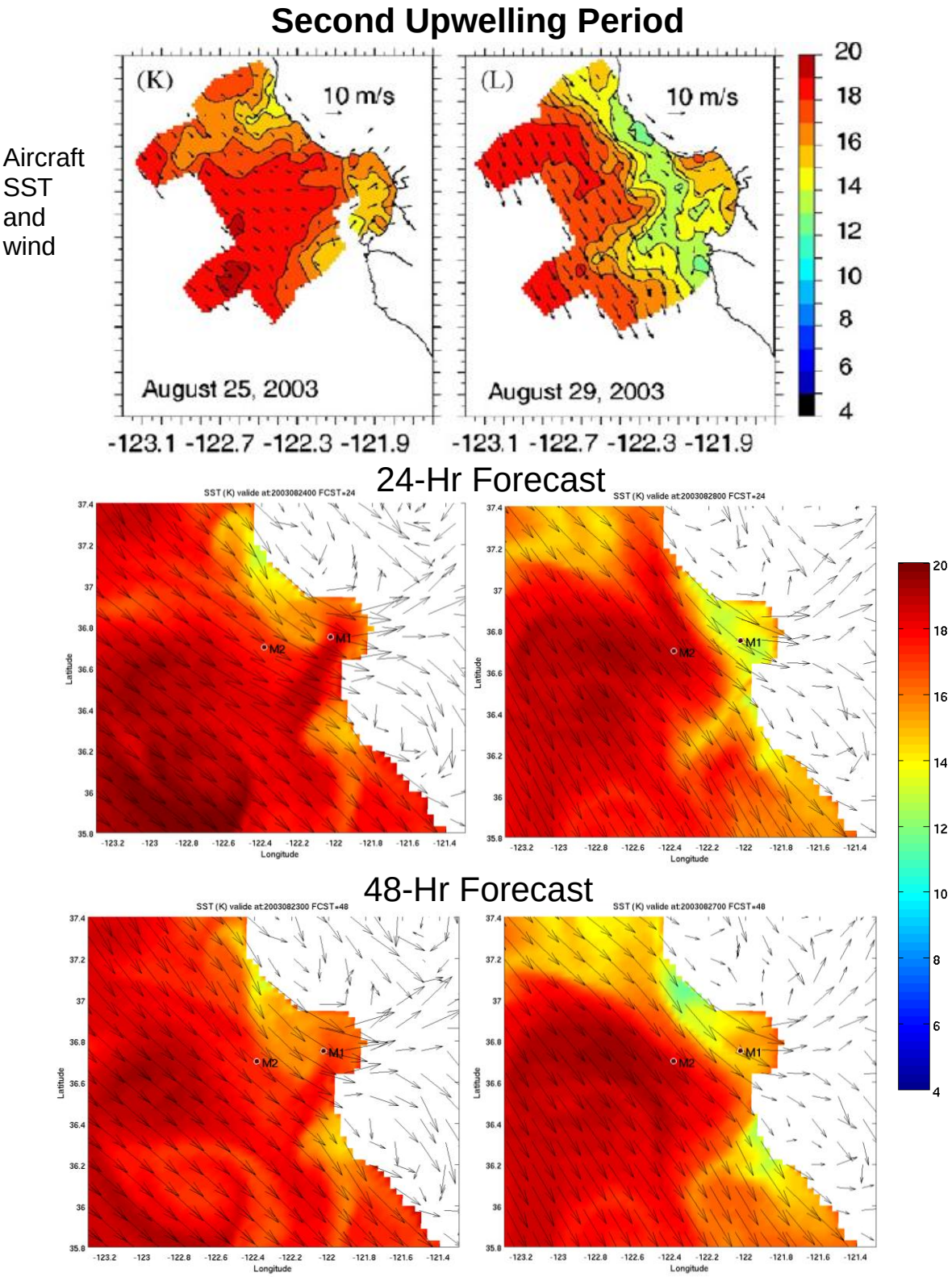

Figure 3-7: Comparison of the Control SST and aircraft observations for the second upwelling period. Vectors indicate wind magnitude and direction. The color scale represents SST (°C).

3.3.3.2 Sensitivity tests

Two sensitivity runs were conducted to investigate the effect of data assimilation and coupling. Sensitivity test one (S1) was identical to the COAMPS two-way coupled Control run discussed in Section 3.3.3.1 except there was no data assimilation. Sensitivity test two (S2) was a one-way coupled run with no ocean SST feedback to the atmosphere. The NCODA analysis SST was used in the atmospheric model, and the SST was held constant throughout the 48-hr forecast period. Figures 3-8 and 3-9 show the COAMPS 24-hr forecast SST bias at the M1 and M2 moorings. At the M1 location (inside the Monterey Bay), the SST bias from the two sensitivity runs began to increase after a two week simulation time. Both runs had a 3°C maximum warm bias toward the final week of the month-long run time. The Control run had an average cold bias throughout this period. All three model runs had cold SST biases at the M2 location just outside Monterey Bay. The two sensitivity simulations had larger mean SST biases than the Control run. The episodic spikes in the SST bias plots were associated with model errors in predicting the growth and retreat of the cold upwelling SST at the mooring location.

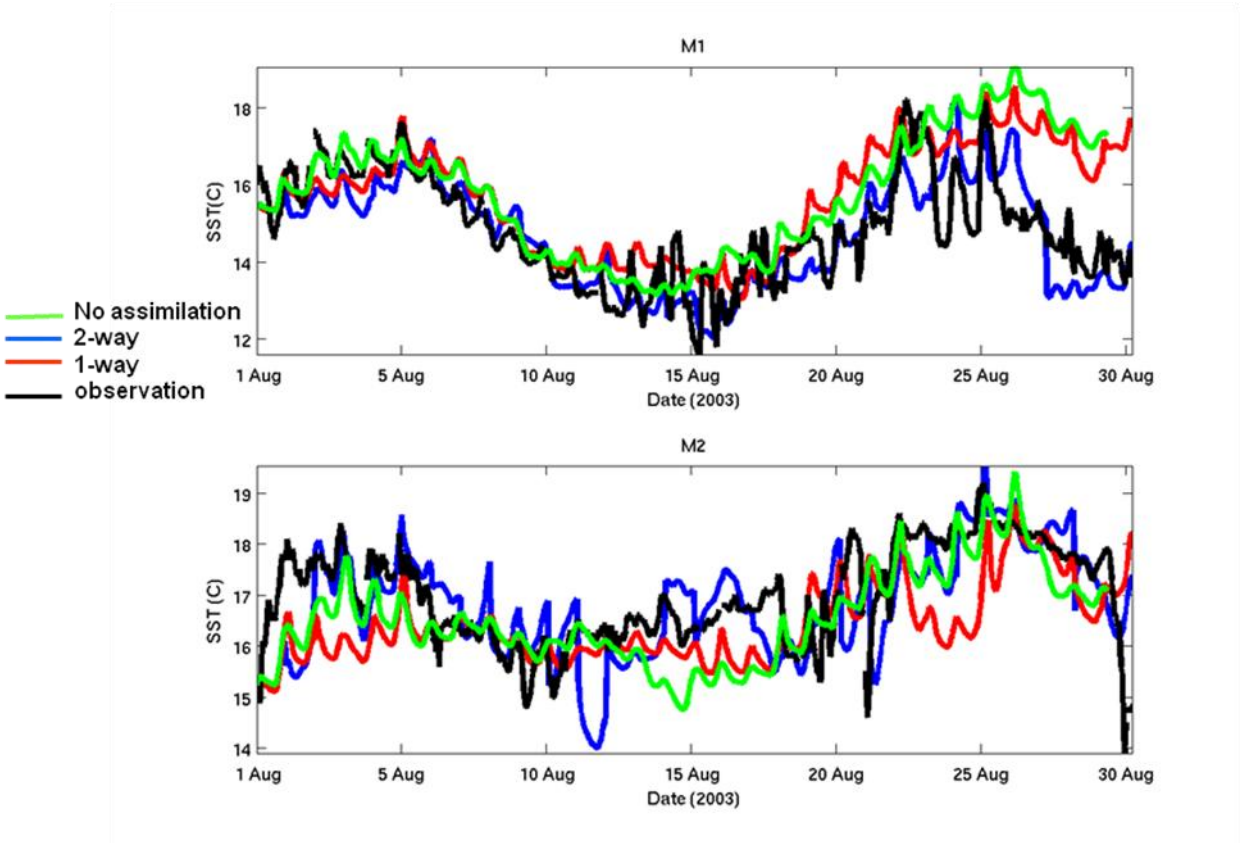

Figure 3-8: Comparisons of the model-forecast SST with the mooring observations at (a): M1 and (b): M2.

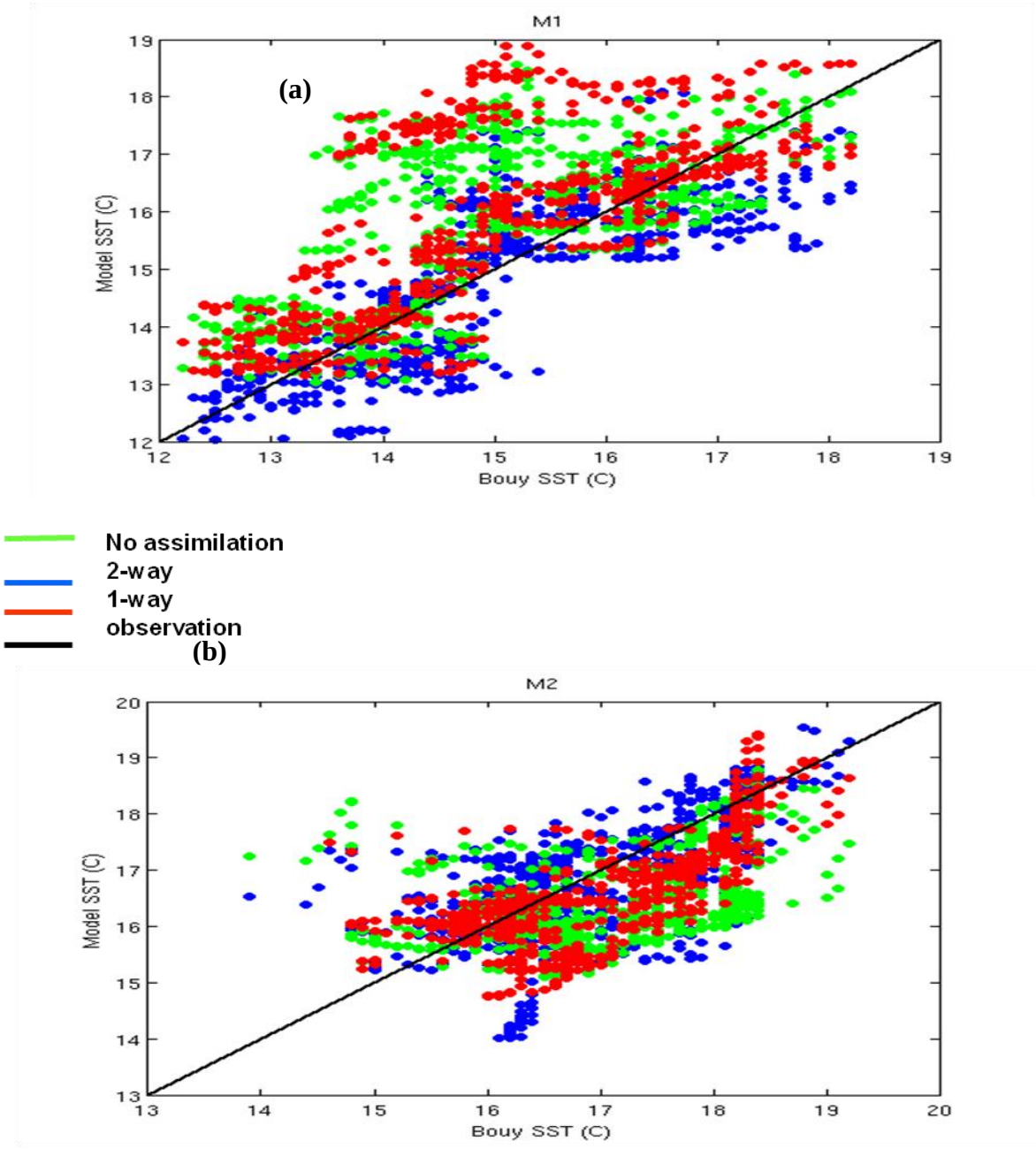

Figure 3-9: Scatter plot of the SST bias at (a): M1 and (b): M2.

While the Control's mean SST biases at the M1 and M2 moorings were less than -0.2°C, the Control's mean cold air temperature biases were an order of magnitude larger than the SST bias (Tables 3-1 and 3-2). Comparisons between the COAMPS Control air temperature, the S2 run (one-way coupled with no forecast SST feedback to the atmosphere) and observations show that two-way coupling has a negative impact on air temperature prediction (Tables 3-3 and 3-4).

Table 3-1: Statistics for comparison of M1 mooring SST to COAMPS for a month-long

simulation from 1-31 August, 2003. The time step is one hour. The number of observations (N)=704.

SST °C	**Obs Mean**	**Obs STD**	**COAMPS Mean**	**COAMPS STD**	**CC [c]**	**MB [c]**	**RMSE [c]**
Two-Way	14.83	1.40	14.71	1.39	0.81	-0.13	0.86
One-Way	14.83	1.40	15.68	1.41	0.67	0.84	1.41
No Data Assim.	14.83	1.40	15.76	1.6	0.69	0.87	1.47

Table 3-2: Statistics for comparison of M2 mooring SST to COAMPS for a month-long simulation from 1-31 August, 2003. The time step is one hour. The number of observations (N) = 708.

SST °C	**Obs Mean**	**Obs STD**	**COAMPS Mean**	**COAMPS STD**	**CC [c]**	**MB [c]**	**RMSE [c]**
Two-Way	16.97	0.96	16.80	1.05	0.63	-0.17	0.88
One-Way	16.97	0.96	16.42	0.75	0.45	-0.54	1.05
No Data Assim.	16.97	0.96	16.54	0.92	0.71	-0.43	-0.83

Table 3-3: Statistics for comparison of M1 mooring atmospheric observations to the two-way coupled COAMPS for a month-long simulation from 1-31 August, 2003. The time step is one hour. The number of observations (N)=720.

Variable	**Obs Mean**	**Obs STD**	**COAMPS Mean**	**COAMPS STD**	**CC [c]**	**MB [c]**	**RMSE [c]**
Air Temp °C	15	1.39	12.96	1.78	0.44	-2.0	2.64
Rel. humidity (%)	94.66	4.24	96.8	5.5	0.031	-2.39	4.37
Wind speed (m/s)	4.91	2.88	6.49	3.13	0.48	-1.59	3.46
Wind dir.	269.45	91.27	289.36	31.38	0.34	-19.9	87.9

Table 3-4: Statistics for comparison of M2 mooring atmospheric observations to the two-way coupled COAMPS for a month-long simulation from 1-31 August, 2003. The time step is one hour. The number of observations (N)=720.

Variable	Obs Mean	Obs STD	COAMPS Mean	COAMPS STD	CC [c]	MB [c]	RMSE [c]
Air Temp °C	16.35	0.89	14.0	1.53	0.29	-2.63	3.07
Rel. humidity (%)	90.82	3.34	95.26	5.8	0.073	-4.46	8.21
Wind speed (m/s)	6.29	2.74	6.66	3.0	0.68	-0.37	2.33
Wind dir.	287.35	79.37	306.29	37.92	0.526	-15.33	66.08

It is clear from Fig. 3-10 that, although COAMPS tended to raise the air temperature at the data assimilation times (00 and 12 UTC), it actually reduced it during the first relaxation/upwelling event (3-15 August). The air temperature prediction was influenced by the complex interactions between radiation, cloud, turbulent mixing in the atmospheric boundary layer, advection, and air-sea sensible heat flux exchange. Since the relative humidity, wind direction, and wind speed biases were not large (Fig. 3-10, 3-11), the cloud cover and air-sea temperature differences likely contributed more to the Control cold air temperature bias. Comparison of the Control integrated cloud mixing ratio with S2 reveals that the Control run had more clouds than S2 at the mooring locations (Fig. 3-12). In the first two weeks, the Control SST at M2 had a warm bias compared to observations. The warmer SST forced a larger sensible and latent heat flux transfer from the ocean to the atmosphere, creating favorable conditions for stratus cloud formation. However, the exact cause of this cold air temperature bias over the ocean requires further investigation into the temperature budget analysis in the atmospheric boundary layer.

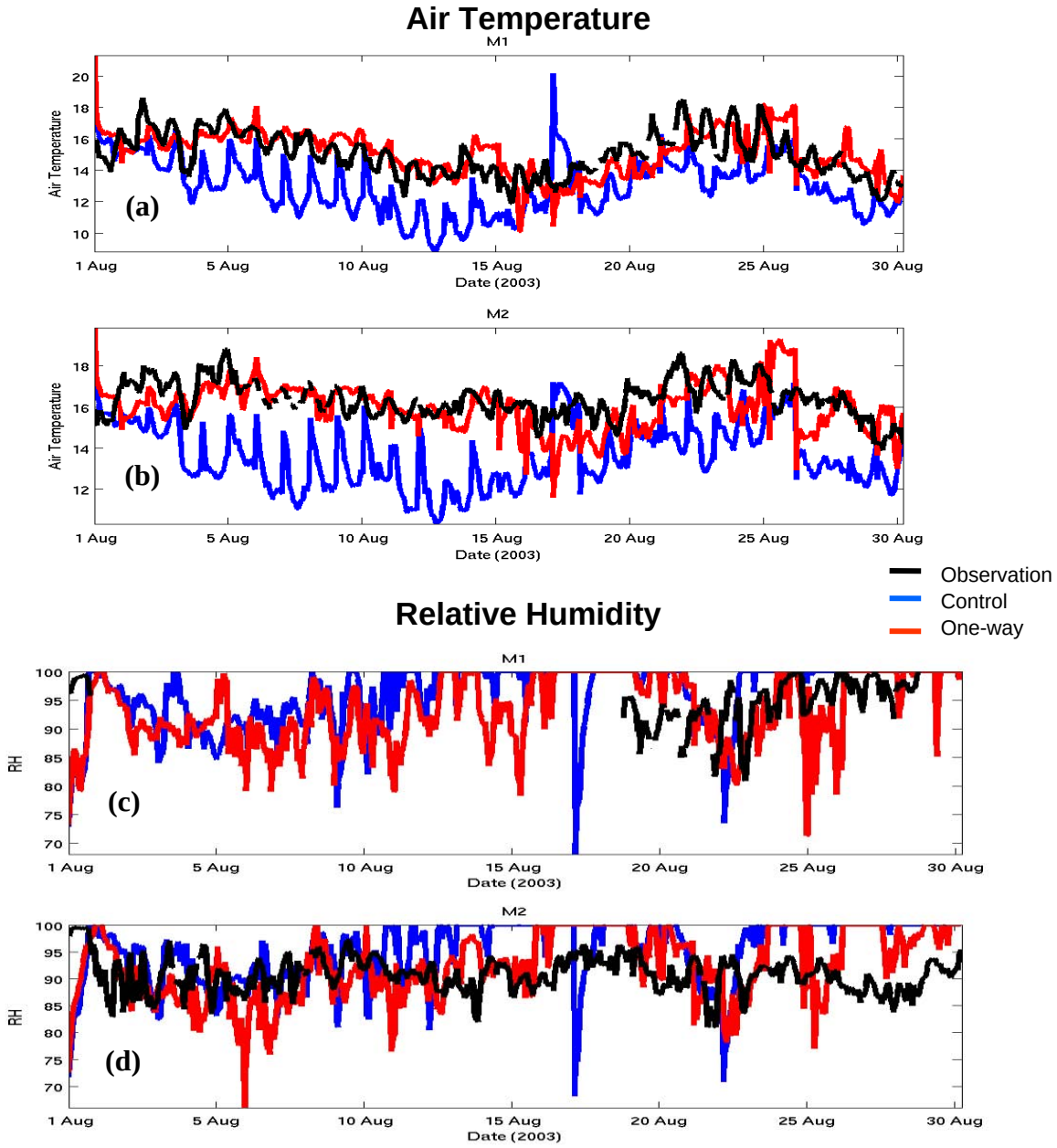

Figure 3-10: Comparisons of the month-long model-forecast for (a): M1 and (b): M2 2 m air temperature (°C) and (c): M1 and (d): M2 relative humidity (%). Statistics are found in Table 3-2. The Control is a two-way coupled COAMPS run.

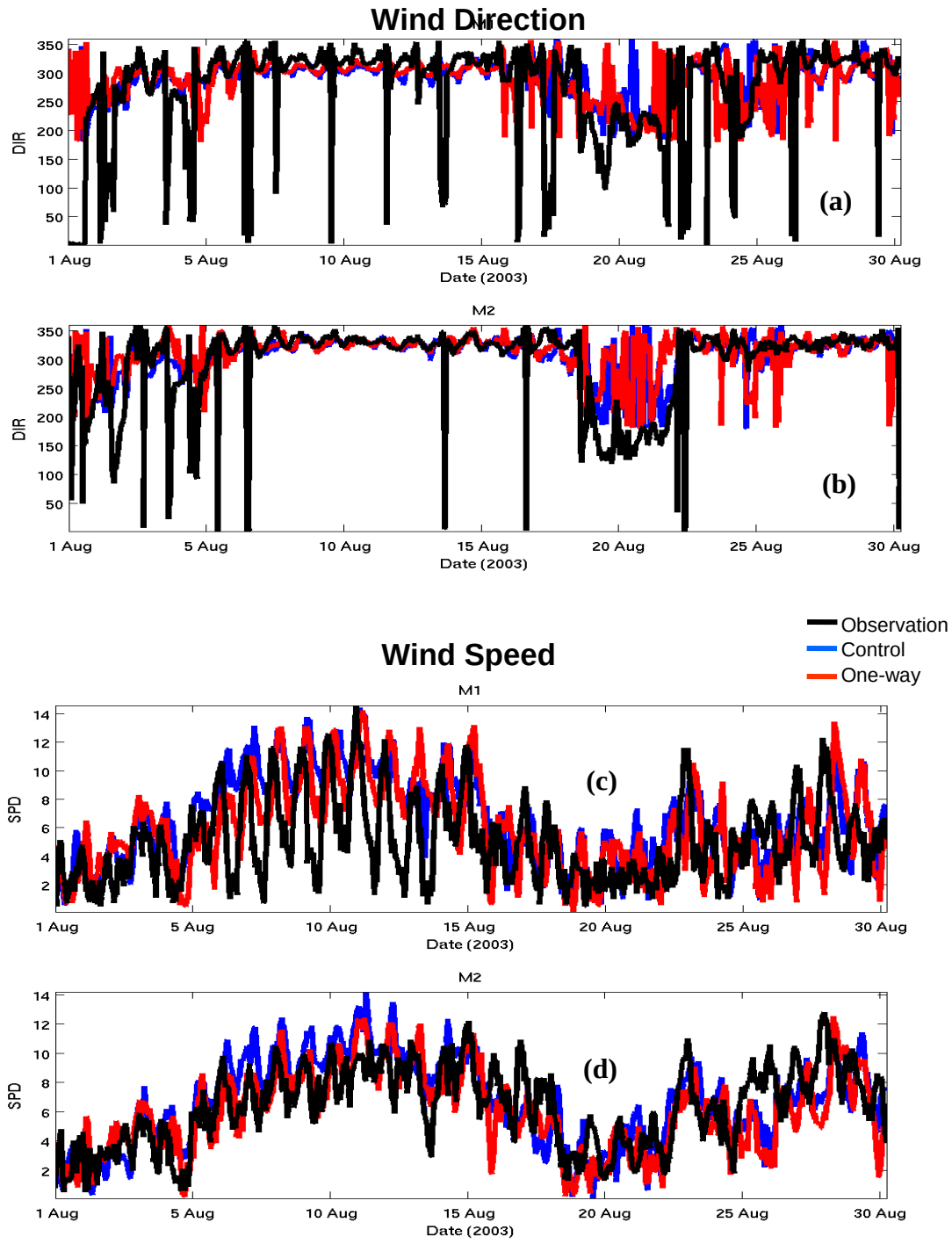

Figure 3-11: Comparisons of the month-long model-forecast for (a): M1 and (b): M2 10 m wind and direction (degree) and (c): M1 and (d): M2 speed (m/s) bias. Statistics are found in Table 3-2. The Control is a two-way coupled COAMPS run.

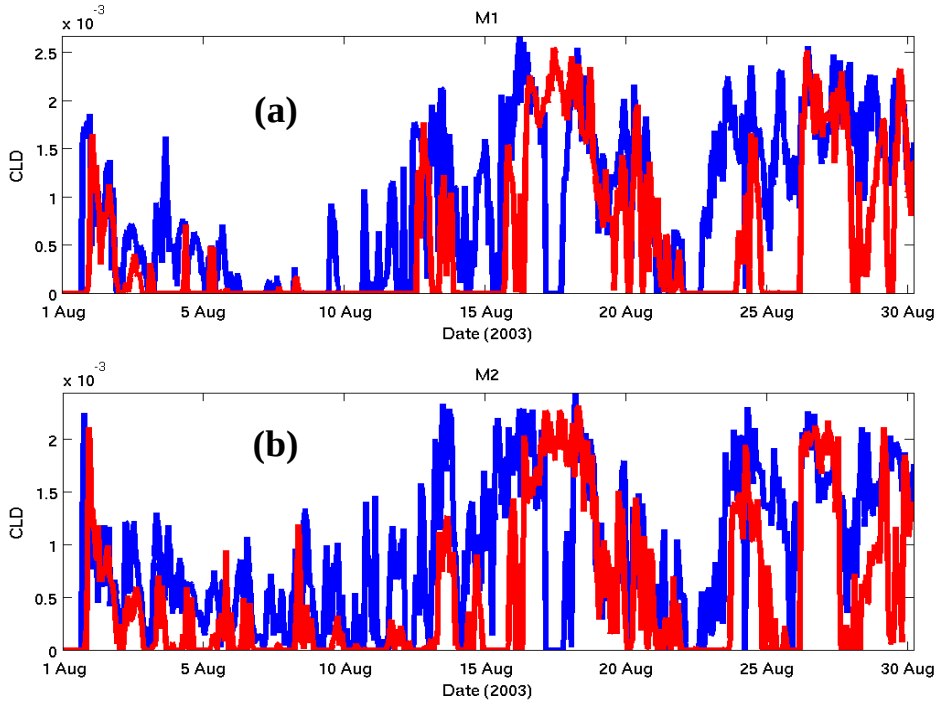

Figure 3-12: The integrated cloud mixing ratio (kg/m^3) comparisons between the Control (two-way; blue) and S2 (one-way; red) runs for (a): M1 mooring and (b): M2 mooring.

3.4 Test Case 4: Kuroshio Extension System Study (KESS)

The Kuroshio Extension and its recirculation are an integral part of the Earth's climate system, particularly in the Pacific Basin. It has a significant influence on the west coast of the U.S and on Pacific storms, both in intensity and direction. Therefore, the Kuroshio Extension System Study (KESS), conducted from late 2003 through early 2007, was established to better understand the dynamics and thermodynamics that dominate the Kuroshio Extension and its recirculation gyres. The KESS observational instrumentation was designed to observe the Kuroshio Extension in a more complete way, such as mapping the jet as it evolved (using Current-Pressure-Inverted-Echo-Sounders (C-PIES) with current meters) and quantifying the cross-frontal fluxes (with moored profilers). Profiling floats monitored the upper ocean structure around the extension and gyres. NOAA established a long term mooring that measured surface meteorology and upper ocean temperature, salinity and currents. Profiling floats monitored the upper ocean structure around the extension and gyres. Test Case 4 uses some of these observations to validate COAMPS in this region.

3.4.1 Purpose

The Kuroshio Extension system is an opportune area to test hypotheses formulated from previous observational and modeling studies because of its distinct stratification, bathymetry, strong fronts and thermohaline circulation. The primary goal of Test Case 4 was to examine air-

sea fluxes at a strong SST front, focusing more closely on boundary layer processes and air-sea interaction in synoptic storms, particularly on weekly to intra-seasonal time scales.

3.4.2 Test Case Characteristics

3.4.2.1 Test Area and Observations

The Kuroshio Extension is the region of the North Pacific Ocean occupied by the Kuroshio Current after it separates from the coast of Japan near 35°N and becomes a warm, eastward-flowing, free inertial jet. Joining this region from the north, the cold waters of the Oyashio Current flow south along the east coast of Japan and depart the coast to flow as another eastward jet near 40°N. The Kuroshio Extension is the major crossroads for the exchange of heat and fresh water between the subtropical and subpolar gyres in the North Pacific and is one of the most intense air–sea heat exchange areas on the globe. The average heat flux from ocean to atmosphere (Da Silva et al., 1994) is among the highest in the world. The Kuroshio Extension region is one of especially high eddy kinetic energy (*e.g.*, Wyrtki et al. 1976, Qiu 2002). A recirculation gyre exists to the south of the Kuroshio Extension and another possibly to the north (Talley, 1997). Figure 4-1 shows the flow pattern of the Kuroshio Current and Kuroshio Extension flowing along the west and east coasts of Japan, respectively.

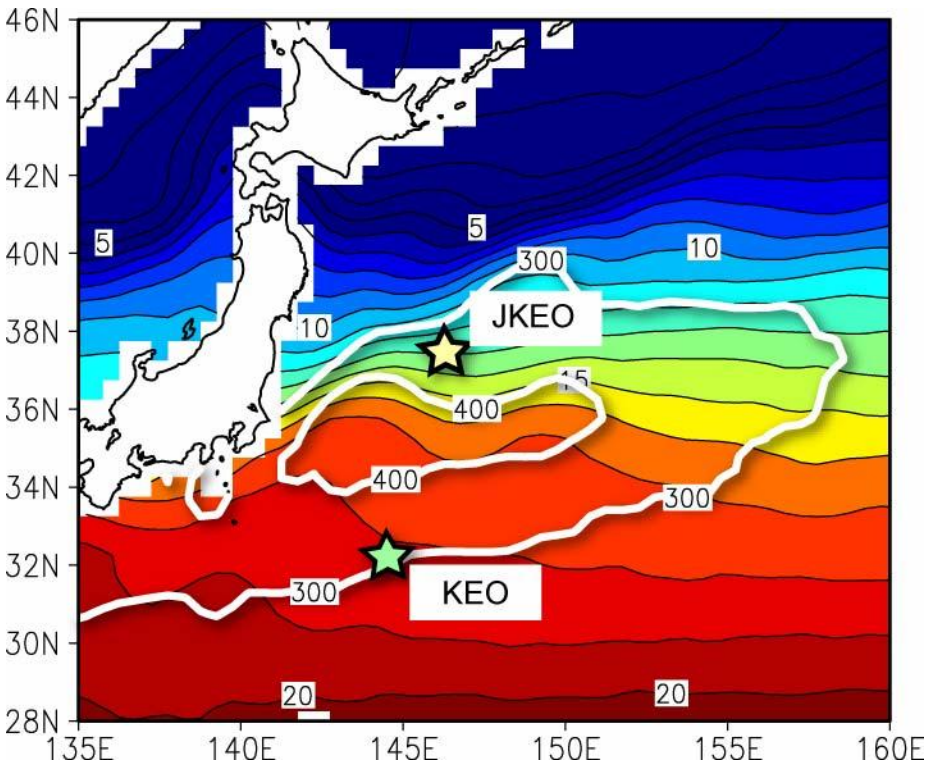

Figure 4-1: The Kuroshio Extension, showing locations of the JAMSTEC (JKEO) and KEO buoys. Black contour and color represent SST (°C). White contour is turbulent heat flux (W/m^2); (Cronin et al., 2008).

Observational data collected during the KESS included 48 Argo floats, 45 C-PIES echo sounders with ADCP, seven moorings with ADCP from 0-250 m, T/S (plus ADCP) profilers from 250 m to 1500 m, ship radiosondes, a CTD (conductivity, temperature and depth instrument), and four deep current meters from 1500-5000 m. Wind data was measured by satellite using the QuikSCAT scatterometer. A National Oceanographic and Atmospheric Administration (NOAA) surface buoy gathered data at 144.6 °E, 32.4°N, as well as a Japan Agency for Marine-Earth Science and Technology (JAMSTEC) buoy (146.6°E, 37.9°N) measuring surface meteorology and upper ocean T, S, dynamic height, and currents. The Tropical Rainfall Measuring Mission *(*TRMM*)* satellite gathered wind, water vapor, liquid cloud water, and precipitation rate. Sea surface height (SSH) data came from the TOPEX/Poseidon-Jason 1 satellites. The testing windows were from 30 January to 7 February, 2005 and from 15 June to 17 July, 2006. Figure 4-2 illustrates the test area and observational instrumentation deployed.

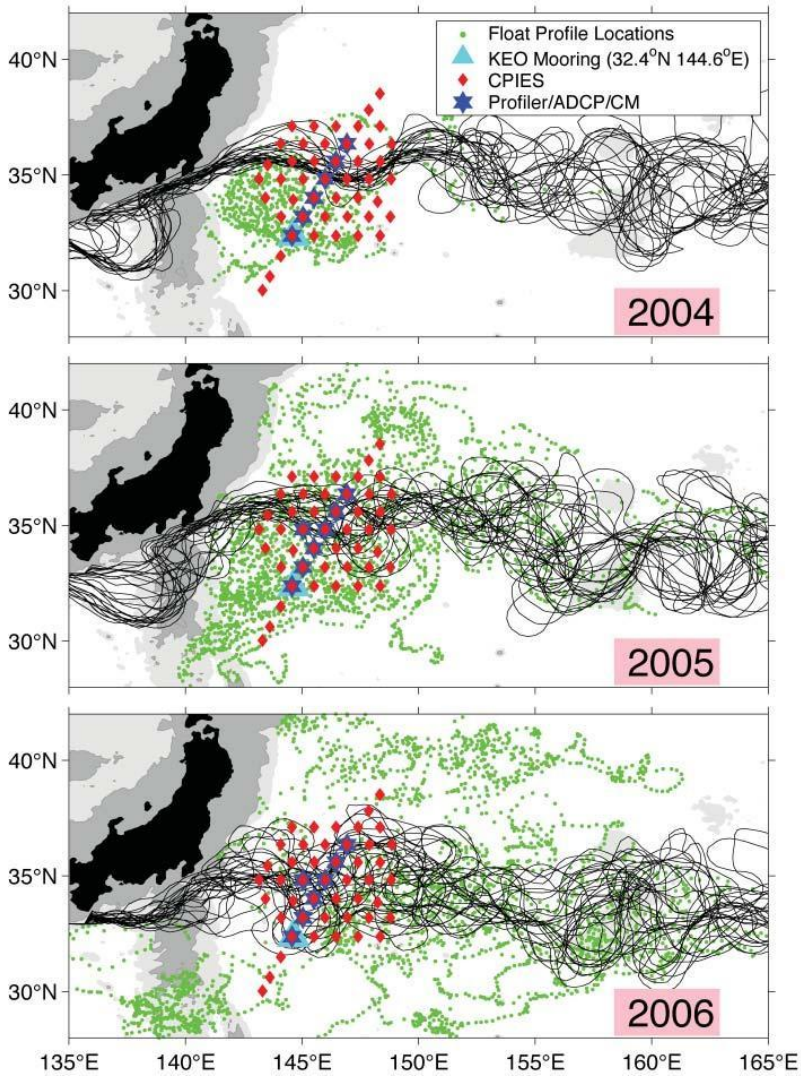

Figure 4-2: Overview of observations in the KESS region. The black curves show the biweekly 1.7 m contour of SSH, defining the path of the Kuroshio Extension. The green dots are ARGO float locations. Red diamonds indicate locations of current-inverted

echosounders (C-PIES). Blue stars represent ADCP, moored profiler and deep current meter locations. The light blue triangle shows the location of the KEO buoy. From Donohue et al, 2008.

3.4.2.2 Model Setup

COAMPS covers the KESS region over an area of about 5400 km x 2700 km using a Lambert conformal projection centered on 142°E, 35°N, extending from the Asian continent to the date line and from about 25°N to 45°N. The model uses three nested grids: a 27 km coarse grid (199 x 100), a 9 km resolution grid spanning from about 140°E to 155°E and 30°N to 42°N (199 x 169) with a resolution of 9 km covering the NCOM grid area, and a 3 km resolution grid (283 x 277) extending from about 142°E to 151°E and 32°N to 38.5°N. The atmospheric model uses 40 vertical levels. The time step is 80 sec in the coarse grid model. Initial and boundary conditions come from NOGAPS.

The first NCOM nest covers the area from 140°E to 155°E and 30°N to 42°N with a horizontal resolution of 1/16° (5.7 km (at 35°N) x 7 km) and 50 vertical levels (15 *z*-levels and 35 sigma levels). It has a 241 x 193 x 50 grid. The second nest is a 1/48° grid (1.89 km (at 35°N) x 2.3 km) covering a region from 142°E to 150°E and 32°N to 38°N with the same vertical levels. It has a 389 x 293 x 50 grid. Tidal potential for the first eight diurnal and semi-diurnal tidal constituents (K1, O1, P1, Q1, K2, M2, N2 and S2) are included in the forcing. The COAMPS model is initialized and its boundaries forced by output from the East Asian Seas NCOM Nowcast/Forecast System (Riedlinger et al., 2006). The EAS NCOM has the same vertical and horizontal resolution, covering the Western Pacific from 17°S to 52°N from the Asian continent to 158°E and includes the same tidal components. The boundary conditions for the EAS NCOM come from the 1/8° Global NCOM and the surface forcing is from NOGAPS. Both surface forcing and boundary conditions are provided every three hours. Figure 4-3 shows the various nests for Test Case 4.

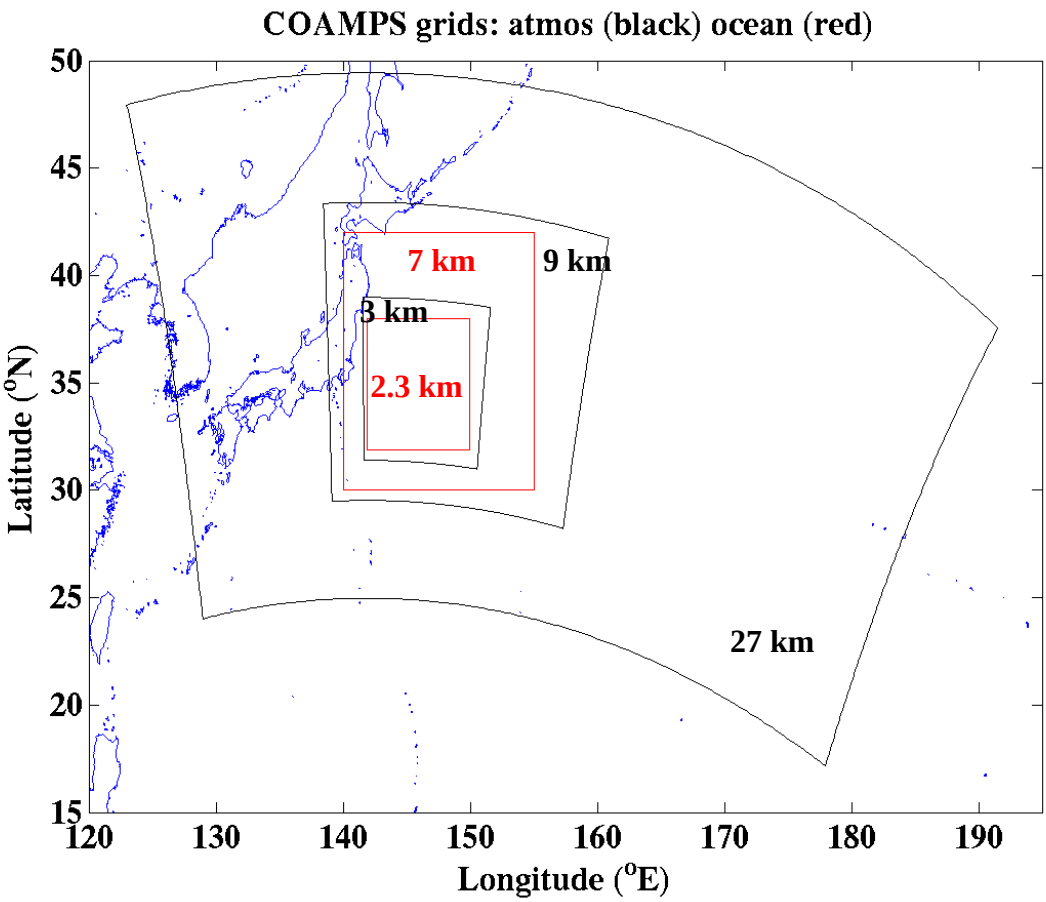

Figure 4-3: Area covered by the COAMPS triply nested atmospheric grid (shown in blue lines) of 27 km, 9 km and 3 km and two-nested ocean grids (red lines) of 7 km and 2.3 km for the KESS test case.

3.4.3 Results

Test Case 4 simulations were run as both fully coupled and uncoupled. In the uncoupled runs, the atmospheric model used SST from NCODA rather than from NCOM. In both cases, the system ran in an operational forecast mode with 12-hour updates. Since ocean conditions were updated twice daily, the uncoupled run actually experienced changes in the ocean surface temperatures. Because the NCODA temperature updates include air-sea interaction and ocean dynamics, the atmosphere in the uncoupled run actually experiences a feedback, but with a longer time lag and in a less consistent way than the fully coupled run that uses a 12-min coupling interval.

3.4.3.1 Cold air outbreak over the Kuroshio

The warm subtropical waters south of the Kuroshio Extension, around 35°N, are an area where some of the largest sensible and latent heat fluxes can be observed. The annual sensible heat flux mean is ~50 W/m^2 and latent heat flux is ~150 W/m^2. However, during winter when cold

air outbreaks are rapidly advected from the Asian continent, the sum of those heat flux components can exceed 1000 W/m^2. In this test we investigate a cold air outbreak event that occurred from 30 January through 3 February, 2005. Figure 4-4 illustrates the event through measurements of SST, air temperature, wind velocity and speed at the NOAA Kuroshio Extension Observatory (KEO) buoy (144.6°E, 32.4°N). From 30 January to 3 February, winds were west-northwesterly at about 10 m/s, increasing up to 20 m/s on 1 February. The air temperature dropped by more than 8°C, resulting in air-sea temperature differences of the same magnitude. Figure 4-5 shows the KEO buoy's ocean temperature measurements at the surface and at four subsequent depths. Note that the surface temperature (1 m) and the 200 m temperature are identical after 1 February, indicating a mixed layer of 200 m or deeper. The temperatures at 300 m are about 1-1.5°C cooler than at 200 m, an indication of a mixed layer depth somewhere between 200 m and 300 m.

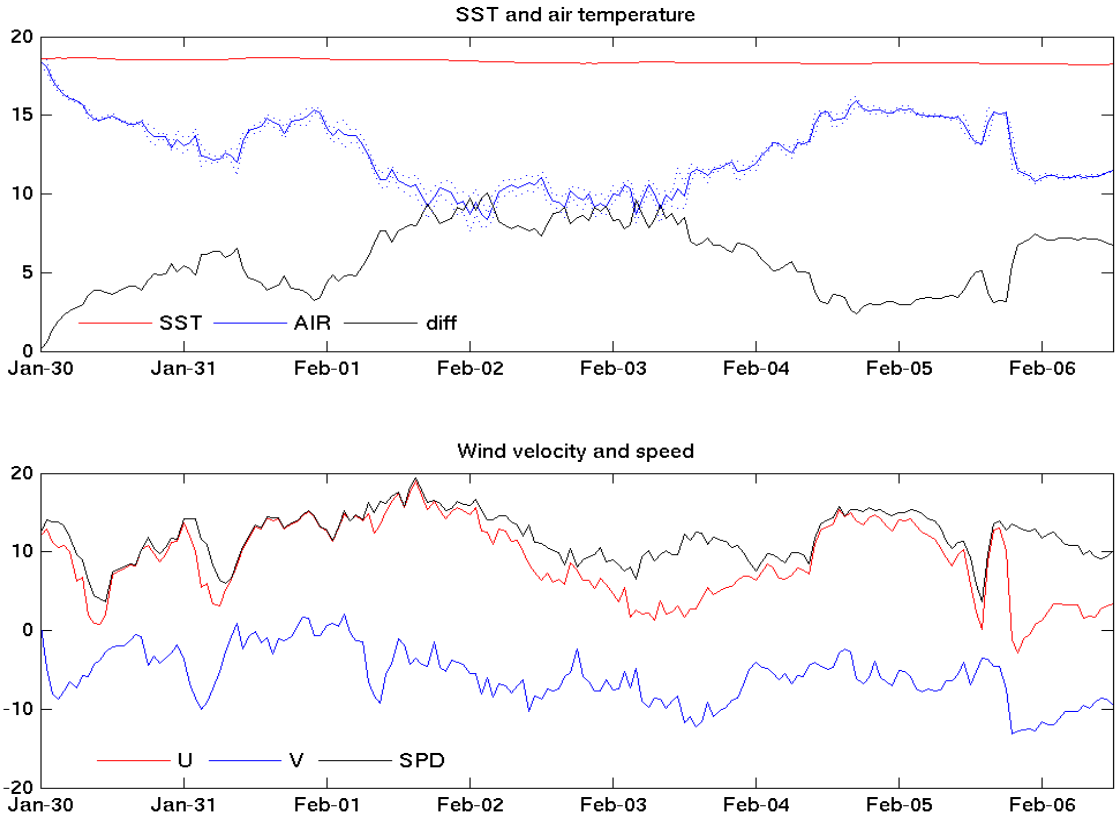

Figure 4-4: Observed SST and air temperature (top) and wind velocity components and speed (bottom) at the KEO buoy during the cold air outbreak event. The blue dotted lines around air temperature (top) show the range of one STD calculated from the hourly mean and the original 10 min air temperature observations.

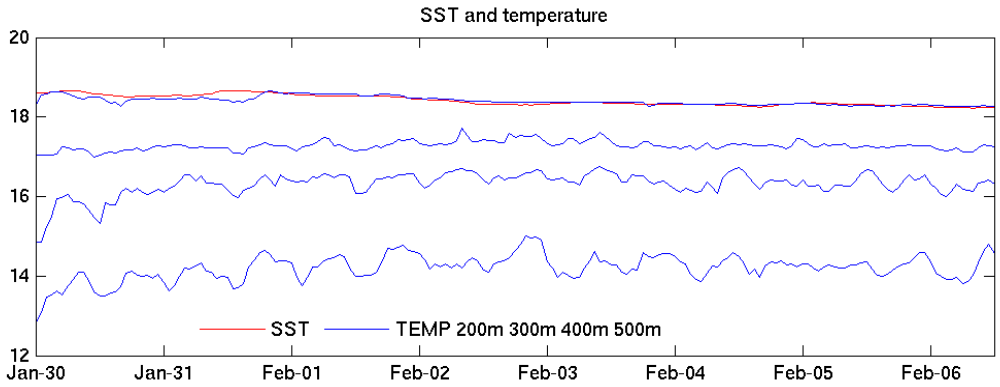

Figure 4-5: Observed ocean temperature from the KEO buoy at the surface (red line) and at 200 m, 300 m, 400 m and 500 m (blue lines).

The initial surface temperature and currents in the ocean are shown in Fig. 4-6 for both NCOM grids. South of the main axis of the Kuroshio, near 35°N, a cyclonic recirculation gyre is present. Its core is at 144.5°E and 33.5°N, which is close to the KEO buoy location. The recirculation gyre extends deeper than 1000 m and has significantly cooler temperatures, both at the surface and at depth, than the surrounding waters in the warm pool region.

Figure 4-7 shows the 10 m wind vectors and wind speed for all three atmospheric grids after the initial analysis based on NOGAPS. Since this initial condition was from a much coarser grid, the state was much smoother than subsequent forecasts. The KEO buoy is marked in the 9 km grid (top right). COAMPS simulated the cold air outbreak event from 30 January to 6 February, 2005 using 12-hourly update cycles. Figure 4-8 shows the surface currents and SST minus the 2 m air temperature for 2 February, 2005 over the entire model domain covered by the 27 km grid and the 10 m wind speed on the 9 km grid.

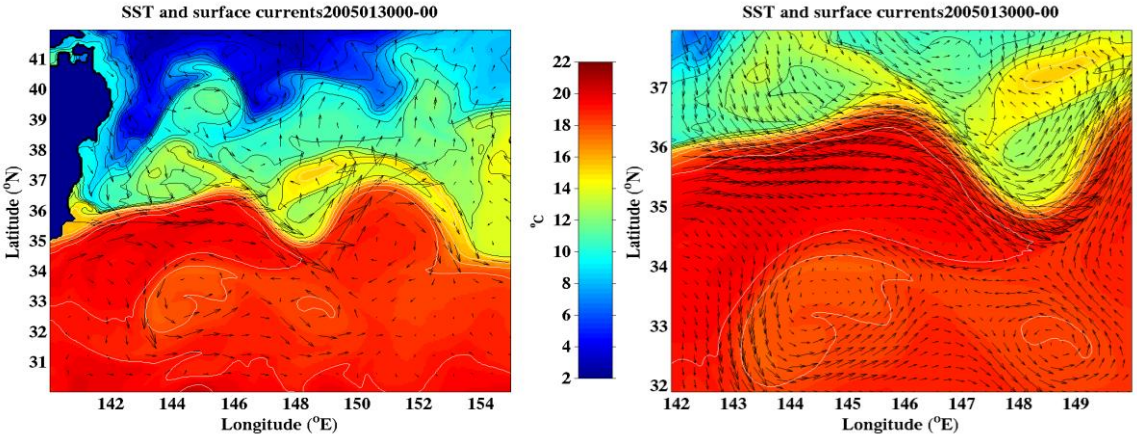

Figure 4-6: Initial currents and SST in the ocean model on the 9 km (left) and 3 km (right) grids.

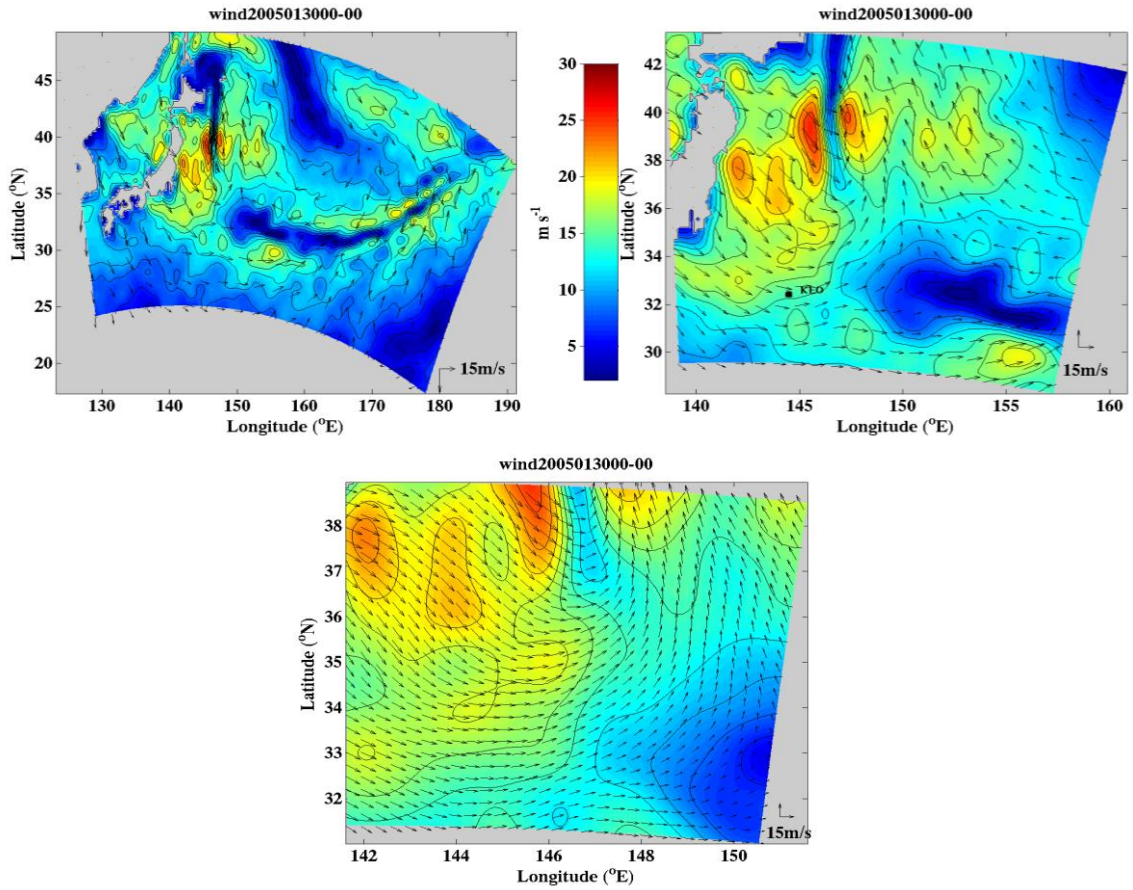

Figure 4-7: Initial winds after the atmospheric analysis on 30 January on each of the three atmospheric grids. Top left: 27 km; Top right: 9 km; Bottom: 3 km.

Due to the cold air outbreak, COAMPS revealed a large drop in air temperature over the Sea of Japan and the Kuroshio region, as well as a significant air-sea temperature difference (Fig. 4-8, left). The model predicted cold air propagation from the northwest with a maximum wind speed of 15-20 m/s, which agreed with the KEO buoy observations (Fig. 4-8, left). The wind field, shown on the 9 km grid (Fig. 4-8, right), had sharp wind shear regions associated with the passage of fronts.

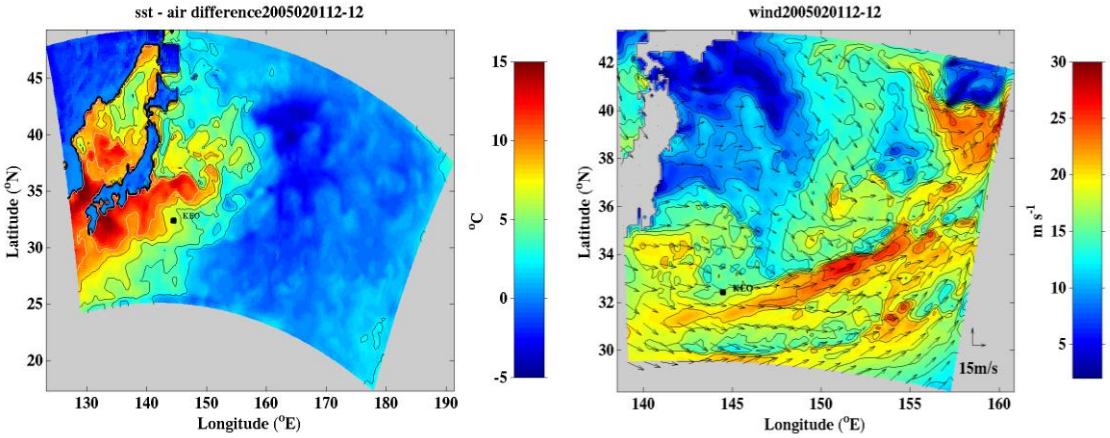

Figure 4-8: COAMPS atmospheric model surface fields on 2 February, 2005. (Left): SST minus 2 m air temperature on the coarse model grid (27 km) showing large ocean atmosphere temperature differences over the Sea of Japan and over the subtropical gyre south of the Kuroshio Current. (Right): Wind velocity and wind speed at 10 m shown on nest 2 (9 km grid). The color represents the total wind speed.

During the cold air outbreak, the sum of the model latent and sensible heat fluxes exceeded 1000 W/m^2 in the warm pool region that encompasses the KEO buoy location (Fig. 4-9, left). This is similar to observations of the Gulf Stream region (Xue et al., 1995), where air-sea temperature differences exceeding 20˚C have been observed (Grossman and Betts, 1990). SST contours on the atmospheric grid are shown in Fig. 4-9 (left) and also in the bottom figure in the color shading of the ocean model grid. It is clearly evident that high heat fluxes were confined to the warm subtropical waters south of the Kuroshio front. Also note the cyclonic cold core eddy visible at the KEO buoy location (Fig. 4-9, right). This recirculation gyre was present during the entire model simulation.

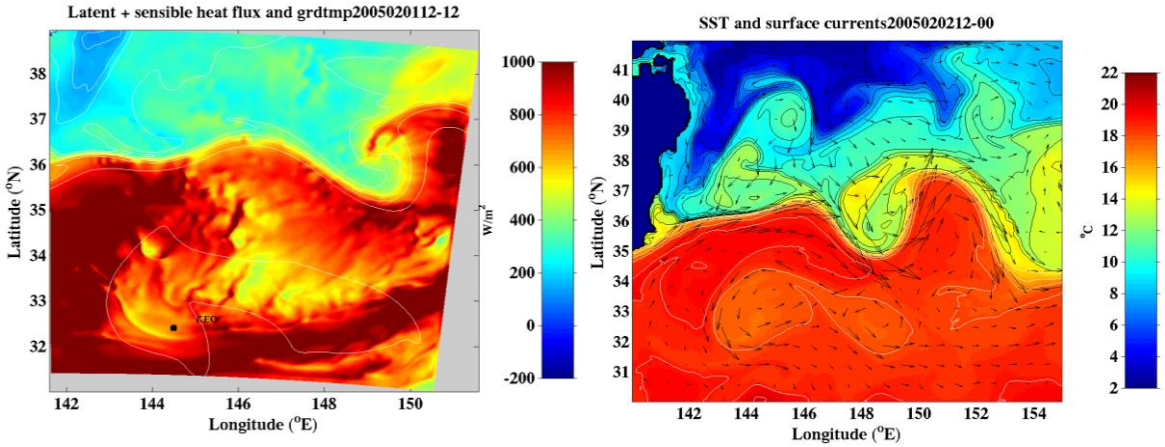

Figure 4-9: (Left): The sum of latent and sensible heat flux (W/m^2) from COAMPS atmospheric 3 km grid on 2 February, 2005 00UT. (Right): SST and current vectors from the 1/16^o grid NCOM model.

3.4.3.2 COAMPS Validation using KEO in Winter

COAMPS was run coupled to NCOM (COAMPS) as described in Section 3.4.2.2 and as an atmosphere-only model run from 30 January through 6 February, 2005. During the simulation, the wind of the KEO location was generally westerly with wind speeds in excess of 10 m/s. Air temperatures began at 18°C and decreased to a low of 8°C on 2 February.

A comparison was done between the KEO buoy observation and the closest grid point in atmospheric models. The COAMPS zonal wind speed was somewhat higher than observed, with a positive bias of about 3 m/s and a correlation coefficient of 0.75 for the fully coupled run and 0.70 for the uncoupled run (Fig. 4-10). Correlations for the meridional component were slightly higher, 0.77 and 0.73 for the coupled and uncoupled runs, respectively, with mean biases of 2.33 m/s and 1.97 m/s (Table 4-1). In general, the air temperature agreed well with the KEO observations (Fig. 4-11). The coupled run had a -0.27°C bias and the uncoupled run a -0.11°C bias, both with correlations of around 0.85. The simulations did not reach the extreme lows as observed, but stayed above 10°C. The COAMPS relative humidity (Fig. 4-11) was underestimated by about 15%. For the uncoupled model the bias was 16%, and the correlation between the KEO buoy humidity with both the coupled simulation (0.21) and the uncoupled simulation (-0.03) was low. There was a slight improvement for nest 3 compared to nest 2 for the model/observation correlations of zonal winds and air temperature and less bias in humidity. For model nest 3, the bias in relative humidity was lower than for the two coarse nests and the extreme low air temperatures were closer to observations.

Fig. 4-12 shows the total wind speed for the 3 km nest compared to buoy observations. The coupled simulation had better correlations than the uncoupled grid and slightly less bias. Statistical values for the atmospheric quantities are given in Table 4-1.

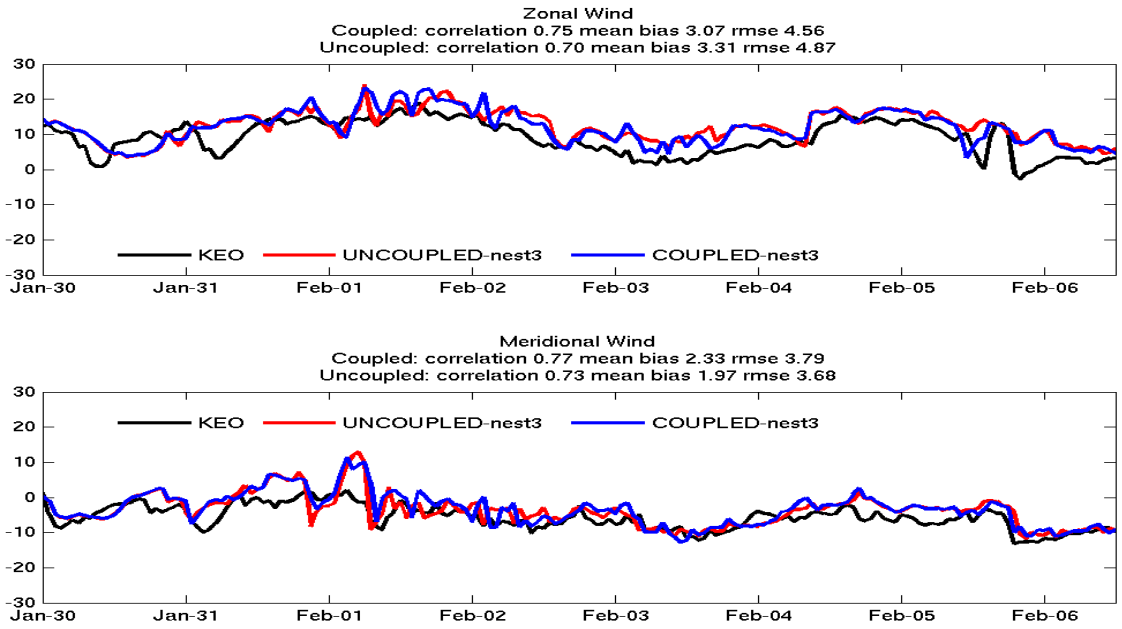

Figure 4-10: Zonal and meridional winds for the 3 km COAMPS atmospheric nest 3 grid

for the uncoupled model (red line), the fully coupled model (blue line), and KEO buoy observations (black).

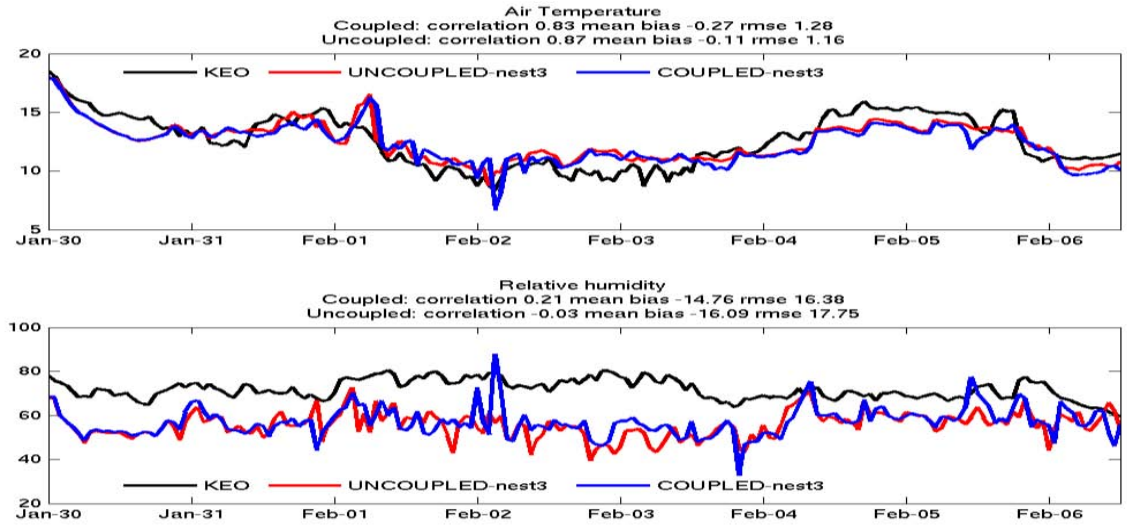

Figure 4-11: Two meter air temperature (top) and relative humidity (bottom) on the 3 km atmospheric grid for the uncoupled model (red line), the fully coupled model (blue line), and KEO buoy observations (black).

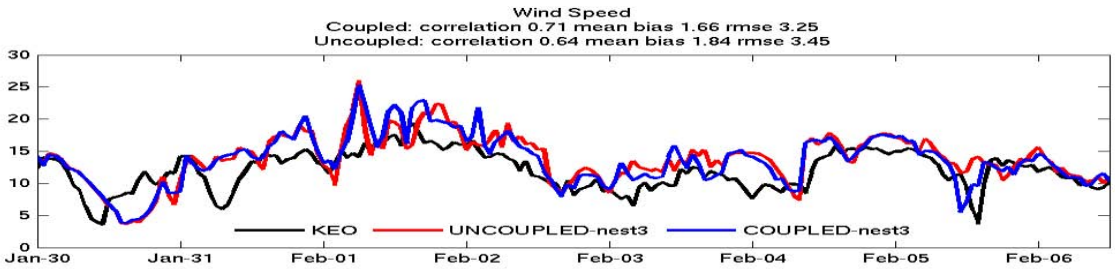

Figure 4-12: Comparison of 10 m wind speed KEO observations with the uncoupled and coupled runs for the 3 km resolution atmospheric nest.

Table 4-1: Statistics for atmospheric quantities from the 3 km nest COAMPS uncoupled [u] and coupled [c] runs for 30 January through 6 February, 2005 compared to the KEO buoy.

	KEO Buoy Mean	Mean [u]	Mean [c]	CC [u]	CC [c]	MB [u]	MB [c]	RMSE [u]	RMSE [c]	KEO RMSE
Air Temp ^{o}C	12.60	12.50	12.33	0.87	0.83	-0.11	-0.27	1.16	1.28	1.34
Rel. Hum. %	71.73	55.86	56.97	-0.03	0.21	-16.09	-14.76	17.75	16.38	19.53
Zonal Wind m/s	8.95	12.26	12.03	0.70	0.75	3.31	3.07	4.87	4.56	5.29
Merid. Wind m/s	-5.75	-3.78	-3.43	0.73	0.77	1.97	2.33	3.79	3.84	3.84

	KEO Buoy Mean	Mean [u]	Mean [c]	CC [u]	CC [c]	MB [u]	MB [c]	RMSE [u]	RMSE [c]	KEO RMSE
Wind Spd m/s	11.93	13.77	13.59	0.64	0.71	1.84	1.66	3.45	3.25	3.54

COAMPS had a fairly large cold bias in the ocean. For SST, it was about 0.5°C. Since the mixed layer is about 200 m deep, the same bias was found until that depth. At 300 m the observations were about 1°C warmer than the model and at 400 m, the difference increased to over 2°C (Fig. 4-13).

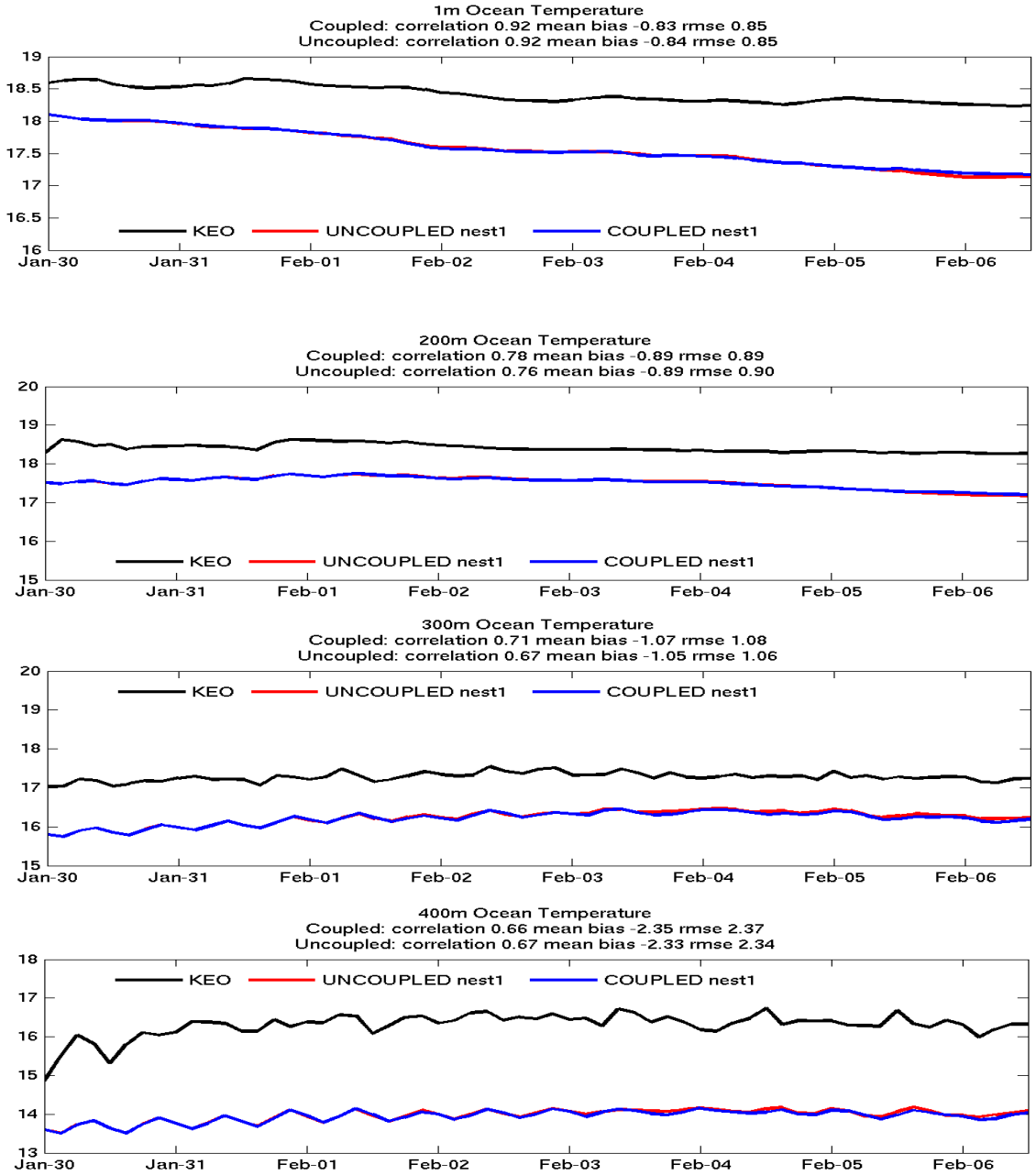

Figure 4-13: SST (from top to bottom): 1 m, 200 m, 300 m, and 400 m temperature from KEO (black line) and COAMPS ocean nest 1 (27 km) (blue line). The uncoupled run is

shown in red.

3.4.3.3 COAMPS and QuikSCAT Comparisons in Winter

COAMPS uses satellite observations in its data assimilation but they do not come from the QuikSCAT scatterometer. QuikSCAT provides an independent data set against which to compare our simulations. It provides surface winds with a spatial resolution of 25 x 25 km. Rain may influence the accuracy of the measurements, but the following results show measurements without masking out rainy areas. There is remarkably good agreement between COAMPS and QuikSCAT. The KESS area was covered by three descending satellite passes beginning with the first about 6 UTC near the date line, a second around 8 UTC, near 155°E, and a third around 10 UTC (near 130°E). Since Japan is nine hours ahead of Greenwich, these measurements were taken in the late afternoon local time. Similarly, three ascending passes provided coverage over the same longitudes at 18 UTC, 20 UTC, and 22 UTC.

Fig. 4-14 shows the wind field near the beginning of the simulation. The strong north-south front aligned poleward of 35°N and starting near 160°E, was well simulated, as were other high wind regions southeast of Hokkaido and near the dateline at 40°N. The fronts were rapidly developing, followed by cyclogenesis, which was also captured by the model.

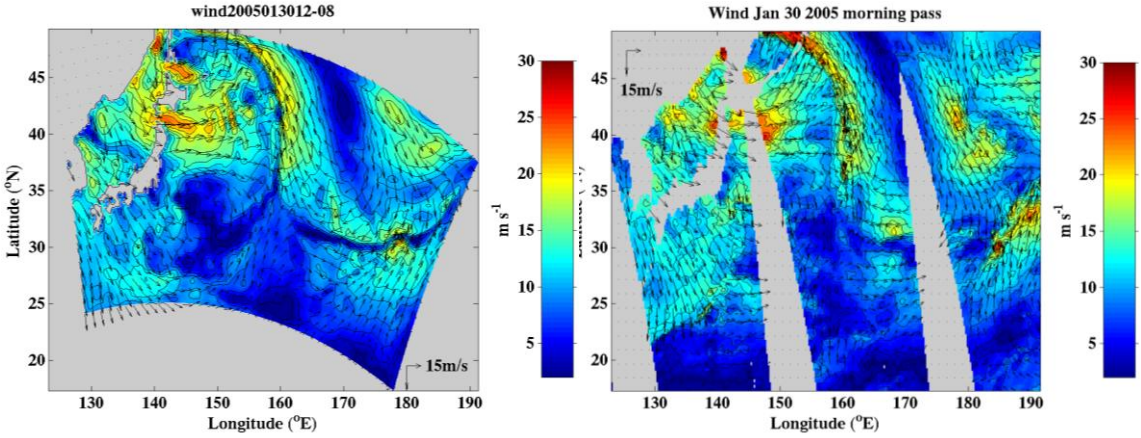

Figure 4-14: (Left): Winds at 10 m from 27 km COAMPS for the 30 January, 2000 UTC forecast. The forecast was initialized at 1200 UTC. (Right): QuikSCAT winds from ascending pass.

The main cold air outbreak over the KESS region is seen in Fig. 4-15. Compared to QuikSCAT, the COAMPS winds were too weak in areas where the wind speeds were the highest, but the wind pattern was simulated very well in general.

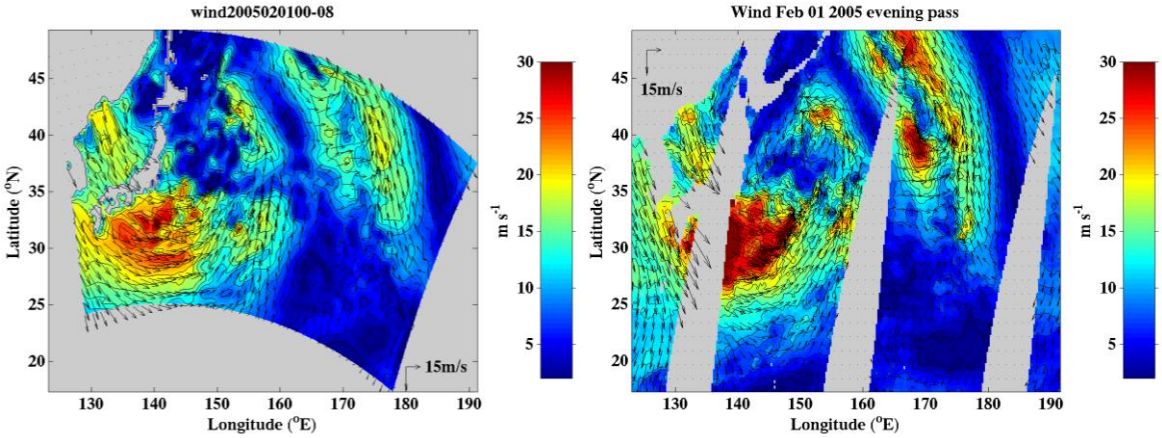

Figure 4-15: (Left): Wind at 10 m from fully coupled 27 km COAMPS forecast for 1 February, 800 UTC. The forecast was initialized at 0000 UTC. (Right): QuikSCAT winds from descending pass.

The differences between the fully coupled and uncoupled runs were fairly small. An example given in Fig. 4-16 displays the 3 km coupled and uncoupled atmospheric forecasts for 2100 UTC on 31 January, 2005. Also shown are wind differences between the coupled and uncoupled runs with SST contours illustrating the Kuroshio temperature fronts. QuikSCAT winds for the same time are shown in the fourth panel. The most notable difference was near 148°E, 36.5°N. From the QuikSCAT it is clear that a small cyclonic motion existed, with easterlies to the east and northeast of its center.

In the coupled run (upper right panel), a cyclonic flow, although much less developed, is seen at a position slightly further east, while it is absent in the uncoupled run. The difference plot between the coupled and the uncoupled run also shows the contours of SST between 14°C and 19°C to mark the position of the Kuroshio front. Note that the closed cyclonic wind motion is located over the warm water intrusion to the north. This feature is absent in the uncoupled run that uses NCODA for SST.

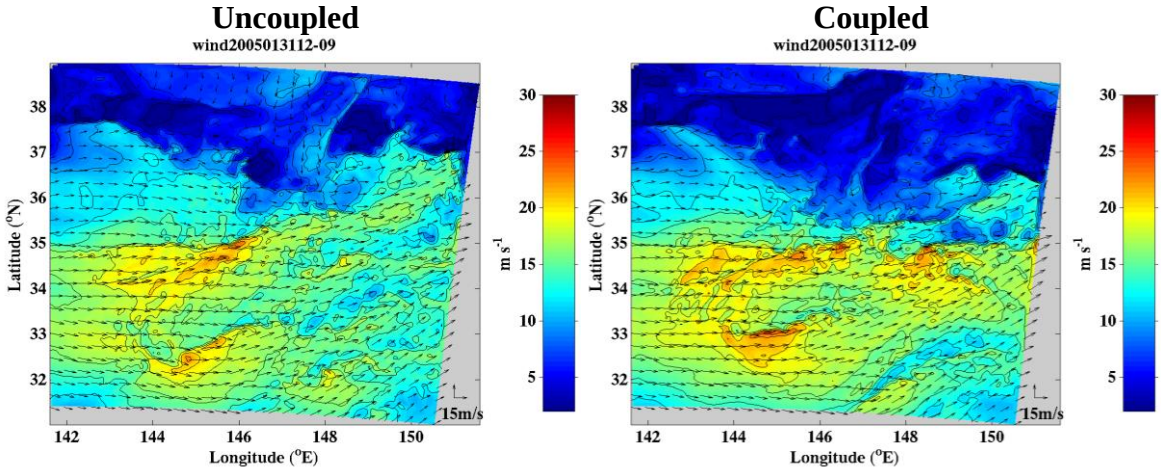

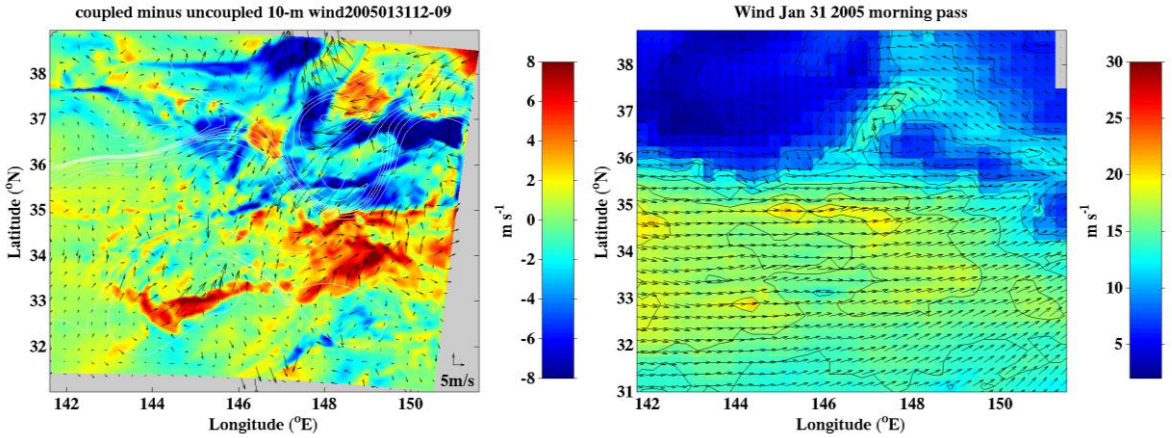

Figure 4-16: COAMPS 3 km uncoupled and coupled atmospheric forecasts for 2100 UTC on 31 January, 2005 (top two panels). The lower left panel displays coupled and uncoupled wind differences, with SST contours illustrating the Kuroshio temperature fronts. QuikSCAT winds for the same time are shown in the lower right panel.

3.4.3.4 COAMPS Validation in Summer

During the summer, the ocean mixed layer in the northern portion of the Kuroshio Extension is much shallower, allowing for a stronger ocean feedback to the atmosphere. A summer COAMPS simulation was conducted from 15 June through 17 July, 2005. The oceanic temperatures at the KEO buoy are shown in Fig. 4-17 below.

3.4.3.4.1 Atmospheric Results

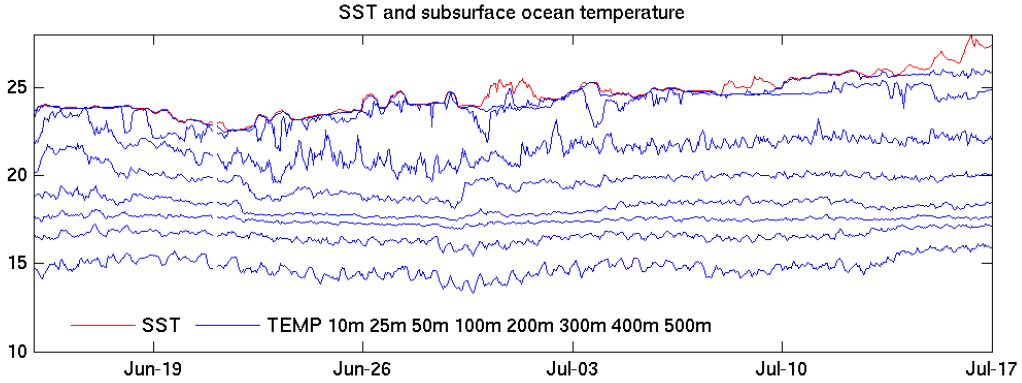

Figure 4-17: Hourly averaged ocean temperature at selected depths from the KEO buoy. The red line shows the surface temperature.

A typical summer weather scenario is shown in Fig. 4-18 for the testing time frame of 18 June, 2005 in the Kuroshio Extension. The wind over the KEO buoy region was characterized by moderate south-southwesterlies and a low pressure region. Its associated cyclonic 10 m winds were situated near 160°E, 45°N. A front was visible near the axis of the Kuroshio Extension, as is often the case. A daily composite of the wind measurements from the two QuikSCAT

satellite passes during that day is also shown in Fig. 4-18. The average wind velocity components were used if both measurements were available; otherwise a single measurement was used. There was excellent agreement between COAMPS and QuikSCAT.

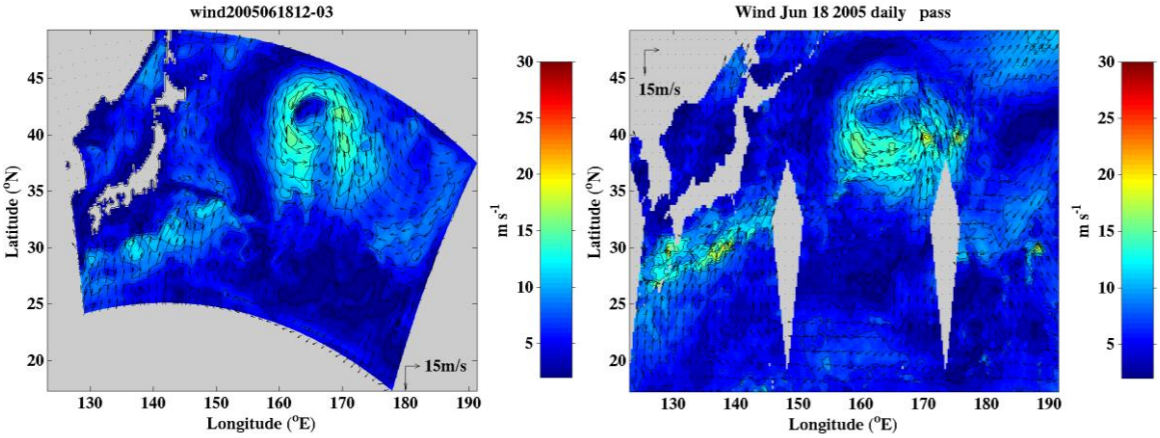

Figure 4-18: Left: COAMPS 10-m wind forecast for 18 June, 1500 UTC and Right: QuikSCAT daily composite of the two wind measurements from the same date.

During the month-long summer simulation the air temperature was increasing at a near constant rate from 23°C to 27°C. The bias was just over 1°C for the coupled run and 0.5°C or less for the uncoupled run, but the correlation was slightly better for the coupled run (0.86 – 0.89) than the uncoupled run (0.82 – 0.84). With relative humidity, the correlations were much smaller, but higher than during winter. The bias was small, about -2.5% for the uncoupled run and about -1% for the coupled run (Fig. 4-19).

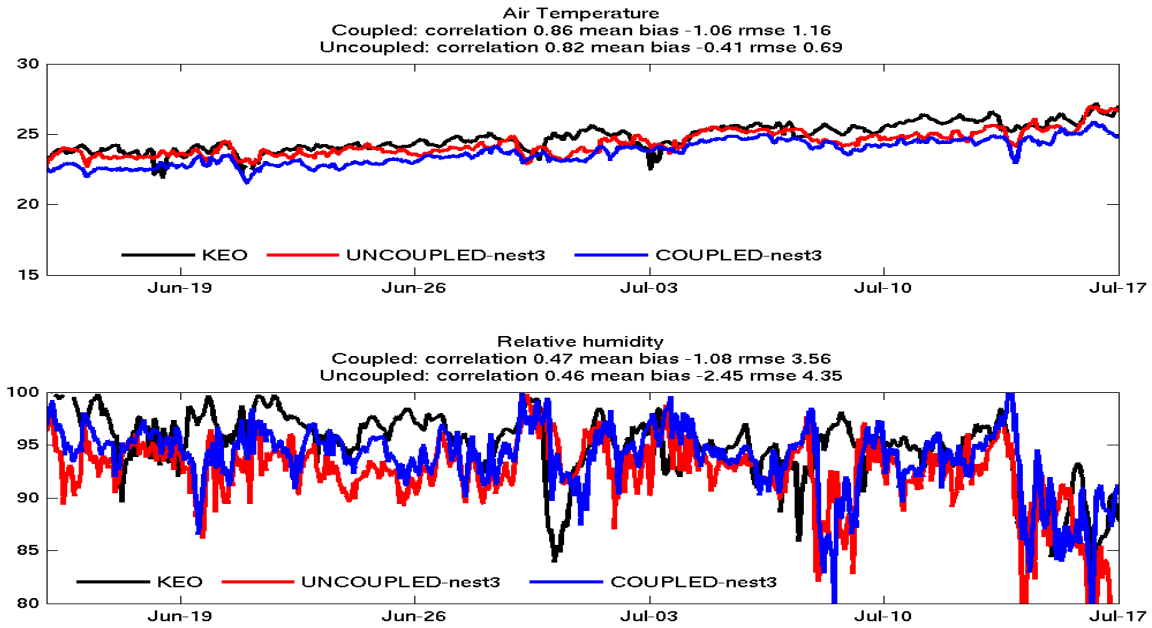

Figure 4-19: Air temperature and relative humidity results for atmospheric nest 3 (3 km grid) during 15 June to 17 July, 2005 for the KEO buoy (black), the uncoupled model (red) and the fully coupled model (blue).

The summer winds were in excellent agreement with the KEO buoy observations. For the total wind speed, the bias was only about 0.1 m/s for the coupled run and about 0.3 m/s for the uncoupled run. Correlations are about 0.8 (Fig. 4-20; Table 4-2).

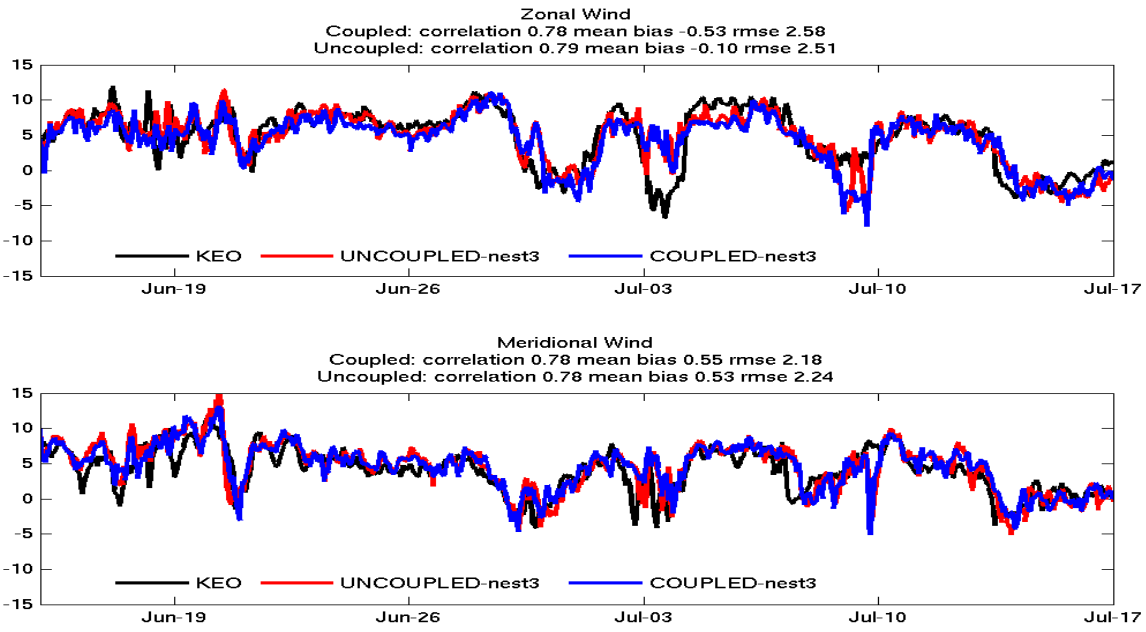

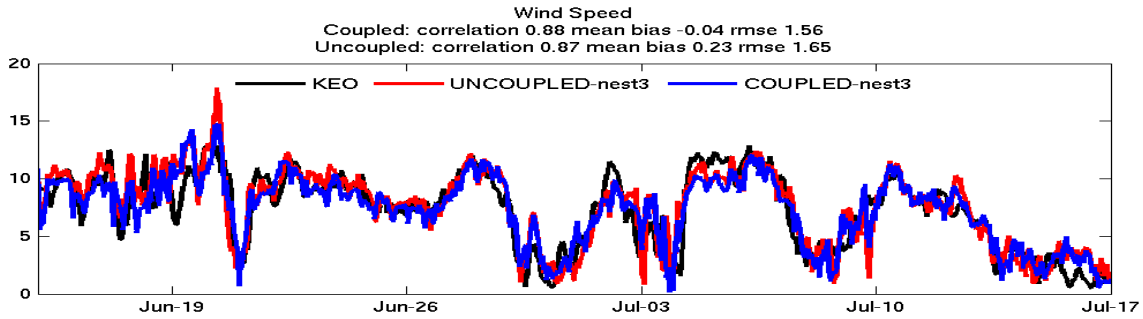

Figure 4-20: Zonal wind (top), meridional wind component (middle) and wind speed (bottom) for atmospheric nest 3 (3 km grid) for 15 June to 17 July, 2005 at the KEO buoy. The observations are in black, the uncoupled model in red, and the fully coupled model is shown in blue.

Table 4-2: Statistics for atmospheric quantities from the 3 km nest COAMPS uncoupled [u] and coupled [c] run from Jun 15 through July 16, 2005.

	KEO Buoy Mean	Mean [u]	Mean [c]	CC [u]	CC [c]	MB [u]	MB [c]	RMSE [u]	RMSE [c]
Air Temp. (^{o}C)	24.74	24.33	23.68	0.82	0.86	-0.41	-1.06	0.69	1.16
Relative Hum. (%)	94.71	92.26	93.63	0.46	0.47	-2.45	-1.08	4.35	3.56
Zonal Wind (m/s)	4.75	4.65	4.22	0.79	0.78	-0.10	-0.53	2.51	2.58
Merid. Wind (m/s)	3.96	4.50	4.51	0.78	0.78	0.53	0.55	2.24	2.18
Wind Spd (m/s)	7.31	7.54	7.27	0.87	0.88	0.23	-0.04	1.65	1.56

3.4.3.4.2 Ocean Temperature Results

During the summer simulation month the SST increased from about 24^{o}C to above 27^{o}C (Fig. 4-21). However, both the uncoupled and the coupled model had significant cold biases of more than 1^{o}C. As seen during the winter, the deeper water was too cold, which may have influenced the upper ocean temperatures as well.

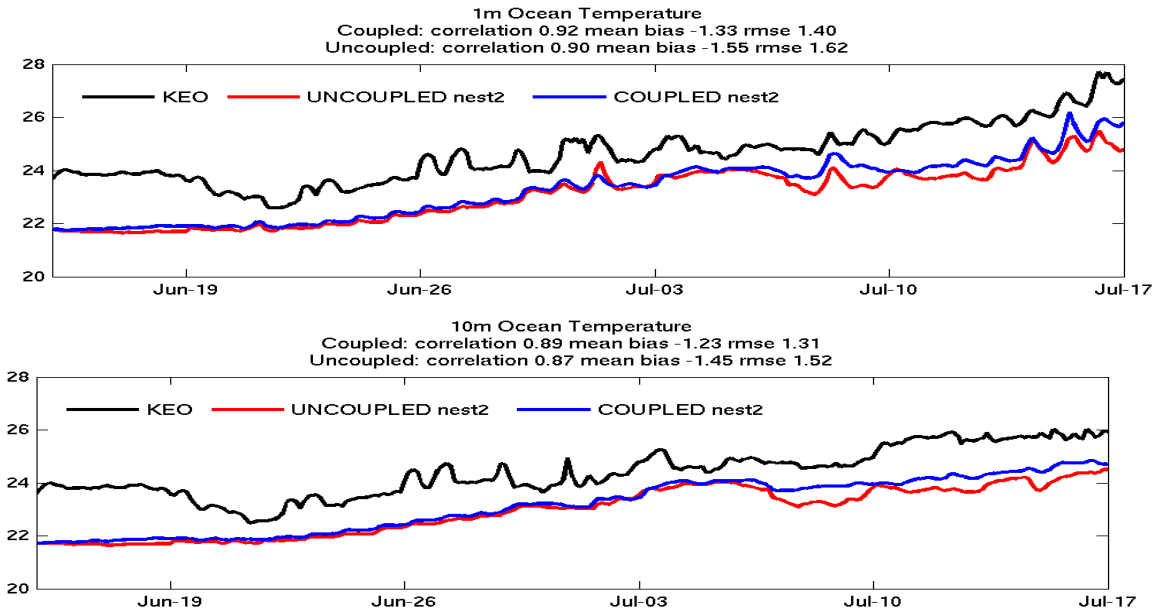

Figure 4-21: 1 m (top) and 10 m (bottom) SST comparisons of 9 km coupled (blue) and uncoupled (red) COAMPS to KEO (black) observations. Statistics are shown above each plot and in Table 4-3.

The near surface temperature in the coupled run showed a smaller bias than the uncoupled run towards the end of the simulation. The large heat capacity of the ocean mixed layer, even during the summer when it is shallow, required a large difference in heat flux to respond to differences in atmospheric heat flux. Statistics are shown in Table 4-3.

Table 4-3: Mean ocean temperatures and CC, MB and RMSE for the 27 km (Nest 1) and 9 km (Nest 2) grids from Jun 15 through Jul 16, 2005.

	KEO Buoy	Nest 1 [u]	Nest 1 [c]	Nest 2 [u]	Nest 2 [c]
1 m Temp (^{o}C)	24.60	23.08	23.27	23.05	23.27
CC		0.91	0.93	0.90	0.92
MB				-1.55	-1.33
RMSE				1.62	1.40
10 m Temp (^{o}C)	24.37	22.94	23.14	22.92	23.14
CC		0.88	0.90	0.87	0.89
MB				-1.45	-1.23
RMSE				1.52	1.31

3.4.3.5 Comparison with Satellite Altimetry

A weekly average of sea surface height anomalies (SSHA) from TOPEX/Poseidon, ERS and Jason1 satellites is shown in Fig. 4-22a. The gradient of SSHA shows that the axis of the Kuroshio is situated along 35.5°N in a standing wave pattern with crests at 146°E and 151°E. Two strong SSHA minima are seen along 33°N near 145°E and 149°E, demonstrating a manifestation of the recirculation gyre. For comparison with COAMPS, the mean sea level computed by Maximenko and Niiler (2005) (Fig. 4-22b) was added after interpolating the fields to a common spherical grid with 0.05° resolution. The total field is shown in Fig. 4-22c after subtracting the average SSH (39.5 cm) over the area. The coupled COAMPS SSH averaged from 30 January through 5 February, 2005 is shown in Fig. 4-22d, after subtracting 40.2 cm, the area average SSH.

Based on the satellite observations (Fig. 4-22c), a cyclonic eddy was located to the northeast in the vicinity of the KEO site. In the COAMPS simulation, the center of the eddy was located just to the northwest of the KEO buoy. The differences in the eddy location resulted in large differences between observed and model current directions. More importantly, the cyclonic eddy was associated with lower ocean temperatures from the surface to depths of more than 1000 m. The fact that the KEO site was closer to the eddy center in the model than observed may explain the lower ocean temperatures found in the COAMPS simulation and hence the cold bias in COAMPS.

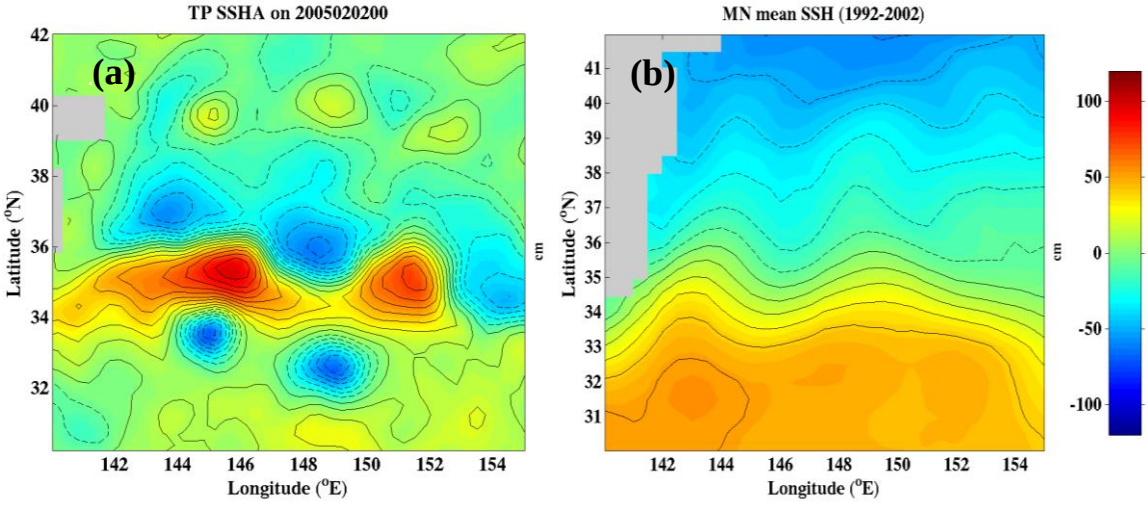

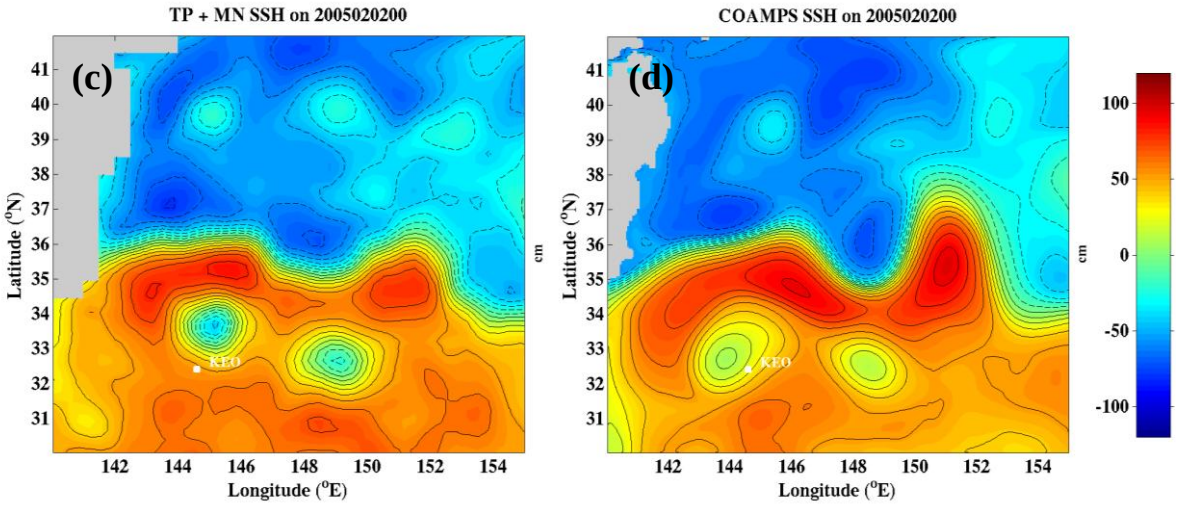

Figure 4-22: (a): Weekly averaged sea surface height anomaly from TOPEX/Poseidon, ERS and Jason-1 altimetry centered on 2 February, 2005. (b): Average sea surface height (SSH) from 1992-2002 from Maximenko and Niiler, (2005). (c): Absolute SSH computed as the sum of (a) and (b) minus the area average SSH. (d): COAMPS SSH minus its area average.

3.4.3.6 Objectively Analyzed Turbulent Heat Flux Comparisons

In January 2008, Woods Hole Oceanographic Institution (WHOI) developed enhanced surface latent, sensible, net shortwave and net longwave radiation fluxes for the global oceans and called the product Objectively Analyzed Air-Sea Fluxes (OAFlux). OAFlux integrates satellite observations with surface moorings, ship reports, and atmospheric model reanalyzed surface meteorology onto a 1^{o}x1^{o} grid, with monthly fields of observations dating from 1958 - 1984 and daily fields from 1985-2006 (Yu and Weller, 2007; Yu et al., 2008). Daily means of sensible and latent heat flux were computed from COAMPS hourly output for both the uncoupled and fully coupled runs. Fig. 4-23 compares sensible heat flux for each run against the OAFlux data.

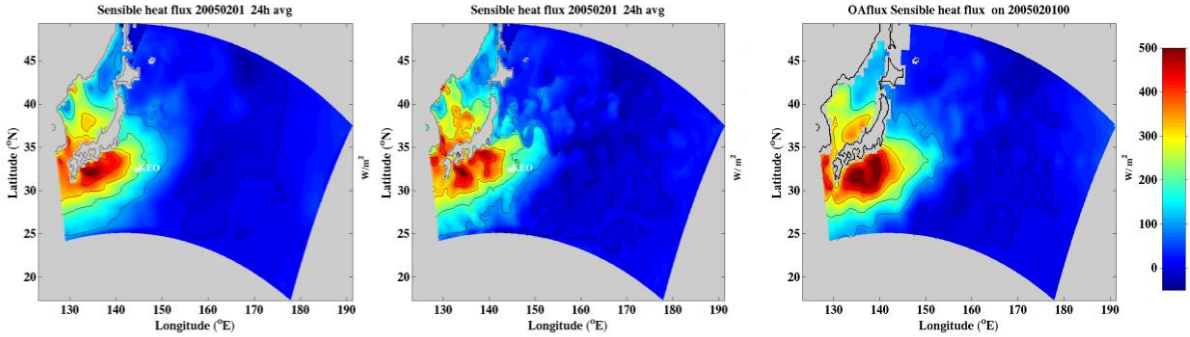

Figure 4-23: Daily average of sensible heat flux from the uncoupled run (left), fully coupled run (middle) and objectively analyzed from the OAFlux product on 1 February, 2005 (right). The contour interval is 100 W/m^2 for positive values (full line) and 20 W/m^2 for negative values (dashed line). The color scale range is from -50 W/m^2 to 500 W/m^2.

The observed daily sensible heat flux from OAFlux had a maximum of 560 W/m^2, slightly higher than found in COAMPS. The uncoupled run had fluxes up to 526 W/m^2, while the coupled run's maximum was 514 W/m^2. Note that both the coupled run and the observed sensible heat flux have two distinct maxima, while the uncoupled run has a single maximum. The coupled run solution includes many more small scale features than the uncoupled run, due to the presence of small scale features in the model SST field.

On 1 February, the maximum latent heat flux from the objective analysis was 995 W/m^2 (Fig. 4-24). The model fluxes were about 10% higher, with 1080 W/m^2 and 1122 W/m^2 for the uncoupled and coupled runs, respectively. There was a slightly better agreement between the OAFlux analysis and the coupled run compared to the uncoupled run. In the Sea of Japan, for example, the uncoupled run had a slightly smaller latent heat flux, and the local heat flux minimum off the southern coast of Japan (near 32^{o}N) was much less pronounced in the uncoupled case.

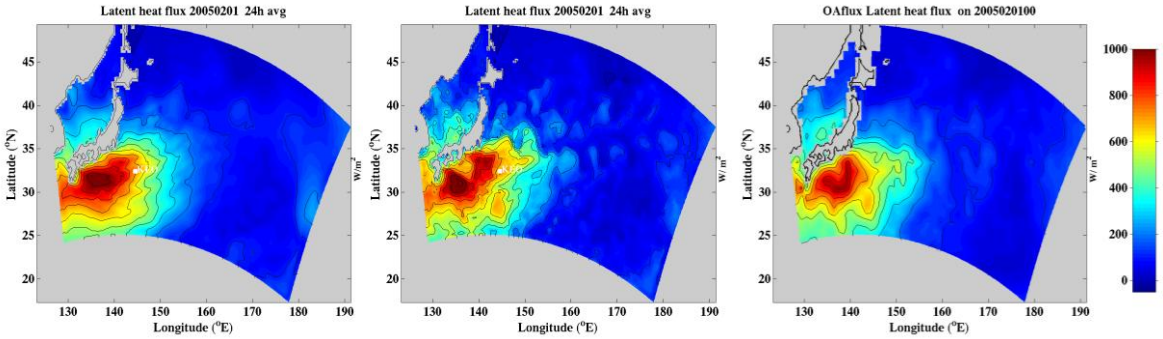

Figure 4-24: Daily average of latent heat flux from the uncoupled run (left), fully coupled run (middle) and objectively analyzed from the OAFlux product on 1 February, 2005. Contour interval is 100 W/m^2. The color scale range is from -20 W/m^2 to 1000 W/m^2.

The total heat flux by turbulent transfer is shown in Fig. 4-25. The maximum flux was 1576 W/m^2 in the uncoupled model and 1584 W/m^2 in the coupled run. By comparison, the OAFlux data had a maximum of 1520 W/m^2. This is excellent agreement (within a 5% difference between COAMPS and observations) considering the extreme nature of the cold air outbreak event and the rather coarse spatial resolution of the analysis heat fluxes. Instantaneous total turbulent heat fluxes up to 2300 W/m^2 were found during 1 February, 2005. The OAFlux synthesis uses Numerical Weather Prediction re-analyses (NCEP2 and ERA40), AVHRR SST, Special Sensor Microwave/Imager (SSM/I) humidity, Advanced Microwave Scanning Radiometer - Earth Observing System (AMSR-E) and QuikSCAT wind. However, the COAMPS runs assimilate the same datasets, so the calculations are not independent.

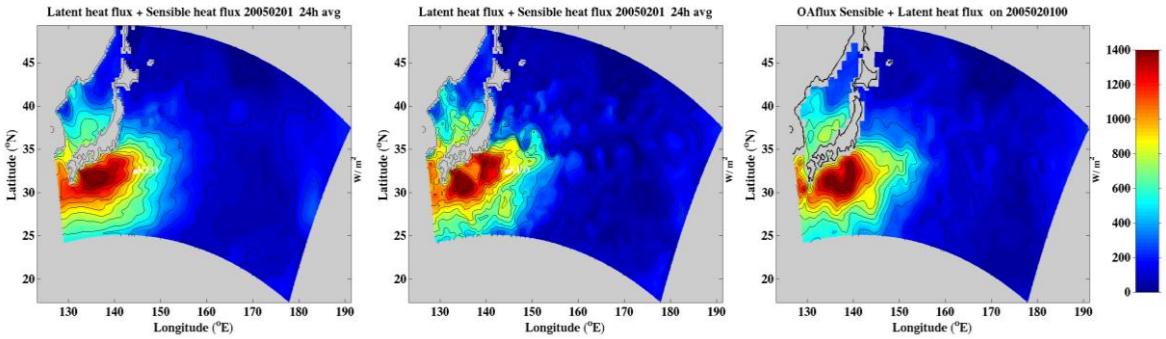

Figure 4-25: Daily average of the sum of sensible and latent heat flux from the uncoupled run (left), fully coupled run (middle) and objectively analyzed from the OAFlux product on 1 February, 2005. The contour interval is 100 W/m^2. The color scale range is from 0 W/m^2 to 1400 W/m^2.

3.4.3.7 Advantages of a Coupled Run

The basic prognostic quantities such as wind, air temperature and specific humidity are not greatly altered by coupling COAMPS to a fully interactive NCOM rather than running COAMPS forced by NCODA. Similarly, the NCOM simulation of the ocean varies little from runs in which the ocean is forced by COAMPS output. However, there are several advantages to running a fully coupled model rather than a separate COAMPS/NCODA run.

First, running the ocean model in addition to COAMPS alone is an additional computational expense of 20-30% depending on the configuration. Secondly, if the ocean state is needed, running a fully coupled model rather than separate models only requires a few percent more computational resources.

The most important advantage is the greater consistency in air-sea flux predictions and the realism obtained from a fully coupled run. In particular, a number of atmospheric quantities show sharp gradients in the vicinity of ocean fronts. Figures 4-26 through 4-30 provide graphical examples of coupled and uncoupled comparisons for several air-sea parameters.

Figure 4-26 gives an example of the daily averaged latent heat flux on the 9 km grid. The area integrated total latent heat flux does not vary greatly, but the coupled run reveals strong gradients in air-sea exchange in the vicinity of the front, clearly following sharp sea surface temperature gradients. This has implications for other quantities.

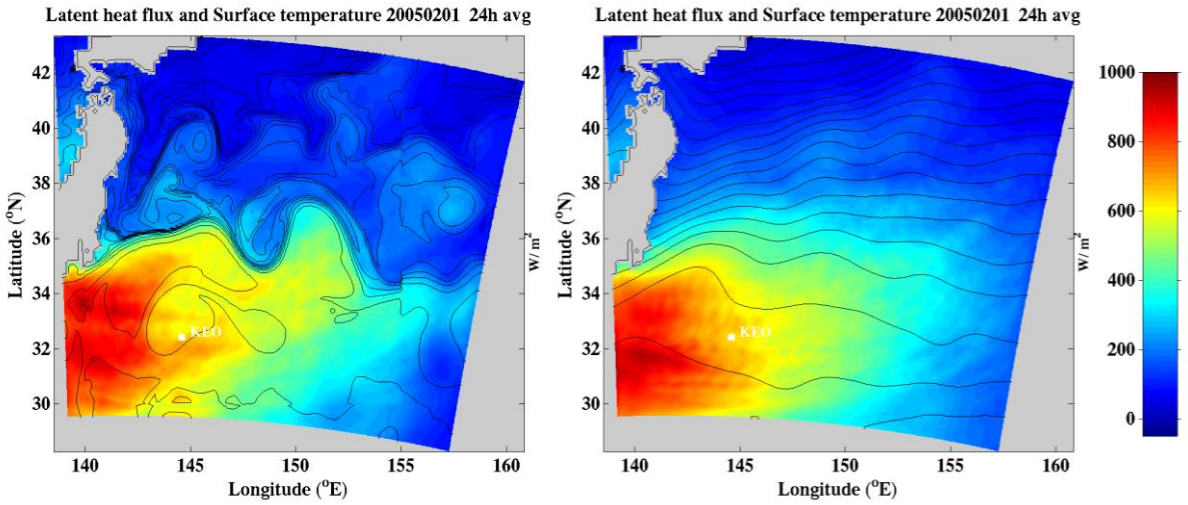

Figure 4-26: Daily averaged latent heat flux and surface temperature for the coupled run (left) and the uncoupled run (right). The 24 hour average is centered on 1 February, 2005 12UT.

Figure 4-27 below shows the planetary boundary layer height averaged over 48 hours from 1 to 3 February. While the planetary boundary layer height in the uncoupled run is consistent with the SST from NCODA, it is inconsistent with NCOM. A deep PBL over the warm region and a shallow PBL over cold water were both expected and seen in the fully coupled run. Figure 4-28 shows the turbulent kinetic energy at 50 m averaged over 30 hours. It is clear that gusty winds, due to the deep PBL height, are much more likely to occur over the subtropical warm water than over the cold water to the north.

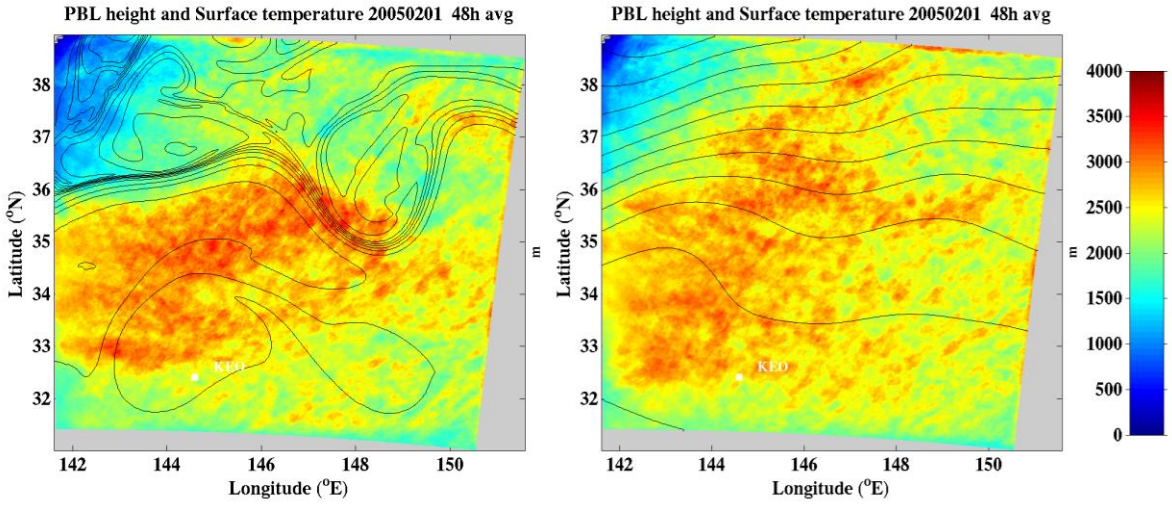

Figure 4-27: Planetary Boundary Layer height (color) and SST (contours) averaged over 48 hours, centered on 2 February at 00 UT for the coupled run (left) and the uncoupled run (right). The contour interval is 1°C. The model SST at KEO is very close to 17.5°C in both runs.

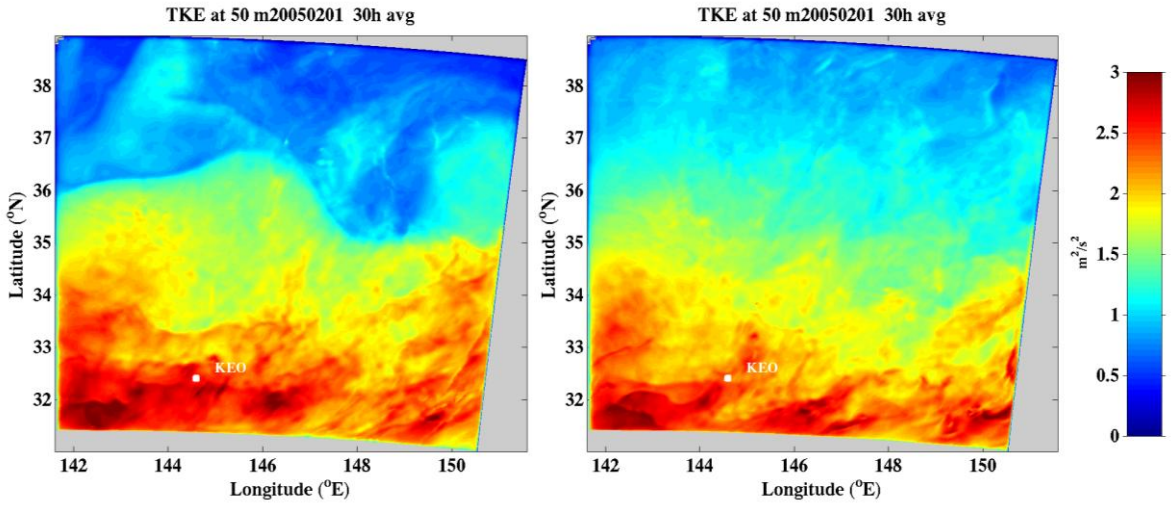

Figure 4-28: Turbulent kinetic energy averaged over 30 hours centered on 1 February at 12 UT for the coupled run (left) and the uncoupled run (right).

During the summer there were extended periods of calm winds and strong stratification below a shallow mixed layer, which increased the importance of air-sea interaction. On 10 July, 2005, the winds in the KESS region began decreasing from about 10 m/s to a few meters per second on 12 July. Figure 4-29 shows the latent heat fluxes averaged from 9-15 July, 00UT. As previously noted, the heat flux followed the SST gradient very closely. In Figure 4-30, the SST and currents on 15 July at 12UT are shown for both runs. The coupled run had strong ocean cooling (a large latent heat flux) occurring on the warm side of the front. On the cold side of the front, the fluxes were close to zero. This negative feedback tends to decrease the SST gradients. In contrast, the latent heat fluxes in the uncoupled simulation were obtained from NCODA. The inconsistency with the NCOM SST leads to increased temperature gradients compared to the coupled run.

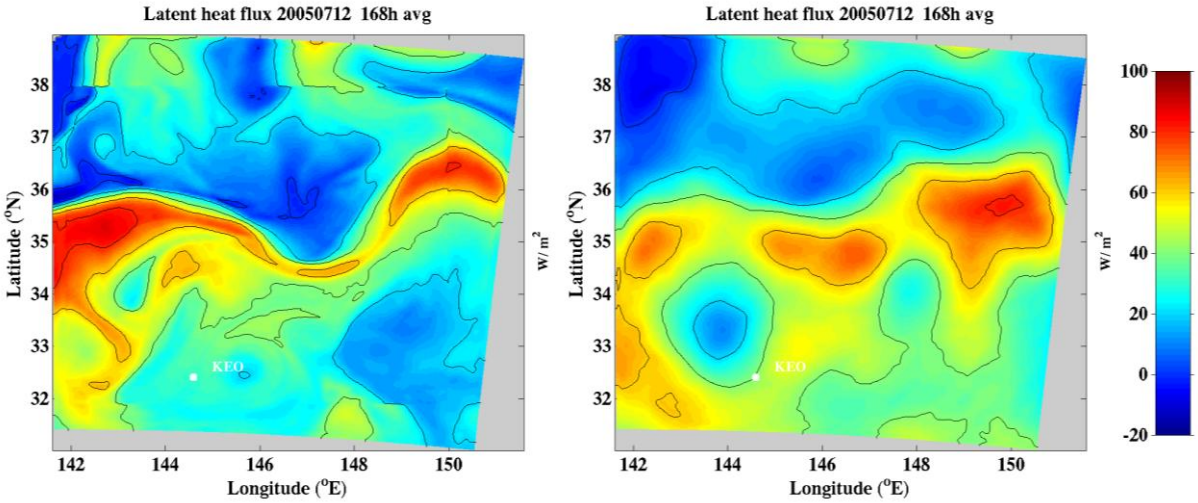

Figure 4-29: Latent heat flux for the coupled run (left) and the uncoupled run (right). A 168 hour average is centered on 7 July, 2005 12UT.

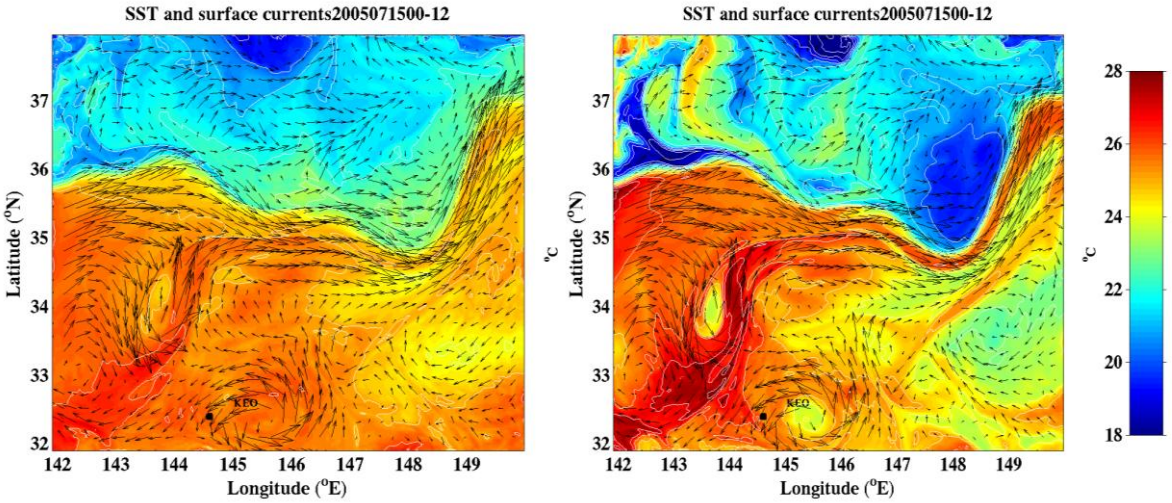

Figure 4-30: Forecast of sea surface current vectors and sea surface temperature for the coupled run (left) and the uncoupled run (right) on 15 July, 2005 12UT.

3.5 Test Case 5: The VAMOS Ocean-Cloud-Atmosphere-Land Study (VOCALS)

The VAMOS (Variability of the American Monsoon Systems) Ocean-Cloud-Atmosphere-Land Study (VOCALS) is an international CLIVAR (Climate Variability and Predictability) program sponsored by NSF and NOAA with contributions from the Office of Naval Research (ONR) and the Department of Energy (DoE). The primary goal of VOCALS is to develop and promote scientific activities leading to improved understanding of the Southeast Pacific (SEP) coupled ocean-atmosphere-land interaction on diurnal to inter-annual timescales. VOCALS is organized into two tightly coordinated components, a regional experiment (VOCALS-Rex), and a modeling program (VOCALS-Mod). Extended observations will provide important contextual datasets that will help to link the field and modeling components. The coordination through VOCALS of observational and modeling efforts will accelerate the rate at which field data can be used to improve simulations and predictions of the tropical climate variability. More information about VOCALS can be found at http://www.eol.ucar.edu/projects /vocals/.

The interactions between cloud, aerosols, atmospheric marine boundary layer, and upper-ocean are poorly observed or understood in the SEP region. Coastal cold upwelling is frequently forced by a strong coastal jet that parallels to the coasts of Chile and Peru. Mesoscale ocean eddies 50 to 200 km across play a major role in the transport of heat and fresh water from coastally upwelled areas to regions further offshore and can affect sea surface temperature (SST) distribution. The cold SST in conjunction with the warm and dry air aloft maintains the world's largest stratocumulus deck, which greatly influences the Earth's radiation budget.

3.5.1 Purpose

Test Case 5 aims to elucidate the feedback among oceanic upwelling, mesoscale eddies, a low-level coastal jet, and clouds in the SEP area through the coupled COAMPS. The study uses the SEP as a testbed for improved simulations of the atmospheric boundary layer and oceanic heat budget and their feedback to the atmosphere. The performance of coupled and uncoupled simulations will be evaluated through various observational datasets that were collected in the VOCALS-Rex from 20 October to 30 November 2008.

3.5.2 Test Case Characteristics

3.5.2.1 Test Area and Observations

The Southeast Pacific is characterized by along-shore southerly winds that are directly linked to the subtropical high pressure system. The southerly wind is often strong, and a low-level jet, situated off the coast of central Chile, exhibits powerful vertical shear above and below the wind maximum, located near the inversion base at about 200 m (Rutllant, 1993). This low-level coastal jet occurs year-round, with larger variability in magnitude during austral winter and spring and a near-weekly alternation of strong and weak alongshore winds (Rutllant et al., 2004). The jet is strong and has a wide aerial coverage when the center of the subtropical high is located to the east of 100°W. When the center of subtropical high is located to the west of 100°W, it is weak and has a narrow areal coverage.

NOAA ship R/V *RONALD H. BROWN* participated in collecting data for VOCALS off the coasts of Chile and Peru in October and November of 2008. It fielded one of the most comprehensive sets of observing systems ever assembled on a research vessel. Sounding datasets were gathered for a period of about a month for verification of the vertical structure of the atmospheric boundary layer. Buoy data from Woods Hole Oceanographic Institution (WHOI), including surface meteorological data and SST, were utilized for the surface variables validation at (20°S, 85°W). QuikSCAT winds and TRMM TMI satellite SST are used in the COAMPS validation, as well as cloud liquid water path taken from the TMI satellite, the AMSR-E, and the Special Sensor Microwave/Imager (SSM/I) observations.

3.5.2.2 Model Setup

The COAMPS domain is triply nested in a Lambert conformal grid projection (Fig. 5-1). The horizontal resolutions of the three nested domains are 45, 15, and 5 km with horizontal grid points of 151 × 151, 199 × 181, and 181 × 181, respectively. There are 45 sigma levels in the vertical. The NCOM and NCODA domains are 15 km in the horizontal (199x181) with 41 and 30 levels in the vertical, respectively. The two-way coupled simulation was run twice daily using a 12-hr data assimilation update cycle so that each forecast was initialized using a first-guess analysis from the previous 12-hr forecast, combined with current observational data using an MVOI scheme.

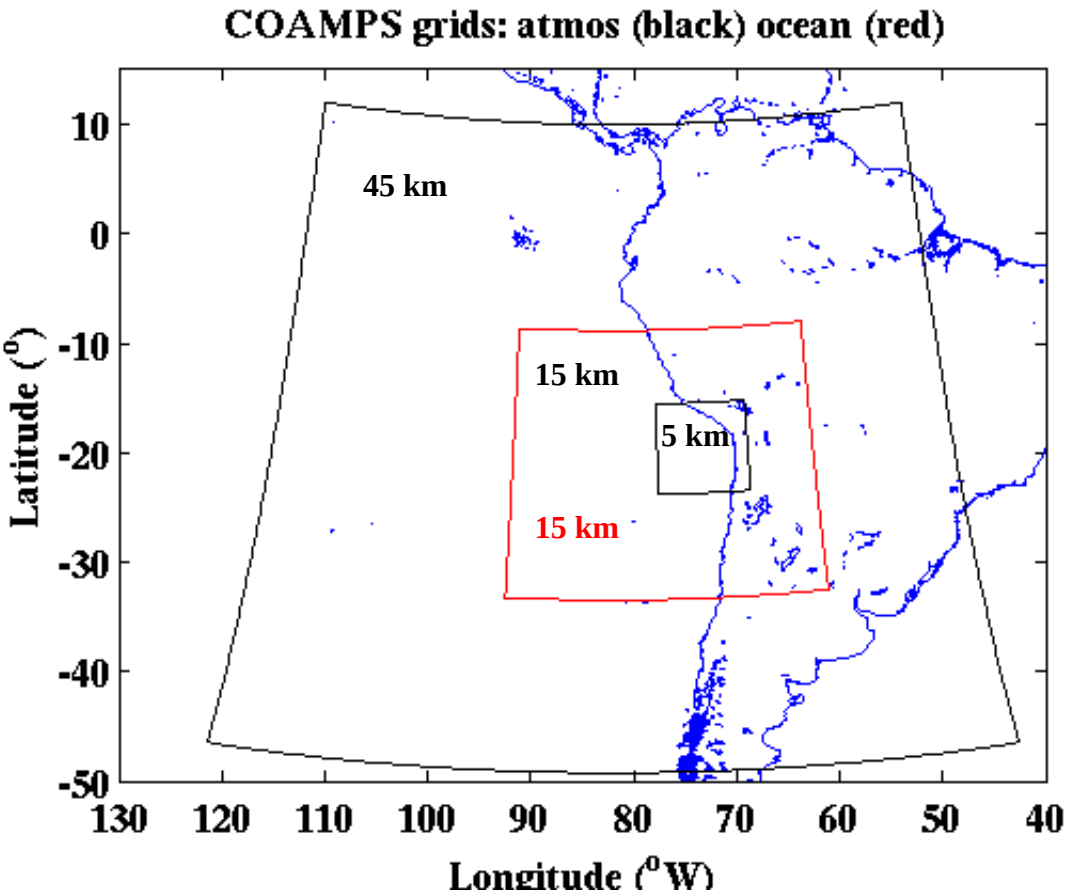

Figure 5-1: COAMPS atmospheric grid nests (45 km, 15 km and 5 km) and the 15 km NCOM/NCODA grid.

3.5.3 Results

3.5.3.1 Variability of the Low-Level Coastal Jet

There was significant variability in the coastal jet as seen in the time series of wind stress at 30°S, 75°W (Fig. 5-2a). Two strong and two weak coastal jet periods, marked as (1) through (4), wind speed, and sea level pressure are displayed in Fig. 5-2b and 2c, respectively. The mean wind speed difference between the weak and strong coastal jet in the Chilean coast can reach up to 5 m/s.

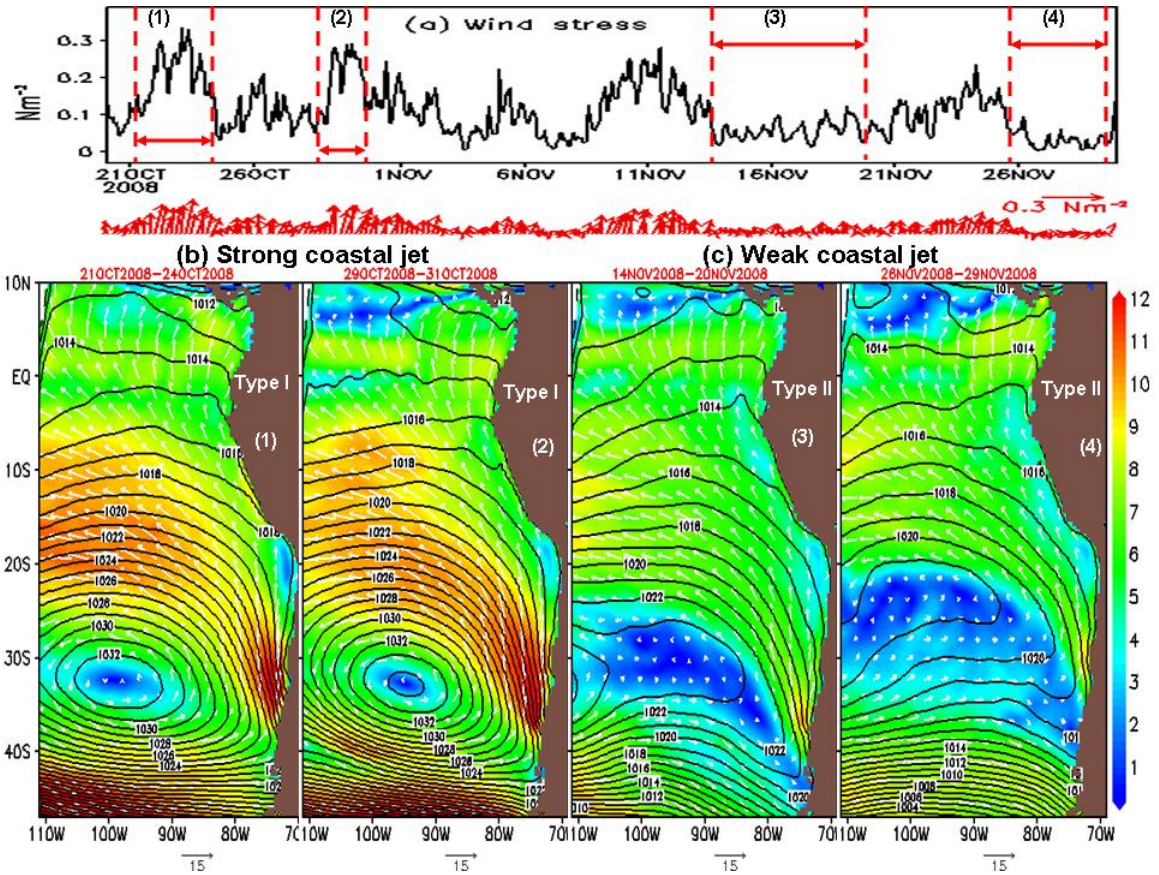

Figure 5-2: (a): Time series of magnitude (black contour) and direction (arrows) of wind stress at 30°S, 75°W. COAMPS 10 m wind speed, direction and sea-level pressure for (b): strong coastal jet period and (c): weak coastal jet period. The values are from the COAMPS 45 km grid.

During the strong coastal jet period, cold, dry air associated with the high pressure system located offshore of the Chilean coast produced large wind stress north of the high (Fig. 5-3). As a result, the atmosphere received significantly greater latent heat flux. The boundary layer height during the strong coastal jet period was about 500 m more than during the weak coastal jet period.

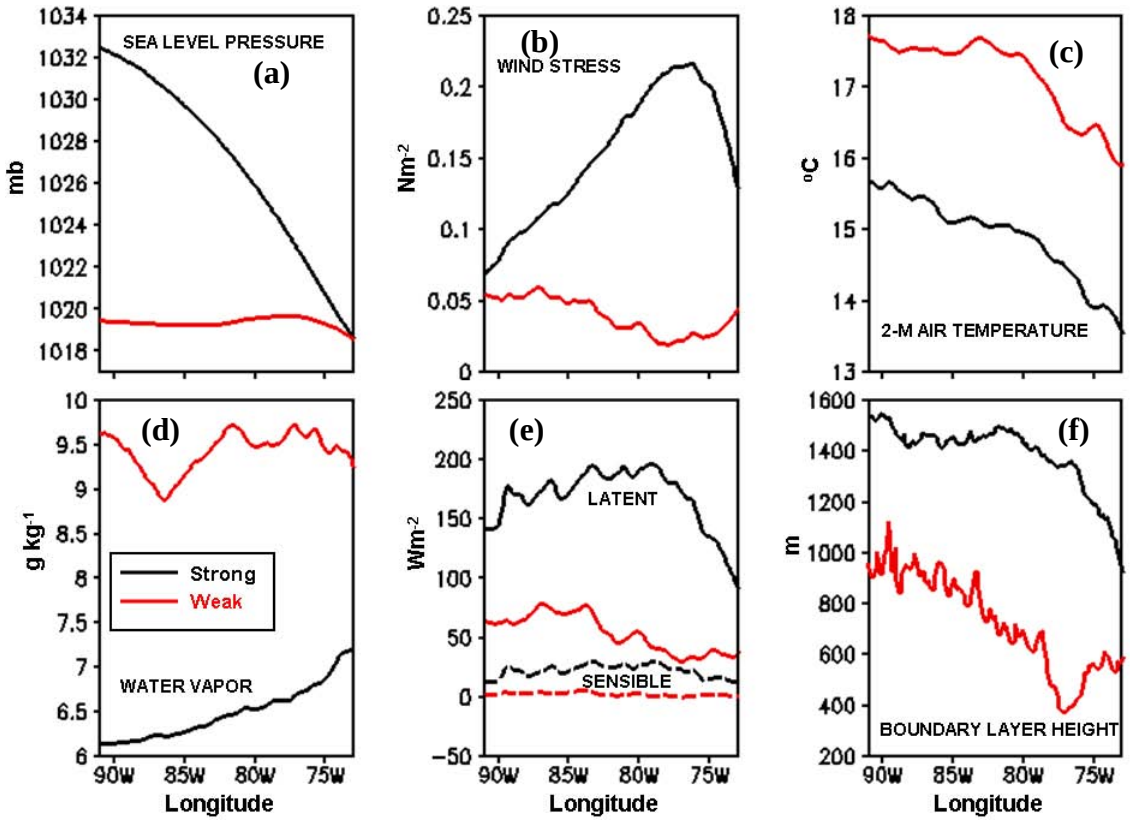

Figure 5-3: COAMPS surface fields along 30°S during strong (29-31 October) and weak (26-28 November) coastal jet periods for (a): sea-level pressure (mb), (b): wind stress (N/m^2), (c): 2 m air temperature (°C), (d): water mixing ratio (g/kg), (e): latent (solid line) and sensible (dashed line) heat flux (W/m^2), and (f): boundary layer height (m).

3.5.3.2 Ocean Response to the Coastal Jet

The strong wind stress pattern can be clearly seen from grid nest 2 (Fig. 5-4a), which covered most of the 15 km grid nest domain. The strong wind stress forced significant upwelling along the southern coast of Chile. There were cyclonic and anticyclonic eddies embedded along the current stream lines (Fig. 5-4b and 5-4c). These eddies were generated by the barotropic or baroclinic instability associated with upwelling. The kinetic energy denotes the energy propagation offshore from the upwelling center (Fig. 5-4c).

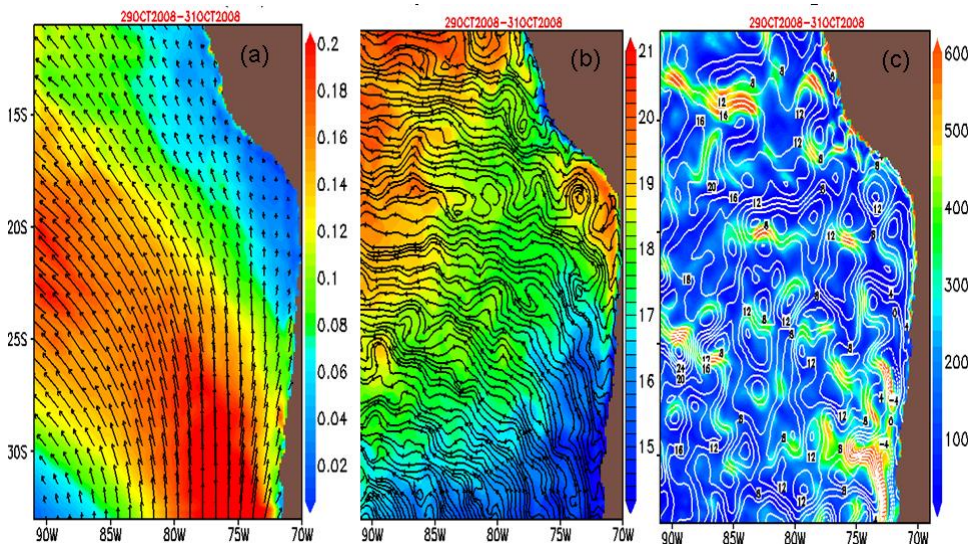

Figure 5-4: Two-way coupled model output from the 15 km grid nest 2 during a strong coastal jet period (29-31 October 00 UTC) for (a): COAMPS wind stress, (b): NCOM surface current (streamlines) and temperature (color gradient), and (c): NCOM surface height (contour) and kinetic energy (color gradient).

These oceanic eddies were more visible (Fig. 5-5b) during the weak coastal jet period when the effect of larger scale forcing was small (Fig. 5-5a). Warm water moved back onshore and reduced the area of upwelled cold water. Energy from the upwelling center then propagated westward with greater distance than during the strong coastal jet period.

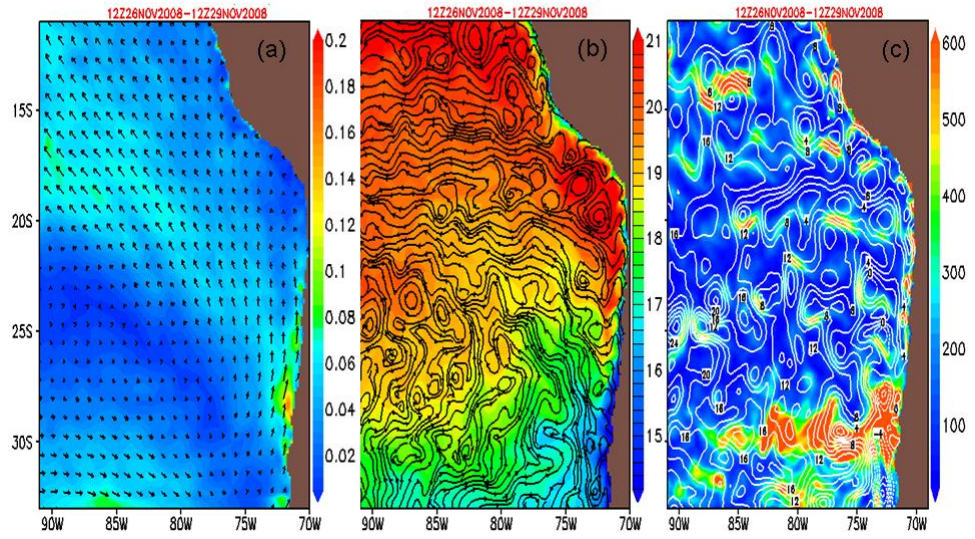

Figure 5-5: Two-way coupled model output from grid nest 2 during a weak coastal jet period (12 UTC 26-29 November) for (a): COAMPS wind stress, (b): NCOM surface current (streamlines) and temperature (color gradient), and (c): NCOM surface height (contour) and kinetic energy (color gradient).

Inertial oscillation at 30°S was due to wind stress variability. The oscillation was weaker during the strong coastal jet period but was more significant during the weak coastal jet period when large scale forcing was decreased (Fig. 5-6). The phase shifting between the upper and deeper layer was also greater during the weak coastal jet period.

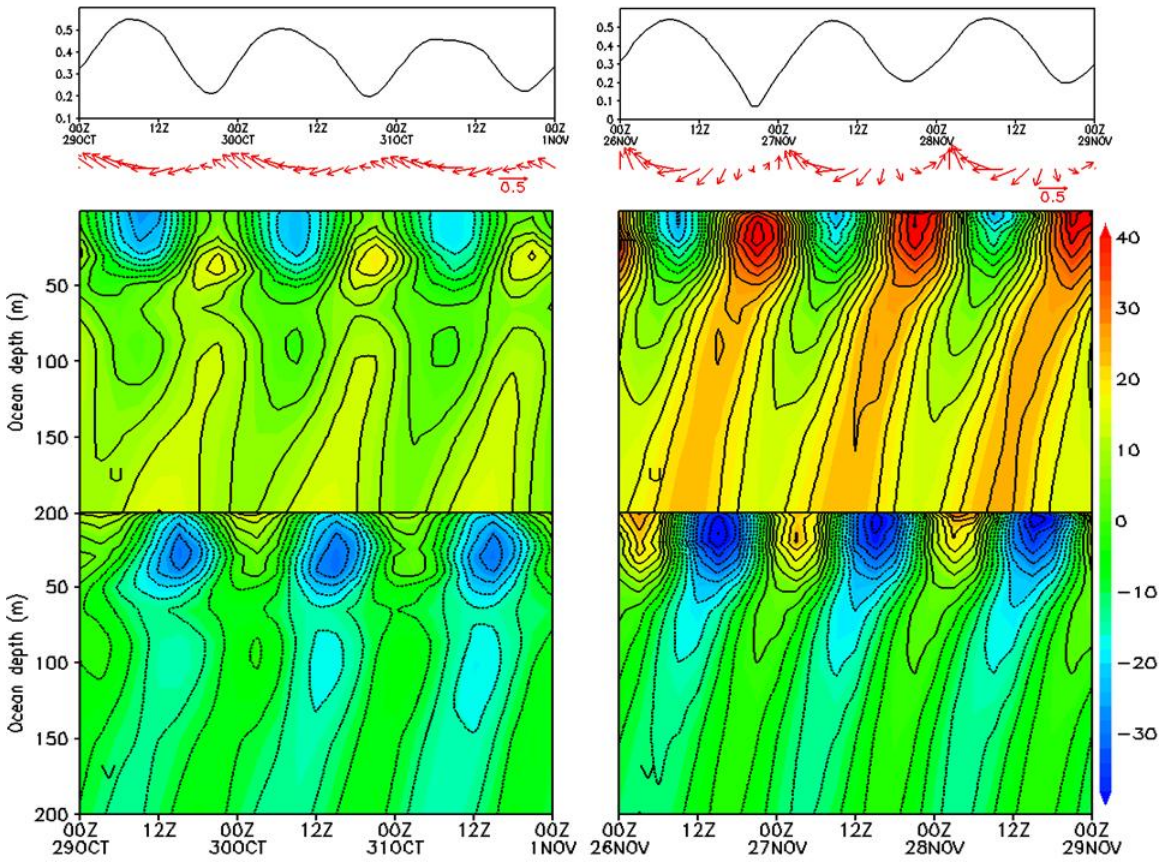

Figure 5-6: Time variation of NCOM currents at 30°S, 75°W during strong (left panel) and weak jet periods (right panel).

3.5.3.3 Feedback between the Atmospheric and Oceanic Boundary Layers

As illustrated in Figure 5-7a, when cold, dry air with strong jet flows moved over the warm ocean surface, the atmospheric and oceanic boundary layers became unstable. Greater heat then fluxed from the ocean to the atmosphere. The negative buoyancy flux induced vertical mixing and increased the mixed layer depth in the ocean. Near the strong upwelling areas along the coast and offshore, the temperature gradient was up to 4°C. Warm water moved onshore during the weaker coastal jet period (Fig. 5-7b), when warm, moist air was recovered.

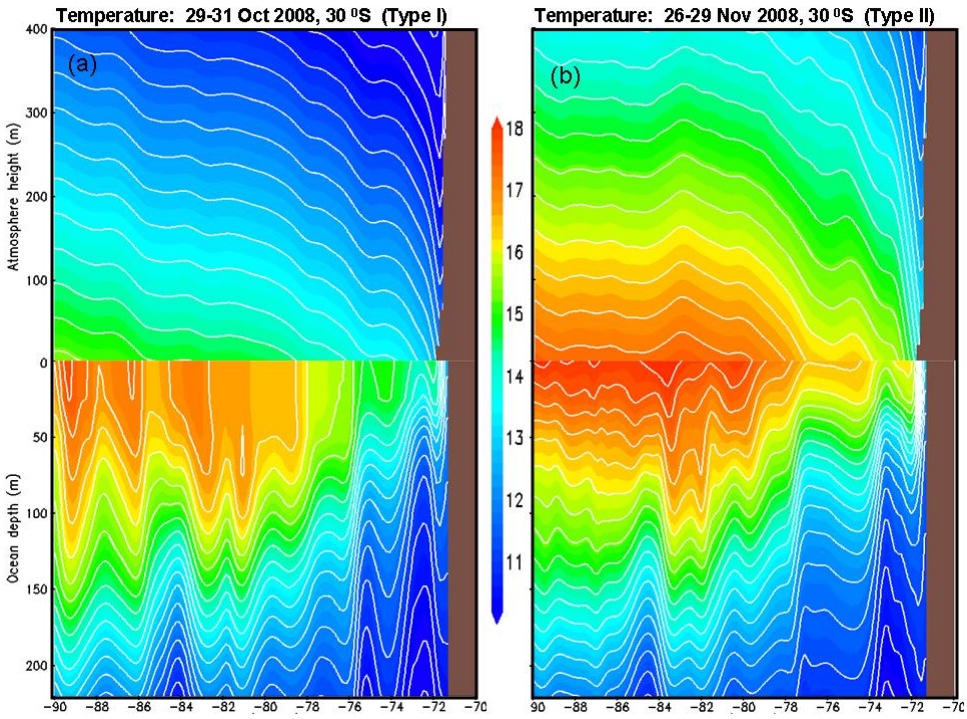

Figure 5-7: Cross section of COAMPS (upper panel) and NCOM (lower panel) temperature during (a): the strong coastal jet period and (b): weak coastal jet period along 30°S.

More cloud water was generated in the unstable conditions of the strong coastal jet period than in the weak. The cloud was also more organized than that generated during the weak coastal jet period. See Figures 5-8a and 5-8b below for a cross section of the cloud water at 30°S.

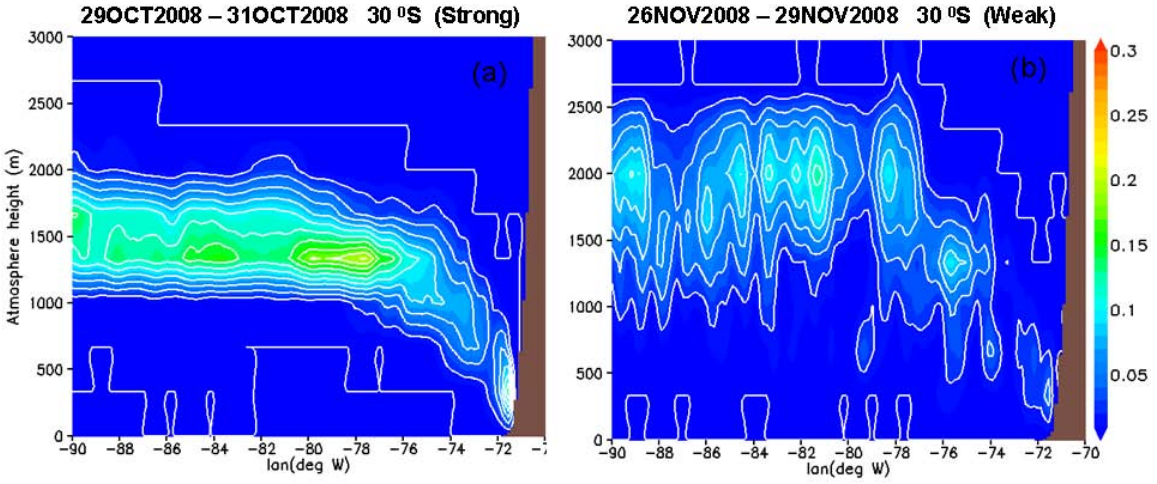

Figure 5-8: Cross section of COAMPS cloud water during (a): the strong coastal jet period and (b): weak coastal jet period along 30°S.

3.5.3.4 COAMPS Validation using VOCALS Field Observations

3.5.3.4.1 Comparison to R/V *BROWN* Soundings

During the strong coastal jet period the coupled simulation provided an atmospheric vertical structure (Fig. 5-9b) that was closer to the observed sounding profile (Fig. 5-9a) than the uncoupled simulation (Fig. 5-9c). Both the observed and model results showed that the typical marine layers in the SEP were composed of cool moist air capped by drier warm air. However, in the uncoupled simulation it was too dry above the boundary layer. The subsidence inversion shown from the soundings compares well to both the coupled and uncoupled runs. The strong southeast wind in the lower layer switched to the northwest at ~750 mb in the observation, at ~800 mb in the coupled COAMPS and ~850 mb in the uncoupled run. The cloud layer could be clearly seen in both the observed and coupled COAMPS sounding profiles, but it was not as clear in the uncoupled run. However, the coupled run's cloud layer was about 40 mb lower than the observed layer.

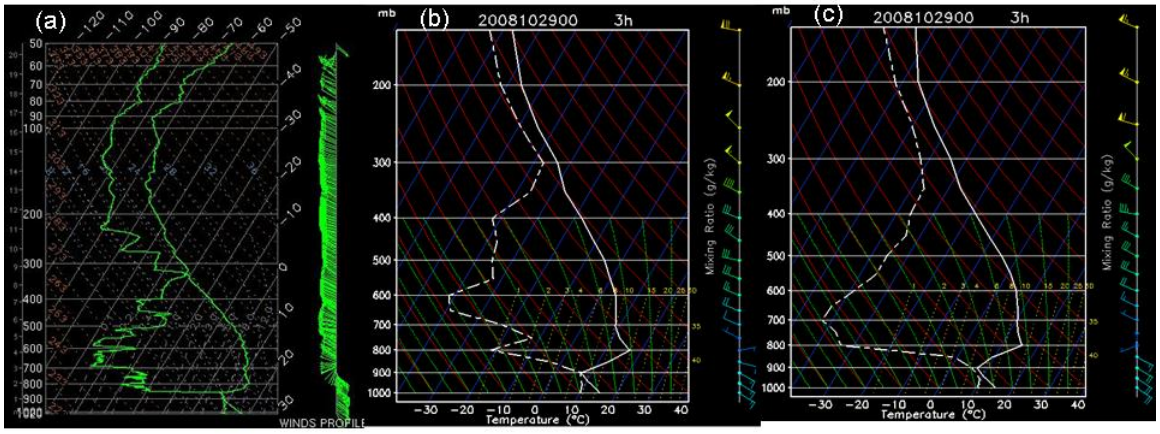

Figure 5-9: Soundings (a): observed from the R/V *BROWN*, (b): from coupled COAMPS, and (c): from uncoupled COAMPS at 03 UTC 29 October 2008 during the strong coastal jet period. Ship location: -19.6°S and -77.6°W.

During the weak coastal jet period (Fig. 5-10), the southeast wind in the low level decreased significantly. There was a diminished northwest wind during the strong coastal jet period. The wind profile from the coupled simulation resembled the observed profile better than the uncoupled simulation. The cloud layer reached a similar height between the observations and the coupled COAMPS. It was not as well simulated in the uncoupled run.

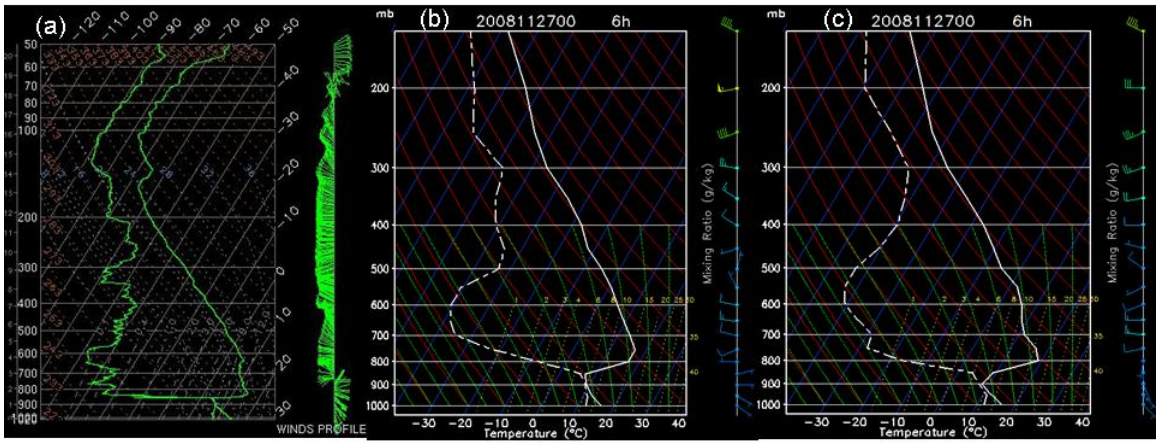

Figure 5-10: Soundings (a): observed from the R/V *BROWN*, (b): COAMPS coupled simulation, and (c): COAMPS uncoupled simulation at 06 UTC 27 November 2008 during the strong coastal jet period. Ship location: -20.1°S and -77.3°W.

Atmospheric vertical structure from COAMPS coupled and uncoupled simulations were verified using the sounding profiles from the R/V *BROWN*. A total of 182 profiles were collected from 22 October through 28 November, 2008. The RMSEs were small at the surface and upper layers for all variables (Fig. 5-11). The largest errors occurred near the top of the boundary layer for potential temperature, relative humidity, and water vapor. The error for potential temperature was about 6°C for the coupled run and 8°C for the uncoupled run, both about 5-7°C larger than at the surface. The errors for the u- and v-components of wind speed were about 2 m/s at the surface and increased steadily upward. Coupled and uncoupled simulations did not show large differences for wind speed.

The COAMPS simulations revealed a cold bias, with more moisture and water vapor near the top of the boundary layer. The uncoupled run was about 6°C colder than the observations and the coupled run reduced the cold bias to 3°C. More moisture was provided in the coupled run, resulting in a smaller bias. For both coupled and uncoupled simulations, the biases were significantly smaller at the surface layer for potential temperature, relative humidity, and water vapor. The bias below 10 km for the wind speed remained small with a value less than 2 m/s. The difference in wind speed bias between coupled and uncoupled simulations became larger above the boundary layer.

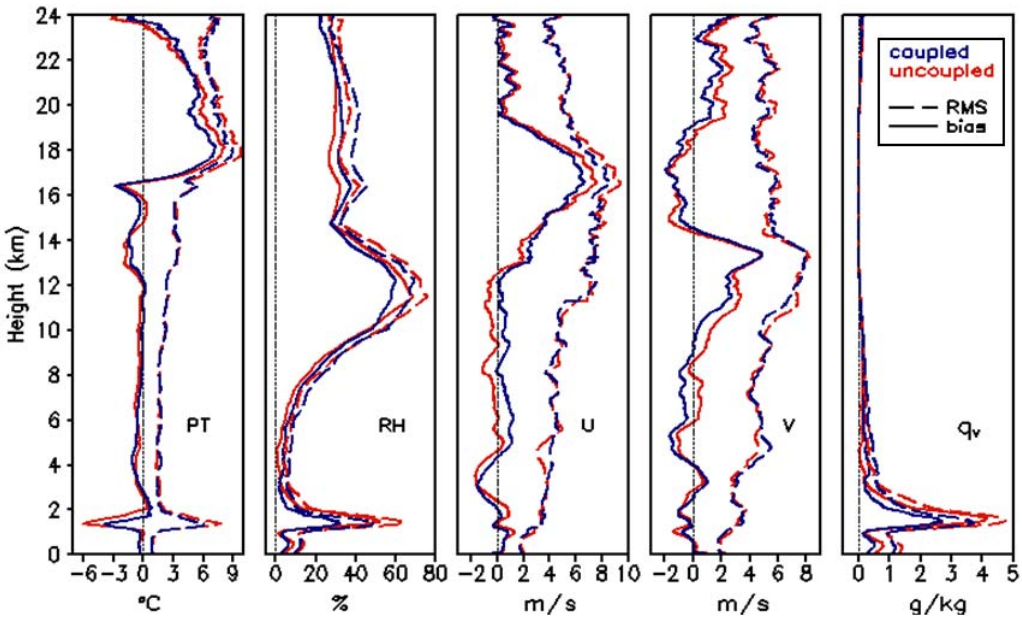

Figure 5-11: Bias and RMSE of (from left) potential temperature (PT), relative humidity (RH), u-component (U) and v-component (V) of wind speed, and water vapor (q_v) for the coupled and uncoupled simulations against the sounding profiles from the R/V *BROWN*.

3.5.3.4.2 Cloud Liquid Water Path Comparisons

The liquid water path from the COAMPS forecast was comparable to the TMI, AMSR-E, and SSM/I satellite observations (Fig. 5-12) from 20 October through 30 November, 2008. There was large cloud cover over the open ocean and less near the coastal area due to strong subsidence. The two-way coupled model was able to reproduce a similar liquid water path distribution along the southern Peruvian coast, where a narrow strip of cloud appeared, according to observations. The uncoupled model showed the smallest amount of liquid water path and less diurnal variation.

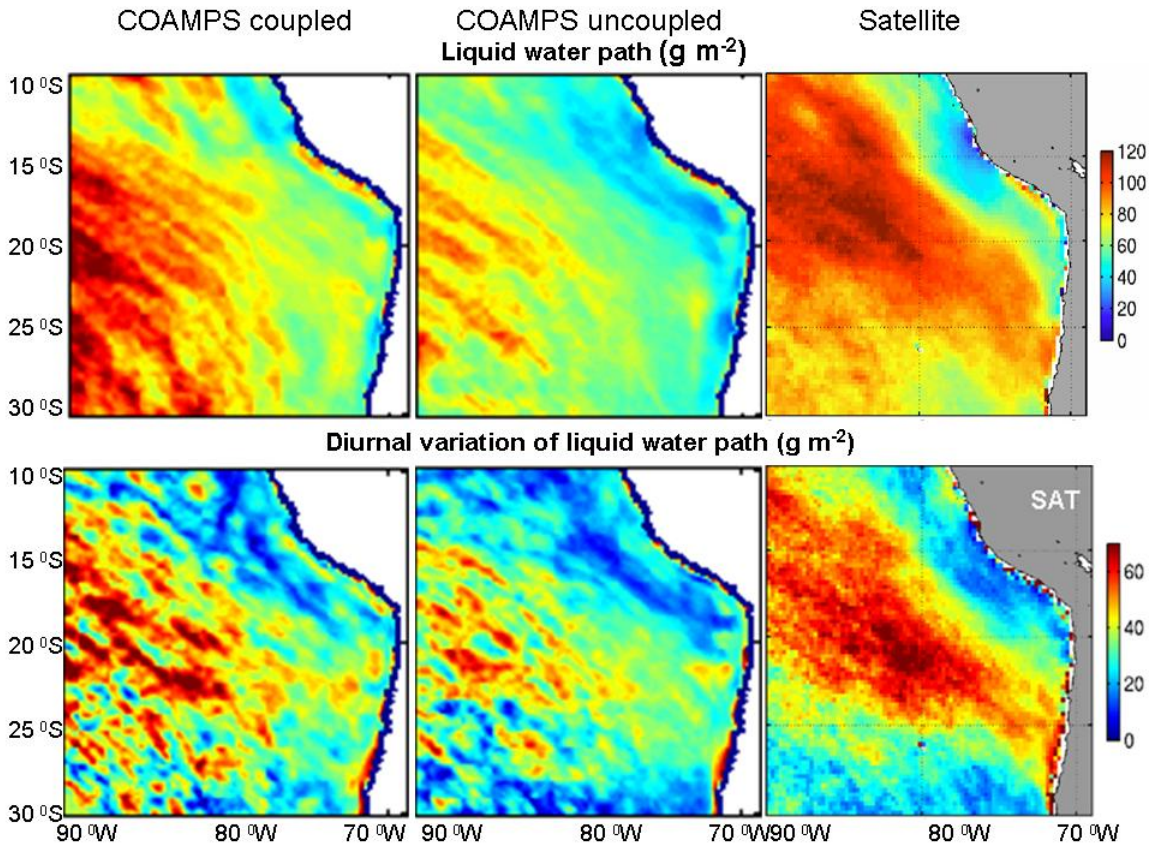

Figure 5-12: COAMPS coupled and uncoupled simulations compared to the satellite observation for liquid water path (g/m^2) (upper panel) and diurnal variation of liquid water path (g/m^2) (lower panel). All values are averaged from 20 October to 30 November, 2008.

3.5.3.4.3 Comparisons to Buoy Data

Statistics for comparisons of WHOI buoy observations to COAMPS coupled [c] and uncoupled [u] simulations from the 15 km grid 2 domain are provided in Table 5-1. In general, the coupled simulation improved the mean and standard deviation and reduced the bias and RMSE. There were smaller cold biases in 2 m air temperature and SST in the coupled simulation than observed in the uncoupled simulation. The sea level pressure from the coupled simulation was consistently more accurate than the uncoupled simulation (Fig. 5-13). Most correlation coefficients were above 0.5 for both simulations except for wind direction and relative humidity, due to mismatched phases between the simulation and observation. The statistical differences between the coupled and uncoupled runs were relatively small.

Table 5-1: Statistics for comparison of WHOI buoy (20°S, 85°W) data to the coupled and uncoupled COAMPS for a 40-day simulation. The time period for the statistics is from 25 October to 30 November, 2008. The time step is one hour. The number of observations (N) is 864.

Variable	Obs mean/STD	COAMPS mean/STD [c]	COAMPS mean/STD [u]	CC [c]	CC [u]	MB [c]	MB [u]	RMSE [c]	RMSE [u]
U-wind (m/s)	-4.77/1.39	-5.32/1.56	-5.50/1.61	0.55	0.52	-0.54	-0.72	1.60	1.65
V-wind (m/s)	3.77/1.62	4.90/1.51	4.91/1.53	0.61	0.56	1.13	1.14	1.92	1.95
Total wind (m/s)	6.23/1.63	7.36/1.67	7.43/1.69	0.67	0.65	1.13	1.19	1.75	1.76
Wind dir.	127.5/13.46	132.7/11.48	133.1/11.75	0.25	0.23	5.21	3.63	17.02	15.56
Air temp (°C)	18.42/0.61	18.14/0.41	18.04/0.48	0.64	0.62	-0.28	-0.35	0.54	0.61
SST(°C)	18.91/0.27	18.71/0.28	18.75/0.36	0.67	0.65	-0.19	-0.20	0.29	0.30
Rel. humidity (%)	74.05/5.36	70.81/5.56	69.64/5.63	0.17	0.10	-3.24	-4.41	8.61	8.73
Sea-level pressure (mb)	1018/1.60	1020/1.54	1022/1.67	0.67	0.64	1.73	1.96	2.14	2.58

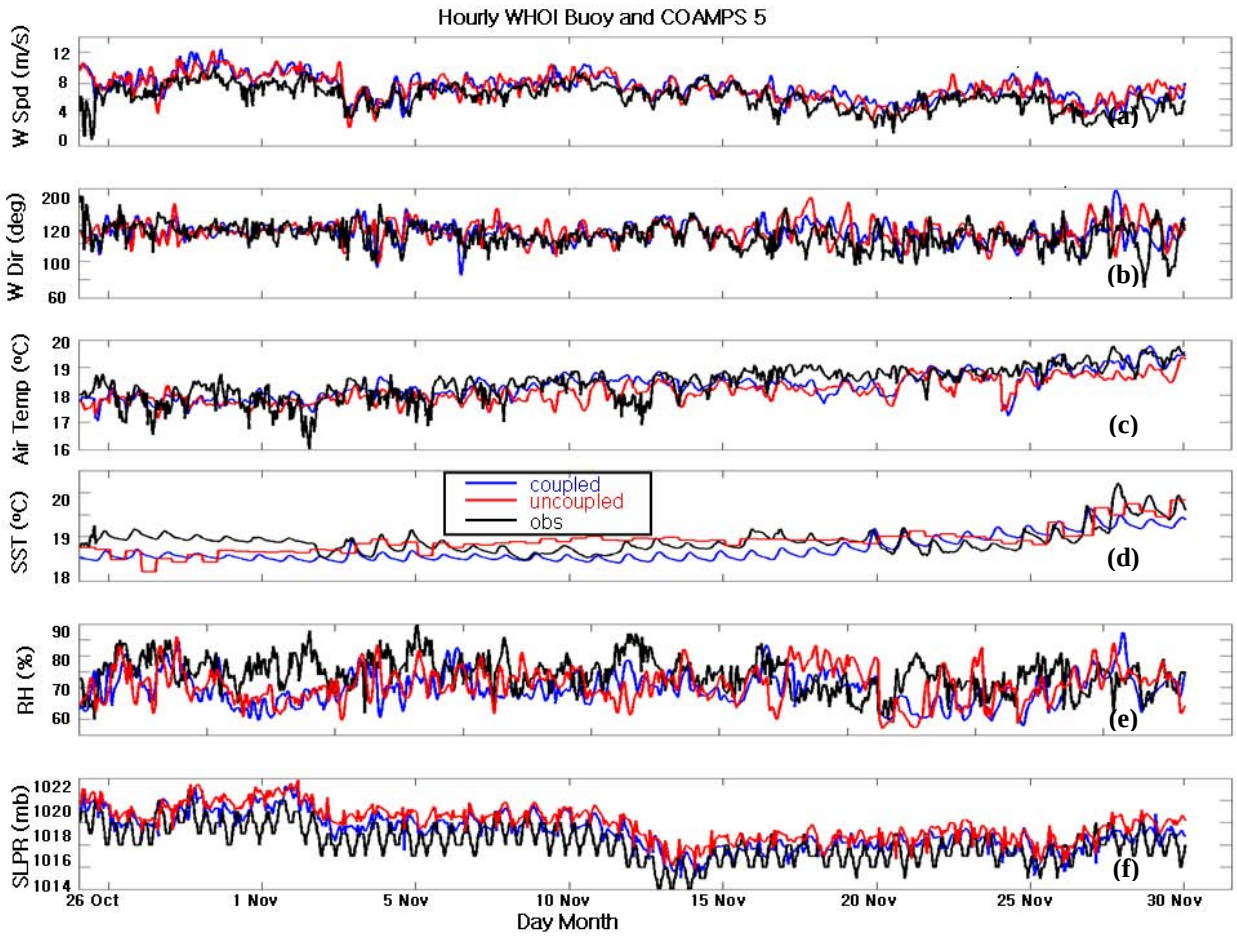

Figure 5-13: Time series of WHOI buoy measurements (black) and COAMPS coupled (blue) and uncoupled (red) simulations from the 15 km grid 2 domain for (a): wind speed (m/s), (b): wind direction, (c): air temperature (°C), (d): SST (°C), (e): relative humidity (%), and (f): pressure (mb). Statistics are shown in Table 5-1.

3.5.3.4.4 QuikSCAT Wind Comparisons

During the strong coastal jet period the COAMPS simulated 10 m wind speeds were larger than the QuikSCAT observed, especially near the coast (Fig. 5-14, top panels). The maximum speed near the coast covered a smaller area in the coupled simulation, which was more similar to the QuikSCAT observations than the uncoupled run. The second maximum at 20°S and 90°W was more obvious in the model simulations. The weak wind was confined to the coast near the border of Peru and Chile by the model simulations but extended southward in the observations.

During the weak coastal jet period (Fig. 5-14, bottom panels) the coupled and uncoupled runs predicted larger areas of low wind speeds than the QuikSCAT observations. The coupled simulation performed slightly better than the uncoupled and the coupled COAMPS wind distribution patterns were more similar to observations.

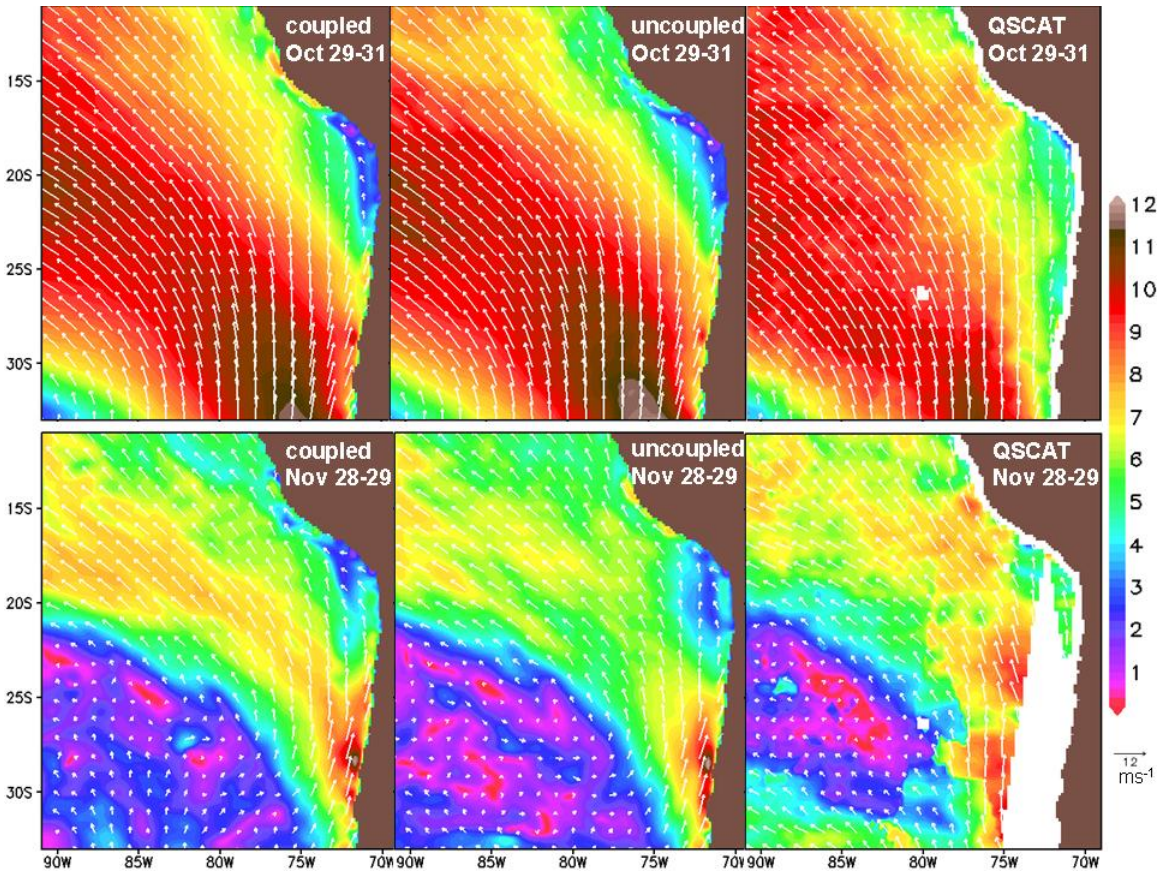

Figure 5-14: Mean COAMPS 10 m wind and QuikSCAT wind for the strong coastal jet period of 29-31 October, 2008 (upper panels) and for the weak coastal jet period of 28-29 November, 2008 (lower panels).

3.5.3.4.5 TRMM Microwave Imager (TMI) Comparisons

NCOM SSTs from coupled and uncoupled simulations were compared with TMI SST observations (Fig. 5-15, top panels) in cold, upwelled waters near the Chilean coast during the strong coastal jet period. The coupled simulation produced more cold water than the uncoupled run. The westward propagation of upwelled cold water had similar patterns between the coupled simulation and the TMI SSTs. The cold water extension northward in the coupled simulation also closely resembled the observed SST distribution.

During the weak coastal jet period (Fig. 5-15, bottom panel), warm water returned to the coastal area from the north and recapped the upper surface. The uncoupled simulation produced warmer water than both coupled COAMPS and TMI SST. There were still some upwelled cold waters that remained at the surface. A trace of cooler water related to the coastal jet was evident from observations, but not reproduced in COAMPS.

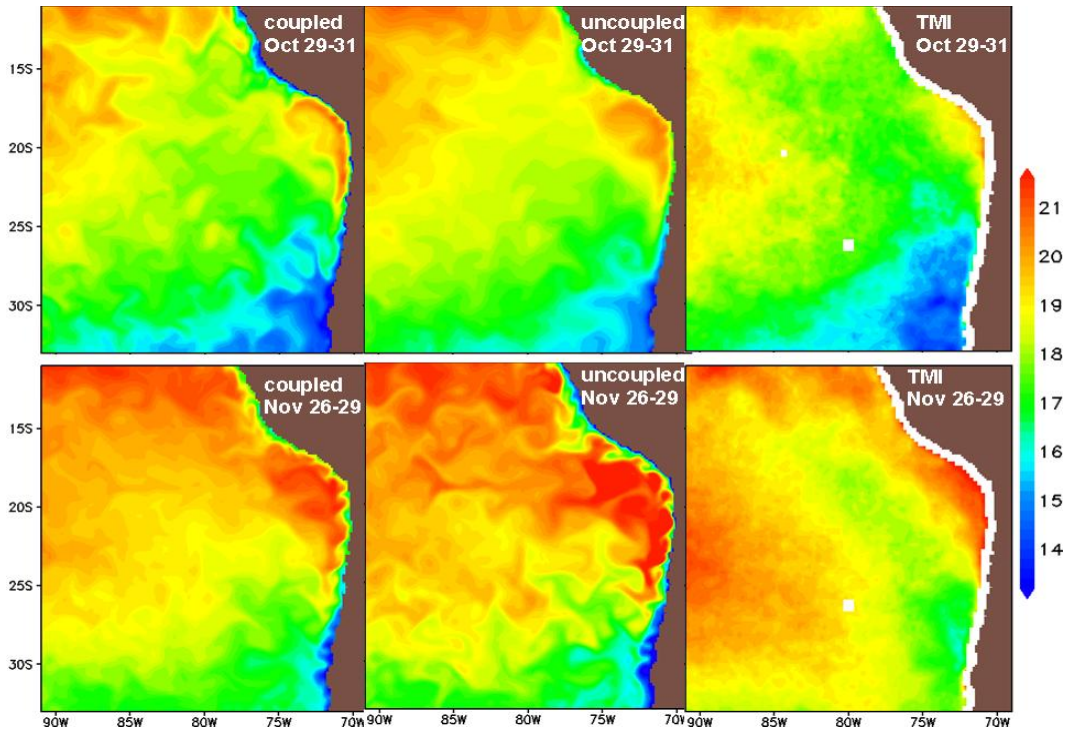

Figure 5-15: Mean NCOM SST for the strong coastal jet period of 29-31 October, 2008 (upper panels) and for the weak coastal jet period from 28-29 November, 2008 (lower panels).

4.0 OPERATIONAL IMPLEMENTATION

The ESMF-based coupled atmosphere-ocean COAMPS system will be run operationally at both FNMOC and NAVOCEANO. At FNMOC, the coupled system will be configured and run using the COAMPS-On Scene (COAMPS-OS®[2]) software suite developed and maintained by NRL Monterey. COAMPS-OS contains a Graphical User Interface to allow setup of the atmosphere and ocean model grids. COAMPS-OS version 2.2 (V2.2) will support this two-way coupled system on FNMOC's A2 and Centralized Atmospheric Analysis and Prediction System (CAAPS) clusters. A script-based version of the coupled system will be available for operational implementation at NAVOCEANO. COAMPS-OS V2.2 will also support the setup of wave models.

4.1 Required Inputs

Coupled COAMPS requires real-time access to all available atmospheric and ocean observations such as those routinely stored on the NAVOCEANO HPC archive systems (e.g., *NEWTON*). The system also needs real-time access to the latest available analysis and forecast fields from both NOGAPS and global NCOM (run at NAVOCEANO) for initial and lateral boundary conditions in the event of a cold start. Furthermore, the system must include all relevant surface data bases (e.g., terrain, bathymetry, land/sea boundary, ground wetness, ice cover, etc.) and would benefit from a single, consistent, combined global terrain-bathymetry database.

4.2 Recommended Spin-Up Time

The required spin-up time for a standalone data assimilative atmospheric model (e.g., no coupling) is no more than 12 hours (Jim Doyle, pers. comm.). For example, in the Adriatic bora studies of Test Case 1, a 24-hour spin-up was shown to be quite sufficient for the atmosphere (with little difference between a one and seven-day spin-up for simulating bora jets successfully). However, when the atmospheric model is coupled to the ocean model, the spin-up time can depend heavily on the location and application. For some oceanographic processes such as deep circulation, very large spin-up times on the order of years may be required. This is not realistic for standard applications. However, for the more common operational applications of predicting the upper ocean (e.g., the top 200 m), some recommendations may be made as follows, based on the current study. For Test Case 2, the LASIE07 case, a five-day spin-up was sufficient to capture the surface and shallow summer mixed layer variability. However the structure of the thermocline, say, at 50 m, did not change much from the initial conditions over the course of the one month simulation. Therefore, either a spin-up of much longer than a month or improved data assimilation in either GNCOM or the coupled model ocean is required to realistically model the LASIE07 thermocline. For the wintertime KESS study, a regional East Asian Seas NCOM provided the initial conditions for the nested higher

[2] COAMPS-OS is a registered trademark of the Naval Research Laboratory.

resolution NCOM validation studies. In that case, the mixed layer was over 200 m deep. If the initial SST field was in error, it would take months to spin-up the mixed layer in response to fluxes in order to correct the SST field. In that case, the best solution is to improve data assimilation in either GNCOM or the coupled model, rather than use an unrealistically long spin-up time. However, the KESS summer simulations had a short spin-up of about 3 days, which may improve the equilibrium of SST and mixed layer thickness within the COAMPS atmosphere. In summary, a spin up of a few days to a week is recommended, as this will allow the atmosphere and uppermost ocean layers to adjust in many, but not all cases. For situations that depend on deeper processes (such as the winter KESS case), the focus should be on providing sufficient observations for an effective data assimilation scheme that makes realistic predictions.

4.3 Resource Requirements

Testing with the ESMF-based coupled COAMPS (two-way coupling) has shown that the overhead is under 2% compared to the models running individually. The actual requirements may vary considerably, based on the areas covered and the exact configuration of the ocean model grids compared to the atmospheric model grid, as the ocean models are typically of a higher resolution than the atmospheric driver grid.

4.4 Future Work

Validation testing will begin in FY10 for the two-way coupled ocean-wave prediction system. Wave information such as Stokes drift and wave radiation stresses are passed to the ocean model (NCOM), and water levels and surface currents are passed back to the wave model (SWAN or WW3). Future work will address the validation of atmosphere-wave and atmosphere-ocean-wave coupled prediction systems. We plan for all of these systems to be configured and run using COAMPS-OS. Additionally, NRL-MRY has been developing and testing COAMPS-TC for tropical cyclone prediction. A coupled COAMPS-TC with both ocean and wave components will be ready for validation testing within the next few years.

5.0 TEST CASE SUMMARIES

5.1 Test Case One: Adriatic Circulation Experiment (ACE) Conclusions

Overall, the fully coupled COAMPS model run for the Adriatic Sea showed improvements over the uncoupled run, especially with regard to heat fluxes produced by the NCOM SSTs in the fully coupled run versus the NCODA SSTs in the uncoupled run. The correlation coefficients for the winds, wind stresses, and heat fluxes showed no appreciable differences between the coupled and uncoupled runs, while the RMSE for winds in both the R/V *KNORR* and Gulf of Trieste buoy observations were only slightly lower for the uncoupled run.

The NCOM validation results for the fully-coupled run demonstrated that the surface currents were sensitive to both the strength and position of the Trieste and Senj bora jets. The discrepancies between the NCOM results and the observations can largely be attributed to the southward shift of the Trieste jet in the atmospheric model. The wind stress curl pattern associated with COAMPS produced a double gyre surface current pattern that was shifted slightly southward compared to the mooring observations. The fully-coupled run showed some slight improvements in the current speed and direction at several of the ADCP stations; however, since the wind forcing was similar for both the coupled and uncoupled runs, little improvement in the double gyre current pattern was noted.

5.2 Test Case Two: Ligurian Air-Sea Interaction Experiment (LASIE07) Conclusions

The coupled COAMPS model has been validated against *in situ* and satellite data from the LASIE07 experiment in the Ligurian Sea (western Mediterranean) during the summer of 2007. First, a month long simulation was performed with atmospheric data assimilation for both a fully coupled and uncoupled case using an analysis SST to compute bulk fluxes. Second, a short 3-day run was performed in non-assimilating mode to isolate the effects of coupling more clearly.

The fully coupled model performed well in the month-long simulation when compared against the observational data. The time-mean structure of the near-surface wind field matched up to QUIKSCAT satellite data and added enhanced detail to that seen by satellite. When evaluated against independent (non-assimilated) buoy data, the wind speed correlation coefficient was 0.68 at a deep ocean station, and 0.43 at a coastal station. The model slightly under-predicted wind speeds at the deep station and overestimated wind speeds at a coastal station, due to an overly strong land breeze in the model.

Solar radiation at the deep water station was generally larger in the model than in observations on days of observed cloud cover. As a result, the coupled model had a much larger diurnal SST cycle than observed. Also, about 10 days into the run the model SST developed a warm bias relative to the deep water station, partly due to the underestimation of a strong wind event from

25-27 June. Comparisons with multiple SST data sources (satellite and *in situ*) confirm the warm bias.

Correlations between the model and observations for sensible and latent heat fluxes were 0.53 and 0.62 respectively, significant at 99%. The model tends to have large daytime spikes in heat flux which often have no observed counterpart. These are associated with cold, dry air and a possibly inflated atmospheric tide and/or land/sea breeze circulation. The net longwave radiation correlation coefficient was 0.61 between model and observations, but the model exhibited events of near-zero net radiation in early morning more frequently than observed.

In the month-long assimilative run at the deep water ODAS site, the differences between the coupled and uncoupled runs were generally small. This may be partly attributed to the use of atmospheric data assimilation. A short, three-day, non-assimilating run was performed to investigate this possibility. Both the coupled and uncoupled runs started with the same initial conditions. The SST for the uncoupled run was kept fixed at the initial value. The 3-day run encompassed a strong Mistral wind event that caused significant ocean surface cooling in both observations and model. In the areas of strongest cooling, the coupled response to the winds led to a significant reduction in surface stress (up to 20%) and latent heat flux (up to 50%) relative to the uncoupled run.

While differences between the coupled and uncoupled runs were negligible in deeper water, the coupled COAMPS model performed significantly better at the coastal site. The use of SEPTR temperature data in conjunction with METEO buoy atmospheric variables allowed for a closer examination of model performance in the coastal zone. The highlights of this study included a much improved coupled COAMPS SST compared to the NCODA SST. Even before and after the appearance of an erroneous cold eddy in NCODA, the coupled model was still closer to the observations. This was likely due to an overly smooth representation of the coastal zone in the standard NCODA analysis (NCODA ‘default settings’ were used with no attempt to modify length-scales for coastal regions). Further, SST analyses such as NCODA and the CNR GOS satellite product are designed to represent a ‘bulk’ or ‘foundation’ temperature, below the direct influence of diurnal warming. For air-sea interaction and coupled model purposes, it is important to incorporate the effects of diurnal warming and other near-surface processes. As a result, the near-surface air temperature was much improved in the coupled model but still tended to be biased low compared to observations. Relative humidity was also slightly improved in coupled COAMPS.

Latent heat flux was greatly improved in the coupled model in terms of mean bias and RMSE, due to a strong dependence on the SST via its saturation specific humidity. Saturation specific humidity is an exponential function of SST (the Clausius-Clapeyron equation), and differences in absolute SST are important. The uncoupled model exhibited periods of zero or below-zero latent heat flux that were not observed. However, coupled COAMPS had no discernable improvement in sensible heat flux. Although absolute SST and air temperature were improved, their differences were not, and the coupled model tended to be too unstable. Wind stress differences between the coupled and uncoupled models were small. It should be noted that data assimilation was used in the atmospheric model. This may complicate the analysis by correcting both the coupled and uncoupled models towards ‘reality’.

Further analysis was done on the spatial variations of changes in SST and heat fluxes and their impact on the ocean and atmosphere. Averaged over one-month, the coupled COAMPS SST was higher than NCODA SST in the coastal LASIE07 zone by up to 2ºC. Analysis of observed SEPTR data showed that the coupled model SST was more accurate for the LASIE07 time frame. This caused stability differences between the coupled and uncoupled runs. There was a 50-100% enhancement of combined sensible and latent surface heat flux and a 25% enhancement of wind stress in the coupled model. The total heat flux out of the ocean was increased by 50-100 W/m^2, a 50-100% change. This total heat flux change affected the ocean model SST: averaged over a month it caused a 1º- 2ºC difference between the coupled and uncoupled ocean run, with a lower coupled SST (with less temporal averaging, differences of up to 3ºC were seen). This is consistent with a rough estimate that assumed the mixed layer temperature change was due solely to surface heat fluxes. Unfortunately, it was impossible to validate these SST differences against *in situ* data, as the observational data record stopped when the differences arose.

The changes in SST and heat fluxes lead to modifications of the atmospheric planetary boundary layer (PBL) and the ocean mixed layer depth (MLD). For a one month average, the height of the PBL was increased by 50-100 m with coupling, an increase of up to 25%. The absolute MLD changed by just 1 m, or ~10%, in the coastal zone (Again, with less temporal averaging, we saw MLD changes of 2 to 3 m, or up to 20%). There was good spatial correspondence between the PBL and SST changes, as well as between the MLD and SST changes, showing that it was indeed the influence of coupling that was causing these modifications (rather than unrelated internal ocean or atmospheric dynamics). In addition to changes in MLD, coupling caused a significant reduction in near-surface vertical sound speed gradient, such that there was less downward refraction compared to the uncoupled run.

The results from the coastal METEO site and previous results from ODAS may be compared to those found in the Adriatic Test Case 1. In the northern Adriatic Sea, the coupled model exhibited significantly better turbulent heat fluxes at the coastal sites (particularly in mean bias) than in the deeper waters surveyed by the R/V *KNORR*. This is largely due to poor representation of a cool coastal current by NCODA (Section 3.1.3.1.3; Pullen et al., 2007). Likewise, in the LASIE07 region there were improvements to latent heat flux at the coastal site but not at ODAS. This seemed to be due to poor representation by NCODA of a narrow band of warm SST near the coast. Hence, one of the primary advantages of the coupled model is in the representation of fine scale coastal features and their potential air-sea feedbacks.

5.3 Test Case Three: Autonomous Ocean Sampling Network (AOSN) Conclusions

The two-way coupled model was able to predict the onset of the relaxation and upwelling events very well. The coupled model-forecast of the upwelling area west of Point Año Nuevo was generally too narrow and did not exhibit a strong SST gradient as shown in the aircraft observations. However, the width of the upwelling west of Point Sur was close to the aircraft observations. The warm SST biases at the M1 and M2 moorings gave a larger negative air temperature feedback than the one-way coupled run. The cloud comparisons showed that the two-way coupled run predicted excessive stratus clouds, thus reducing the ability of the

incoming shortwave radiation to warm the low level atmospheric temperature. The results suggest that a longer spin-up time for the weak wind regime case is needed to reduce the initial model bias. Since the ocean and atmospheric model errors seemed to reinforce each other in the first two weeks of the AOSN simulation, a different coupling strategy may help reduce the bias by spinning up the mesoscale ocean in a one-way coupled mode.

5.4 Test Case Four: Kuroshio Extension System Study (KESS) Conclusions

During the wintertime extreme cold air outbreak over the warm pool region, COAMPS produced remarkably good surface winds. Both the uncoupled and coupled runs showed very similar results. The very deep ocean mixed layer (200 m) limited feedback from the ocean to the atmosphere during the short simulation. The coupled run had a smaller negative bias in relative humidity and a slightly smaller positive bias in wind speed, with better correlation than the uncoupled run, but not significantly so. Near the Kuroshio front, there was one instance where the surface winds from the coupled run were in better agreement with QuikSCAT, but the improvement was minor.

During summer, the mixed layer was shallower than 50 m. The coupled COAMPS showed less bias in relative humidity than the uncoupled run, but the air temperature was 0.5^{o}C cooler than the uncoupled run, which was already 0.5^{o}C too cold compared to observations. Wind speeds were in excellent agreement with the KEO observations, with only a 0.1 m/s bias for the coupled model. The coupled model 1 m ocean temperatures were in slightly better agreement with observations than the uncoupled run, particularly towards the end of the simulation. The bias was -1.33^{o}C versus -1.55^{o}C. Comparisons with QuikSCAT were excellent both for summer and winter. The latter is remarkable since the evolution of the storm systems was very rapid.

5.5 Test Case Five: The VAMOS Ocean-Cloud-Atmosphere-Land Study (VOCALS)

Two-way coupled COAMPS was able to capture clouds, mesoscale eddies, oceanic upwelling, and the complex environment of the low-level coastal jet in the VOCALS area. The characteristics of the strong coastal jet include dry and cold air, a high pressure system, and large wind stresses both nearshore and offshore of the Chilean coast. The atmosphere received significant latent heat flux and an unstable boundary condition that produced more clouds, as well as clouds that were more organized. In the ocean, COAMPS induced a large mixed layer depth. Strong upwelling associated with the coastal jet caused either barotropic or baroclinic instability and generated oceanic anti-cyclonic and cyclonic eddies that propagated westward with strong kinetic energy, especially in the upwelling center. The inertial oscillation along the 30°S latitude was significant, with phase shifted between the upper and lower layers.

During the strong coastal jet period, the coupled simulation provided better vertical structure of the atmosphere than did the uncoupled simulation when compared with the observed sounding profile from the R/V *BROWN*. Although the cloud layer was also better simulated by the coupled simulation, it was still about 40 mb lower than observed. Both coupled and uncoupled simulations resolved the subsidence inversion layer well. During the weak coastal

jet period, the coupled COAMPS cloud layer prediction compared better with the observations than the uncoupled simulation. The air above the cloud layer was also too dry in the uncoupled COAMPS. The coupled run predicted the height of the low-level jet well compared to observations during both strong and weak coastal jet periods.

For both coupled and uncoupled simulations, the mean bias and RMSE for potential temperature, relative humidity, wind speed and water vapor had similar values. The uncoupled run showed slightly smaller bias and RMSE than did the coupled run. A larger mean bias and RMSE appeared near the top of the boundary layer where the cloud layer was formed.

The coupled COAMPS gave reasonable results of the liquid water path along the southern Peruvian coast, where a narrow strip of cloud was simulated. The coupled liquid water path and diurnal variation were smaller than the observed. However, the coupled run compared more closely to observations than the uncoupled run, which had values even smaller than the coupled run.

The statistical comparisons of WHOI buoy data with the coupled COAMPS showed that the coupled run improved the mean and standard deviation and reduced the bias and RMSE. The coupled simulation decreased the cold biases for both 2 m air temperature and SST. The sea level pressure from the coupled simulation was consistently more accurate than the uncoupled simulation. Most correlation coefficients were above 0.5 for both simulations. The statistical differences between the coupled and uncoupled runs were relatively small.

During the strong coastal jet period, comparison between QuikSCAT and COAMPS winds indicated that the uncoupled model produced larger maximum wind speeds in the jet area than observations. The coupled simulation improved the SST forecast, comparing well to TRMM TMI observations.

6.0 CONCLUSION

The fully-coupled COAMPS system performed well in a wide range of conditions and areas, comparing favorably against observational datasets. Most importantly, we found that using high-resolution NCOM sea surface temperatures (SSTs) in the coupled model generally improves upon the use of NCODA SSTs in the uncoupled model to accurately predict surface heat fluxes. This is especially true in regions with a complex SST field (such as mesoscale eddies and fronts) and/or intense atmospheric events (e.g., the Adriatic Sea mesoscale bora and cold air outbreaks over the Kuroshio Extension), where turbulent heat fluxes have high spatial homogeneity and large gradients. The additional processing time and cost to couple both the ocean and atmosphere models is very small, furthering the advantages of using coupled COAMPS.

Specifically, the coupled COAMPS results produced improved SST relative to NCODA at the Adriatic coastal stations, the LASIE07 coastal site, the KESS summer case, and the AOSN and VOCALS cases. At the LASIE07 deep site, the coupled SST had larger errors than NCODA, mainly because of underpredicted wind forcing, while little difference was seen in the KESS winter case. The coupled SST was also better than standalone NCOM ocean simulations of SST at the LASIE07 deep site. Winds and wind stresses were generally well predicted by COAMPS in all test cases, with little difference between coupled and uncoupled runs. In the Kuroshio Extension area, for example, there was very good agreement between coupled COAMPS and QuikScat winds during a powerful storm system. However, at the LASIE07 coastal station COAMPS over-predicted the land breezes.

The near surface air temperature and relative humidity results varied from test case to test case and were much less conclusive. The coupled model air temperature was worse at AOSN, but better at VOCALS and the LASIE07 coastal site. The LASIE07 simulations provided good correlation coefficients and small biases, with little difference between coupled and uncoupled runs. However, AOSN, VOCALS and the winter KESS case exhibited poor correlations (and also a large bias in the KESS case), with only small differences between coupled and uncoupled runs. Sea level pressure was well predicted at the VOCALS and LASIE07 sites.

Turbulent heat fluxes were significantly improved in KESS and in the Adriatic and LASIE07 coastal sites but were not significantly different in the Adriatic and LASIE07 deep sites. For example, the mean heat flux biases were reduced by at least half at most of the coastal stations in the Adriatic. The heat flux changes were mostly due to SST improvements in the coupled model, rather than to any changes in the wind field or the air temperature and humidity.

Regarding the atmospheric boundary layer structure, the coupled model had better thermodynamic (temperature, moisture, clouds) and wind structure in VOCALS than the uncoupled model, but there was little difference at the LASIE07 deep site. In AOSN, the coupled run predicted more clouds than the uncoupled run, which may have contributed to air temperature biases.

The temperature structure of the oceanic mixed layer was improved in the KESS summer case, while little difference was seen between the coupled and uncoupled runs at the LASIE07 deep site. The validation results for near-surface currents were very location-dependent. In the Adriatic, correlation coefficients of 0.5 (significant at 99%) were found at one station, with the coupled model performing better than uncoupled, but most other stations had correlations less than 0.3. At the KESS site, ocean current predictions were sensitive to the model's ability to accurately simulate the location and strength of meanders and eddies in the Kuroshio Extension, and in the winter case a mislocation of an eddy close to the KESS site led to poor current predictions.

It should be noted that although atmospheric data assimilation was used in most of the test cases, ocean data assimilation was only used in the AOSN and VOCALS test cases, due to difficulties in implementing the NCODA 3D analysis in multiply-nested ocean domains. This problem is currently being addressed. However, the fact that the coupled model without ocean data assimilation produced better SSTs than NCODA (e.g., in the Adriatic, Ligurian Sea coastal stations, and the KESS summer case) demonstrates the impressive ability of the coupled model to simulate air-sea interaction processes.

In conclusion, the fully coupled COAMPS forecast system demonstrates a performance that in most cases equals or exceeds the forecast skills of the uncoupled system with very modest additional resource requirements. This is particularly true for simulations of turbulent heat flux and atmospheric boundary layer conditions over seas with high spatial SST variability.

7.0 ACKNOWLEDGEMENTS

The authors were supported by the High Performance Computing Modernization Program's Battlespace Environments Institute and NRL's 6.2 Core Program "Coupled Ocean-Wave Prediction System" (Program Element PE 0602435N).

We thank Clark Rowley, Lucy Smedstad, Shelley Riedlinger and James Dykes at NRL-Stennis Space Center for their assistance with model setup and for providing data for boundary and initial conditions. Special thanks to Jeff Book for providing Adriatic observational data and Sean Ziegeler of the User Productivity Enhancement, Technology Transfer and Training [PETTT] (PETTT) program for technical assistance. Sandro Carniel for providing LASIE07 turbulence data and discussions. Richard Hodur, Saša Gaberšek, Hao Jin, and Paul May from NRL-Monterey supported us with various infrastructure software used in the validation tests. We are grateful to Julie Pullen for R/V *KNORR* ship data, as well as Daniel Geiszler and John Cook for their many contributions to the validation effort. Joao Teixeira (NASA/JPL) and the LASIE07 experiment team are thanked for providing their extensive dataset.

8.0 TECHNICAL REFERENCES

8.1 COAMPS Software Documentation

Chen, S., J. Cummings, J. Doyle, R.H. Hodur, T. Holt, C. Liou, M. Liu, A. Mirin, J. Ridout, J.M. Schmidt, G. Sugiyama, and W.T. Thompson, (2003). "COAMPS Version 3 Model Description--General Theory and Equations". NRL/PU/7500--03-448, 145 pp.

Goerss, J., T. Hogan, K. Sashegvi, T. Holt, M. Rennick, T. Beeck, and P. Steinle. (2003). Validation Test Report for the NAVDAS/NOGAPS Data Assimilation System. Naval Research Laboratory, Monterey, CA., 26 pp.

Martin, P.J., C.N. Barron, L.F. Smedstad, A.J. Wallcraft, R.C. Rhodes, T.J. Campbell, C. Rowley, and S.N. Carroll, (2008a). "Software Design Description for the Navy Coastal Ocean Model Version 4.0." NRL/MR/7320--08-9149, Ocean Modeling Division, Naval Research Laboratory, Stennis Space Center, MS.

Martin, P.J., C.N. Barron, L.F. Smedstad, T.J. Campbell, A.J. Wallcraft, R.C. Rhodes, C. Rowley, T.L. Townsend, and S.N. Carroll, (2008b). "User's Manual for the Navy Coastal Ocean Model (NCOM) Version 4.0." NRL/MR/7320--08-9151, Ocean Modeling Division, Naval Research Laboratory, Stennis Space Center, MS.

Reidlinger, S., R. Preller and P. Martin, (2006). "Validation Test Report for the 1/16^{o} East Asian Seas Navy Coastal Ocean Model Nowcast/Forecast System." NRL/MR/7320/06/8978, Ocean Modeling Division, Naval Research Laboratory, Stennis Space Center, MS.

Smith, T.A., T.J. Campbell, R.A. Allard, and S.N. Carroll, (2010). "User's Guide for the Coupled Ocean Atmospheric Mesoscale Prediction System (COAMPS) Version 5.0". NRL/MR/7320--10-9208, Ocean Modeling Division, Naval Research Laboratory, Stennis Space Center, MS.

8.2 General Technical References

Artale, V., M. Astraldi, C. Buffoni and G. P. Gasparini, (1994). The seasonal variability of gyre-scale circulations in the northern Tyrrhenian Sea. *J. Geophys. Res.*, **99**: 14127-14137.

Barron, C.N., A.B. Kara, P.J. Martin, R.C. Rhodes, and L.F. Smedstad, (2006). Formulation, implementation and examination of vertical coordinate choices in the Global Navy Coastal Ocean Model (NCOM). *Ocean Modelling*, **11**: 347-375.

Becker, J.J., D.T. Sandwell, W.H.F. Smith, J. Braud, B. Binder, J. Depner, D. Fabre, J. Factor, S. Ingalls, S-H. Kim, R. Ladner, K. Marks, S. Nelson, A. Pharaoh, G. Sharman, R. Trimmer, J. vonRosenburg, G. Wallace, P. Weatherall, (2009). Global Bathymetry and Elevation Data at 30 Arc Seconds Resolution: SRTM30_PLUS, *Marine Geodesy*, in press.

Bignani, F., E. Bohm, E. D'Acunzo, R. D'Archino and E. Salusti, (2008). On the dynamics of surface cold filaments in the Mediterranean Sea. *J. Mar. Sys.*, **74**: 429-442.

Blumberg, A.F. and G.L., Mellor, (1983). Diagnostic and prognostic numerical circulation studies of the South Atlantic Bight. *J. Geophys. Res.*, **88**: 4579-4592.

Blumberg, A.F. and Mellor, G.L., (1987). "A description of a three-dimensional coastal ocean circulation model." In: Three-Dimensional Coastal Ocean Models. N. Heaps, ed., American Union, New York, N.Y., p. 208.

Book, J.W., H. Perkins, R.P. Signell, and M. Wimbush, (2007). The Adriatic Circulation Experiment winter 2002/2003 mooring data report: A case study in ADCP data processing, NRL Memo. Rep. NRL/MR/7330-07-8999, U. S. Naval Res. Lab., Stennis Space Center, MS.

Cronin, M.F., C. Meinig, C.L. Sabine, H. Ichikawa, and H. Tomita, (2008). Surface Mooring Network in the Kuroshio Extension. *IEEE Systems Journal*, 2(3): 424-430.

Cummings, J.A., (2005). Operational multivariate ocean data assimilation. *Q.J.R. Meteorol. Soc.*, **131**: 3583–3604.

Daley, R. and E. Barker, (2000). *The NAVDAS Source Book*, Naval Research Laboratory Publication NRL/PJ/7530-01-441. NRL, Monterey, CA.

Daley, R. and E. Barker, (2001). NAVDAS—formulation and diagnostics. *Mon. Weather Rev.* **129**: 869–883.

Da Silva, A.M., C.C. Young, and S. Levitus, (1994). Atlas of Surface Marine Data 1994, Vol.1: Algorithms and Procedures, NOAA Atlas NESDIS 6, U.S. Dept. of Commer., Washington, D.C., 83 pp.

Defant, F., (1951). Local winds, in Compendium of Meteorology, edited by T. F. Malone, Am. Meteorol. Soc., Boston, MA., pp. 655-672.

Dorman, C.E., S. Carniel, L. Cavaleri, M. Sclavo, J. Chiggiato, J. Doyle, T. Haack, J. Pullen, B. Grbec, I. Vilibic, I. Janekovic, C. Lee, V. Malacic, M. Orlic, E. Paschini, A. Russo, and R.P. Signell, (2006). February 2003 marine atmospheric conditions and the bora over the northern Adriatic, *J. Geophys. Res.*, **111**: C03S03.

Doyle, J.D., Q. Jiang, Y. Chao, J. Farrara, (2009). High-resolution atmospheric modeling over the Monterey Bay during AOSN II. *Deep-Sea Research II*, **56**: 87–99.

Drobinski, P., S. Bastin, V. Guenard, J.-L. Caccia, A.M. Dabas, P. Delville, A. Protat, O. Reitebuch, and C. Werner, (2005). Summer mistral at the exit of the Rhone valley. *Q.J.R. Met. Soc.*, **131**: 353-375.

Fairall, C.W., E.F. Bradley, D.P. Rogers, J.B. Edson, and G.S. Young, (1996a). Bulk parameterization of air-sea fluxes for Tropical Ocean-Global Atmosphere Coupled-Ocean Atmosphere Response Experiment. *J. Geophys. Res.*, **101**: 3747-3764.

Fairall, C.W., E.F. Bradley, J.S. Godfrey, G.A. Wick, J.B. Edson and G.S. Young, (1996b). Cool-skin and warm layer effects on sea surface temperature. *J. Geophys. Res.*, **101**: 1295-1308.

Grossman, R.L. and A.K. Betts, (1990). Air-sea interactions during an extreme cold air outbreak from the eastern coast of the United States. *Mon. Wea. Rev.*, **118**: 324-342.

Hodur, R.M., (1997). The Naval Research Laboratory's Coupled Ocean/Atmosphere Mesoscale Prediction System (COAMPS). *Mon. Wea. Rev.* **125**: 1414-1430.

Hogan, T., and T. Rosmond, (1991). The description of the Navy Operational Global Atmospheric Predictions System's spectral forecast model. *Mon.Wea. Rev.*, **119**: 1786-1815.

Jerlov, N.G., (1976). Marine Optics. Elsevier, New York.

Jurcec, V., (1988). The Adriatic frontal bora type, *Croatian Meteorol*., **23**: 13-25.

Kain, J.S., and J.M. Fritsch, (1993). Convective parameterization for mesoscale models: The Kain-Fritsch scheme. The representation of Cumulus Convection in numerical models, Meteor. Monogr., *Am. Met. Soc*., **46:** 165-170.

Kara, A.B., P.A. Rochford and H. E. Hurlburt, (2000). An optimal definition for mixed layer depth. *J. Geophys. Res*., **105**: 16803-16821.

Kundu, P.K., (1976). Ekman veering observed near the ocean bottom, *J. Phys. Oceanogr*., **6**: 238-242.

Kuzmic, M., I. Janekovic, J.W. Book, P.J. Martin, and J.D. Doyle, (2006). Modeling the northern Adriatic double-gyre response to intense bora wind: A revisit, *J. Geophys. Res*., **111**: C03S13.

Large, W.G., J.C. McWilliams, and S.C. Doney, (1994). Oceanic vertical mixing: a review and a model with a nonlocal boundary layer parameterization. *Rev. Geophys.*, **32**: 363-403.

Liu, W.T., K.B. Katsaros, and J.A. Businger, (1979). Bulk parameterization of air–sea exchanges of heat and water vapor including the molecular constraints at the interface. *J. Atmos. Sci.,* **36:** 1722–1735.

Louis, J.F., M. Tiedtke, J.F. Geleyn, (1981). A short history of the operational PBL-parameterization, at ECMWF, Workshop on Planetary Boundary Layer Parameterization, 25-27 Nov. 1981, pp. 59-79.

Louis, J.F., (1979). A parametric model of vertical eddy fluxes in the atmosphere. *Bound. Layer Meteor*., **17**: 187-202.

Martin, P.J., J.W. Book, and J.D. Doyle, (2006). Simulation of the northern Adriatic circulation during winter 2003, *J. Geophys. Res*., **111**: C03S12.

Martin, P.J., G. Peggion, and K.J. Yip, (1998). "A comparison of several coastal ocean models." NRL Report NRL/FR/7322--97-9692. Naval Research Laboratory, Stennis Space Center, MS., pp. 96.

Marullo, S., B. Buongiorno Nardelli, M. Guarracino and R. Santoleri, (2007). Observing the Mediterranean from space: 21 years of Pathfinder-AVHRR sea surface temperatures (1985 to 2005): re-analysis and validation. *Ocean Science*, **3**: 299-310.

Maximenko, N.A., and P.P. Niiler, (2005). Hybrid decade-mean global sea level with mesoscale resolution. In N. Saxena (Ed.) Recent Advances in Marine Science and Technology, 2004, pp. 55-59. Honolulu: PACON International.

Perilli, A., V. Rupolo and E. Salusti, (1995). Satellite investigations of a cyclonic vortex in the central Tyrrhenian Sea (western Mediterranean Sea). *J. Geophys. Res*., **100**: 2487-2499.

Perkins, H.T., F. de Strobel, and L. Gualdesi (2000), The Barny Sentinel Trawl-resistant ADCP bottom mount: Design, testing, and application, *IEEE J. Oceanic Eng*., **25**: 430-436.

Pierce, S.D., R.L. Smith, P.M. Kosro, J.A. Barth, C.D. Wilson, (2000). Continuity of the poleward undercurrent along the eastern boundary of the mid-latitude Pacific. *Deep-Sea Res. II*, **47**: 811-829.

Pullen, J., J.D. Doyle, and R. Signell, (2006). Two-way air-sea coupling: a study of the Adriatic, *Mon. Weather Rev*., **134**(5): 1465-1483.

Pullen, J., J.D. Doyle, T. Haack, C. Dorman, R.P. Signell, and C.M. Lee, (2007). Bora event variability and the role of air-sea feedback, *J. Geophys. Res*., **112**: C03S18.

Qiu, B., P. Hacker, S. Chen, K.A. Donohue, D.R. Watts, H. Mitsudera, N.G. Hogg and S.R. Jayne, (2006). Observations of the Subtropical Mode Water evolution from the Kuroshio Extension System Study. *J. Phys. Oceanogr.*, **36**: 457-473.

Ramp, S.R., Davis, R.E., Leonard, N.E., Shulman, I., Chao, Y., Robinson, A.R., Marsden, J., Lermusiaux, P., Frantantoni, D., Paduan, J.D., Chavez, F., Bahr, F.L., Liang, S., Leslie, W., Li, Z., (2009). Preparing to predict: the Second Autonomous Ocean Sampling Network (AOSN-II) experiment in the Monterey Bay. *Deep-Sea Res. II*, **56**: 68-86.

Rixen, M., J.W. Book, A. Carta, V. Grandi, L. Gualdesi, R. Stoner, P. Ranelli, A. Cavanna, P. Zanasca, G. Baldasserini, A. Trangeled, C. Lewis, C. Trees, R. Grasso, S. Giannechini, A. Fabiani, D. Merani, A. Berni, M. Leonard, P. Martin, C. Rowley, M. Hulbert, A. Quaid, W. Goode, R. Preller, N. Pinardi, P. Oddo, A. Guarnieri, J. Chiggiato, S. Carniel, A. Russo, M. Tudor, F. Lenartz, and L.Vandenbulcke, (2009). Improved ocean prediction skill and reduced uncertainty in the coastal region from multi-model super-ensembles. *J. Mar. Sys*. **78**(1): S282-S289.

Rosenfeld, L.K., F.B. Schwing, N. Garfield, D.E. Tracy, (1994). Bifurcated flow from an upwelling center: a cold water source for Monterey Bay. *Cont. Shelf Res.*, **14**: 931-964.

Rutllant, J., (1993). Coastal lows and associated southerly winds in north-central Chile. Preprints, Fourth Int. Conf. on Southern Hemisphere Meteorology, Hobart, Australia, *Amer. Meteor. Soc*., pp. 268-269.

Rutllant, J., I. Masotti, J. Calderon, and S. Vega, (2004). A comparison of spring coastal upwelling off central Chile at the extremes of the 1996-1997 ENSO cycle. *Cont. Shelf Res*., **24**: 773-787.

Salusti, E., (1998). Satellite images of upwellings and cold filament dynamics as transient effects of violent air-sea interactions downstream from the island of Sardinia. *J. Geophys. Res*., **103**: 3013-3031.

Shinoda T., (2005). Impact of the Diurnal Cycle of Solar Radiation on Intraseasonal SST Variability in the Western Equatorial Pacific. *J. of Climate*, **18**(14): 2628.

Shulman, I., C. Rowley, S. Anderson, S. DeRada, J. Kindle, P. Martin, J. Doyle, J.A. Cummings, S. Ramp, F. Chavez, D. Fratantoni, R. Davis, (2009). Impact of glider data assimilation on the Monterey Bay model. AOSN II: The Science and Technology of an Autonomous Ocean Sampling Network. *Deep Sea Research Part II: Topical Studies in Oceanography*, **56**(3-5): 188-198.

Small, R.J., T. Campbell, J. Teixeira, T.A. Smith, J. Dykes, S. Chen, and R. Allard, (2010). Air-Sea Interaction in the Ligurian Sea: Numerical Simulation and In-Situ Data in the Summer of 2007. In preparation.

Talley, L. D., (1997). North Pacific intermediate water transports in the mixed water region. *J. Phys .Oceanogr.*, **27**: 1795-1803.

Teixeira, J., (2007). Ligurian Sea Air-Sea Interaction experiment (LASIE) trial plan. NATO Undersea Research Center, La Spezia, Italy, 30pp. NATO UNCLASSIFIED.

Tseng, Y.H., D.E. Dietrich and J.H. Ferziger, (2005). Regional circulation of the Monterey Bay Region-Hydrostatic versus non-hydrostatic modeling. *J. Geophys. Res.-Ocean*, **110**: C09015.

Vesecky, J., J. Drake, M. Plume, C. Teague, L. Meadows, Y. Fernandez, K. Davidson, J. Paduan, (2001). Multifrequency HF radar observations of surface currents:

measurements from different systems and environments. OCEANS, 2001. MTS/IEEE Conference and Exhibition, **2**: 942-948.

Wyrtki, K., L. Magaard, and J. Hagar, (1976). Eddy energy in the oceans. *J. Geophys. Res.*, **81:** 2641–2646.

Xue, H., J. M. Bane and L. M. Goodman, (1995). Modification of the Gulf Stream through strong air-sea interaction in winter: Observations and numerical simulations. *J. Phys. Oceanogr*., **25**: 533-557.

Yu, L., X. Jin, and R.A. Weller, (2008). Multidecade Global Flux Datasets from the Objectively Analyzed Air-sea Fluxes (OAFlux) Project: Latent and sensible heat fluxes, ocean evaporation, and related surface meteorological variables. Woods Hole Oceanographic Institution, OAFlux Project Technical Report. OA-2008-01, 64pp. Woods Hole, Massachusetts.

Yu, L., and R.A. Weller, (2007). Objectively Analyzed air-sea heat Fluxes (OAFlux) for the global oceans. *Bull. Ameri. Meteor. Soc.*, **88**: 527-539.

9.0 NOTES

9.1 Acronyms and Abbreviations

Acronym	Description
3D-VAR	Three-dimensional VARiational data assimilation
ACE	Adriatic Circulation Experiment
ADCP	Acoustic Doppler Current Profiler
AMSR-E	Advanced Microwave Scanning Radiometer-Earth Observing System
AOSN	Autonomous Ocean Sampling Network
AUV	Autonomous Underwater Vehicle
AVHRR	Advanced Very High Resolution Radiometer
CAAPS	Centralized Atmospheric Analysis and Prediction System
CC	California Current
CC	Correlation Coefficient
CLIVAR	Climate Variability and Predictability
CNR	Consiglio Nazionale delle Ricerche
COAMPS	Coupled Ocean and Atmosphere Mesoscale Prediction System
COAMPS-OS	Coupled Ocean and Atmosphere Mesoscale Prediction System- On Scene
COAMPS-TC	Coupled Ocean and Atmosphere Mesoscale Prediction System-Tropical Cyclone
CODAR	Coastal Ocean Dynamics Applications Radar
CPIES	Current-Pressure-Inverted-Echo-Sounders
CTD	Conductivity, Temperature and Depth
CU	California Undercurrent
DBDB2	Digital Bathymetric Database, resolution 2 km
DEM	Digital Elevation Model
DoE	Department of Energy
EAS	East Asian Seas
ENEA	Italian National Agency for New Technologies, Energy and Environment
ESMF	Earth System Modeling Framework
FNMOC	Fleet Numerical Meteorology and Oceanography Center
FWG	Forschungsanstalt der Bundeswehr für Wasserschall u. Geophysik
GNCOM	Global Navy Coastal Ocean Model
GOES	Geostationary Operational Environmental Satellite
GOS	Gruppo di Oceanografia da Satellite

Acronym	Description
GVC	General Vertical Coordinate
HPC	High Performance Computing
I/O	Input/Output
IC	Inshore Countercurrent
JAMSTEC	Japan Agency for Marine-Earth Science and Technology
JKEO	JAMSTEC Kuroshio Extension Observatory buoy
KEO	Kuroshio Extension Observatory
KESS	Kuroshio Extension System Study
LASIE07	Ligurian Air-Sea Interaction Experiment
LPC	Ligurian-Provençal Current
MB	Mean Bias
MLD	Mixed Layer Depth
MVOI	Multi-variate Optimum Interpolation
MYL2/2.5	Mellor-Yamada (vertical mixing) Level 2/2.5
NASA	National Aeronautics and Space Administration
NAVDAS	NRL Atmospheric Variational Data Assimilation System
NCAR	National Center for Atmospheric Research
NCEP	National Centers for Environmental Prediction
NCODA	Navy Coupled Ocean Data Assimilation
NCOM	Navy Coastal Ocean Model
NOAA	National Oceanographic and Atmospheric Administration
NOGAPS	Navy's Operational Global Atmospheric Prediction System
NRL	Naval Research Laboratory
NURC	NATO Undersea Research Centre
OAFlux	Object Analyzed Air-Sea Fluxes
ODAS	Ocean Data Acquisition System
PBL	Planetary Boundary Layer height
POM	Princeton Ocean Model
QuikSCAT	Quick Scatterometer
R/V	Research Vessel
RMSE	Root Mean Square Error
S	Salinity
SDD	Software Design Description
SeaWiFS	Sea-viewing Wide Field-of-view Sensor
SEP	Southeast Pacific
SEPTR	Shallow-water Environmental Profiler in Trawl-safe, Real-time configuration
SFSU	San Francisco State University
SRTM	Shuttle Radar Topography Mission

Acronym	Description
SSH (A)	Sea Surface Height (Anomaly)
SSM/I	Special Sensor Microwave/Imager
SST	Sea Surface Temperature
SWAN	Simulating WAves Nearshore
T	Temperature
T/ P	TOPEX/Poseidon
TC	Tyrrhenian Current
TMI	TRMM Microwave Imager
TRMM	Tropical Rainstorm Measuring Mission
UTC	Coordinated Universal Time
VAMOS	Variability of the American Monsoon Systems
VOCALS	VAMOS Ocean-Cloud-Atmosphere-Land Study
VTR	Validation Test Report
WCC	Western Corsica Current
WHOI	Woods Hole Oceanographic Institution
WW3	WaveWatch III

ANNEX A: Importance of SST to the Bulk Fluxes

In coupled ocean-atmosphere (no surface wave) models the air-sea interaction is governed by the bulk flux formulation. The sensible heat flux Q_{sen}, latent heat flux Q_{lat}, and wind stress $\underline{\tau}$ are given by

$$Q_{sen} = \pm\rho\, c_p \underline{\underline{C_H}} U (\underline{\underline{T_s}} - T_a) \tag{1a}$$

$$Q_{lat} = \pm\rho L_v \underline{\underline{C_E}} U (\underline{\underline{q_s}} - q_a) \tag{1b}$$

$$\underline{\tau} = \mp\rho \underline{\underline{C_D}} \left|\underline{U}\right| \underline{U} \qquad |\underline{\tau}| = \rho \underline{\underline{C_D}} U^2 \tag{1c}$$

where C_D is the drag coefficient, C_H is the exchange coefficient for heat, and C_E is for moisture. $\underline{U}$ is the wind velocity in the surface layer (typically at 10 m height). T and q are temperature and specific humidity: T_s denotes the SST and q_s the saturation specific humidity at the surface temperature, while the subscript *a* denotes the air value in the constant flux layer. ρ, c_p and L_v are the air density, specific heat capacity and latent heat of vaporization, respectively (Here the convention for sensible and latent flux is such that the plus sign is for the atmosphere and the minus sign for the ocean. For stress, the negative sign is for the atmosphere).

The terms that are double-underlined in (1) are directly influenced by the SST. In addition to the obvious dependence of T_s and q_s, the drag coefficients and exchange coefficients also depend on SST through the static stability. For example, the drag coefficient is given by

$$C_D = \frac{\kappa^2}{\ln\frac{z}{z_0} - \Psi_M\left(\frac{z}{L}\right)},$$

where κ is the Von Karmon constant, z_0 the roughness length, and ψ_M the stability function that depends on the height *z* and Obukhov length L. The Obukhov length L, in turn, depends on friction velocity and the static stability (related to air-sea temperature difference and humidity difference). Examples of how the drag coefficients and exchange coefficients depend on stability can be found in Liu et al. (1979).